# CHARACTERIZATION OF MULTISCALE POROSITY IN CEMENT-BASED MATERIALS: EFFECTS OF FLAW MORPHOLOGY ON MATERIAL RESPONSE ACROSS SIZE AND TIME SCALES

A Dissertation
Presented to
The Academic Faculty

by

Nathan Paul Mayercsik

In Partial Fulfillment
of the Requirements for the Degree of
Doctor of Philosophy in the
School of Civil and Environmental Engineering

Georgia Institute of Technology
August 2015

# CHARACTERIZATION OF MULTISCALE POROSITY IN CEMENT-BASED MATERIALS: EFFECTS OF FLAW MORPHOLOGY ON MATERIAL RESPONSE ACROSS SIZE AND TIME SCALES

Approved by:


Dr. Kimberly E. Kurtis, Advisor
School of Civil and Environmental Engineering
*Georgia Institute of Technology*

Dr. Lori Graham-Brady
Department of Civil Engineering
*Johns Hopkins University*

Dr. Laurence J. Jacobs
School of Civil and Environmental Engineering
*Georgia Institute of Technology*

Dr. Arun M. Gokhale
School of Materials Science and Engineering
*Georgia Institute of Technology*

Dr. Chloé Arson
School of Civil and Environmental Engineering
*Georgia Institute of Technology*


Date Approved: 13 July 2015

*Science! true daughter of Old Time thou art!*

*Who alterest all things with thy peering eyes.*

*Why preyest thou thus upon the poet's heart,*

*Vulture, whose wings are dull realities?*

*How should he love thee? or how deem thee wise,*

*Who wouldst not leave him in his wandering*

*To seek for treasure in the jewelled skies,*

*Albeit he soared with an undaunted wing?*

*Hast thou not dragged Diana from her car,*

*And driven the Hamadryad from the wood*

*To seek a shelter in some happier star?*

*Hast thou not torn the Naiad from her flood,*

*The Elfin from the green grass, and from me*

*The summer dream beneath the tamarind tree?*

- Edgar Allen Poe, 1829

# ACKNOWLEDGEMENTS

My deepest gratitude goes to Prof. Kimberly Kurtis. I still recall that bleak February day in 2010 when she gave me a follow-up call regarding my graduate school application and changed my life forever. We talked about pottery wheels and Europe, and I knew I did not want to earn my doctorate anywhere else. Thank you for your guidance, insights, patience, and support, and thank you for giving me the creative freedom that I have enjoyed working on this project.

I am indebted to my thesis committee, Prof. Chloé Arson, Prof. Arun Gokhale, Prof. Lori Graham-Brady, and Prof. Laurence Jacobs. They have been crucial teachers, mentors, and collaborators throughout my work on this dissertation. Additionally, this undertaking would not have come to full fruition were it not for collaboration with many professionals at other universities. In particular, I would like to thank Prof. M. Tyler Ley at Oklahoma State University for the concrete samples in Chapter 3, Prof. K.T. Ramesh at the Johns Hopkins University for guidance in experimental design in Chapter 4, and Prof. Matthieu Vandamme at École Nationale des Ponts et Chaussées for his guidance in Chapter 5.

I must acknowledge my mentors at the University of Delaware. Prof. Jack Puleo believed in me and pushed me to pursue graduate studies, and Prof. Jennifer McConnell provided me with my first research experience.

I have had the privilege of working with a brilliant research group. All of you – Dr. Jun Chen, Dr. Robert Moser, Dr. Bo-Yeon Lee, Dr. Amal Jayapalan, Prof. Chris Shearer, Dr. Passarin Jongvisuttisun, Mr. Bradley Dolphin, Ms. Elizabeth Nadelman, Mr. Álvaro Paul, Mr. Ahmad Shalan, Mr. Mehdi Niki-Rashidi, Ms. Behnaz Hosseinzadeh,

Dr. Lisa Burris, Dr. Giovanni Loreto, and many others – have enriched this experience in your own unique ways. I also thank Dr. Falak Shah, who joins me in thanking our trivia team, the State of Georgia, and the South Carolina Board of Pyrotechnic Safety.

My transition to Georgia Tech and Atlanta was made possible by the help and friendship of Dr. Karthik Ramanathan, Dr. Timothy Wright, Dr. Brittany Luken Wright, Prof. Abdollah Shafiezadeh, Dr. Jieun Hur, and Dr. Stephanie German.

I would like to thank Sam Nunn Security Fellowship, funded by the John D. and Catherine T. MacArthur Foundation, under the direction of Prof. Seymour Goodman, for adding a fascinating dimension to my doctoral experience. My colleagues Dr. Soheil Shayegh, Adrienne Little, Dr. Kelly Nicholson, Dr. Ariel Marshall, and Dr. Oded Green, have made this an intellectually stimulating and uproariously fun experience.

Since I was a child, my parents have moved heaven and earth to provide me with every opportunity for success. Their unconditional love and support have seen me through life's highs and lows. From cultivating my interest in social and natural sciences to providing piano, art, golf, and fencing lessons, their guidance has made me the person I am today. It's been a long road; thanks Mom and Dad for seeing me through.

And of course, thank you Jacob, for putting up with the whole process.

# TABLE OF CONTENTS

# LIST OF TABLES

# LIST OF FIGURES

# LIST OF SYMBOLS AND ABBREVIATIONS

SYMBOLS*

| | | |
|---|---|---|
| $A_b$ | = | Cross-sectional area of the Kolsky bar |
| $A_s$ | = | Cross-sectional area of the specimen |
| $b$ | = | Biot coefficient |
| $C_b$ | = | Rayleigh wave speed of the Kolsky bar material |
| $C_R$ | = | Rayleigh wave speed of mortar |
| $D$ | = | Fractal dimension |
| $D_{crit}$ | = | "Critical" fractal dimension |
| $\mathcal{D}$ | = | Air void diameter |
| $d$ | = | Nominal diameter of a sieve |
| $d_b$ | = | Diameter of the incident and transmitter bars in the Kolsky apparatus |
| $d_{\text{trans}}$ | = | Distance from the specimen interface to the strain gage on the transmitter bar |
| $E$ | = | Young's modulus |
| $E_0$ | = | Undamaged Young's Modulus |
| $E_b$ | = | Young's modulus of the Kolsky bar material |
| $E_s$ | = | Young's modulus of the Kolsky bar tes specimen |
| $E_\Omega$ | = | Damaged Young's modulus |
| $\mathrm{E}[\mathcal{r}]$ | = | Expected value of the round flaw radius (entrained air voids) |
| $\mathrm{E}[\mathcal{s}]$ | = | Expected value of the slit flaw length (ITZ/fine aggregate) |
| $e_V(y)$ | = | Entrained air void "exclusion" probability |
| $f(\mathcal{R})$ | = | 3D entrained air void size distribution in terms of radius, $\mathcal{R}$ |
| $f(\mathcal{r})$ | = | 2D entrained air void size distribution in terms of radius, $\mathcal{r}$ |
| $f(\mathcal{s})$ | = | Size distribution of slit flaws (ITZ/fine aggregate) in terms of slit flaw half-length, $\mathcal{s}$ |
| $F(\varrho)$ | = | Size distribution of capillary pores with throat radius $\varrho$ |
| $G$ | = | Shear modulus |
| $g(z)$ | = | Radial distribution function |
| $\acute{g}(z)$ | = | Averaged radial distribution function |
| $h_V(y)$ | = | Entrained air void nearest-surface probability density function |
| $K$ | = | Bulk modulus |
| $K_C$ | = | Bulk modulus of ice crystals |
| $K_{Ic}$ | = | Critical stress intensity of mortar |
| $K_{I\mathcal{r}}$ | = | Critical stress intensity around round flaws (entrained air voids) |
| $K_{I\mathcal{s}}$ | = | Critical stress intensity around slit flaws (ITZ/fine aggregate) |
| $K_S$ | = | Bulk modulus of liquid water |
| $k_{rL}$ | = | Relative permeability |
| $k_S$ | = | Bulk modulus of pure solid |
| $L$ | = | Thickness of the shell of influence around entrained air voids |
| $\overline{L}$ | = | ASTM C457 spacing factor |
| $L_s$ | = | Length of the mortar specimen in the Kolsky bar test |

| | | |
|---|---|---|
| $L_{(i)}(z)$ | = | Lineal-path function for phase *i* |
| $l_r$ | = | Length of crack tip stemming from round flaws (entrained air voids) |
| $l_s$ | = | Length of crack tip stemming from slit flaws (ITZ/fine aggregate) |
| $\langle l_{(i)} \rangle$ | = | Mean chord length for phase *i* |
| $\ell$ | = | Percentage of parent flaws in a Neyman Type A distribution |
| $\overline{M}$ | = | "Maximum" spacing factor |
| $\overline{M}_{CF}$ | = | "Maximum" spacing factor calculated using the closed-form equations with size distribution parameters obtained from x-μCT |
| $\overline{M}_{D}$ | = | "Maximum" spacing factor calculated directly from x-μCT |
| $m$ | = | Mass (various contexts) |
| $m_{exp}$ | = | Mass of water expelled from a shell during freezing |
| $m_s$ | = | Mass of water in a shell |
| $m_v$ | = | Van Genuchten shape parameter |
| $m_k$ | = | Weibull modulus of mode *k* of the trimodal Weibull distribution (*k* = 1,2,3) |
| $N$ | = | Number of freeze/thaw cycles |
| $N_f$ | = | Number of features (when calculating fractal dimension) |
| $N_{IJ}$ | = | Biot modulus of phase *I* with respect to phase *J* |
| $N_{tot}$ | = | Total number of micromechanics simulations per air content |
| $p_{(i)}(z)$ | = | Chord length probability density function for phase *i* |
| $p_C$ | = | Pressure due to ice crystals |
| $p_{cap}$ | = | Capillary pressure |
| $p_M$ | = | Mean pore pressure |
| $p_{max}$ | = | Maximum pore pressure |
| $p_L$ | = | Pressure due to liquid water |
| $q'$ | = | Flux of air |
| $\mathcal{R}$ | = | Air void radius (when considering 3D air voids) |
| $R_c$ | = | Cluster radius |
| $\langle \mathcal{R}^k \rangle$ | = | $k^{\text{th}}$ moment of the size distribution (also expressed $E[\mathcal{R}^k]$); $k$ = 1, 2, 3 |
| $r$ | = | Round flaw (entrained air void) radius (when considering 2D air voids) |
| $S_C$ | = | Saturation of ice crystals |
| $S_L$ | = | Saturation of liquid water |
| $S_r$ | = | Van Genuchten parameter for unfrozen liquid water |
| $SGF$ | = | Gage factor |
| $s$ | = | Specific surface |
| $s$ | = | Slit flaw (ITZ/fine aggregate) radius |
| $T$ | = | Temperature |
| $T_m$ | = | Melting temperature of ice |
| $\mathring{T}$ | = | Cooling rate |
| $t_{peak}$ | = | Point in time when $\sigma(t) = \sigma_{DYN}$ during the Kolsky bar tests |
| $t_G$ | = | Time reading from the transmitter bar strain gage in the Kolsky apparatus |
| $u_r$ | = | Radial displacement |
| $V_{abs}$ | = | Volume of water absorbed by an entrained air void |

| | | |
|---|---|---|
| $V_{exc}$ | = | Volume of water in entering an entrained air void in excess of the entrained air void's capacity |
| $V_{exp}$ | = | Volume of water expelled from a shell around an entrained air void |
| $V_G(t)$ | = | Voltage reading from the transmitter bar strain gage in the Kolsky apparatus |
| $v_{in}$ | = | Input velocity into the Kolsky bar |
| $V_s$ | = | Volume of a shell of influence of length $L$ surrounding an entrained air void |
| $V_{void}$ | = | Volume of an entrained air void with radius $\mathcal{R}$ |
| $V_W$ | = | Volume of water in entrained air voids |
| $W_{tot}$ | = | Total number of windows per micromechanical simulation sample |
| $\alpha$ | = | A crack growth parameter |
| $\alpha_S$ | = | Coefficient of thermal expansion of the solid phase |
| $\beta_k$ | = | Scale parameter of mode $k$ of the trimodal Weibull distribution ($k$ = 1,2,3) |
| $\gamma$ | = | A crack growth parameter |
| $\gamma_{CL}$ | = | Interfactial energy between the ice crystals and liquid water |
| $\Delta S_m$ | = | Melting entropy of ice |
| $\epsilon$ | = | Volumetric strain |
| $\boldsymbol{\varepsilon}$ | = | Strain tensor |
| $\varepsilon$ | = | Yardstick length (Appendix A) |
| $\varepsilon_{rr}$ | = | Strain in the radial dimension |
| $\varepsilon_{\theta\theta}$ | = | Strain in the $\theta$ direction |
| $\varepsilon_{\phi\phi}$ | = | Strain in the $\phi$ direction |
| $\dot{\varepsilon}$ | = | Strain-rate |
| $\varepsilon_I(t)$ | = | Strain-time history of the incident stress wave in the Kolsky bar |
| $\varepsilon_R(t)$ | = | Strain-time history of the reflected stress wave in the Kolsky bar |
| $\varepsilon_T(t)$ | = | Strain-time history of the transmitted stress wave in the Kolsky bar |
| $\lambda$ | = | Inclined crack length (round flaws only) |
| $\eta$ | = | Viscosity of liquid water |
| $\theta$ | = | Contact angle between the ice crystal phase and liquid water |
| $\kappa$ | = | Intrinsic permeability of a porous solid (hydrated cement paste) |
| $\lambda$ | = | Inclined crack length (round flaws only) |
| $\mu$ | = | Coefficient of friction of the flaw interface |
| $\mu_x^{(k)}$ | = | Mean of parameter $x$ in damage mode $k$ ($k$ = I, II, III) |
| $\nu$ | = | Poisson's ratio |
| $\xi$ | = | Location parameter for a lognormal probability density function |
| $\pi_0$ | = | Van Genuchten scale parameter |
| $\rho_A$ | = | Number density of features resolved per unit area |
| $\rho_{air}$ | = | Number density of entrained air voids per unit volume in the bulk material |
| $\rho_{air}^0$ | = | Mass density of air |
| $\hat{\rho}_{air}$ | = | Number density of entrained air voids per unit volume in the paste alone |
| $\rho_b$ | = | Mass density of the Kolsky bar |
| $\rho_{FA}$ | = | Mass density of fine aggregate |
| $\rho_C$ | = | Mass density of ice crystals |

| | | |
|---|---|---|
| $\rho_C^0$ | = | Initial (uncompressed) mass density of ice crystals |
| $\rho_L$ | = | Mass density of liquid water |
| $\rho_L^0$ | = | Initial (uncompressed) mass density of liquid water |
| $\rho_s$ | = | Number density of slit flaws (ITZ/fine aggregate) per unit area |
| $\varrho$ | = | Capillary pore throat radius |
| $\sigma(t)$ | = | Stress time history |
| $\sigma_{11}^{local}$ | = | Local stress in an elliptical area around flaws (11 direction) |
| $\sigma_{22}^{local}$ | = | Local stress in an elliptical area around flaws (22 direction) |
| $\sigma_c$ | = | Static compressive strength of mortar specimens |
| $\sigma_{DYN}$ | = | Dynamic compressive strength of mortar specimens |
| $\sigma_{global}$ | = | Global applied compressive strength in the micromechanics model |
| $\dot{\sigma}$ | = | Stress rate |
| $\sigma_{Nk}$ | = | Normalizing stress of mode *k* of the trimodal Weibull distribution (*k* = 1,2,3) |
| $\varsigma$ | = | Scale parameter for a lognormal probability density function |
| $\tau$ | = | Critical shear stress at the flaw interface |
| $\phi_0$ | = | Initial hydrated cement paste porosity |
| $\phi_{air}$ | = | Entrained air void volume fraction in the bulk material |
| $\hat{\phi}_{air}$ | = | Entrained air void volume fraction in the paste/entrained air void phase alone |
| $\hat{\phi}_{HCP}$ | = | Volume fraction of hydrated cement paste (HCP) in the paste/entrained air void matrix alone |
| $\hat{\phi}_{HCP,init}^{(i)}$ | = | Initial (i.e., before redistribution of shell thicknesses) hydrated cement paste (HCP) in shells surrounding entrained air voids of size class *i* |
| $\phi_{(i)}$ | = | Volume fraction of phase *i* |
| $\varphi_J$ | = | Change in porosity of phase *J* |
| $\Omega$ | = | Damage parameter in the micromechanics model |

*Some symbols have been neglected if their use was mentioned only once in the review of literature and not used for calculations in the subsequent chapters.

ABBREVIATIONS

| | | |
|---|---|---|
| AEA | = | Air entraining admixture |
| ASTM | = | American Society for Testing & Materials |
| DIF | = | Dynamic increase factor |
| HCP | = | Hydrated cement paste |
| ITZ | = | Interfacial transition zone |

| | | |
|---|---|---|
| MIP | = | Mercury intrusion porosimetry |
| NIST | = | National Institute of Standards and Technology |
| VCCTL | = | Virtual cement and concrete testing laboratory |
| x-μCT | = | X-ray microtomography |

# SUMMARY

The objective of this dissertation is to advance the state-of-the-art of quantitative characterization of voidspace (i.e., flaws) in cement-based material microstructure towards better prediction of their performance under extremes in loading (specifically, extremes in loading rate and extremes in temperature). Air entrained mortar or concrete served as an example material throughout this research. Chapter 3 introduces an analytical technique to reconstruct the 3D entrained air void distribution in hardened concrete using 2D image analysis. This method proposes a new spacing factor, which is believed to be more sensitive to microstructural changes than the current spacing factor commonly utilized in practiced, and specified in ASTM C457, as a measure of concrete's ability to resist to damage under cyclic freeze/thaw loading (i.e., extremes in temperature). This advancement in voidspace characterization has the potential to improve economy by improving the quality of petrographic assessment of concrete and reducing the need for more expensive and time-consuming freeze/thaw tests, while also promoting the durability of concrete. Additionally, the method may be useful for optimizing the air void system. Appendix A provides further analysis into the effects of image resolution on the model parameters.

In Chapter 4, quantitative measurements of the sizes, shapes, and spatial arrangements of flaws which are through to drive failure at strain rates above 100/s were obtained in order to model mortar subjected to high strain-rate loading (i.e., extremes in load rate). A micromechanics model was used to study the ways in which flaw geometry and flaw interaction govern damage. A key finding suggests that dynamic strength may be multimodal, with larger flaws shifting the dynamic strength upwards into the highest

strength failure mode. The model may allow the entrained air void system to be engineered to be beneficial to a concrete element subjected to blast or impact loading. Experimental validation suggests the model is useful for predicting dynamic strength.

In Chapter 5, a robust theoretical approach, based upon poroelasticity, is presented to further validate the utility of the new spacing factor proposed in Chapter 3. The concretes in Chapter 3 were modeled using this poroelastic model. The model is truly multiscale, using in its formulation pore size data ranging from the nanoscale to the micro-scale, entrained air void data from the micro-scale to the millimeter scale, and infers a representative volume element on the centimeter scale.

# CHAPTER 1

# INTRODUCTION

## 1.1 Background

It is perhaps paradoxical that many material properties arise from the *absence* of material rather than the presence of it. For example, the strength, stiffness, and toughness of a concrete are related to its pore structure. Furthermore, the volume, size distribution, and interconnectivity of porosity is important for understanding permeability, diffusivity, and capillary action occurring in concrete, which are necessary for predicting service lives in aggressive environments [1]. For example, entrained air voids are understood to be crucial for concrete's resistance to freezing and thawing cycles and salt scaling [2], while larger entrapped air voids are deleterious to the material's overall strength [3].

The x-ray microtomographic images in Figure 1.1 illustrate some types of voidspace[1] associated with the inherent structure of cement-based materials. From this representation, the multi-scale, heterogenous, and complex geometry of the voids are immediately apparent. The figure also highlights the multiscale complexity of voidspace: the entire porous microstructure in Figure 1.1a can fit in the cube at the top left-hand corner of Figure 1.1b. While the size range of entrained air voids is reasonably well-resolved in Figure 1.1b, capillary pores (pores arising from the process of cement hydration) like those pictured in Figure 1.1a can vary from 2.5 nm to over $10^5$ nm in

[1] In this research/document, the term "voidspace" will refer to porosity (micro- and macropores) and entrained air voids, and will include the special case of locally-higher porosity in the interfacial transition zone (ITZ) at the paste/aggregate interface.

throat diameter, making it challenging to accurately depict the full range of capillary porosity in a single image.

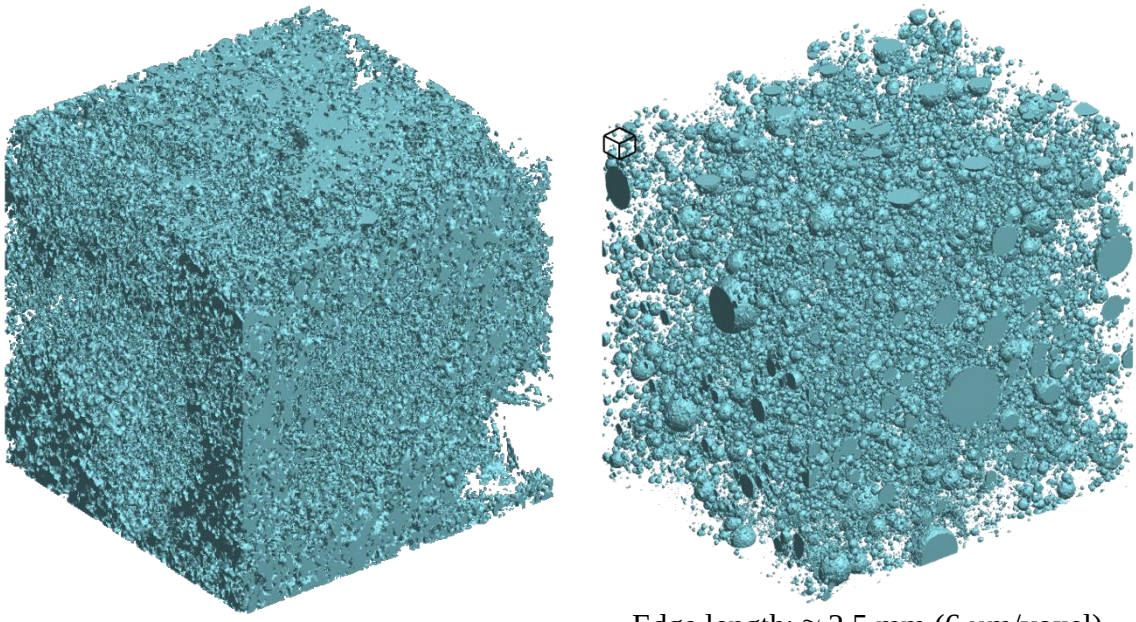

Edge length: ≈ 100 μm (0.5 μm/voxel)
(a)

Edge length: ≈ 2.5 mm (6 μm/voxel)
(b)

**Figure 1.1**: X-ray microtomographic images of voidspace: (a) macropores in hydrated cement paste and (b) entrained air voids in mortar

## 1.2 Research Motivation

Two "extremes" in loading have been identified as instances where multiscale voidspace has a critical effect on material response: extremes in load rate, and extremes in temperature. In particular, the emphasis on material behavior at extremes is useful for better appreciating and predicting their response in practice. Notably, use of cement-based materials in growing in frost-prone regions (e.g., Arctic exploration, sub-arctic development) and for applications requiring resilience at high strain rate (e.g., materials subject to blast, whether by industrial accidents or by terrorism). While a relatively larger

volume of work has been dedicated to quasistatic material behavior, improvements are needed in understanding of structure-property relationships at these extremes.

As a brittle material under extreme rates loading (strain-rates from $10^2 - 10^3$ $s^{-1}$), concrete under blast loading shares many of the same characteristics of other material systems, such as ceramic armor under impact loads and rock under explosive loads during mining. As is well-documented in the literature [4], high strain rates have a dramatic effect on the constitutive properties of brittle materials. In particular, tensile and compressive strengths increase with increasing strain-rate. The effect is small for changes in strain-rate from static loading to approximately $10^0$ $s^{-1}$ (typical for traffic, gas explosions, earthquakes, pile driving); however, the dynamic strength can increase almost an order of magnitude over static strength for strain rates over $10^2$ $s^{-1}$ (typical for ballistic impact and blast). Recent experimental and theoretical work [5, 6, 7, 8, 9] has increased the understanding of strain-rate effects on failure in brittle materials. In particular, a model developed by Paliwal and Ramesh [10] enables estimation of the strain-rate dependent constitutive behavior of brittle materials under uniaxial loading using interacting rectilinear ("wing") cracks. The model shows good qualitative agreement with Kolsky bar experiments on ceramics; however, the model does not capture the localization of failure that occurs in these materials. Additionally, rectilinear cracks alone are unable to account for the multiform morphologies of flaws and inclusions in cement-based materials. In order to capture this localization and flaw heterogeneity, a multi-scale approach is necessary.

Extremes in temperature (those ranging 0° C to -18° C) can result in degradation of saturated or nearly saturated concrete. Protection is provided by introducing entrained

air voids, of appropriate size and spacing, into the hydrated cement paste. Ideally, this should create a well-dispersed system of nucleation sites for ice crystals to form, while additionally serving as cyropumps to drain free water held in the porespace. While air entrainment is crucial for ordinary concrete's resistance to damage during cycles of freezing and thawing and salt scaling, the potential role of concrete quality in recent failures in both the accelerated laboratory test and field performance has led to renewed interest in assessing the air entrainment in concrete [11, 12, 13, 14]. In particular, questions have been raised about the quality of current metrics for assessing air entrainment [15]. Currently, the quality of an entrained air system in concrete is quantified by specific surface, void frequency, and spacing factor ($\overline{L}$). Based on pioneering work by Powers [2], this approach has been used for five decades, having first been adopted by ASTM in 1960. With advances in image analysis [16] and improvements in understanding of the mechanisms of air entrainment in concrete [17] and role of air entrainment in freeze/thaw damage mitigation [18, 19], there seems a potential opportunity to improve upon (or at least refine) methods for assessing the quality of air entrainment in concrete. Motivated by this need for a more detailed description of the microstructure, another objective the current research is to integrate microstructural statistics and image analysis to derive an improved spacing factor – one based on the reality of the distance water must migrate to reach an entrained air void site.

### 1.3 Research Objectives

The thrust of this research will be to examine the structure-property relationships between the morphology of voidspace. The effect of voidspace on the performance of the material – specifically, to study the effects of voidspace under extremes in exposure

conditions – will be examined in this research. The extreme exposure conditions will include extremes in loading rate (as experienced under hard impact and blast loads, to strain-rates of $10^2$ $s^{-1}$) and extremes in temperature (as experienced during repeated freezing and thawing cycles, to -18° C). Figure 1.2 presents an overview of the size and time scales that are to be studied in this work. Each dark blue box represents an area that spans the time to failure (abscissa) and the flaw length scales involved (ordinate) for the different tasks to be completed in this thesis. Materials experiencing extremes in loading rate are expected to fail within microseconds, while materials experiencing extremes in temperature may fail within hours or may last several years. Table 1.1 has been prepared to put the diversity of flaw length scales into perspective. The cartoons are meant to be representative of voidspace at each order of magnitude ranging from one nanometer to one centimeter. Descriptions accompanying each cartoon discuss the role of water in the porespace and discuss the types of flaws present. The primary objectives of this proposed research are:

1. Advances in materials characterization

    1.A. To develop a novel and improved method for characterizing entrained air void systems in hardened concrete. Advanced image analysis techniques will be used to construct a 3D size distribution of entrained air voids from 2D images.

    1.B. To develop a technique to extract statistical information about porosity from three-dimenstional microstructures. These microstructures may be obtained by x-ray nano- and microtomography and computer simulations. Statistical information will be obtained using correlation functions that

arise elsewhere (e.g. [20], [21]) in the study of random heterogeneous materials.

2. Material properties under extremes in loading rate

   2.A. To predict dynamic compressive strength of mortar using a micromechanics model that uses statistical parameters developed earlier as inputs. The effects of capillary pores, entrained air voids, and the ITZ on dynamic compressive strength will be evaluated.

   2.B. To validate the micromechanics model predictions through high strain-rate experiments performend on cement mortars (with strain-rates on the order of $10^2$ $s^{-1}$)

   2.C. To evaluate the effect of voidspace on mortar behavior under extreme loading and to make recommendations for tailoring cementitious materials to mitigate damage under hard impact or blast loads.

3. Extremes in temperature

   3.A. To contribute to the understanding standing of damage evolution in the local region around entrained air voids during freezing using poromechanics and a multiscale approach. Capillary pore sizes on the order of $10^0$ to $10^5$ nm in throat diameter measured by mercury intrusion porosimetry, and entrained air voids characterized by two-dimensional (Task 1.A.) and three-dimensional (Task 1.B.) characterization techniques will be considered.

   3.B. To improve understanding of the effect of size distribution and spatial arrangement of entrained voids on damage under extremes in loading

temperature (from 4° C to -18° C). Specifically, this will enable a numerical assessment of alternatives to the ASTM C457 spacing factor using the mechanics and physics of porous media rather than pure statistical or numerical studies.

3.C. To verify the multiscale poromechanics model (developed in 3.A) using experimental data obtained from specimens exposed to extreme temperature (ASTM C666).

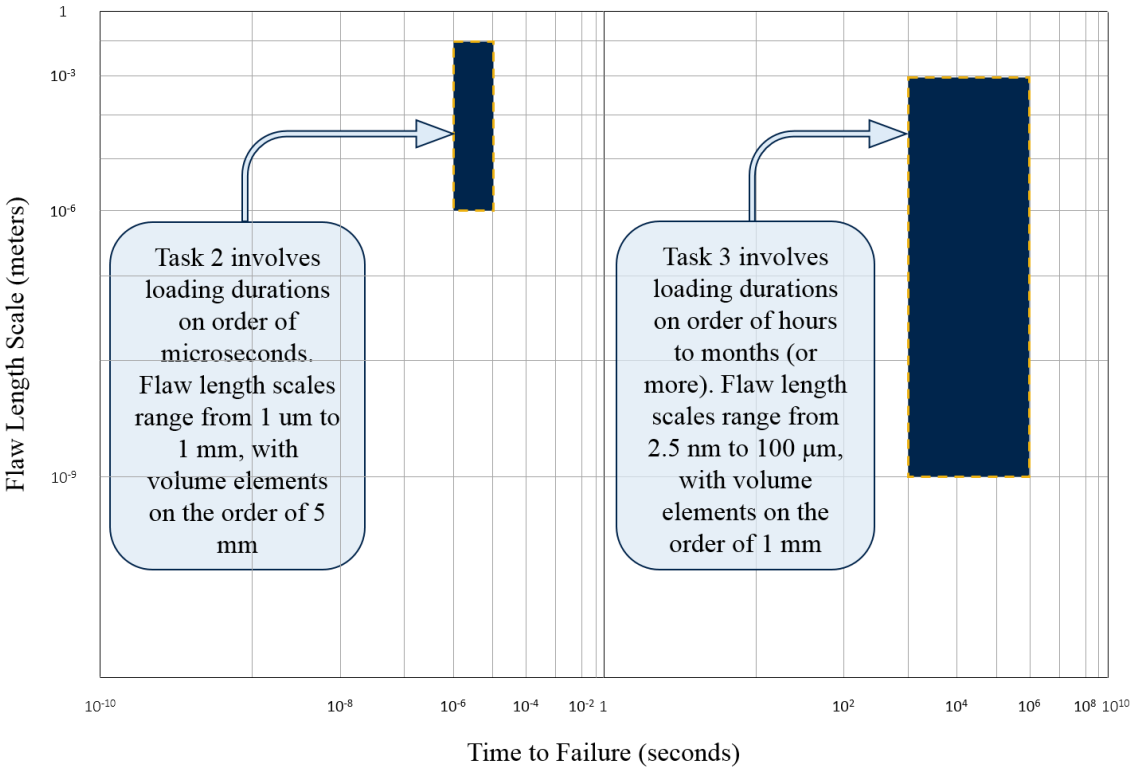


**Figure 1.2:** Size and time scales associated with the tasks in this dissertation

**Table 1.1:** Voidspace across length scales

| | |
|---|---|
| $10^{-9}$ meter<br> 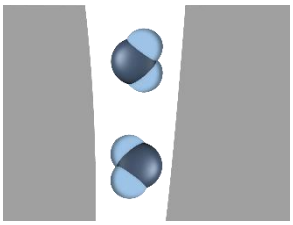 <br>Water molecules are held *interlayer space* less than 0.5 nm between C-S-H sheets | $10^{-5}$ meter<br> 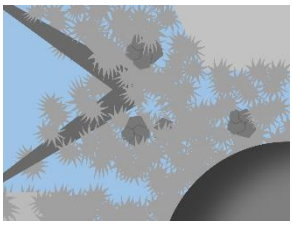 <br>Water behaves as free water in *macropores* (50-10,000 nm). Ettringite (1x10 μm) and CH (10-100 μm) crystals visible in the porespace. Smallest *entrained air voids* (12 μm diameter) visible. |
| $10^{-8}$ meter<br> 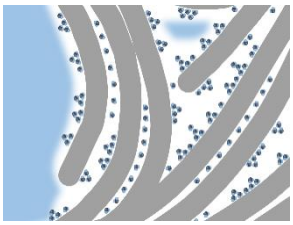 <br>Water molecules in *micropores* (0.5-2.5 nm) adsorbed to C-S-H sheets (0.85-1.05 nm thick). The largest of the gel pores, *small mesopores* (2.5-10 nm), are visible, where water experiences "large" surface tensions. | $10^{-4}$ meter<br> 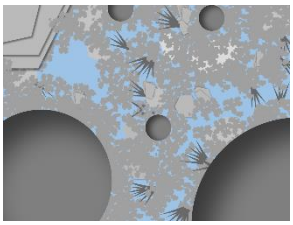 <br>Largest *entrained air voids* (100 μm diameter visible) along with large *macropores*. Length scale corresponds to VCCTL simulations. |
| $10^{-7}$ meter<br> 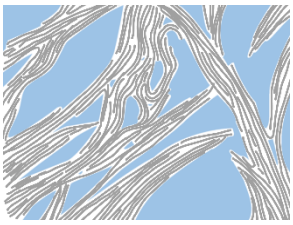 <br>Smallest class of capillary pores, *large mesopores* (10-50 nm), are visible around spiny crystals of C-S-H (0.01-1 μm). Water experiences "small" surface tensions. | $10^{-3}$ meter<br> 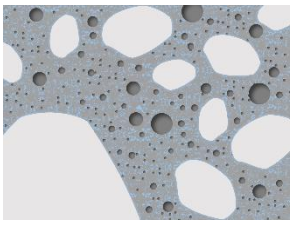 <br>Fine aggregate particles 0.2-1 mm in diameter are visible. Aggregates introduce an *interfacial transition zone* (≈15 μm thick) of locally-higher capillary porosity. |
| $10^{-6}$ meter<br> 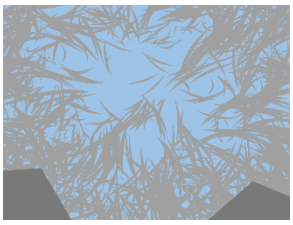 <br>Water behaves as free water in *macropores* (50-10,000 nm), which exist outside aggregates of C-S-H particles (0.8-2 μm) and monosulfoaluminate crystals (1 μm) | $10^{-2}$ meter<br> 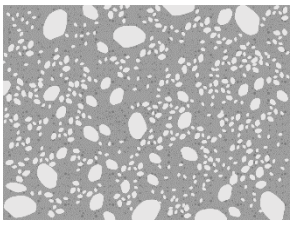 <br>Material appears as bulk mortar as observed by the naked eye. |

# CHAPTER 2

# LITERATURE REVIEW

Both dynamic response and freeze/thaw durability have been explored by researchers in cement and concrete technology for decades. Each of these fields of studies represents an area where better characterization of voidspace could lead to advances in engineering better construction materials. This chapter presents a comprehensive survey of the available literature on these topics. Section 2.1 outlines the need for research in "extreme conditions." Section 2.2 is a state-of-the-art review of high strain-rate studies of cement-based materials, which corresponds to Task 2. Section 2.3 is a critical review of theoretical and experimental analysis of entrained air voids, which corresponds to Task 1 and Task 3.

## 2.1 Overview: Extreme Conditions

### 2.1.1 High Strain-rate Loading

Mitigating the effects of impact loading on critical structural systems and reducing human vulnerability in the wake of such events is challenging because the central question remains unanswered: how does concrete fail under high strain-rate loadings? A 1996 study of injuries sustained by U.S. Air Force personnel in the aftermath of a bombing in Saudi Arabia found that fragmented concrete was second only to fractured glass as a source of injury, and stressed the need for improved design tools to prevent building fragmentation under blast or impact loading [22]. More recently, physicians removed concrete fragments as large as two inches from survivors of the 2013 Boston Marathon tragedy [23]. Due to the scarcity of blast-related injuries outside of

combat, few U.S. health professionals have experience treating them, thereby creating an additional challenge for medical personnel and first responders [24]. Innovations such as blast doors and reinforced windows have done much to protect buildings from damage. As Figure 2.1 demonstrates, these implementations performed as intended in a 2013 bombing of the U.S. embassy in Ankara, Turkey, but the surrounding concrete sustained immense damage and failed [25]. Cement-based materials technology must catch up if concrete is to remain a safe, resilient construction material in an age of global terrorism.

**Figure 2.1:** U.S. embassy in Ankara, Turkey, in February of 2013. The specialized glass in the reinforced window performed well by creating no shrapnel, but the entire casing has been dislodged due to the damage sustained by the concrete.

Both ductile and brittle materials are known to fail in a brittle manner when subjected to very high loading rates, and their apparent yield strengths are also known to increase. In brittle materials loaded in compression, the general understanding of this "strain-rate effect" on compressive failure stress is attributed to the generation, growth

and coalescence of microcracks from defects (including, but not limited to, grain boundaries, cavities, pores, and preexisting cracks).

Cementitious materials like concrete are considered a brittle materials, and understanding the strain-rate effect in concrete is crucial for designing infrastructure subjected to shock and impact. However, research in this field is relatively immature compared to the study of other durability concerns (such as chemical attack), and inconsistencies exist in the test methods, modeling efforts, and analysis techniques, making it challenging to develop a unified theory.

Researchers have developed analytical models for concrete's dynamic behavior based on observations that the dynamic strength increase with increasing strain-rate, and hypothesized that this behavior is due to a range of phenomena observed at the microscale, mesoscale, and structural scale, including micro-cracking, viscoplasticity, and inertial confinement. Model development remains challenging due to inherent difficulties in the dynamic testing of material like concrete, which is heterogeneous on multiple scales. For example, heterogeneities vary considerably in size; the range from micropores to coarse aggregates alone represents seven orders of magnitude. This presents a challenge in sizing specimens to meet the specifications of the testing apparatus. Further, the available strength data are very scattered, making it difficult to assess model validity. A comprehensive failure model which incorporates various failure theories across a range of high rates of strain is still outstanding.

### 2.1.2 Cyclic Freezing and Thawing

Freezing of water held in capillary pores is understood to generate inward tensile pressures in mortar and concrete. If the material is not adequately engineered to combat

these stresses, it may rupture from within. The deleterious effects of freeze/thaw cycling are mitigated by deliberately introducing millions of tiny air voids into the material, known as entrained air voids. These voids act as expansion reservoirs for water in the porespace, and also as cyropumps to drain the porespace of free water. However, the voids are deleterious to the material's strength and durability, acting as stress concentrators and obviously offering no contribution to strength. Since the freeze/thaw durability is so intimately related to these flaws, it will serve as another application of the materials characterization employed in this research.

In the United States, freeze/thaw cycling is not just a problem confined to the northeast. As shown in Figure 2.2, the regions defined as having a "severe" risk of freeze/thaw damage (denoted in blue) extends into nearly all of the contiguous United States. Recently, spalled pieces of concrete falling from an overpass were attributed to freeze/thaw damage [13]. Additionally, projects have been launched to insulate high-speed rail tracks against freeze/thaw damage [12]. The cost of freeze/thaw damage is staggering. ACI estimates the total cost of repair, including rehabilitation, strengthening, and protection (including waterproofing) of the concrete structures in the U.S. is estimated at $18-21 billion/year [26]. Although freeze/thaw alone is not the sole cause of this expense, it is often among the top aggravating factors that contributes to a structure's need for repair.


**Figure 2.2:** U.S. climate zones. Blue regions denote portions of the country with severe risk of damage to concrete due to freeze/thaw cycling [27]

## 2.2 Extreme Condition: High Strain-rate Loading

A spectrum of loading rates which defines the general orders of magnitude for different loading regimes (earthquakes, impact, etc.) may be found in Figure 2.3 [28]. Early research on the topic, such as by Duff Abrams in 1917 [29], focused on defining a loading rate that is suitable for determining concrete's static compressive strength. By 1991, Bischoff and Perry's seminal paper [28] declared that the state-of-the-art of testing for and assessing concrete's dynamic strength was roughly comparable to the state-of-the-art of static testing in the 1960s; that is, much research was needed to truly understand dynamic behavior compared to the relatively well-researched static behavior. A key contribution of Bischoff and Perry was a compilation of all available literature on the topic, which was sparse, when compared to the extensive research that has been conducted since then in the last two decades. The relative increase in compressive strength (also known as the dynamic increase factor, or $DIF = \sigma_{DYN}/\sigma_c$) versus strain rate from the seminal work may be found in Figure 2.4. These data have often been cited, albeit at times selectively, which in some cases has produced relatively better agreement with a particular modeling approach, but it must be cautioned that this may be potentially

due to sampling bias. As a result, it is important to recognize the entirety of the data set presented in Figure 2.4.

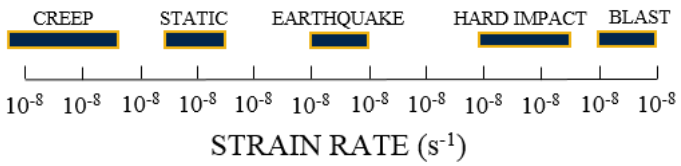


**Figure 2.3:** Magnitude of strain-rates expected for loading conditions (after [28])

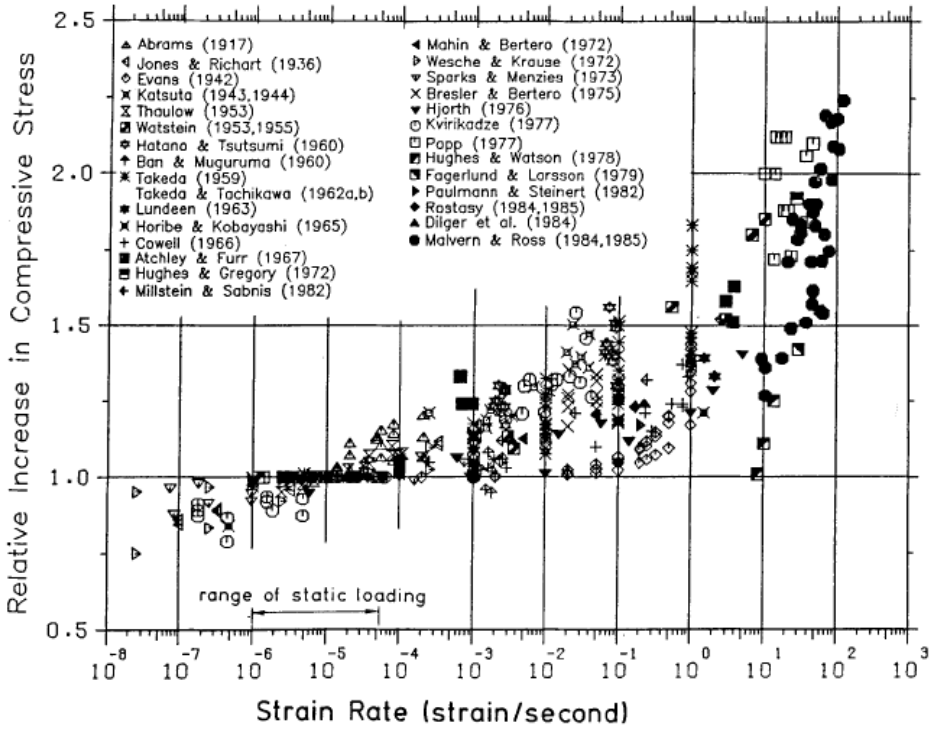


**Figure 2.4:** Strain-rate influence on dynamic compressive strength [28]

### 2.2.1 The Split-Hopkinson Pressure Bar

The literature describes the use of several common test methods, including Charpy impact tests, hydraulic testing machines, drop-weight impact tests, and split-Hopkinson pressure bars, for impact testing of cement-based materials. While the various methods have their advantage and disadvantages, it is noteworthy that research in this

field suffers from the lack of a standard test method (e.g., an ASTM standard test) for impact testing of concrete. Identification of a suitable testing apparatus and methodology for high strain-rate testing is a fundamental challenge for research in this area, but one which must be addressed to provide a consistent basis for evaluation and characterization of material behavior so that research in this area may advance. The split-Hopkinson pressure bar is the most appropriate of the available test methods for high strain-rate assessments in cement-based materials due to its ability to test across a large range of strain-rates [30], sometimes up to $10^6$ $s^{-1}$ or greater. Note that $10^0$ $s^{-1}$ – $10^3$ $s^{-1}$ encompasses the loading range where Portland cement concrete is a suitable choice for a protective material[2]. Therefore that test will be the subject of further review herein.

The split-Hopkinson pressure bar (SHPB) is the most common experimental technique used for high strain rate research due to its ability to load the specimen at rates between $10^1$ and $10^3$ $s^{-1}$ [31]. The SHPB consists of two long bars which sandwich a specimen between them. A striker applies an instantaneous pressure to one bar, called the incident bar, which delivers a compressive pulse to the specimen by wave propagation. A portion of the pulse travels into the other bar, called the transmitter bar, while another portion reflects back to the incident bar [32]. For a diagram of the setup, see Figure 2.5.

[2] Strain rates on the order of $10^6$ $s^{-1}$ – $10^8$ $s^{-1}$ correspond to advanced military weaponry, while $10^2$ $s^{-1}$ – $10^3$ $s^{-1}$ correspond to hard impact or chemical explosions. Portland cement concrete may be a viable protective material in the latter range of strain-rates, but the former range of strain-rates likely requires more advanced composite cladding or armoring techniques.

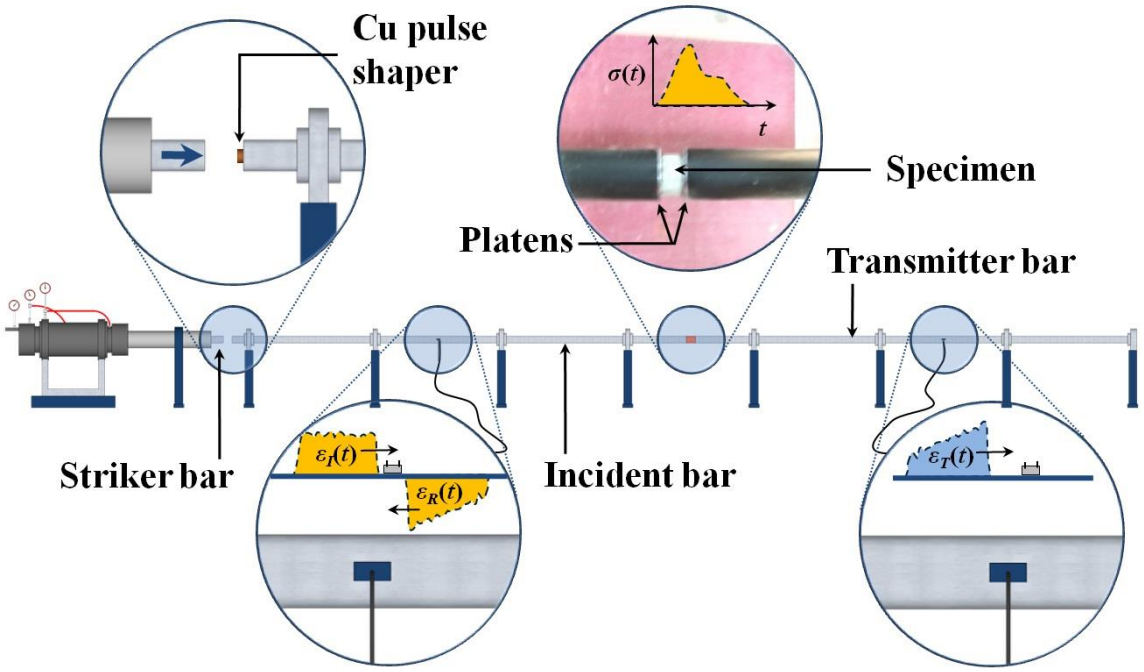


**Figure 2.5:** Schematic of a split-Hopkinson pressure bar

The SHPB was originally devised for testing metals. The system is based on one-dimensional wave theory, wherein the stress wave is considered to act mainly along the axial dimension of the bar since the radius of the bar is negligible with respect to its longitudinal dimension. The elastic properties of metal specimens are such that they may be cast in small sections such that the entire system complies with one-dimensional wave theory. When adapting this test for concrete, as with other tests on concrete, the specimen size is governed by the nominal dimension of the maximum size aggregate (MSA). Bischoff and Perry [28] report that the specimen size should be four to five times the MSA for the specimen to be representative of a larger concrete volume, which may not be practical given the constraints on specimen diameter in the typical test set up. Also, Davis and Hunter [33] report an optimum specimen length-to-depth ratio, $L/D = \frac{1}{2}\sqrt{3\nu_s}$, where $\nu_s$ is Poisson's ratio for the specimen. Differing impedance values between the

specimen and pressure bars, as well as the stress wave dispersion which results if the bar diameter is large, create differences in measured stresses at opposite ends of the specimen [32].

The classical derivation for wave motion in an elastic, thin rod assumes a uniform wave distribution and neglects the effects of lateral inertia. Dispersion occurs when pure plane waves of different wavelengths have different propagation velocities, so that mixed wavelengths tend to spread out in space. Dispersion in the apparatus may cause stresses at the two specimen/bar interfaces to be unequal until the system reaches maximum stress. This could lead to inaccurate readings in the rising portion of the stress-time curve.

Tang et. al. [34] corrected stress-wave dispersion using a Pochhammer-Chree analysis, as shown in Figure 2.6 (where $\sigma_1$ is taken at the incident interface and $\sigma_2$ is taken at the transmitter interface). As is evident from Figure 2.6b, the stresses $\sigma_1$ and $\sigma_2$ are in much better agreement with one another. Cadoni et al. [35] proposed a means of mitigating dispersion by storing elastic energy. A bar is placed between the actuator and the incident bar and is pre-stressed by static tensioning, thus storing elastic energy. A brittle component (point A in Figure 2.7) between this pre-stressed bar and the pre-stressing force is suddenly broken, generating an elastic wave pulse which is propagated down to the incident bar. The resulting pulse length is much greater than the transverse dimension of the bar (several meters versus a few centimeters).

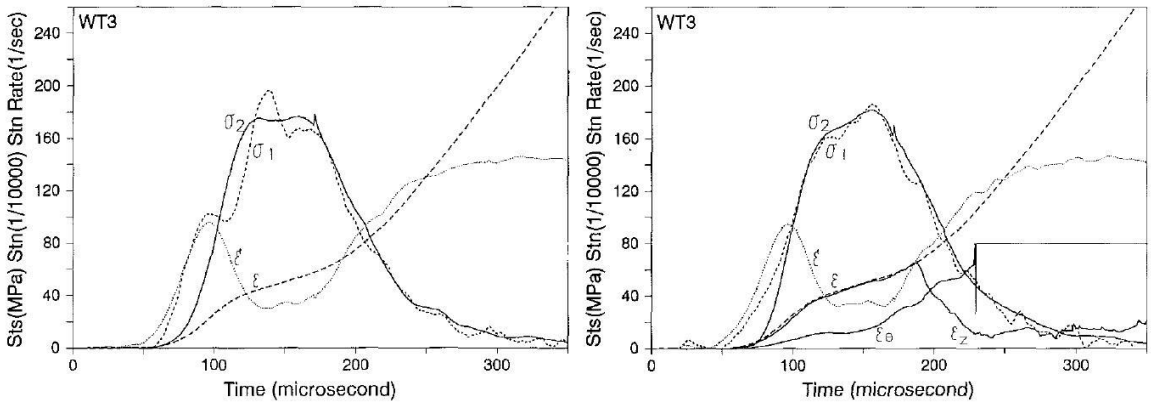


(a) (b)

**Figure 2.6:** Stresses and strain versus time (a) without and (b) with dispersion correction [34]

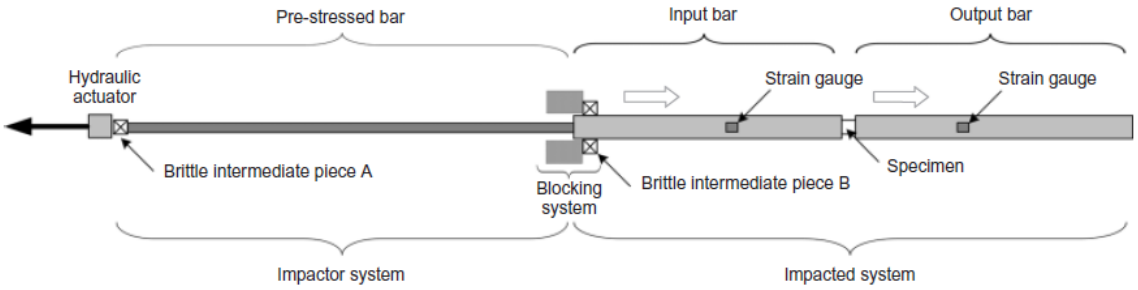


**Figure 2.7:** Modified SHPB as described by Cadoni et. al. [35]

Radial confinement is essentially the material confining itself under high rates of strain because the material cannot "get out of the way" at the same rate that the load is being applied. Its effect as it relates to blast resistance may be that the strain-rate effect could be a pseudo-effect caused by the specimen itself – or perhaps it interplays with some other parameters effecting blast response to an extent that is yet to be quantified. ACI Committee 446: Fracture Mechanics stated in their 2004 report [32] that inertia was not often considered by researchers, but argued that doing so was overly simplistic. Li et. al. [36] and Zhang et. al. [31] presented companion papers investigating the role of radial confinement in the SHPB setup. Radial stress is given by Eq. 2.1, where *b* is the

specimen radius, $\rho$ and $v$ are the specimen density and Poisson's ratio, respectively, and $\ddot{\varepsilon}_z^0(t)$ is the axial strain acceleration in the specimen. The strain-rate at the failure point was used as the representative strain rate throughout the study. Specimens with 37 mm, 50 mm, and 74 mm outer diameters were tested, with inner diameters varying from 0 mm (i.e., a solid specimen) to 45 mm (in the largest specimens). Axial strain acceleration was nearly independent regardless of whether the specimen was solid or tubular for a given outer diameter. However, Figure 2.8 shows that the dynamic increase factor varied when the inner free surface was introduced, thus lowering the dynamic increase factor with growing inner diameters.

$$\sigma_r = -\frac{\nu(3-2\nu)}{8(1-\nu)}\left[r^2 - b^2\right]\rho\ddot{\varepsilon}_z^0(t) \qquad \text{Eq. 2.1}$$

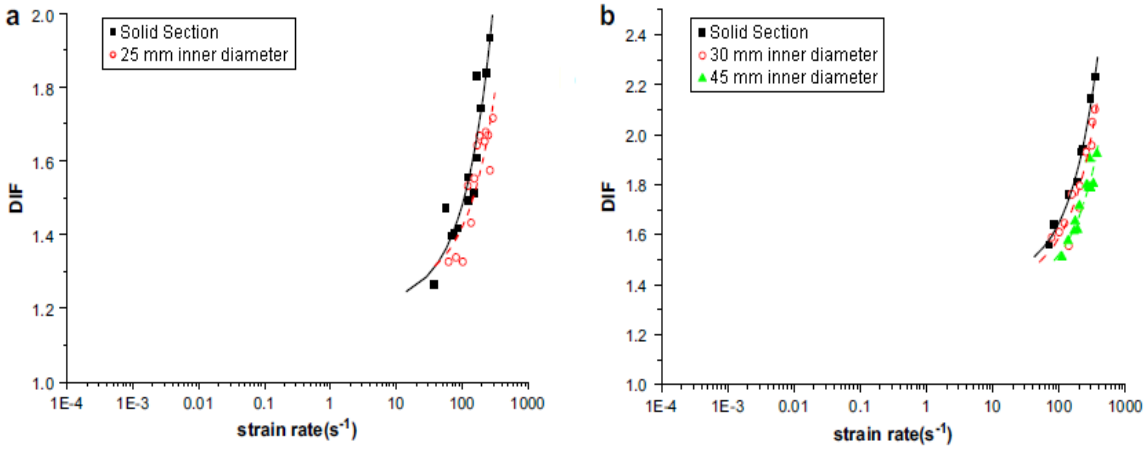


**Figure 2.8:** Variation in dynamic increase factor (a) for 50 mm and (b) 74 mm solid and tubular specimens [31]

Li et. al. [36] performed investigations using numerical modeling techniques. First, the compressive strength of the concrete was assumed to be *insensitive* to loading rate, thereby using a quasi-static constitutive equation and strength model. This allows any discrepancies in the input stress-strain relationship and the output stress-strain

relationship to be correlated to factors other than the material strain-rate effect. Numerical studies were carried out using ABAQUS/Explicit using reduced-integration axis symmetric elements which utilize a Drucker-Prager material model [37]. Numerical models confirmed the trends observed in Zhang et. al. [31], reinforcing the conclusion that the dynamic increase factor is a pseudo strain-rate effect resulting from radial confinement.

However, Tang et. al.'s 1990 study (mentioned previously in Section 2.1.2.2.) concluded that radial inertia in their dispersion-corrected SHPB tests did not contribute *significant* lateral confining pressure. Radial confining pressure was calculated by Eq. 2.2, where $\rho$ is specimen density, $\ddot{\varepsilon}_\theta$ is transverse strain acceleration, and $R$ is the outer radius. The average of $\ddot{\varepsilon}_\theta$ from the start to the point of maximum $\dot{\varepsilon}$ – the method used in the paper – should overestimate $\sigma_r$. Still, the confining pressure was only found to be 243 psi (1.67 MPa), which should be an insufficient pressure to explain strength increase by radial confinement.

$$\sigma_r = -\tfrac{1}{2}\rho\ddot{\varepsilon}_\theta R^2\left[1-\left(\tfrac{r}{R}\right)^2\right] \qquad \text{Eq. 2.2}$$

There are manifold reasons for these discrepancies. Tang et. al. examined a high-strengh concrete with a static compressive strength of 97 MPa and a specimen diameter of 76.2 mm, versus the concretes studied in the companion paper to Li et. al.'s work, in which the 74 mm specimens had a compressive strength of 44.9 MPa. Furthermore, Tang et. al. studied concretes containing coarse aggregate, while Zhang et. al. tested mortar specimens consisting of cement, water, and fine aggregate.

### 2.2.2 Effects of High Strain-rate on Engineering Properties

Since Young's modulus and Poisson's ratio are common material properties that are utilized for any computer simulation work, they will be addressed briefly in this section.

The dynamic elastic modulus of concrete is taken to be the initial tangent modulus from the compression stress-strain relationship, and is usually used as the modulus of elasticity for blast loading studies. Bischoff and Perry [38] showed that the dynamic elastic modulus for concrete is largely independent of strain rate.

Bischoff and Perry [28] suggested that Poisson's ratio in concrete should decrease in compression and increase in tension, but at that time no data or modeling efforts had clearly established this. Nearly two decades later, the effect on Poisson's ratio remains largely unexamined, with Paliwal and Ramesh [10] noting, "there is in general not sufficient experimental data on transverse dilatancy in brittle materials under dynamic loading to determine the Poisson's ratio as a function of damage, but the classical expectation is that it will increase." Notably, Poisson's ratio was kept constant in their model. Xiao et. al. [39] however observed that Poisson's ratio of concrete is not dependent on the loading rate in either tension or compression. This inconsistency probably stems from the idea that lateral confinement is evidently not well understood, yet Poisson's ratio is usually measured by using lateral expansion.

### 2.2.3 Review of Modeling Work

Given the variation in experimental results and testing regimes (discussed in Section 2.1.2), validation of existing models for high strain-rate effects in concrete with experimental data is challenging. These models tend to be generally valid for brittle

materials, but are sometimes better suited to particular length scales (e.g. micro- or meso-scale, but perhaps not structural scale).

Various approaches for modeling cement-based materials under high strain-rates have been developed. These may be broadly classified as "phenomenological models" and "structural models." Phenomenological models include those based on microcracking, plasticity, or viscoplasticity, where the strain-rate effect is attributed to some "phenomenon" unique to the material itself, and is accounted for by some dynamic influence in the respective model's fundamental assumption. In contrast, structural models, which view the specimen as a mass defined by its compressive strength, view the strain-rate effect as a pseudo effect due to the specimen's inertia [40].

#### 2.2.3.1 Structural Modeling

Ignoring radial confinement may result in unconservative blast-resistant design [31]. Cotsovos and Pavlovic's [40, 41, 42] research represents a major departure from current thinking regarding models of concrete by assuming that material properties are independent of loading rate, and that the problem is not a material problem but a structural dynamics problem. Therefore, the finite element package used in their research is based on that hypothesis, thus relying on static loading and the effect of inertia on the mass matrix of the structural form under investigation. The models are fully defined by the concrete's static compressive strength, $f'_c$. This approach thus does not use parameters that often make the finite element packages used in analysis overly sensitive to the particular case being observed. The authors argue that other numerical analyses reported in the literature are highly parameterized, and that concrete used in real-world applications will seldom be characterized exhaustively to obtain all the parameters.

For high loading rates, the numerical results indicate that the failure of the specimen (in the top portion) precedes the development of reactions at the bottom. This indicates the stress wave does not reach the bottom of the specimen within the time interval between loading and failure. Numerical results indicate that the axial and lateral displacements of the nodes at the bottom sections of the specimen gradually decrease with increasing strain-rate (shown qualitatively in Figure 2.9). This raises an interesting point that is difficult to ascertain from experimental setups.

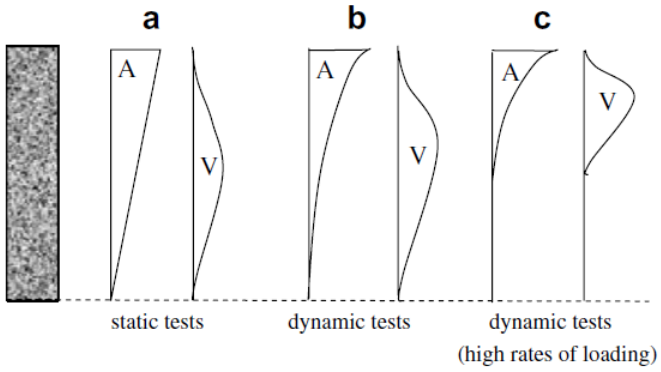


**Figure 2.9**: Qualitative schematic of axial displacement (A) and vertical displacement (V) for varying strain rates [40]

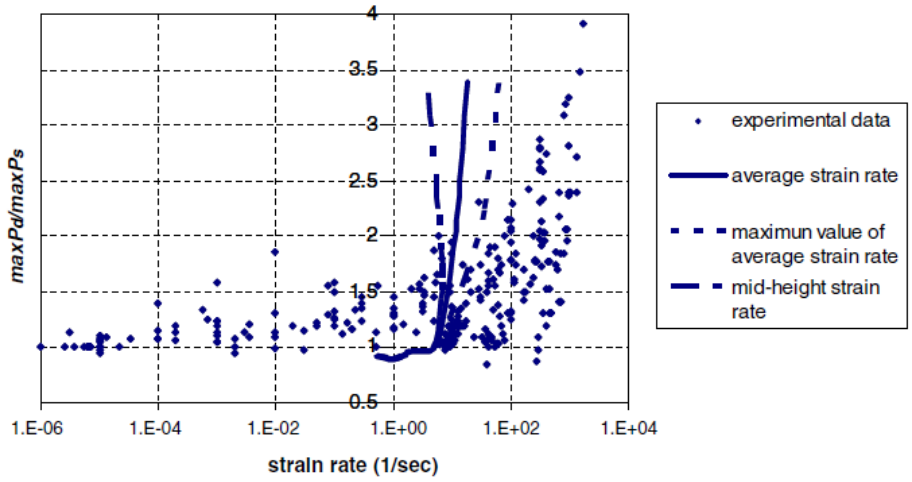


**Figure 2.10:** Experimental data for DIF versus strain rate overlain by results per Cotsovos and Pavlovic's model [40]

A weakness of Cotsovos and Pavlovic's work is the often-made assertion that experimental results are so varied that any stress-path dependency in concrete behavior disappears within the scatter of data. In this sense, the authors concluded any effect attributed to stress-path dependency cannot be quantified, and argued it is both realistic and accurate to consider that concrete behavior is stress-path independent. While scatter does exists in data, it is far from a reasonable defense of any model. A number of constitutive models for dynamic compressive strength of cementitious materials that generally show increased strength with loading rate can conclude that the scattered data makes it impossible to truly validate the model.

#### 2.2.3.2 Mesoscale Modeling

Mesoscale models are a class of phenomenological models which idealize complex concrete composite in some way. For example, Zhou and Hao [43] idealized concrete as a three-phase material consisting of a mortar matrix, interfacial transition zone (ITZ), and aggregate. The rate dependent properties of the material arise out of rate-dependent phenomenon observed within these idealized regions or their interactions.

Brara et. al. [44] modeled concrete in tension utilizing the lattice method approach, which simplifies a continuous solid by modeling it as a network of structural units with well-defined relationships between them. Elastic and failure properties are meant to be representative of the mesoscale, with an interaction law connecting elements. Therefore, the units represent a few grains of fine aggregate embedded in a homogeneous matrix of hardened cement paste and some voids. The model considers macroscopic behaviors such as strain softening, dilation, failure, and post-failure behavior, and spalling. The authors concluded that fracture stress can be accounted for by the

cumulative fracture criterion, which in turn is based on the process of material separation (shown therein to be rate-dependent).

Zhou and Hao [43] performed a comparative study of a homogeneous macroscale model and a three-phase (i.e., mortar mix, aggregate, and ITZ) mesoscale model. Both models initially assumed no material sensitivity to strain-rate, thus considering only inertial confinement. Another simulation was then carried out assuming strain-rate dependent material properties, and the results were compared, thereby assessing the relative contribution of radial confinement. Throughout, Zhou and Hao used the software AUTODYN.

For the macroscale homogeneous model by Zhou and Hao, the stress tensor was separated into the hydrostatic stress tensor (to control volumetric change) and the deviatoric stress tensor (to control shape deformation). The model used a Drucker-Prager model for yield criterion (an approach also taken in viscoplastic models by Georgin and Reynouard [45] and Xiao et. al. [39]). The model geometry and material properties replicated an experimental study by Tedesco [46].

The mesoscale model considered the interaction of sand (no coarse aggregate was considered), the cement paste, and the ITZ, where the aggregates were modeled as spheres in the matrix surrounded by ITZ (Figure 2.11). The ITZ was modeled as a spherical "shell" around the spherical aggregate particles. The ITZ and the mortar matrix shared the same solid density, solid compaction pressure, damage parameters, tensile damage threshold, and compressive damage threshold. The mortar matrix had a higher initial density, initial sound speed, initial compaction pressure, shear modulus, tensile strength, compressive strength, and cutoff tensile strength than the ITZ (in these cases,

the values used for the mortar matrix were larger than the ITZ's values by a factor usually between 2 and 3). Effective strain concentrations found during numerical simulation were considered to be cracks. The mesoscale model shed light on the failure process zone, as the first crack always occurred in the ITZ.

In all cases, the dynamic increase factors of models which assumed no strain-rate sensitivity were consistently lower than the models which were strain-rate sensitive. This suggests that the radial confinement cannot fully explain the strain-rate effect. Figure 2.12 shows the contribution percentages of inertial confinement on the homogenous and mesoscale models. From the figure, it is evident that the increase in compressive strength is very rapid after a transition point of around 200 $s^{-1}$. At rates up to 200 $s^{-1}$, a strain rate effect at the material level appears to have governed failure, whereas inertial confinement became significant at strain-rates higher than 1000 $s^{-1}$. It should be noted that not many experimental researches have utilized strain-rates above $10^3$ $s^{-1}$ due to limitations of testing concrete at very high strain-rates.

A criticism of the study may be the relative sizes of the models; the homogeneous model was 12 mm in diameter and 6 mm in length, compared to the 50 μm square mesoscale model. Inertial confinement is known to depend on specimen size, and thus could not be fully appreciated in this study due to the limited size of the models considered.

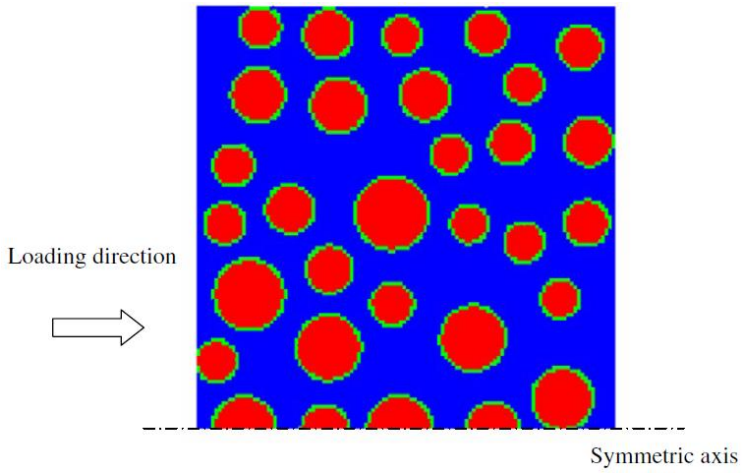


**Figure 2.11:** Mesoscale model: aggregates (red), ITZ (green), and cement matrix (blue) [43]

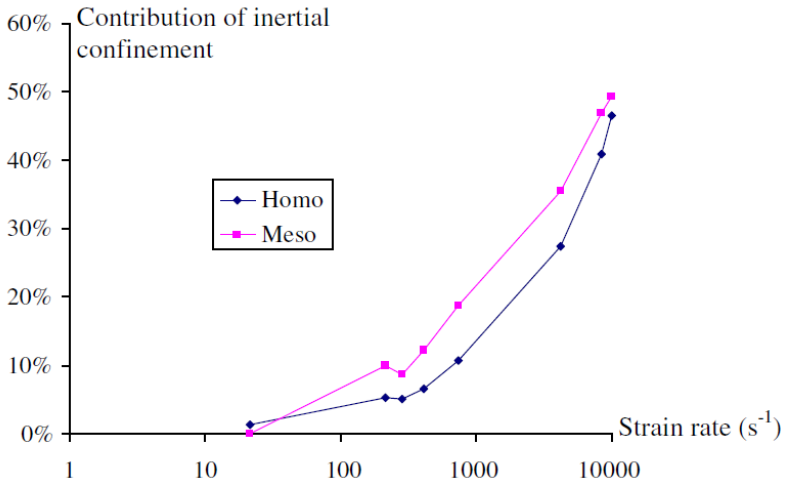


**Figure 2.12:** Contribution of inertial confinement to failure strength [43]

### 2.2.3.3 Microcracking Modeling

Microcracking is believed to play a key role in the failure of brittle materials [10, 47]. The most recent report by ACI Committee 446 [32] on the topic asserts that it is "widely recognized" that the fracture process zone involves initiation and growth of microcracks. In concrete under stresses of sufficient magnitude, these cracks propagate

outward from flaws and inclusions, which collectively may include pores, voids, or pre-existing microcracks.

Zheng et. al. [48] studied the effect of microcrack propagation and interaction in concrete (idealized as cement paste and aggregate) under dynamic loading using the Kachanov method [49], which is based on the superposition technique and the ideas of self-consistency applied to the average tractions on individual cracks. The authors utilized the wing crack model (Figure 2.13), found in work by Nemat-Nasser and Hori [50]. A wing crack is so named due to "wings" that propagate outward from a flaw, which is assumed to be penny-shaped, and serves as a descriptor of the tortuous crack pattern expected to arise in brittle composites like cement-based materials.

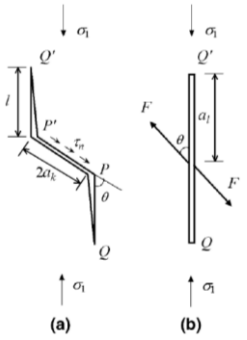


**Figure 2.13:** A "wing crack" (a) as modeled and (b) 2D equivalent crack [48]

The dynamic increase factor (a non-dimensional number defined as the material's dynamic strength divided by the static strength) proposed by this model is in good agreement as a lower-bound with the experimental results compiled in Bischoff and Perry for data in the range of earthquake through hard impact and blast loading (Figure 2.14). The model accounts for both inertial effects and free water viscosity, the former being the main emphasis of Bischoff and Perry's contribution [28].

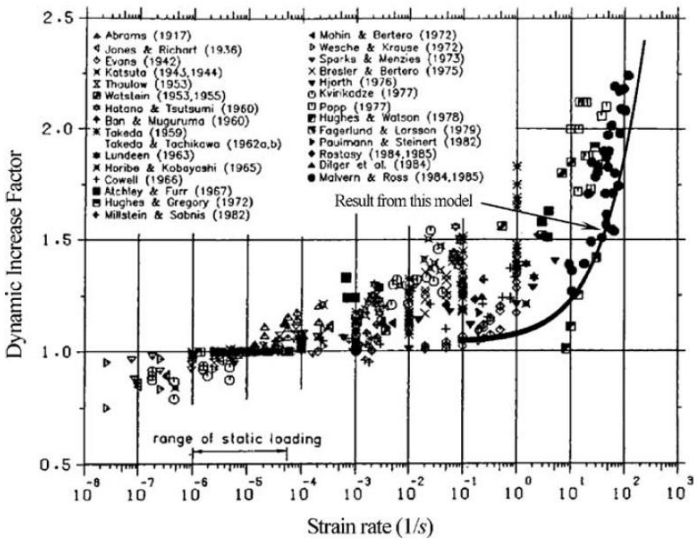


**Figure 2.14:** Model by Zheng et. al. [48] overlaid atop Bischoff and Perry's data

Paliwal and Ramesh's [6] model also relies on microcrack growth, but provides a much more comprehensive treatment than the 2006 work by Zheng et. al. Their model accounts for a size distribution of defects, which are generalized as rectilinear slits. While this approach assumes these defects are randomly-distributed, clustering of defects around aggregate is likely in concrete. New microcracks may initiate due to stress concentrations and elasticity mismatches at the site of defects or inclusions. The constitutive law relates stress-rate to strain-rate and damage evolution. Damage evolution, in turn, is related the flaw size distribution and number density, along with the rate of crack growth. Dynamic crack growth toughness (e.g. the criterion necessary for crack growth) is assumed to be constant, as the underlying mechanisms of dynamic fracture toughness is still unclear. The crack growth law relates the Rayleigh wave speed, $C_R$, of the material to equations for the stress intensity factor, $K_I$. Stress intensity factor $K_I$, in turn, depends mainly on the applied macroscopic stress, $\sigma$ (see [10] for a more thorough treatment), and on defect size and geometry.

More recently, Graham-Brady [47] applied Paliwal and Ramesh's model to brittle materials, and introduced a more complete statistical treatment by accounting for a clustered flaw distribution, which can lead to localization of failure. Using work developed by Neyman in 1939 [51], the flaws were viewed as either "parent" or "children" flaws, the former referring to flaws which are the center points of the latter (which are essentially satellite flaws of the parent). For example, an unclustered microstructure would be 100% parent flaws (Figure 2.15). Table 2.1 shows the increase in compressive strength with increasing strain-rate for 5% and 100% parent flaw microstructures, corresponding to (b) and (c) in Figure 2.15, while Figure 2.16 shows the coefficient of variation (COV) of the compressive strength with increasing element size for the three clustering parameters. From Figure 2.16, it is evident that the COV is sensitive to element size. Table 2.1 suggests that a clustered microstructure produces a higher strength increase regardless of whether the flaw sizes are fixed or distributed. This finding is significant as it relates to heterogeneous materials like mortar and concrete. For example, at the mesoscale (on the order of millimeters), the hydrated cement paste phase of mortar may be modeled as a "cluster" containing a set of flaws (e.g. entrained air voids, capillary pores, microcracks) which is visually quite similar to Figure 2.15a. Therefore, while the clustering parameters seem to be chosen somewhat arbitrarily in this statistical study to illustrate the effect of clustering [47], a detailed statistical characterization of flaws in actual cement-based material systems would enable this model to be used to interpret the strain-rate effect in cement-based materials.

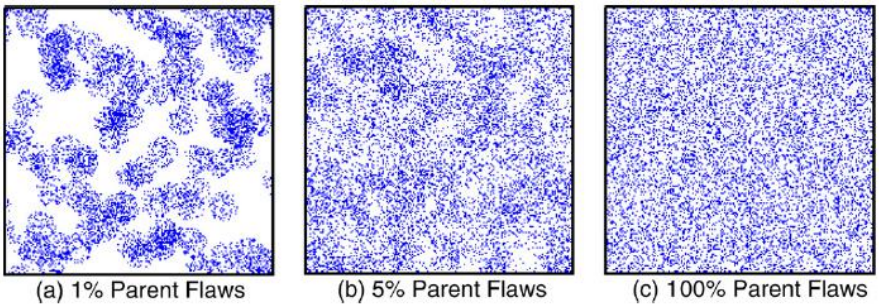


**Figure 2.15:** Clustering in a 1 mm × 1 mm microstructure defined by percentage of parent flaws

**Table 2.1:** Sample mean element strength (GPa) for a $4.44 \times 10^{-5}$ $m^2$ element [47]

| Strain Rate | 100% Parent Flaws | | | 5% Parent Flaws | | |
|---|---|---|---|---|---|---|
| | Fixed Size | Distributed Size | Percent Difference | Fixed Size | Distributed Size | Percent Difference |
| Static | 3.2 | 2.33 | -27.2 | 3.21 | 2.34 | -27.2 |
| $10^2$/s | 3.19 | 2.94 | -7.92 | 3.21 | 2.95 | -7.92 |
| $10^4$/s | 3.25 | 3.06 | -5.98 | 3.27 | 3.07 | -5.94 |
| $10^6$/s | 8.6 | 8.5 | 1.85 | 8.66 | 8.85 | 2.18 |

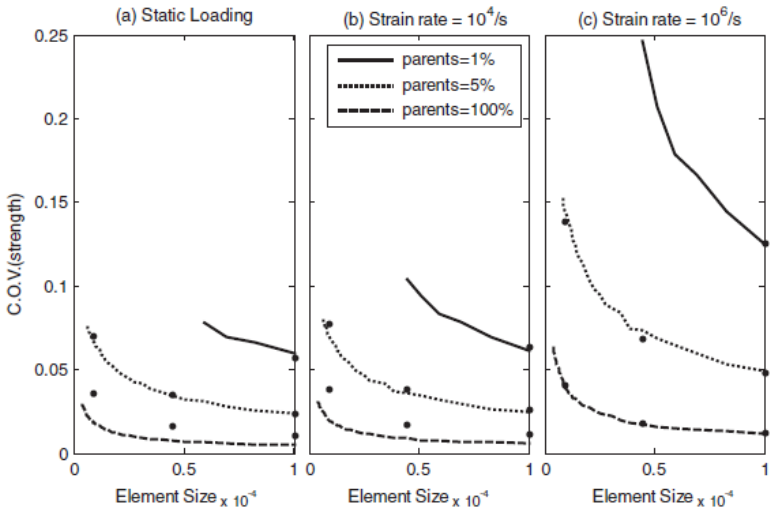


**Figure 2.16:** Coefficient of variation of uniaxial compressive strength with increasing element size for different clustering parameters [47]

### 2.2.4 Recommendations

While many of the constitutive models in the literature utilize parameters obtained from the concrete microstructure, the origins of the values are not often clear. An example of this may be found in Zhou and Hao [43], where the material properties are stated in the paper, but the source of these properties is not cited. In other cases, parameters are assumed based on ease of computing, such as when Zheng et. al. [48] assumed a value of unity for the ratio between interacting cracks.

Microcracking models would greatly benefit from data quantifying the shapes, sizes, locations of flaws present in the microstructure of cement-based materials. Most prior research was not coupled with extensive material characterization. Rather, the simulations which rely upon highly-parameterized inputs known to be influenced by many factors such as *w/cm*¸ degree of hydration, and cement fineness produce results which are commonly compared with general SHPB results for which only static compressive strength is known. In such an approach, it is difficult to isolate individual factors that may drive failure from the noise in the experimental data. It is thus necessary to couple a material characterization scheme with a modeling and experimental effort, as discussed in Chapter 4.

## 2.3 Extreme Condition: Cyclic Freezing and Thawing

Since concrete damage due to cyclic freezing and thawing is heavily dependent on the quality of the entrained air void system, this review will focus on mathematical models for the entrained air void system's statics and on experimental techniques to obtain information about the system. Most exterior concrete placed in the United States is intentionally entrained with tiny air bubbles (called "entrained air" or the "air void

system") by using an air entraining admixture (AEA). When water held in the pores of saturated concrete freezes, the water expands. This expansion causes a tensile pressure to develop that could damage the concrete from within, because concrete is very weak in tension. The entrained air voids are considered to be a "pressure release valve" designed to improve freeze/thaw durability by serving the dual purpose of acting as (1) nucleation sites for ice crystals to form and (2) cyropumps to drain the saturated pore network of excess water. However, an old rule-of-thumb states that each 1% air leads to about a 5% loss in strength, so engineering an adequate entrained air void system in the material is not a trivial task. The potential role of concrete quality in recent failures in both the accelerated laboratory and field performance has led to renewed interest in assessing air entrainment in concrete [11, 12, 13, 14]. It should be noted that entrained air is completely different from a similarly-named type of void space in hardened concrete called "entrapped air;" the latter type of void is a much larger (on the order of 1 mm – 10 mm), irregularly-shaped defect that occurs naturally and improves neither strength nor durability.

Realistic portraits of the entrained air void system in hardened concrete are difficult produce; the problem is quite complex. Concrete is an opaque material, the question of what lies within "black box" has puzzled researchers who have investigated the entrained air void system for over 60 years. What is certain is that entrained air voids are necessary for freeze-thaw resistance – a problem that is not only resigned to northern countries and regions. This review constitutes an attempt to analyze critically some theoretical (Section 2.3.2) and experimental (Section 2.3.3) methods of analyzing the air void system.

### 2.3.1 The Entrained Air Void System

Du and Folliard [53] investigated the mechanisms of air entrainment in concrete, with emphasis on the physical and chemical characteristics of the system. For a given admixture dosage, air entrainment decreases with increasing cement fineness. Aggregates also have various influences; for example, sand gradations between No. 30 and No. 100 promote the persistence of smaller air voids, while fines passing No. 100 decrease air content. The mixer type, mixing time, temperature, transportation to the site, consolidation, and pumping were all found to influence the system as well. Notably, the study also found that SCMs require increased AEA dosages.

While not mentioned explicitly in the paper, an important takeaway of the research is that a single size distribution assumption that is utilized for any air void system may not account for the characteristics of the final system due to the numerous factors that affect the finished product that occur during placing. For example, it is likely that SCMs adsorb the chemical admixture, shifting the size distribution to favor the larger air voids. However, chemical admixtures are typically dosed by cementitious material content, and rarely account for the types of mineral admixtures at play. As SCMs have become the rule more so than the exception, this finding is significant as it suggests that any modeling regime that purports to have generality for all entrained air void systems must be adaptable to the expectations that SCMs will alter the size distribution.

ASTM C 457, Standard Test for Microscopical Determination of Paramters of the Air-Void System in Hardened Concrete [54], is based on the pioneering work by Powers [2]. The standard assumes that the spacing factor is calculated for a system resembling Figure 2.17b. Specifically, it assumes that all entrained air voids are spheres of equal size,

and that each sphere lies on regular cubic lattice. This means that the "maximum" distance from a point in the paste to the periphery of an entrained air void is the distance from the center of a cubic lattice to the edge of an entrained air void lying in one of the corners. As noted in a previous section, in reality the entrained air void system is more likely represented by Figure 2.17a than Figure 2.17b. The entrained air void system in Figure 2.17b suggests a regularity found in the study of crystalline structure (i.e., it resembles a simple cubic lattice) with none of the regularity of performance that one might expect from such a system (as has been explored and exploited by researchers on the topic, such as in [55]).

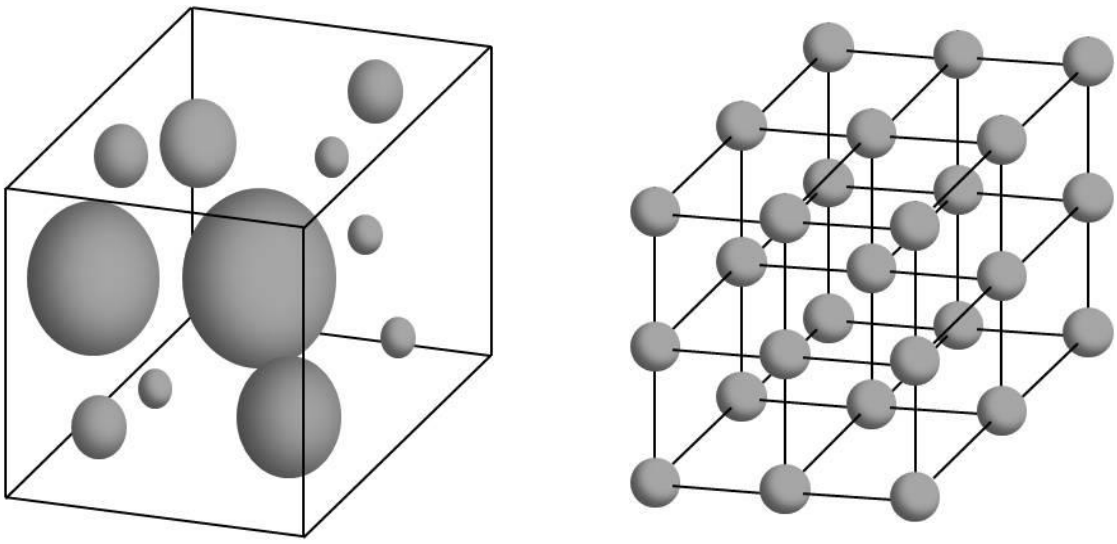

(a) (b)

**Figure 2.17**: Schematic showing (a) reality of the air void system's geometry and (b) assumptions per ASTM C 457

### 2.3.2 Review of Modeling Efforts

While the Powers factor [2] is the most widely-used spacing factor, it is subject to two misconceptions: that spacing factor is an estimate of the distance between air voids, and that it represents the maximum distance water must travel to reach the nearest air void in a concrete specimen [56, 57]. As noted by Snyder [55], there is no theoretical maximum value for paste-void spacings. There only exist percentiles of the distribution that one may quantify to characterize the fraction of paste within some distance to the nearest air void surface. The Powers factor was developed in the late 1940s, and is not the subject of this review. However, it still holds great importance because of its wide acceptance; one rarely encounters literature that does not acknowledge it or compare the results to it. The data in Figure 2.18 suggest that concretes that run the gamut of spacing

factors may be considered “durable,” with few exceptions. However, work by Tanesi and Meiniger [58] suggests that some concretes with improperly-low spacing factors exhibit good freeze-thaw durability while others with acceptable spacing factors failed to remain durable after many freeze-thaw cycles. The authors noted that the reason for this is unknown. It was noted from their work that Vinsol admixtures performed well even if their spacing parameters exceeded ASTM C457 limits, while synthetic admixtures performed poorly even if they insured an entrained air void system that met the specifications per ASTM C457; this suggests that more complicated factors may have an effect than merely void system geometry, despite the complex problem that the entrained air void system’s morphology poses.

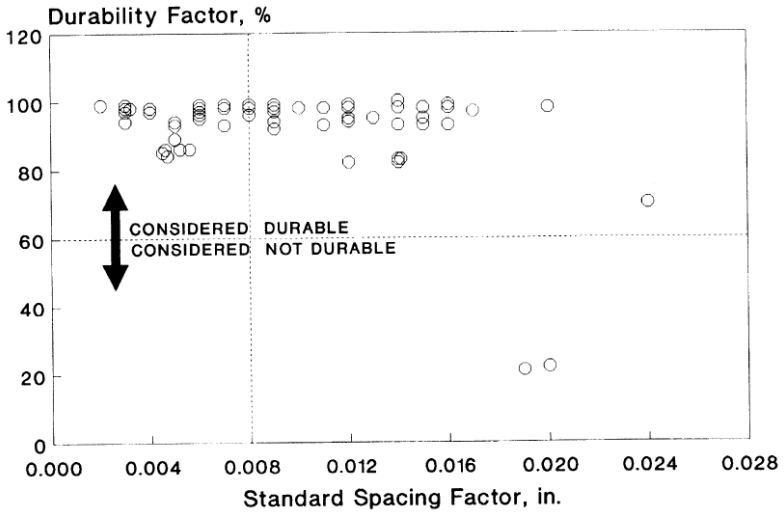


**Figure 2.18**: Durability factor versus spacing factor

Pleau and Pigeon [59] introduced their flow length concept for analysis of entrained air void spacing. They used $h(x)$ to represent the probability density function of the distance between a random point in the system and the center of the nearest air void. The joint probability that a random point is a distance $s$ from the surface of an air void with radius $\mathcal{R}$ is

$$\beta(s,\mathcal{R}) = h(\mathcal{R}+s)\,f(\mathcal{R}) \qquad \text{Eq. 2.3}$$

where the function $h(x)$ is approximated by a Hertz distribution (as used by Philleo [60]):

$$h(x) = 4\pi\rho_{air}\exp\left(-\frac{4\pi\rho_{air}}{3}x^3\right) . \qquad \text{Eq. 2.4}$$

Snyder [55] criticized this distribution for being equal to the volume fraction of overlapping spheres in the monodisperse case. As the monodisperse case is unphysical, it is not clear why this is an issue. The Pleau and Pigeon acknowledged this fact, and even suggested it was physically reasonable since air voids sometimes appear to overlap when sectioning is done (although this is not the author's experience). The parameter $\mathcal{R}$ is eliminated by from $\beta(s,\mathcal{R})$ by integrating over the radii by

$$k(s) = \int_0^\infty h(\mathcal{R}+s)\,f(\mathcal{R})\Theta(\mathcal{R}+s)d\mathcal{R} \qquad \text{Eq. 2.5}$$

where $\Theta(x)$ is the Heaviside step function, which is equal to zero for negative arguments of $x$ and equal to one otherwise. The cumulative density function is then

$$K'(s) = \int_{-\infty}^{s} k(s')ds' \qquad \text{Eq. 2.6}$$

and may be interpreted as the volume fraction of the entire system within distance $s$ of an entrained air void center. Therefore, $K'(0)$ is an estimate of the total air content. Pleau and Pigeon normalize the volume fraction of paste within $s$ of an entrained air void surface as

$$K'(s) = \frac{1}{1-K'(0)}\int_{-\infty}^{s} k(s')ds' \ . \qquad \text{Eq. 2.7}$$

In a numerical test of lognormally-distributed spheres (that is, a computer simulation where an assemblage of spheres following a lognormal distribution are placed in three-dimensional space), Snyder found Pleau and Pigeon's equation to overestimate the

percentiles of the distribution used to characterize the paste fraction within some distance of the nearest void surface.

Attiogbe [61] proposed a spacing equation that estimates the "mean spacing of air voids" in concrete. Previous models by the author [57] utilized a spacing factor, *F*, given by:

$$F = \frac{8}{\frac{\phi_1}{\phi_2} + 1} \leq 1 \ . \qquad \text{Eq. 2.8}$$

This was later amended to take a size distribution into account. Attiogbe acknowledged the zeroth-order logarithmic distribution's use in other investigations of size distribution. However, he instead chose a Gamma distribution to represent the size distribution of entrained air voids, given by:

$$f(\mathcal{R}) = \frac{1}{\beta^a \Gamma(a)} (2\mathcal{R})^{a-1} \exp(-2\mathcal{R}/\beta) \ . \qquad \text{Eq. 2.9}$$

where

$$a = \frac{\left(2\langle \mathcal{R} \rangle\right)^2}{\sigma^2}; \quad \beta = \frac{\sigma^2}{2\langle \mathcal{R} \rangle} \qquad \text{Eq. 2.10}$$

Attiogbe [61] thereby assumed the *all* air void distributions can be modeled by modifying the shape and scale parameters of a statistical distribution. Statistical distributions carry weight and significance outside their mathematical forms; it is therefore worrisome to choose a distribution based on ease of implementation or inspection of its shape. Furthermore, the distribution is continuous and is therefore defined as $\mathcal{R}$ approaches infinity. The modified *F* is then

$$F = \frac{\left(\frac{18}{\pi}\right)\left[1 + \frac{a+3}{4a}\right]}{\frac{\phi_1}{\phi_2} + 1} \leq 1 \ . \qquad \text{Eq. 2.11}$$

In a numerical test of spacing equations, Snyder [55] found that the Attiogbe equations for estimating percentiles of the void-void spacing distribution was "quite poor," going on to say that "for lognormally distributed sphere radii, it is clear that neither equation has any relevance to any reported statistic of the void-void spacing distribution."

Snyder [55] ultimately discovered that the Lu and Torquato [20] equations gave the greatest agreement in his simulation. The equations are described as follows: the void nearest-surface distribution function $h_V(y)$ is defined such that $h_V(y)dy$ is the probability that at an arbitrary point in the system from the nearest particle surface lies at a distance between *y* and (*y* + *dy*). The void "exclusion" probability $e_V(y)$ is defined as the probability of finding a region $\Omega_V$ surrounding an arbitrary point, where $\Omega_V$ is a spherical cavity of radius *y* devoid of particle material. The functions $h_V(y)$ and $e_V(y)$ are related by

$$e_V(y) = 1 - \int_{-\infty}^{y} h_V(\xi)d\xi \,. \qquad \text{Eq. 2.12}$$

The mean void nearest surface distance, $l_V$, is defined as

$$l_V = \int_0^{\infty} y h_V(y)dy = \int_0^{\infty} e_V(y)dy \,. \qquad \text{Eq. 2.13}$$

More detailed information regarding $h_V(y)$ and $e_V(y)$ as they apply to modeling entrained air voids in hardened concrete may be found in Chapter 3.

Snyder's findings are not surprising; Lu and Torquato derived their equations based on robust series expansions for the probabilities. However, they do not purport to define a size distribution. Lu and Torquato were not proposing an equation for air void

spacing in concrete; they were defining spatial arrangement for a general system of polydispersed spheres. While the analysis in Synder's work is promising for the application of the Lu and Torquato equations, it should be noted that Lu and Torquato propose their distributions in terms of the size distribution $f(\mathcal{R})$ and propose no methods for sampling for it. Therefore, while criticisms of the spacing equations proposed by other authors have their merits, it is understood that a simple method to sample for the three-dimensional size distribution of air voids in hardened concrete is yet outstanding.

### 2.3.3 Review of Experimental Efforts

Several methods exist to experimentally examine the entrained air void system. In some cases, the actual results of the size distribution vary depending on the experimental procedure. There is some evidence to suggest that resolution limits may impact the analysis. When sectioning cuts through a polydispersed sphere system, some large voids will be planed through their extrema, while others will be planed through cross-sections near their poles. The fundamental problem in the analysis is accounting for the fact that two circles may appear the same (in plane) but come from very different spheres [62].

A number of studies have focused on digital image analysis as an alternative to the ASTM C 457 point count or linear transverse method [63, 64]. As computers became ubiquitous in technical fields in the late twentieth century, laser scanning equipment and analysis software became far more commonplace than, say, petrographic microscopes.

Pleau et. al. [64] investigated the usefulness of image analysis in 2001. As motivation, they cited the fact that the spacing factor of ASTM C 457 overestimates the real spacing of air voids. Figure 2.19 shows the correlation between their image analysis results and ASTM C 457. The image analysis technique overestimates the specific

surface and underestimates the air content. The authors assumed this was due to errors in distinguishing between air voids at smaller size ranges. It should also be noted that digital images will have "sawtooth" boundaries, meaning the actual perimeter of a circle is equal to the sum of the edges of square pixels ("$\pi$" equals "4" in this case: an uncomfortable fact for engineers). Regarding the spacing factor, the image analysis and ASTM techniques were in better agreement.

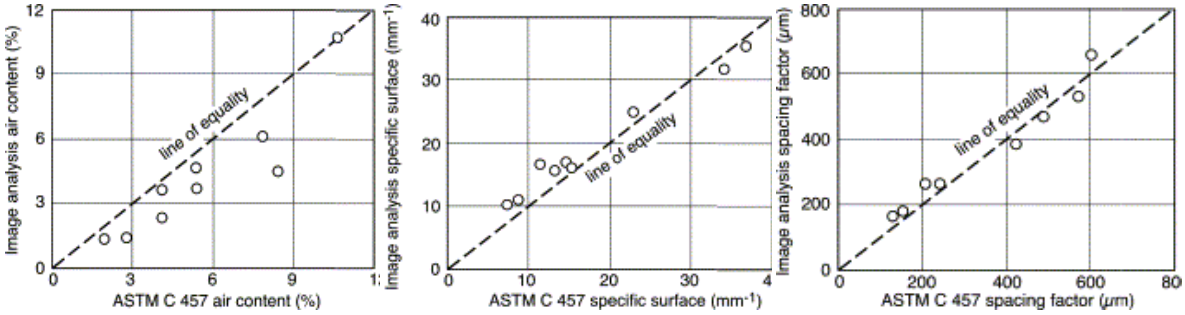


(a) (b) (c)

**Figure 2.19**: Relationship between image analysis and ASTM C 457 for (a) air content, (b) specific surface, and (c) spacing factor

The study found that image analysis had a tendency to over-predict smaller air voids than the visual inspection techniques, as demonstrated in Figure 2.20. The image analysis technique rendered histogram peaks that were 50 – 70% higher for the smallest entrained air void classes in the system. The authors propose that this could be due to overlapping entrained air voids in this size range. However, it is not clear why overlapping smaller entrained air voids would cause *more,* smaller entrained air voids to appear in image analysis; it seems intuitive that the computer would assume these are larger entrained air voids. The study does not attempt to address the problem that three-dimensional diameters are not truly represented by plane cuts. Finally, an overarching question to be raised is as follows: if the motivation of the research stressed the

shortcomings of the ASTM method for air void analysis, why is it the lone test for accuracy utilized in the study?

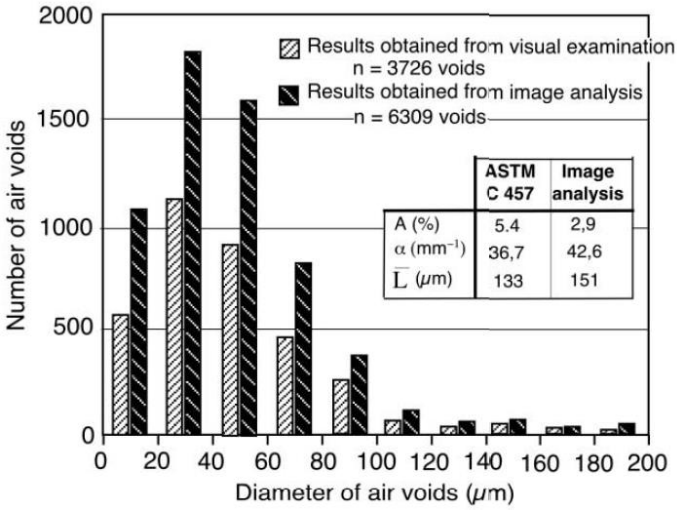


**Figure 2.20**: Typical example of the frequency histogram of the diameter of air-void circles seen on the examined concrete surface as obtained from image analysis and visual examination for an air-entrained concrete.

Peterson et al. [65] investigated image analysis with a flatbed scanner around the same time as Pleau et al.'s investigation. They also observed a lower air content in automated trials. However, they noticed a lower specific surface as well. Overall, they reported an overall accuracy of 90.2 % compared with 570 digital microscope images. They concluded that the resolution of the scanner may be too poor to recognize the smallest entrained air voids (the resolution was 1500 DPI). The study reported a more robust distance analysis (as shown in Figure 2.21), where a histogram of distances from a point in the cement paste to the nearest air void are binned. The authors recognize that this is a two-dimensional cut and not necessarily representative of the three-dimensional data (the problem highlighted in Figure 3.3).

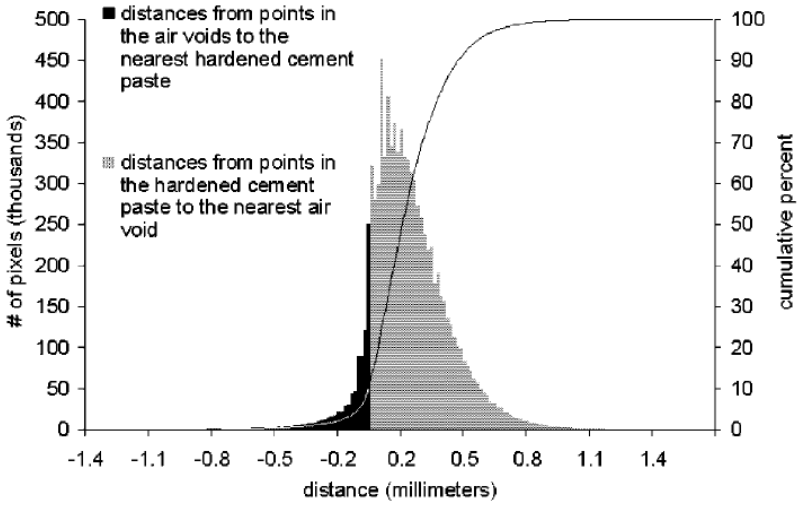


**Figure 2.21**: The spacing distribution derived from a proximity analysis of the quantified image

Image analysis studies in hardened concrete have, however, proposed that there is no substitute for the human eye in terms of feature detection at very small length scales. This seems odd, as other studies have shown that for a single radiograph taken from a slip gauge, a digital image analysis system can be as much as 20 times more accurate than the human eye [66]. As contrast between the paste and the small voids is poor, it is difficult to automatically sample based on threshold values from grayscale image histograms. Future work is still needed in this topic to minimize errors in image analysis.

Elastic wave propagation is another technique commonly employed for nondestructive evaluation of air entrained concrete samples. When wave propagate through solids, they will reflect and scatter as they encounter density contrasts in the material through which they propagate. A familiar example is a prenatal ultrasound, where the fetus has a higher density than the surrounding fluid.

Recently, Lissenden et. al. [67] utilized Rayleigh surface waves to characterize the air void system. The authors observed that four hours of setting time was necessary

for Rayleigh waves to penetrate fresh concrete deeply enough to determine material properties. Figure 2.22 shows the evolution of the wave speed with setting time beginning at five hours after placement. The paper sought to answer the question of whether wave speed measurements are sensitive enough to characterize the entrained air void system. From Figure 2.22, the data appear to be converging as time after setting increases. It is not clear that this data can differentiate between concrete mixes that are similar. The authors suggested that Rayleigh waves may provide a method for evaluating the spacing and specific surface parameters of the entrained air void system. However, they did not provide a means of doing this from the results they presented in the paper.

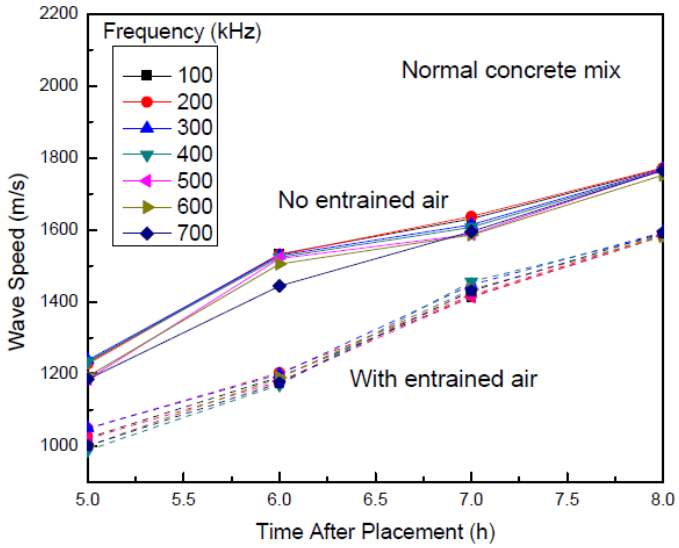


**Figure 2.22**: Rayleigh wave speeds in normal concrete mixes as a function of time after placement [67]

Punuari et. al. [68] utilized an ultrasonic measurement apparatus shown in Figure 2.23. The transducers (labeled T for transmitting and R for receiving) were located on axis (epicenter) on opposite faces of each specimen. Two matched pairs of broadband transducers were used in the transmission and detection of longitudinal ultrasonic waves.

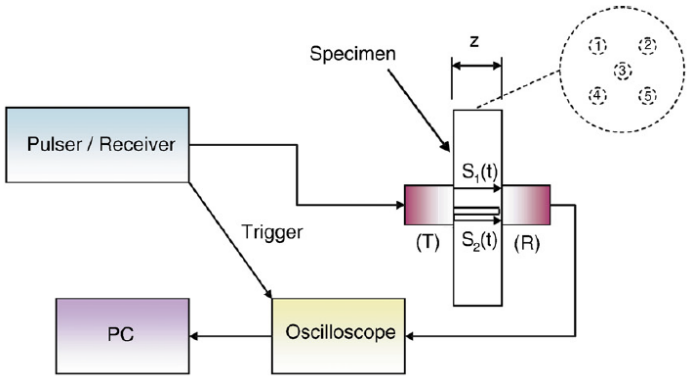


**Figure 2.23**: Experimental setup utilized in Ref. [68]

The authors utilized the following relationship to determine the relationship between the total attenuation, $\alpha$, and the size and volume fraction of the entrained voids:

$$\alpha = \alpha_a + \alpha_s = (1-\phi_{air})\alpha_a + \tfrac{1}{2}\rho_{air}\gamma^{sca}. \qquad \text{Eq. 2.14}$$

In Eq. 2.14, $\alpha$ is the total attenuation, which is the sum of the contribution of absorption occurring within the cement paste matrix ($\alpha_a$) and the scatter due to the presence of voids ($\alpha_s$) with a volume fraction $\phi_{air}$. The number of voids per unit volume has been expressed as $\rho_{air}$, whereas Ref. [68] uses the notation $n_s$ to denote the same quantity. Finally, the scattering cross-section is given in another publication by the authors [69] as

$$\gamma^{sca} = \frac{4\pi}{\mathrm{Re}(k)}\mathrm{Im}(-\sum_{m=0} i^m A_m) \qquad \text{Eq. 2.15}$$

The attenuation results for sample EACP2 ("entrained air cement paste 2", *w/c* = 0.4, AEA added at 0.2% by cement mass) are shown in Figure 2.24a. As is evident from the figure, the error bars suggest much scatter in the data.

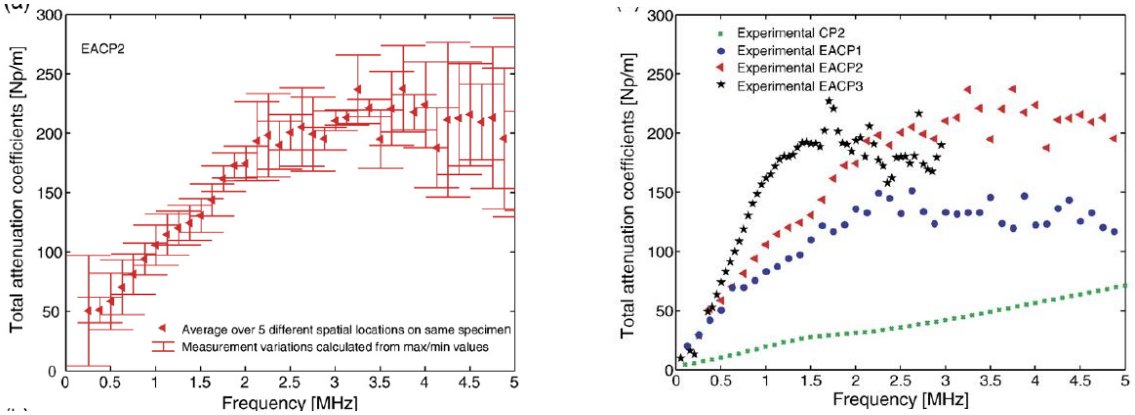


(a) (b)

**Figure 2.24:** Total attenuation results (a) from specimen EACP2 and (b) summary of the average values for all EACP specimens (Ref. [69])

The analyses in [68, 69] assumed the entrained air voids were monodispersed in size. In their analysis of the lineal-path function for polydisperse systems, Lu & Torquato [70] found that polydispersivity has an important impact on the lineal path function[3], $L(z)$. In their analysis, $L(z)$ would correspond to the mortar phase when discussed in the context of air voids in concrete). While $L(z)$ is not necessarily related to the air void parameters of ASTM C457 per se, it does contain information that is pertinent to water transport in the cement paste, and thus its sensitivity to polydispersivity suggests that the assumption of monodispersivity is a flawed assumption.

The average radius, $\langle \mathcal{R} \rangle$ (which the authors originally denoted by $a$), was calculated from $\rho_{air} = 3\phi_{air} / 4\pi \langle \mathcal{R}^3 \rangle$ to yield the results presented in Table 2.2 ("simplex prediction" refers to the results of the wave propagation experiments). To compare it to other experimental regimes, the authors utilized IMAGE-PRO Plus to analyze the images

[3] the lineal path function, $L(z)$, gives the probability of finding a line of length $z$ entirely with a particular phase (see Chapter 3 for a more detailed treatment)

(denoted "image analysis maximum" in Table 2.2). The paper claims to have found very good agreement between the entrained air void sizes predicted by inversion of the attenuation data and those measured by quantitative image analysis. The error in assuming three-dimensional size distribution directly from two-dimensional sections has been discussed; furthermore, Ref. [68] is unclear in what is meant by "image analysis maximum." The maximum air void diameter is expected to be larger than the values in the table. To show how the data would translate to an analysis of spatial arrangement, $l_V$ (see Section 3.2.3 and Eq. 3.9) has been calculated for each sample for the monodispersed case (see final column of Table 2.2). These values appear high for air voids in cement paste. Finally, the paper suggests that the entrained air void size distribution will be normal; however, most other studies acknowledge that the distribution will be heavily skewed towards the smaller voids.

**Table 2.2:** Results from Ref. [68] with $l_V$ calculated for comparison

| | **Ultrasonic inverse volume fraction, $\phi_{air}$** | **Radius, $\langle \mathcal{R} \rangle$ (mm)** | | $l_V$ **(mm)** |
|---|---|---|---|---|
| | | **Simplex prediction** | **Image analysis maximum** | |
| **EACP1** | 3.3 | 0.33 | 0.32 | 0.57 |
| **EACP2** | 7.0 | 0.35 | 0.36 | 0.38 |
| **EACP3** | 11.3 | 0.50 | 0.49 | 0.38 |

X-ray microtomography is similar to medical computed tomography (CT) scans. Images are created that map the variation of the x-ray attenuation coefficient within objects. Three-dimensional information can be obtained from radiographic projections of the specimen taken at many angles or project views, and this can be used in reconstruction algorithms to construct a volume of concrete for analysis.

A recent analysis by Promentilla and Sugiyama [71] used a machine with an ultimate resolution on the order to 10 microns. “Resolution” in this sense refers to the size of a voxel, or volume element, which is the three-dimensional analogue of a pixel (“pixel” comes from “picture element,” and “voxel” comes from “volume element” or “volumetric pixel”). The authors noted that this resolution comes at the expense of sample size. The smallest air voids in the system are classically expected to be around 50 microns in diameter [72], and so this voxel size is reasonable.

Figure 2.25 is a rather landmark contribution of Promentilla and Sugiyama [71]. The three-dimensional reconstructions show colorized reconstructions of the pastes that were investigated, while the graphs show the histograms (probability mass functions) of the air voids. In the figure, “P-AE” denotes “ordinary **p**ortland cement, **a**ir **e**ntrained” and “F-AE” denotes “**f**ly ash, **a**ir **e**ntrained” (the study also investigated void space in non-air entrained mixes, but these studied which visualized entrapped air are of no interest here). The distributions are rather crucial to advising any experimental regime that seeks to reconstruct three-dimensional size distributions from plane sections. Clearly, it can be observed that the data skews toward the larger voids, and shows very little occurrence of voids with a diameter large than 0.2 mm (in the author’s opinion, the first bin of each histogram is likely the contribution of large macropores). This suggests that a log-normal or power-law (e.g., exponential, Pareto) probability density function could model the data better than normal [68, 69] or Gamma [57] distributions.

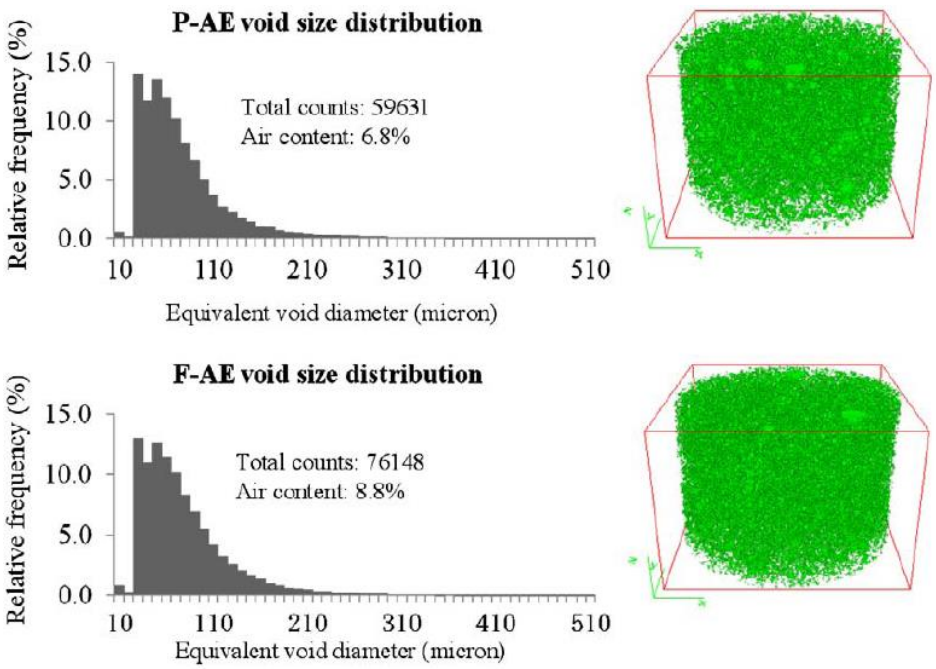


**Figure 2.25**: Air content and void size distributions for two mortars analyzed by x-ray microtomography (Ref. [71])

The study was limited to mortars where no coarse aggregate was present. Du and Folliard [53] noted that crushed rocks generate shear and impact during mixing, thus creating smaller air bubbles. Therefore, while the data considers size distribution and spatial arrangement of entrained air voids from real mortar in three dimensional space (unlike Snyder's review [55], which was able to criticize spacing equations based on a computer simulation of a volume of air entrained concrete, not experimental data from air entrained concrete), it does not necessarily yield a size distribution that is representative of entrained air voids in hardened concrete placed in the field.

### 2.3.4 Recommendations

A wide array of factors affect the final air void system in hardened concrete. It is difficult to assume a one-size-fits-all model for the air void size distribution *a priori*; the finished product must be analyzed. Ultrasonic techniques are currently in their infancy,

and seem relegated to mortars. X-ray tomography techniques are limited to small sample dimensions. However, the small sample dimension is probably not the greatest disadvantage: advanced imaging equipment is unlikely to be easily and economically introduced into the construction industry. By contrast, image analysis software can easily be executed on computers with high computing power and efficiency that are relatively inexpensive and ubiquitous in the twenty-first century. Operators can also incorporate their analyses with personal judgment in a manner that may not be possible with wave propagation techniques. Therefore, it is recommended that future research advance the state-of-the-art of image analysis from plane cuts of concrete to gain knowledge about the actual three-dimensional size distribution of entrained air voids.

While many spacing factors or spatial arrangement models have been proposed, many parameters are measuring very different things (e.g. mean spaces between voids, mean spacing between random points and nearest surfaces, protect volume of paste, etc.). A consensus must be reached to determine which metric is actually meaningful. To date, research on the mesoscale measurement of air voids has emphasized on the inverse problem of reconstructing a size distribution from a plane cut or to extracting statistical information based on certain assumptions. Since the focus of these research studies were on the entrained air void phase, further research is required to couple ice crystallization in pores or fluid flow to the spatial geometry expressed via the entrained air void spacing equations.

More research is necessary on the topic of entrained air void systems and the effect on freeze/thaw durability. Most of the currently-used analytical techniques are based on assumptions that do not always correlate well to actual conditions. Immediate

adoption of the most robust sampling methodologies such as x-ray microtomography is unlikely due to their relatively high cost. ASTM C 457 results might not the best comparison for results from any new investigative technique on freeze/thaw durability for several reasons: it is not based on physical reality, it is time consuming, and it does not compensate for these shortcomings by providing excellent insight into durability.

# CHAPTER 3

# A PROBABILISTIC TECHNIQUE FOR ENTRAINED AIR VOID ANALYSIS IN HARDENED CONCRETE

A novel method that utilizes the lineal-path function to ascertain a probability density function for the three-dimensional size distribution of entrained air voids directly from plane polished sections of hardened concrete is proposed (see Task 1.A.). The results then treat the spacing factor in terms of a probabilistic maximum distance from a random point in the cement paste matrix to the periphery of an air void, where air voids are treated as a polydispersed sphere system. The model was applied to concretes with various air entrainment admixture types and dosages. The results suggest the model could offer a better assessment of the system for use in assessing freeze/thaw durability (see Task 3) and studying admixtures, as well as provide a new tool for spatial characterization of heterogeneous and porous materials.

## 3.1 Introduction

Discovered serendipitously in the early twentieth century, air entrainment is hailed as concrete's protector against damage in cold weather. While air entrainment is crucial for ordinary concrete's resistance to damage during cycles of freezing and thawing and salt scaling, the potential role of concrete quality in recent failures in both the accelerated laboratory test and field performance has led to renewed interest in assessing the quality of air entrainment [11, 12, 13, 14]. In particular, questions have been raised about the quality of current metrics for assessing air entrainment [15].

Currently, the quality of an entrained air system in concrete is quantified by specific surface, void frequency, spacing factor ($\overline{L}$). According to ASTM C457:

> …of the parameters determined with this test method ... $\overline{L}$ …is generally regarded as the most significant indicator of the durability of the cement paste matrix to freezing and thawing exposure of the concrete. The maximum value of the spacing factor for moderate exposure of the concrete is usually taken to be 0.20 mm [0.008 in.].

Based on Pioneering work by Powers [2], this approach has been used for over five decades, having first been adopted by ASTM in 1960.

With advances in image analysis [16] and improvements in understanding of the mechanisms of air entrainment in concrete [17] and role of air entrainment in freeze/thaw damage mitigation [18, 19], there seems a potential opportunity to improve upon (or at least refine) methods for assessing the quality of air entrainment in concrete. Since spacing factor is an average of an average, it is sensitive to outliers, creating the problem of arbitrary deletion of "large" air voids during petrographic analysis [73, 74]. Some recent research has examined the air entrainment characteristics of newer air entraining admixtures using ASTM C457 [18, 75], thereby studying modern materials with dated techniques. Therefore, the objective is this chapter is to integrate microstructural statistics and image analysis to derive an improved spacing factor – one based on the reality of the distance water must migrate to reach an entrained air void site.

## 3.2 Model Overview

ASTM C457 [54] describes methods to quantify parameters associated with the susceptibility of the paste portion of concrete to freeze/thaw damage. The standard assumes that the spacing factor is calculated for a system with monosized and regularly spaced porosity, resembling Figure 3.1b. Mathematically, the system is described by an ensemble of average-sized voids with an average spacing. In reality, the spatial and size distribution of entrained air voids is more likely represented by Figure 3.1a than Figure 3.1b. With this understanding, there are opportunities to improve upon the descriptors used to assess quality of air entrainment in cement-based materials by considering them as irregularly spaced sphere of multiple sizes (polydispersed spheres), as proposed herein. Alternative spacing factors have been proposed by Philleo [60], Attiogbe [76], and Pleau and Pigeon [77]. In both [60] and [77] , the spatial arrangement of the entrained air voids is assumed to follow a Hertz distribution. This suggests that the arrangement follows a Poisson process, which is only true if the spheres have zero radius. In [76] , the air voids are assumed to follow a Gamma distribution with parameters related to the mean diameter and specific surface area of the spheres. However, the procedures in [76] did not accurately estimate any parameter of a simulated air void system when tested in [15]. Furthermore, none of the aforementioned methodologies measure the size distribution directly. (For a comparison of these factors, where they are shown to be unsatisfactory, see [15]).

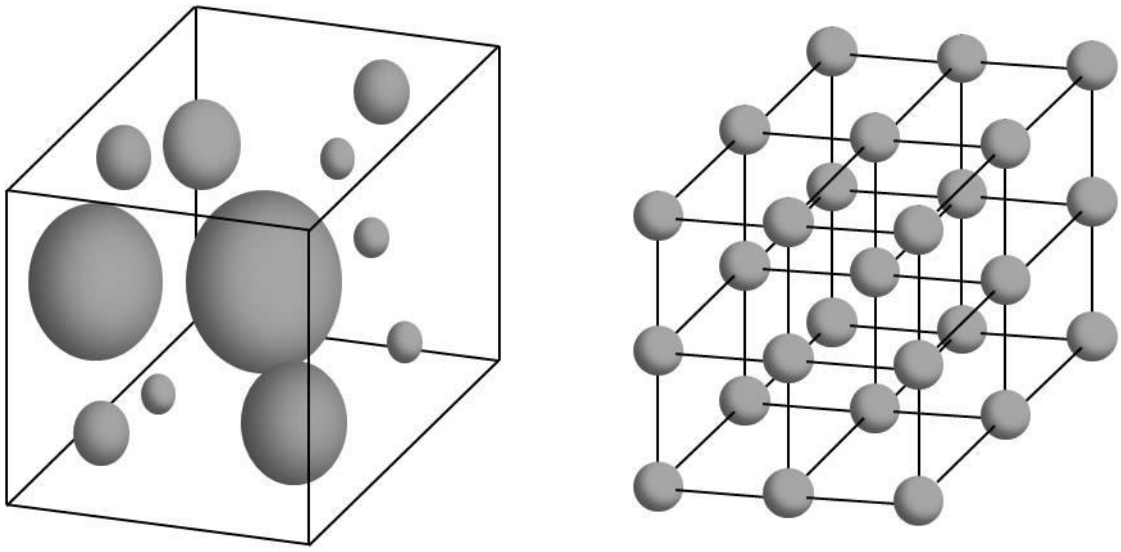

(a) (b)

**Figure 3.1**: Schematic showing (a) a representation of polydispersity typical of entrained air void systems in cementitious materials and (b) assumptions of the air void structure per methods provided in ASTM C457

### 3.2.1 Background

The nearest surface (NS) function provides a statistical description of the spatial arrangement between any point in the paste and its proximity to the surface of a nearby sphere (in this case, an entrained air void). For the case of monodispersed spheres (a system of spheres all of a constant radius $\mathcal{R}$), NS functions contain essentially the same information as "nearest-neighbor distribution" (NND) functions that describe the spatial arrangement between a point in the paste and the proximity to a nearest particle centroid (in this case, center of an entrained air void) and that gives the probability of finding a point's nearest-neighbor within a shell of radius $y$ to ($y + dy$) from a reference point. If all

particles in a system are of uniform size – that is to say the particle size distribution (PSD) is a constant – the probability then may be described by a nearest-neighbor distribution function. However, entrained air voids exist in concrete as a polydispersed sphere system, and such a monodispersed model should be viewed as an inferior descriptor even from a physical sense.

Figure 3.2 illustrates the difference between a nearest-surface function and a nearest neighbor (in this case, nearest centroid) distribution function for a material with polydispersed spheres. Let point *A* be a random point in three-dimensional space. Let point *B′* lie on the surface of the sphere centered at point *B* at the location where line $\overline{AB}$ intersects the sphere's surface (*C′* is defined in kind). As line $\overline{AB} < \overline{AC}$, it defines the nearest-centroid to point *A*. However, as shown for the case in Figure 3.2, line $\overline{AC}'$ defines the nearest-surface to point *A*. The nearest surface, then, is proposed to be a more appropriate descriptor of the quality of a polydispersed entrained air void system. Water is thought to move through the porespace in the cement paste to the *surface* of an entrained air void, not to its centroid [78].

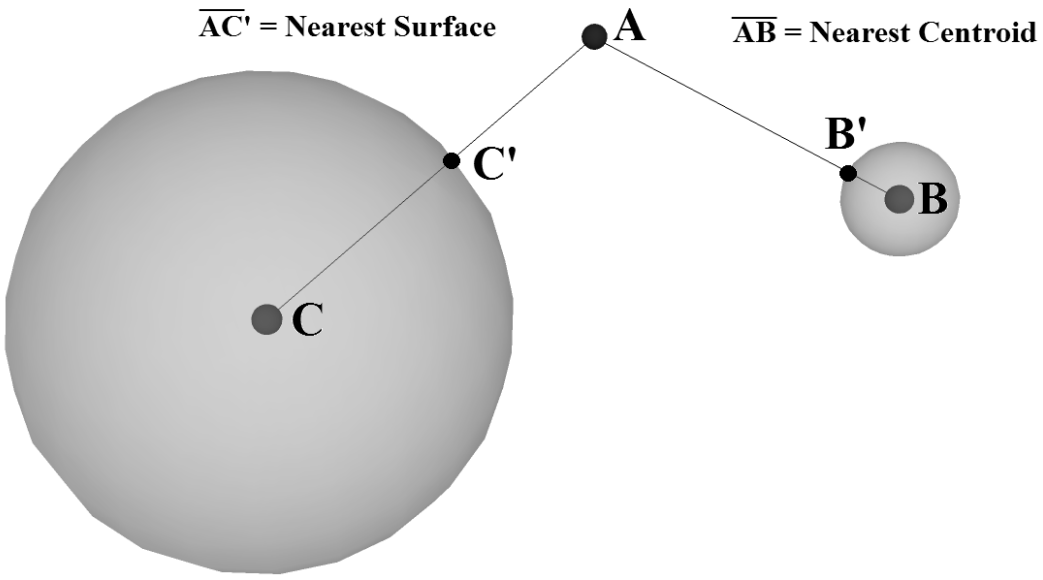


**Figure 3.2:** Local environment about point A, elucidating the need to favor a nearest-surface function over a nearest-centroid function for describing the quality of an entrained air void system

Lu and Torquato [79] first derived equations, which will be discussed in detail in Section 3.2.3, to describe a nearest-surface distribution for a polydispersed sphere system. The model relies on three important parameters describing the polydispersed sphere system:

- The volume fraction of spheres, $\phi$
- The number density of spheres, $\rho$
- The first three moments of the size distribution, $\langle \mathcal{R} \rangle$, $\langle \mathcal{R}^2 \rangle$, and $\langle \mathcal{R}^3 \rangle$.

The following section describes a method to obtain these parameters. However, first, it is useful to describe the inherent challenge in obtaining representations of three-dimensional structures from two-dimensional data.

When sectioning cuts through a polydispersed sphere system, some large spheres will be planed through their extrema, while others will be planed through cross-sections near their equators. The fundamental problem in the analysis is accounting for the fact that two circles may appear the same but come from very differently sized spheres, as illustrated by Figure 3.3. For example, the two circles within the dashed box in Figure 3.3 are indistinguishable from each other, despite the fact that the upper circle is cut from a much larger sphere than the lower circle. Because of the inherent challenge in reconstructing three-dimensional information from two-dimensional sections, a statistical approach is required.

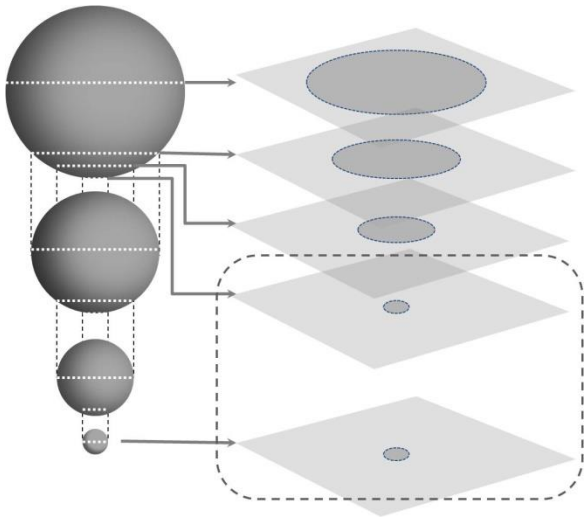

**Figure 3.3**: Illustration of two-dimensional cuts through three-dimensional objects demonstrates that distinguishing information between the circles in the dashed-line enclosure is lost

### 3.2.2 Entrained Air Void Size Distribution

One classical approach to overcome this is a Saltykov Method [62], or variation upon it [80], which has been used to characterize other two-phase heterogeneous materials with spherical inclusions. Saltykov presented a solution to finding the number

density of spheres per unit volume by discretizing Wicksell's solution to unfolding problems of sphere size distributions. Spheres are divided into *k* size classes and subtracting out the number of circles counted in each size class that are likely to belong to spheres of larger size classes. However, the error magnification is typically problematic and limits the Saltykov method's usefulness for a material such as air-entrained concrete where a broader 3D size distribution is typical.

Rather than utilizing the Saltykov method to estimate the 3D size distribution, this study introduces a novel approach for obtaining the 3D size distribution of air voids from 2D data sets. This approach is depicted in Figure 3.4. A key parameter to this new model is the lineal-path function, $L_i(z)$. This function describes the probability that a line segment of length $z$ lies wholly in phase $i$ when randomly placed in a sample [81]. The bounds on the lineal-path function are $L_{(i)}(0) = \phi_{(i)}$ and $L_{(i)}(\infty) = 0$, where $\phi_{(i)}$ is the volume fraction of phase $i$. Another useful function is the chord length probability density function, $p_i(z)$. This function is defined such that $p_i(z)dz$ is the probability of finding a chord of length between $z$ and $(z + dz)$ in phase $i$. Figure 3.4 depicts realizations of $L_i(z)$ and $p_i(z)$. Figure 3.4, line segments of length $z$ are shown in both the hydrated cement paste (HCP) phase (shown in white) and the entrained air void phase (shown in gray) alongside lineal-path functions which give the probabilities that these lines occur in this microstructure.

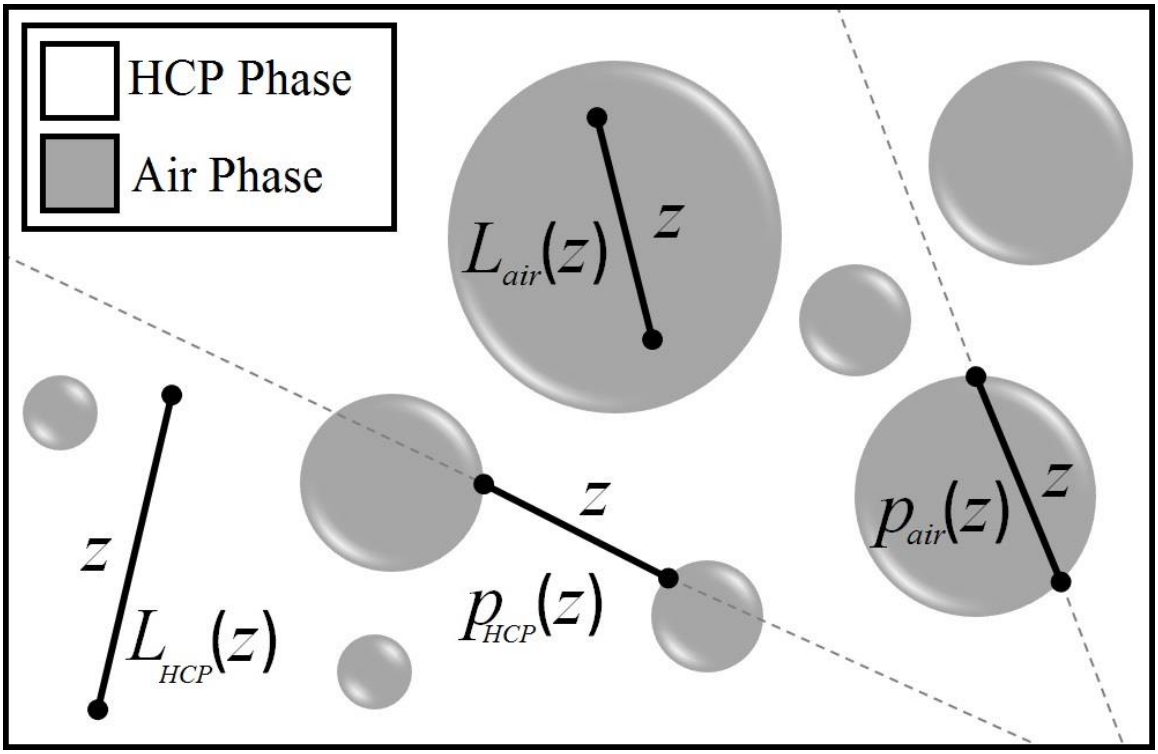


**Figure 3.4**: Events (lines or chords of length $z$) that contribute to functions ($p_i(z)$ or $L_i(z)$) for binary random media.

The choice to express the size distribution in terms of the lineal-path function is justified for two important reasons. First, the lineal-path function may be probed from any two-dimensional plane cut through the material volume if the material is statistically homogeneous and isotropic. It is assumed that any plane cut through a specimen containing entrained air voids is representative of all plane sections cut through the material. This assumption allows the entrained air void size distribution to be determined from plane polished images of air entrained cement pastes, mortars, and concretes, as is common practice [ASTM C457]. The second justification is more specific to the structure of concrete. The polydispersed sphere system exists in the concrete's paste phase, defined as the region of the material occupied by the matrix of entrained air voids, hydrated cement paste, and residual unhydrated cement. In binary images of concretes, large

regions will exist where no entrained air voids appear due to the presence of coarse aggregates, and smaller voidless regions due to the presence of fine aggregates (in this chapter, aggregate volume fractions $\phi_{agg}$ are known a priori from mix designs rather than image analysis). However, $L_{air}(z)$ is not influenced by the "clustering" of air voids, meaning the size distribution may be obtained from images of concretes. Consider the binary images in Figure 3.5a and Figure 3.5b: each image contains the same 2D white circles (the circles are analogous to the air phase), but the circles are randomly-dispersed in Figure 3.5a and clustered in Figure 3.5b. Since the functions are probed inside the "air" phase, the lineal-path functions in Figure 3.5c are indistinguishable.

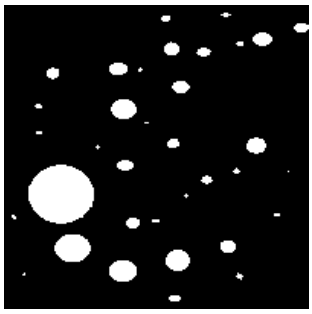

(a) Binary image I

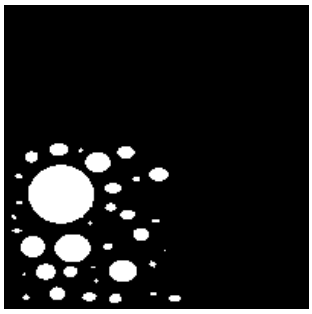

(b) Binary image II

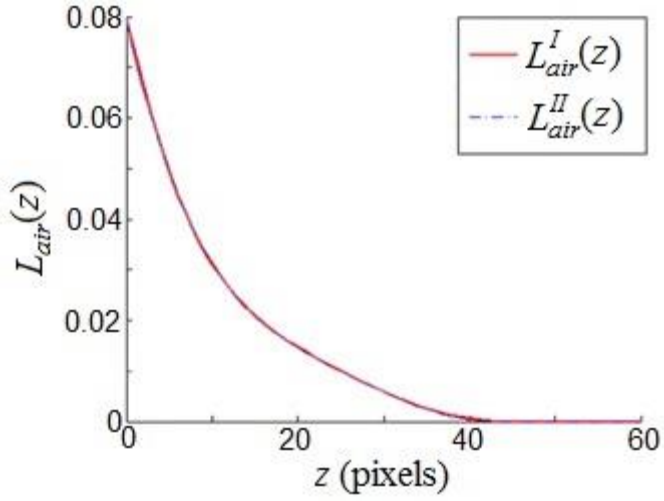


(c) Lineal-path functions for binary images I and II

**Figure 3.5**: Lineal-path function for a polydisperse sphere system will not be influenced by clustering; binary images (a) and (b) will have the same lineal-path function, as shown in (c)

Lu and Torquato derived the relationship between the chord length probability density function and the lineal-path function [21]. The chord length density function may be calculated by the differential relationship

$$p_{air}(z) = \frac{\langle l_{air} \rangle}{\phi_{air}} \frac{d^2 L_{air}(z)}{dz^2} \qquad \text{Eq. 3.1}$$

where $\langle l_{air} \rangle$ is the mean chord length. Note that the average of any function $A(x)$ described by the probability density function $f(x)$ is defined as

$$\langle A(x)\rangle = \int A(x)\, f(x) dx \ . \qquad \text{Eq. 3.2}$$

Therefore $\langle l_{air} \rangle$ is the first moment of $p_{air}(z)$.

Eq. 3.1 is valid for any arbitrary system. For the special case of a system of spheres described by size distribution $f(\mathcal{D})$, where $f(\mathcal{D})\mathrm{d}\mathcal{D}$ is the probability of a sphere with a diameter between $\mathcal{D}$ and $\mathcal{D}$ + $\mathrm{d}\mathcal{D}$, the chord length probability density function is related to the size distribution by the following equation [82]:

$$p_{air}(z) = \frac{2z}{\langle \mathcal{D}^2 \rangle} \int_z^\infty f(\mathcal{D}) d\mathcal{D} \qquad \text{Eq. 3.3}$$

.

Equating the $p_{air}(z)$ terms of Eq. 3.3 and Eq. 3.1

$$f(z) = \frac{\langle \mathcal{D}^2 \rangle \langle l_{air} \rangle}{2\phi_{air}} \left( \frac{1}{z^2} \frac{d^2 L_{air}(z)}{dz^2} - \frac{1}{z} \frac{d^3 L_{air}(z)}{dz^3} \right) \qquad \text{Eq. 3.4}$$

Note that by

$$\langle \mathcal{D}^2 \rangle = 4\langle \mathcal{R}^2 \rangle; \quad \langle l_{air} \rangle = \frac{4\phi_{air}}{s}; \quad s = 4\pi \langle \mathcal{R}^2 \rangle \rho_{air}$$

the first term of Eq. 3.4 may be written as

$$\frac{\langle \mathcal{D}^2 \rangle \langle l_{air} \rangle}{2\phi_{air}} = \frac{2}{\pi \rho_{air}} \ . \qquad \text{Eq. 3.5}$$

The number density $\rho_{air}$ is an unknown. Employing the definition $\int f(\mathcal{D}) d\mathcal{D} = 1$, the number density may be obtained by

$$\rho_{air} = \int_{\Re} \frac{2}{\pi} \left( \frac{1}{z^2} \frac{d^2 L_{air}(z)}{dz^2} - \frac{1}{z} \frac{d^3 L_{air}(z)}{dz^3} \right) dz \ . \qquad \text{Eq. 3.6}$$

The size distribution given by Eq. 3.4 is distributed in terms of spherical diameters, but may be expressed in terms of radii by $\mathcal{D} = 2\mathcal{R}$. With the size distribution, it is straightforward to obtain the moments $\langle \mathcal{R} \rangle$, $\langle \mathcal{R}^2 \rangle$, and $\langle \mathcal{R}^3 \rangle$.

In this work, hardened concrete systems are idealized as a ternary system composed of three phases: aggregates (both fine and coarse), hydrated cement paste (HCP; a matrix of hydration products and residual unhydrated cement), and entrained air voids. The volume fractions of aggregate, HCP, and entrained air voids are represented by $\phi_{agg}$, $\phi_{HCP}$, and $\phi_{air}$, respectively (note that $\phi_{agg} + \phi_{HCP} + \phi_{air} = 1$). However, the polydisperse sphere system really only exists within the matrix occupied by the HCP phase. Therefore, the volume fraction $\hat{\phi}_{air}$ and the number density $\hat{\rho}_{air}$ must be scaled by the equations

$$\hat{\phi}_{air} = \frac{\phi_{air}}{1-\phi_{agg}} \text{ and } \hat{\rho}_{air} = \frac{\rho_{air}}{1-\phi_{agg}} \qquad \text{Eq. 3.7}$$

in order to determine the entrained air void volume fraction and number density in the paste phase (where they are required for freeze/thaw durability) rather than in the bulk material. It is trivially noted that moments $\langle \mathcal{R} \rangle$, $\langle \mathcal{R}^2 \rangle$, and $\langle \mathcal{R}^3 \rangle$ are intrinsic to the entrained air void system itself and require no further normalization.

### 3.2.3 Entrained Air Void Spatial Arrangement

The problem of finding a nearest-surface distribution function (rather than a nearest-neighbor distribution function) for a polydispersed sphere system was first derived by Lu and Torquato [79].This model is ideal for a more robust description of the entrained air void system. The void nearest-surface distribution function $h_V(y)$ is

defined such that $h_V(y)dy$ is the probability that at an arbitrary point in the system the nearest particle surface lies at a distance between *y* and (*y* + *dy*). The void "exclusion" probability $e_V(y)$ is defined as the probability of finding a region $\Omega_V$ surrounding an arbitrary point, where $\Omega_V$ is a spherical cavity of radius *y* devoid of particle material. The functions $h_V(y)$ and $e_V(y)$ are related by

$$e_V(y) = 1 - \int_{-\infty}^{y} h_V(\xi)d\xi \,. \qquad \text{Eq. 3.8}$$

The mean void nearest surface distance, $l_V$, is defined as

$$l_V = \int_0^{\infty} y h_V(y)dy = \int_0^{\infty} e_V(y)dy \,. \qquad \text{Eq. 3.9}$$

This parameter is of great importance in cement-based materials, because it yields an average distance from any point in the paste to the periphery of an entrained air void, a feature which is critical in understanding the durability of the paste fraction to freeze-thaw damage. From Eq. 2.13 it is evident that $l_V$ is the expected value of *y* distributed as $h_V(y)$. The void probabilities are expressed as:

$$e_V(y) = \begin{cases} 1 - \dfrac{4\pi}{3}\hat{\rho}_{air}\left\langle (y+\boldsymbol{\mathcal{R}})^3 \Theta(y+\boldsymbol{\mathcal{R}})\right\rangle, & y < 0 \qquad \text{Eq. 3.10} \\ \left(1-\hat{\phi}_{air}\right)\exp\left[-\pi\hat{\rho}_{air}\left(cy+dy^2+gy^3\right)\right], & y > 0 \qquad \text{Eq. 3.11} \end{cases},$$

$$h_V(y) = \begin{cases} 4\pi\hat{\rho}_{air}\left\langle (y+\boldsymbol{\mathcal{R}})^2 \Theta(y+\boldsymbol{\mathcal{R}})\right\rangle, & y < 0 \qquad \text{Eq. 3.12} \\ \pi\hat{\rho}_{air}\left(c+2dy+3gy^2\right)\left(1-\hat{\phi}_{air}\right)\exp\left[-\pi\hat{\rho}_{air}\left(cy+dy^2+gy^3\right)\right], & y > 0 \qquad \text{Eq. 3.13} \end{cases}.$$

where $\Theta(x)$ is the Heaviside step function, values *c*, *d*, and *g* are defined by

$$c = \frac{4\left\langle \boldsymbol{\mathcal{R}}^2 \right\rangle}{1-\hat{\phi}_{air}}, \qquad \text{Eq. 3.14}$$

$$d = \frac{4\langle \mathcal{R} \rangle}{1-\hat{\phi}_{air}} + \frac{12\xi_2}{(1-\xi_3)^2}\left\langle \mathcal{R}^2 \right\rangle, \qquad \text{Eq. 3.15}$$

$$g = \frac{4}{3\left(1-\hat{\phi}_{air}\right)} + \frac{4\xi_2}{\left(1-\hat{\phi}_{air}\right)^2} + \frac{16}{3}\frac{A\xi_2^2}{\left(1-\hat{\phi}_{air}\right)^3}\left\langle \mathcal{R}^2 \right\rangle, \qquad \text{Eq. 3.16}$$

with

$$\xi_k = \frac{\pi}{3}\hat{\rho}_{air} 2^{k-1}\left\langle \mathcal{R}^k \right\rangle. \qquad \text{Eq. 3.17}$$

The value of *A* depends on an approximation; *A* = 0, 2, 3 correspond to the Percus-Yevick (PY) approximation, the Carnahan-Starling (CS) approximation, and the SP approximation, respectively.

In this study, the quantity $\overline{M}$ is utilized to suggest a statistical "maximum" distance between a point in the paste and the periphery of an entrained air void. $\overline{M}$ is obtained from $H_V(y)$, the cumulative distribution function of $h_V(y)$. Strictly speaking, the distance which *y* cannot exceed without encountering the periphery of an air void is not reached until $H_V(y) = 1$. As noted in [55], the concept of a "maximum" distance is ill-defined because only percentiles of the distribution can be quantified. The percentile threshold was lowered to the 95$^{th}$ percentile value of the void nearest-surface distribution function due to the familiarity of a 95$^{th}$ confidence level in statistics and engineering. Snyder [55] also used this threshold to compare various spacing equations, arguing it was intuitive to one's concept of spacing. Therefore, $\overline{M}$ is expressed as

$$\overline{M} = H_V^{-1}(0.95) \qquad \text{Eq. 3.18}$$

where is $H_V(y)$ the cumulative distribution function of $h_V(y)$.

### 3.3 Model Validation: Proof-of-Concept with Virtual Materials

As an initial proof-of-concept, a virtual polydispersed sphere system was generated. The sphere system was contained within a cube measuring 200 voxels per side. The actual size distribution parameters and nearest surface distances could easily calculated directly from the virtual system. In order to test the efficacy of image analysis on a single slice, a 200 x 200 pixel image was separated from the center of the polydispersed sphere system and analyzed using the method described in the previous sections. Figure 3.6a is the system that was considered, and Figure 3.6b is a representative slice of the polydisperse sphere system.

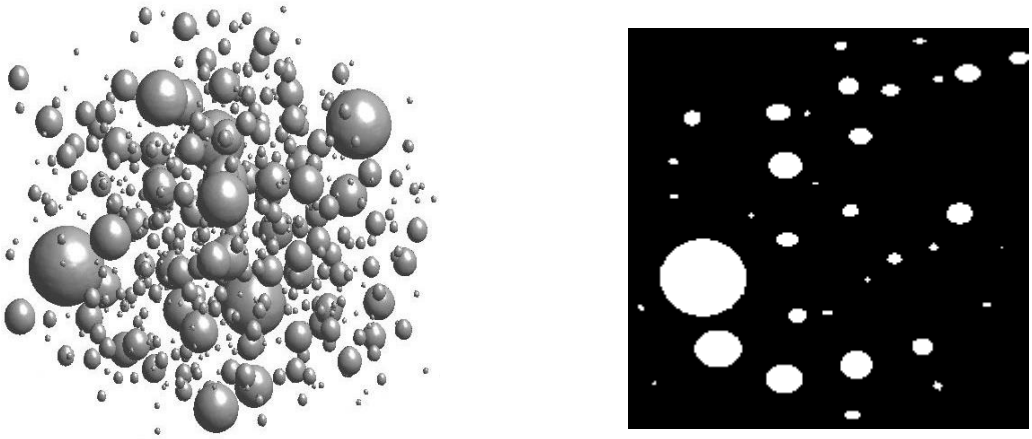

(a) (b)

**Figure 3.6**: Renderings of (a) the entire voxellated system and (b) a single slice under consideration in an initial proof-of-concept

From the resulting data (Table 3.1), it is evident that the method can yield the parameters of the size distribution from a single slice with reasonable accuracy. The first row shows the results from a full 3D analysis of Figure 3.6a. The following rows give the mean, standard deviation, and average error from the full 3D dataset obtained by this

method. It is noted that examination of larger systems would likely produce results with smaller error; however, 3D systems consisting of more than 8,000,000 voxels were not computationally feasible for this study (for a treatment considering a full x-ray microtomographic image, see Appendix A). Instead, real materials were examined, as described in Section 3.4.

**Table 3.1:** Comparison of parameters taken from a simulation and the model

| | $\hat{\rho}_{air}$ | $\hat{\phi}_{air}$ | $\langle \mathcal{R} \rangle$ | $\langle \mathcal{R}^2 \rangle$ | $\langle \mathcal{R}^3 \rangle$ |
|---|---|---|---|---|---|
| **Actual System** | 0.00020 | 7.7% | 2.32 | 9.7 | 70.9 |
| **Average of Slices** | 0.00026 | 8.3% | 1.99 | 8.1 | 62.3 |
| **Std. dev. of slices** | 0.00004 | 1.7% | 0.23 | 1.7 | 17.5 |
| **Average error** | -26% | -8.3% | 14% | 16% | 12% |

A MATLAB script was written to find the nearest sphere voxel to a space voxel, and the results for the system were binned. The resulting histogram (for both the volume inside and outside the sphere system) should be the same as $h_V(y)$. Likewise, it should relate to $e_V(y)$ by Eq. 3.8. Figure 3.7a and Figure 3.7b show the analytical results for $h_V(y)$ and $e_V(y)$, respectively, overlain on the histograms for the 3D sphere system. The gray region in Figure 3.7a and Figure 3.7b represents the spread of all possible plots of $e_V(y)$ and $h_V(y)$, respectively, whereas the black line represents the results calculated from the sphere system shown in Figure 3.6a. The plots suggest the method can yield a reasonable approximation of a polydispersed sphere system's geometry from small slices. Given the small error relative to the small sample size, it is concluded that the method was reasonable to use on a larger system (see Appendix A for a more detailed treatment).

It is worth noting that the "jagged" appearance of the 3D system's histogram is due to a few factors inherent to the virtual microstructure. Most importantly, no "surface" actually exists between voxels, so a single point (corresponding to zero) cannot exist.

Furthermore, voxellated systems create "sawtooth" edges, a common problem encountered in digital image approaches to studying microstructure [83]; this problem will not occur in the smooth, analytical expressions of Eq. 3.10 – Eq. 3.14.

To further assess the validity of the approach, real air entrained concretes were imaged and analyzed. The results are described subsequently.

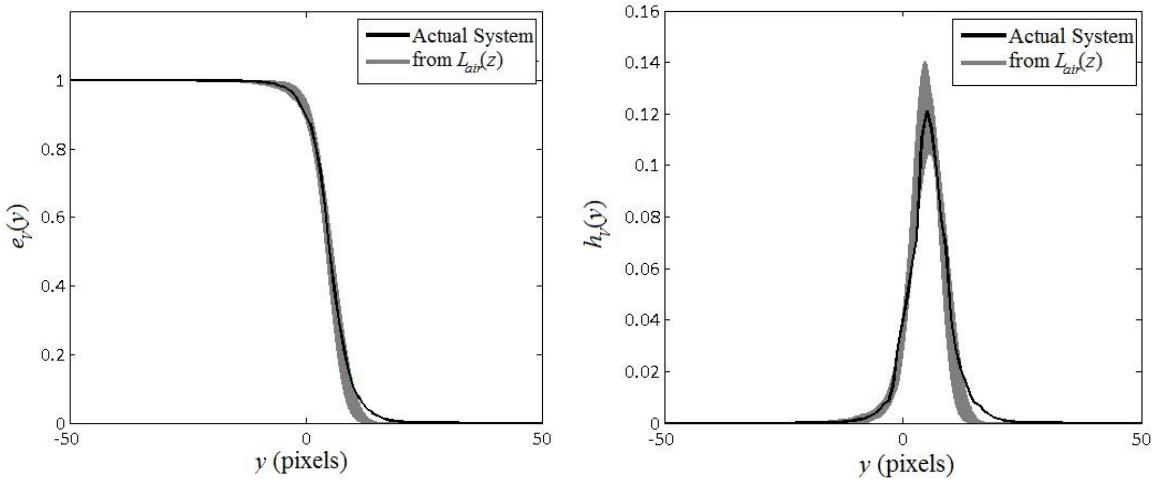


(a) (b)

**Figure 3.7**: Analytical and probed results for (a) void "exclusion" probability and (b) $h_V(y)$

## 3.4 Methods and Materials

The concrete mixtures of were prepared using a Type I/II cement and local crushed limestone coarse aggregate and sand, as described in Ref. [18]. The maximum sized aggregate was ¾ inch. Samples are named in Table 3.2 according to the admixture composition and water-to-cement ratio (*w/c*) used. "W" refers to wood rosin AEA, "S" refers to synthetic, and "V" refers to Vinsol resin.

Concretes were prepared at Oklahoma State University and tested for slump (ASTM C143), fresh air content (ASTM C148) and unit weight (ASTM C231). The freeze-thaw durability (ASTM C666) of the concrete specimens was assessed using a minimum durability factor (DF) of 80% and 300 cycles.

The samples were polished, lacquered and colored in preparation for entrained air void assessment. The concrete surface was colored with a black permanent marker, and a white barium sulfate powder was forced into the air voids to facilitate binarizing the images, similar to the method described in [84]. Rapid Air 457 from Concrete Experts, Inc., was used to determine $\overline{L}$ (see [85]). When converting the images to binary, a threshold of 145 was used. A more detailed description of the experimental testing and ASTM C457 analysis of these concretes can be found in [86, 18].

For analysis using the method presented herein, images of each sample were acquired, also using a flatbed scanner 2400 DPI (flatbed scanners have been shown to yield very comparable results to Rapid Air 457 [85]). The same threshold of 145 was used for consistency.

## 3.5 Results and Discussion

The results comparing the parameters extracted from this analysis technique (namely $\hat{\phi}_{air}$, $\hat{\rho}_{air}$, $\langle \mathcal{R} \rangle$, $l_V$, and $\overline{M}$) are compared alongside AEA dosage, $\overline{L}$, and the durability factor for the 25 mixes investigated in this study in Table 3.2. In general, increasing the AEA dosage increases the air content, decreases $\overline{L}$, and increases the durability factor.

To compare the proposed method for assessing entrained air quality to the standard method, Figure 3.9 plots $\overline{L}$ along the abscissa and $\overline{M}$ along the ordinate. Data points which are not shaded denote samples that have failed ASTM C666. In this data set, $\overline{M}$ ranged from about 10 μm to 40 μm, while $\overline{L}$ ranged from 150 μm to 400 μm. A general correlation exists: as $\overline{L}$ increases, so does $\overline{M}$. However, multiple $\overline{L}$ values may be measured for a given $\overline{M}$, and vice versa, significantly suggesting that $\overline{L}$ and $\overline{M}$ are distinct from one another.

In Figure 3.8, a vertical dashed line denotes the spacing factor suggested ASTM C457 limit of 0.20 mm. As $\overline{L}$ increases, more samples fail the ASTM C666 test. But, concretes perform adequately at $\overline{L}$ *greater* than 0.20 mm, as high as nearly 0.30 mm. Further, there is not a clear delineation in $\overline{L}$ between those concretes that perform adequately in ASTM C666 and those which fail. For example, while S45-2 ($\overline{L}$=0.295) does not fail, W41-1 ($\overline{L}$=0.318) does at 227 cycles. Examining the data in Figure 3.9 for $\overline{M}$ suggests two distinct regions: those which failed (all with $\overline{M}$ > 0.024 mm) and those which did not (specifically, those below $\overline{M}$ ≤ 0.023 mm). Sample V45-1 may warrant additional consideration. This concrete perhaps has a low enough $\overline{M}$ to exhibit good freeze-thaw durability due to its proximity to the cluster of samples passing ASTM C666 (Figure 3.9), yet it failed ASTM C666 at 96 cycles. As noted in Table 3.2, V45-1 cracked in the longitudinal direction during the test, suggesting its failure mechanism may differ from some of the other failed specimens, possibly related to poor consolidation or aggregate quality [87, 88]. Figure 10 shows that sample V45-1 also had

a lower number density than some of its neighboring points in Figure 9, suggesting some interplay between spacing and number density. In Figure 3.9, a horizontal dashed line has been included at 0.023 mm to better define a potential threshold $\overline{M}$ , but certainly further testing must be performed on a wider range of concrete compositions to establish a limit on this parameter (see Chapter 5). Specifically, if V45-1 were regarded as an outlier, the distinction between satisfactory $\overline{M}$ and unsatisfactory $\overline{M}$ would be much clearer.

Figure 10 shows the number density of entrained air voids, $\hat{\rho}_{air}$ , versus mortar air content. These data show a general trend in increasing number density with air content. However, the large spread in number density above about 10% air content underscores the various ways in which a given volume of air can be distributed within the paste. In examining the data with respect to the type of air entraining agent used, where air was entrained by Vinsol resin concretes tend to have lower densities for a given paste air content. This is noted for a range of mortar air contents, from approximately 5% to 15%. Overall this suggests that Vinsol resin admixtures entrain a coarser entrained air void system. This is consistent with results reported by other researchers [89] and could be useful in further describing the quality of the entrained air void system. Additionally, no sample which contained less than 10% mortar air content failed, suggesting a lower air content threshold than that set by Klieger [90, 91] at 18%. With additional development, number density could also be used as a descriptor of entrained air void system quality.

**Table 3.2:** Samples and relevant parameters

| Sample | | Calculated fresh mortar air* (%) | $\overline{L}$ (mm) | Durability Factor** | $\hat{\phi}_{air}$ | $\hat{\rho}_{air}$ (mm$^{-3}$) | $\langle \mathcal{R} \rangle$ (mm) | $l_v$ (mm) | $\overline{M}$ (mm) |
|---|---|---|---|---|---|---|---|---|---|
| W45 | 1 | 6.6% | 0.394 | (85) | 18.0% | 858 | 0.018 | 0.021 | 0.035 |
| | 2 | 9.7% | 0.246 | 94 ± 1 | 32.0% | 1678 | 0.019 | 0.009 | 0.018 |
| | 3 | 12.6% | 0.183 | 82 ± 1 | 38.8% | 1444 | 0.021 | 0.008 | 0.016 |
| | 4 | 13.5% | 0.185 | 87 ± 0 | 32.6% | 1426 | 0.022 | 0.010 | 0.018 |
| S45 | 1 | 7.8% | 0.389 | (119) | 23.3% | 825 | 0.018 | 0.019 | 0.032 |
| | 2 | 11.0% | 0.295 | 100 ± 0 | 30.9% | 1361 | 0.019 | 0.011 | 0.021 |
| | 3 | 13.2% | 0.203 | 88 ± 6 | 33.9% | 1130 | 0.022 | 0.011 | 0.020 |
| V45 | 1† | 7.8% | 0.269 | (300) | 28.6% | 1059 | 0.020 | 0.013 | 0.024 |
| | 2 | 11.9% | 0.208 | 98 ± 1 | 43.5% | 1438 | 0.020 | 0.007 | 0.015 |
| W41 | 1 | 7.7% | 0.318 | (227) | 22.9% | 885 | 0.018 | 0.018 | 0.031 |
| | 2 | 11.1% | 0.244 | 100 ± 0 | 24.6% | 1331 | 0.019 | 0.013 | 0.023 |
| | 3 | 13.9% | 0.152 | 99 ± 1 | 43.6% | 1453 | 0.021 | 0.007 | 0.014 |
| S41 | 1 | 10.5% | 0.246 | 98 ± 1 | 35.9% | 1670 | 0.018 | 0.009 | 0.017 |
| | 2 | 13.3% | 0.244 | 97 ± 1 | 38.2% | 1829 | 0.019 | 0.008 | 0.016 |
| V41 | 1 | 7.4% | 0.353 | (68) | 23.7% | 753 | 0.020 | 0.019 | 0.033 |
| | 2 | 10.8% | 0.262 | 93 ± 1 | 35.6% | 1089 | 0.021 | 0.011 | 0.021 |
| | 3 | 13.6% | 0.211 | 99 ± 1 | 40.4% | 1033 | 0.021 | 0.009 | 0.019 |

* Calculated for mortar from results per ASTM C231 for fresh air content in concrete

**Number in parenthesis indicates freezing and thawing cycles completed when dynamic modulus was measured below 80. Additionally a ± symbols gives the range of values seen by multiple beams of the same mixture

† The samples denoted V45-1 cracked down the middle in the short direction and measurement was not possible after 96 cycles

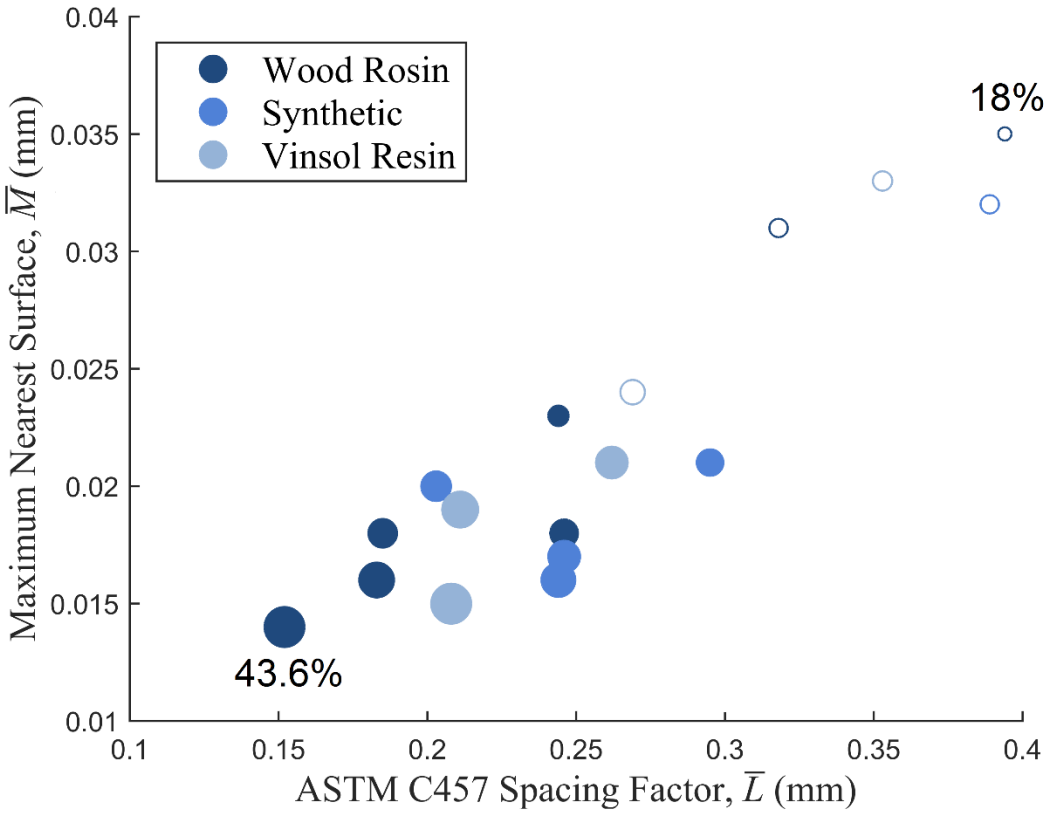


**Figure 3.8**: $\overline{M}$ versus $\overline{L}$. Hollow (unshaded) datapoints indicate samples which failed under ASTM C666. Marker size denotes paste air content. Minimum (18%) and maximum (43.6%) air contents are labeled on the figure for comparison.

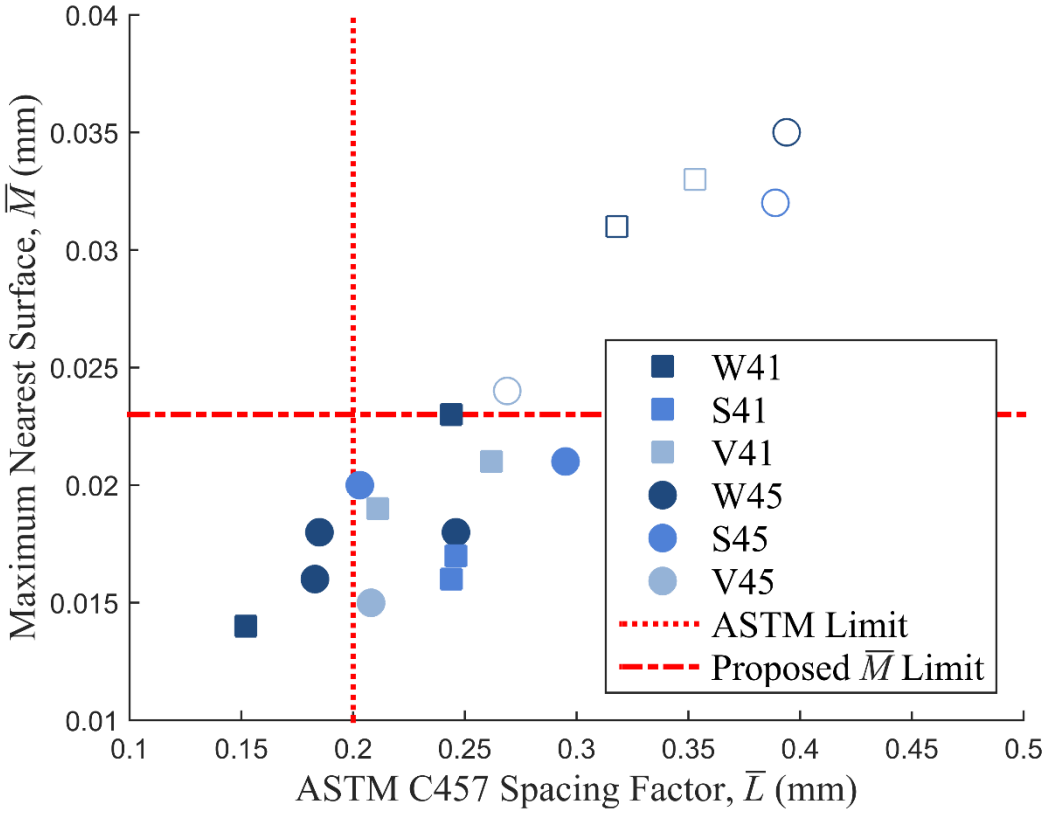


**Figure 3.9:** $\overline{M}$ versus $\overline{L}$ with limits, where hollow (unshaded) datapoints indicated samples which have failed under ASTM C666 testing

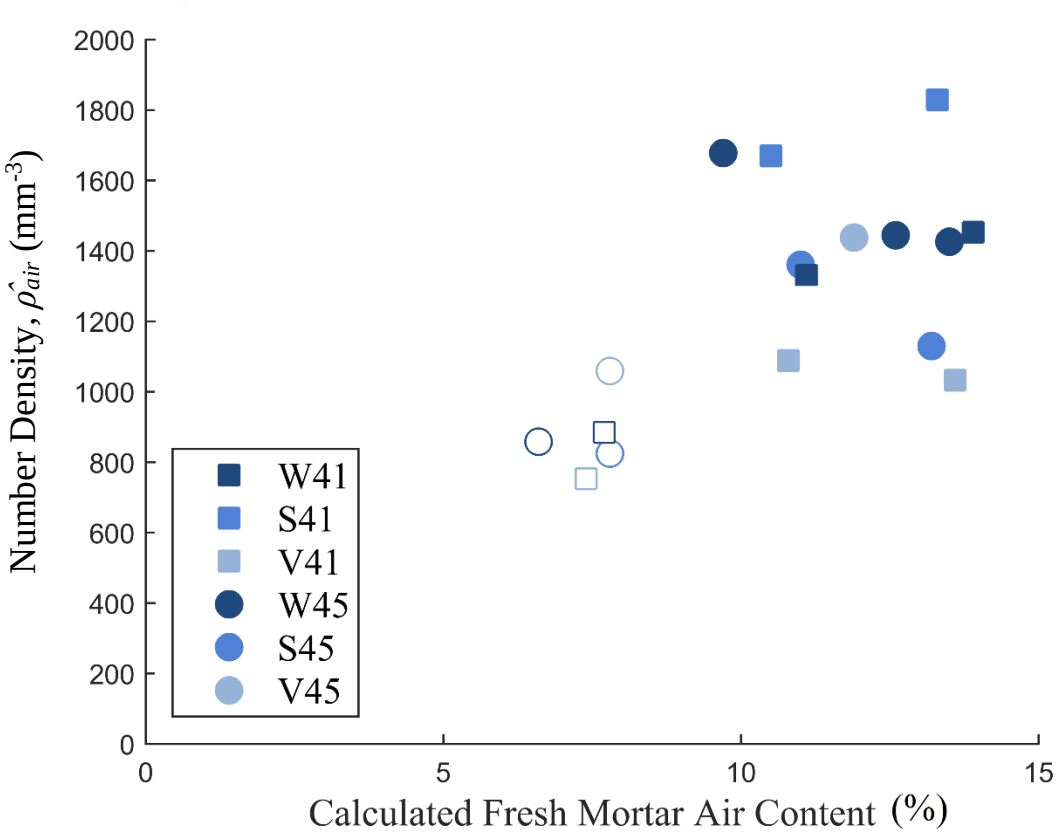


**Figure 3.10:** Number density versus fresh mortar air content

A novel method has been presented to analyze the entrained air void distribution in hardened concrete via image analysis. This method reconstructs the size distribution directly from the samples rather than by assuming a distribution and fitting its parameters, as has been done previously [60, 77]. This probabilistic, image-analysis based method is therefore an alternate method for quantifying air void structures in modern concretes. The method may be useful in optimizing the air void system, specifically as it relates to the interaction between number density, air content, and spacing factor. Knowledge of an "optimum" air void system could aid future chemists in designing a next generation of air entraining admixtures to create improved entrained air void systems. This method has the potential to improve economy by raising the threshold

by which a petrographer must use to assess which samples must be subjected to ASTM C666, as the number of samples which will need to undergo the time-consuming and costly freeze/thaw test may be greatly reduced. More broadly, this approach could be used in characterizing the structure and modeling the properties and behavior of heterogeneous materials.

# CHAPTER 4

# ANALYSIS OF PORTLAND CEMENT MORTAR UNDER IMPACT

Toward the development of a constitutive model for describing high strain-rate behavior of cementitious materials, this chapter couples multiscale quantitative characterization of mortars with micromechanics modeling, validated against dynamic experiments (see Task 2.A). Blast or impact loads create a far-field compressive loading condition that drives local tensile crack growth from flaws. Two flaw types – round (e.g., entrained air voids) and slit (e.g., tandem effect of the interfacial transition zone and the aggregates) flaws – are considered in this flaw-driven, elastic model for predicting strength at high strain-rates. The model sheds light on the linkage between meso-scale fluctuations of the flaw populations (including size, shape, and spatial arrangement) and the material's overall dynamic response. Dynamic strength is interpreted in a statistical framework rather than a deterministic one. Micromechanics results agree with dynamic compressive tests on mortars with and without air entrainment. The model may be useful for engineering potentially at-risk concrete elements.

## 4.1 Introduction

While experimental testing remains the most effective tool for studying the dynamic behavior of concrete [92], given the potential for variability in these materials and in their construction and loading conditions, mitigating the effects of impact loading on critical concrete structural systems and reducing human vulnerability in the wake of such events remains an important challenge for engineers. Strain-rate sensitivity was first described by Abrams in 1917 [29] in his study describing an appropriate loading rate for

static compressive strength. By 1991, Bischoff and Perry [93] concluded that the state-of-the-art of testing and assessing concrete's dynamic strength was roughly comparable to the state-of-the-art of static testing in the 1960s; that is, much research was needed to understand dynamic behavior compared to the relatively well-researched static behavior.

The dynamic behavior of cement-based composites has been studied using viscoplastic models [45, 39], discrete lattice models [92, 44], and dynamic finite element [40, 41, 42, 43] software. Recent experimental and theoretical work [6, 94, 95] in brittle material microcracking has increased the understanding of strain-rate effects on failure in brittle materials. For example, microcrack models have provided some insights for strain-rate effects and impact loading in concrete [48, 96]. While these models show good qualitative agreement with experiments, they lack a direct relationship to the sizes, shapes, and spatial arrangements of the multi-scale flaws found in real concrete. Furthermore, rectilinear slits alone cannot describe the immense variety of material defects in this complex class of materials. Graham-Brady [47] showed that a moving window approach allows the microcrack model of Paliwal and Ramesh [6] to account for clustering, while Katcoff and Graham-Brady [97] showed that the model can be modified to account for round or pore-like flaws in addition to rectilinear slits. For mortar, entrained air voids are ideally suited to be modeled as round flaws in a two-dimensional model due to their spherical shape in three dimensions [98]. The combined effect of the interfacial transition zone (ITZ) around aggregates and the presence of the fine aggregates themselves are interpreted as slit flaws, an approach which is explained in more detail in Section 4.3.1.

This chapter combines material characterization, micromechanics modeling, and dynamic compression testing to explore the effect of the confluence of different flaw types that exist in cement-based material microstructures, particularly as it relates to the localization of failure due to clustering and the variability in dynamic strength test results. Using a variety of characterization techniques, bulk mechanical properties and the sizes, shapes, and spatial arrangements of two flaw types – slit and round flaws – are obtained for real and simulated mortar microstructures. The micromechanics modeling approach is based upon the work of Paliwal and Ramesh [6] and Katcoff and Graham-Brady [97], which consider flaw density and flaw size distribution in two-dimensional space. Flaw clustering is considered through a "moving window" approach [47]. The model was validated experimentally using a compression Kolsky bar (also referred to as a split-Hopkinson pressure bar[4]) to test mortars of varying entrained air content.

## 4.2 Overview of Approach to Characterization, Modeling, and Validation

The modeling framework – detailed in Figure 4.1 – relies upon flaw characterization (details in Section 4.4) and micromechanics modeling (details in Section 4.5). Experimental validation will be discussed later (details in Section 4.6). The modeling procedure begins by characterizing the *global* size distribution and spatial arrangement of the slit flaws (fine aggregate and ITZ) and round flaws (entrained air voids), as shown in Figure 4.1a. From this information, a number $N_{tot}$ of simulated microstructures per sample type may be generated, an example of which is shown in Figure 4.1b. The dimensions of the simulated microstructures corresponds to the through-thickness of the Kolsky bar specimens used for validation (see Section 4.6). For this

[4] Kolsky developed the fundamental concept of determining the dynamic properties of materials using two longitudinal Hopkinson bars in series as transducers, with specimen size much smaller than pulse length

work, $N_{tot}$ = 500 simulations per sample type. For each simulation $N_i$, the microstructure is broken down into an $M \times M$ grid of windows. In this study, $M$ = 5, so the total number of windows for each simulation was $W_{tot}$ = 25 (the choice of window size is discussed in Section 5). As the example in Figure 4.1c shows, each window $W_i$ may have a different *local* size distribution and number density of flaws than the global flaw statistics shown in Figure 4.1a. The local flaw statistics are used as inputs for the micromechanics model of Paliwal & Ramesh [6] and Katcoff & Graham-Brady [97] (see Figure 4.7 for a flowchart). The model applies a uniaxial dynamic compressive load and returns a stress-strain constitutive relationship for each window as shown in Figure 4.1d. The stress contour map in Figure 4.1e shows how the peak stress varies from window to window. In this contribution, a "weakest-link" approach is employed to determine the microstructure's dynamic strength $\sigma_{DYN}$ by selecting the lowest failure strength of the $W_{tot}$ windows. After this has been done for $N_{tot}$ simulations, the dynamic strengths are histogrammed as in the example in Figure 4.1f.

This framework provides two major advantages over conventional deterministic, homogenous models for the dynamic response of cementitious materials. First, the micromechanics model may be used to account for clustering because it has been discretized into windows. Second, the results of the Kolsky bar tests used for model validation may be assessed in a probabilistic rather than deterministic way, which is advantageous since the relatively small samples demanded by the apparatus may be heavily influenced by variability in the flaw population and associated flaw clusters, from one sample's microstructure to the next. Further details on model validation are provided in Section 4.6.

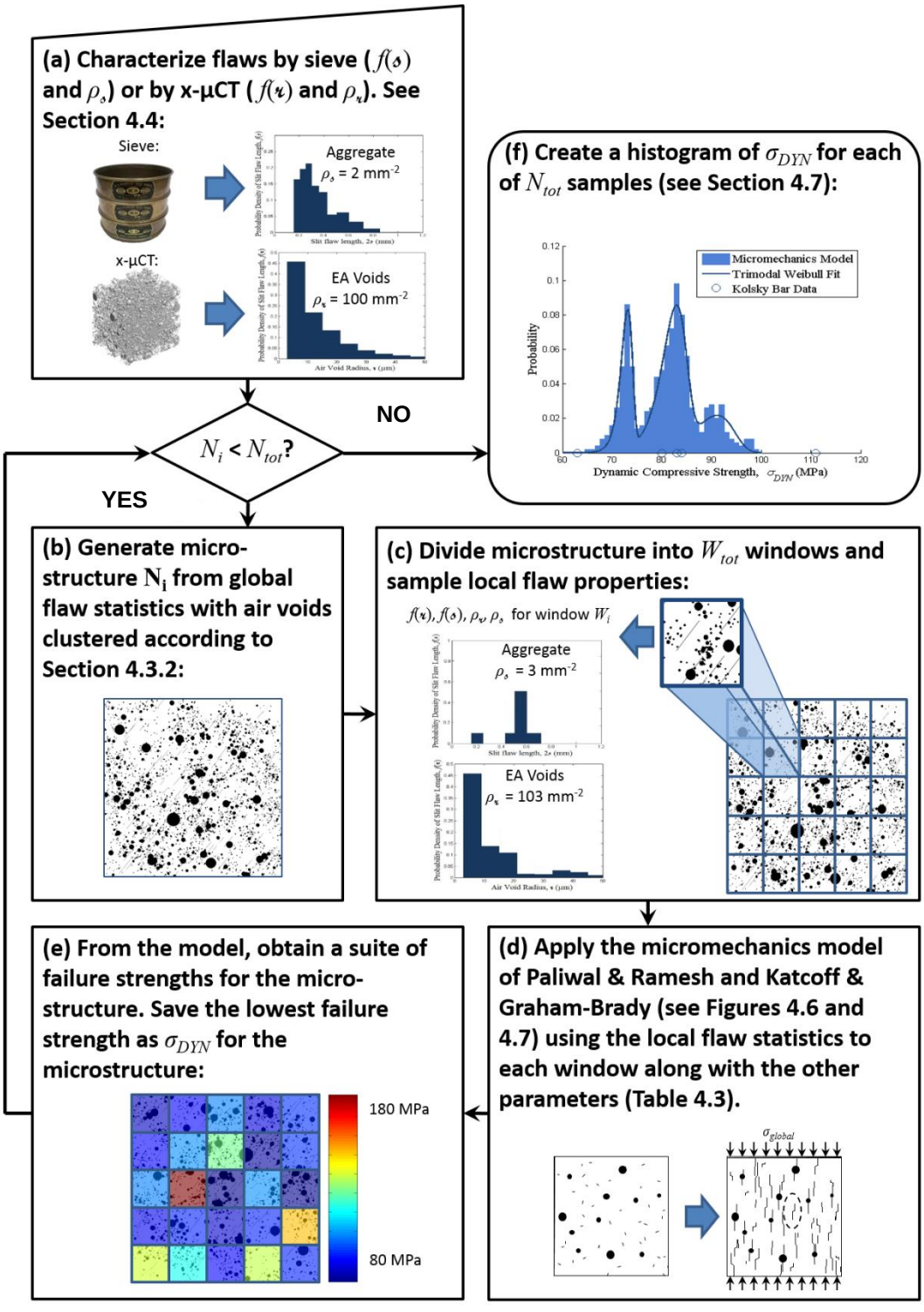


**Figure 4.1:** Framework for analysis

## 4.3 Microstructural Considerations

Heterogeneous composites like mortar and concrete contain a number of multi-scale flaws related to the inherent nature, processing, and service history of the material. Examples include capillary porosity, microcracking due to elasticity mismatch between phases, entrained and entrapped air voids, and microcracking and cracking due to loading or environmental effects. Two types of flaws will be investigated in this contribution: the ITZ and entrained air voids. The ITZ is a region surrounding aggregates which is locally more porous then the bulk cement paste due lower-density packing of cement grains (and supplementary cementitious material and microscale filler particles, when present) and – to a lesser extent – one-sided growth of cement hydration products towards the surface of the aggregate [98]. The density of microcracks is also locally higher in this region due to shrinkage and creep in the paste, as well as elasticity mismatch between the hydrated cement paste and aggregate. In this contribution, the effect of the ITZ is combined with its interaction with the fine aggregate particle that it surrounds. Entrained air voids are spherical bubbles that are deliberately introduced to the material during mixing using a chemical admixture. Entrained air voids play a dual role in protecting the material from damage during cyclic freezing and thawing: they provide a cavity in which ice may nucleate during freezing, and in so doing act as cyropumps to help drain the surrounding pores of water [99]. ACI 201 recommends that all concrete with moderate and severe exposure to cyclic freeze/thaw and moisture contain at least 3% entrained air in the total volume of concrete [100], and the practice of air entrainment is common worldwide. In the United States, for example, only coastal regions around the Gulf of Mexico, the Pacific Ocean, and land regions near the Mexican border are classified as having

"negligible" risk of freeze/thaw damage instead of moderate or severe, though local practice and experience may necessitate air entrainment in these regions as well [101].

### 4.3.1 Flaw Sizes and Shapes

Detailed geometric information about features in an opaque material like mortar may be difficult to observe by conventional methods, and even by more advanced x-ray penetrating techniques due to the relatively low density contrast of its constituent phases. Fortunately, flaws related to aggregate inclusions may be observed *a priori* by sieve analysis. Since this study will focus on mortar, the ITZ is understood to be the region between the fine aggregate (sand) particles and the hydrated cement paste matrix. This study will account for the effect of ITZ using rectilinear slit flaws, the length of which will correspond to the nominal dimensions of the aggregate. This reflects an opinion offered in [102, 100] that the higher dynamic failure strength of concrete may be explained in part by cracks propagating directly *through* aggregate inclusions rather than around them, which has also been suggested by numerical investigation in [92]. Because of this, the slit flaw is accounting for the tandem effect of the locally-weaker ITZ and the aggregate cracking since no discrete inclusions are present (more evidence of this is offered in Section 4.7).

The system of entrained air voids must be measured in hardened mortar because the bubbles stabilize during mixing. Measurements may be made either by analyzing 2D planed polished sections (as in Chapter 3, published as [103]) or by a 3D imaging using x-ray microtomography (x-μCT) [104]. The voids are known to be spherical, so they may be modeled using round inclusions as explained in Section 4.4.

### 4.3.2 Flaw Spatial Arrangement: Clustering

Since fine aggregates are distributed uniformly during the mixing process and exhibit no noticeable clustering behavior at the meso-scale level of observation (on the order of $10^{-3}$ m), their spatial arrangement will be considered to be random in this contribution. However, since entrained air voids are introduced to the material using an admixture which reacts with water during the mixing process, the resulting entrained air void system is only found within the paste phase of the mortar (the matrix consisting of products of cement hydration and residual unhydrated cement). Therefore, a clustering model is needed.

Perhaps the earliest work in clustering phenomena arose in the field of statistical ecology as described by Neyman [105], whence the two-parameter Neyman Type A distribution originated. Graham-Brady [47] demonstrated the applicability of this clustering model to understand the linkage between random meso-scale fluctuations in flaw density and dynamic strength of brittle ceramics at high strain-rates. The Neyman Type A distribution may be interpreted as following a "satellite model." A series of flaw centers – called "parent" flaws – which follow a Poisson process are assumed to exist in space. Around each parent flaw there exist a certain number of satellite – or "children" – flaws, the number of which also follows a Poisson process. The locations of both parent flaws and children flaws (with respect to parent flaws) are independent and identically distributed random variables. The simplest model assumes the children flaws exist in a circular area of radius $R_c$ around each parent flaw. This model for spatial arrangement is advantageous because it allows sample microstructures to be generated rapidly using a simple algorithm (see [47]) using:

- Number density of round flaws per unit area, $\rho_r$
- The percentage of parent flaws, $\ell$
- The cluster radius, $R_c$

Section 4.4.2 presents an overview on the method of calculating these parameters for air voids in mortar.

## 4.4 Materials Characterization

The following section describes the laboratory and simulation techniques used to obtain engineering properties and morphological measurements for use in the micromechanics model.

### 4.4.1 Mix Design and Mechanical Properties

Bischoff and Perry [28] report that the specimen size for Kolsky bar tests should be four to five times the maximum size aggregate (MSA) for the specimen to be representative of a larger concrete volume. This would prescribe specimen sizes on the order of 40 mm – 200 mm for the typical range of MSAs in concrete [98], which would be impractical given the constraints on specimen diameter (less than 12.7 mm) in the testing apparatus employed in this chapter. The length scale of the flaws examined here is on the scale of fine aggregate rather than coarse aggregate. Consequently, mortar specimens were quantified, modeled, and tested rather than concretes, since the large size of coarse aggregates relative to fine aggregates would otherwise cause a high degree of heterogeneity in the Kolsky bar results (test described in detail in Section 4.6). The mortar was designed to be representative of the mortar phase of a standard concrete. The water-to-cement ($w/c$) ratio was 0.40 and cement-to-sand ratio for all mixtures was about 1:1.3. A Type I/II ordinary portland cement was used for the mortar samples. The fine

aggregate used in this study was a locally-available concrete sand sourced from Shorter, Alabama, with a specific gravity of 2.65. To control the size of inclusions, fines larger than those retained on a No. 16 sieve were rejected. The gradation met the gradation limits of ASTM C33 [106]. The mix designs as batched for testing are shown in Table 4.1, which reflect adjustment for a fine aggregate adsorption capacity of 0.5%. The air entraining admixture (AEA) dosage reflects the manufacturer's recommendations.

**Table 4.1**: As-batched mix designs for the Kolsky bar specimens

| Constituent | Content |
|---|---|
| Water | 442 g |
| Cement | 1088 g |
| Aggregate | 1426 g |
| AEA ($\phi_{air}$ = 12%) | 1.60 mL |
| AEA ($\phi_{air}$ = 16%) | 2.58 mL |

The test matrix includes mortars with entrained air contents of 0%, 12%, and 16% to assess the effect of the entrained air void system ("0%" corresponds to samples with no intentionally-entrained air; it is not to be interpreted as a measurement of total residual entrapped air). Air contents were determined by image analysis on polished companion samples [103]. The values match reasonably well with density, measured at 28 days (see Table 4.3), which was used to calculate the Rayleigh wave speed, $C_R$.

Mortar cube specimens were batched in the laboratory as reported in Table 4.1 in compliance with ASTM C305 for mixing mortars [107]. Two-inch mortar cubes were tested for compressive strength after curing in lime-water for 28 days at a temperature of 23° ± 1.7° C (the specimens for the Kolsky bar tests were cured under identical conditions). Mortar strength may be found in Table 4.2. All mortar specimens failed in a Type 1 pattern (according to ASTM C39), defined as "a reasonably well-formed cone on

both ends" [108] (see Figure 4.2). The trends in Table 4.2 are reasonable. Each 1% entrained air in the mortars resulted in about a 3%-4% reduction in strength. As a rule-of-thumb, each 1% additional of entrained air in concrete reduces the strength by about 5% due to the inverse relationship between porosity and strength in materials. For mortars, it is likely that this magnitude is similar but not the same due to the expected difference in porosity between mortar and concrete.


**Figure 4.2:** Failure patterns for (a) control (b) 12% air and (c) 16% air

NIST's Virtual Cement and Concrete Testing Laboratory (VCCTL) was used to model Young's modulus and Poisson's ratio for the mortar based upon material properties, mix proportions, age at testing, and aggregate gradation [109]. The resulting prediction of elastic modulus is shown in Table 4.2. Poisson's ratio was a constant 0.26 for all samples. The values for elastic moduli decrease with increasing air content, as explained by Powers [110] to be due to the increase invoid space.

**Table 4.2:** Strength and stiffness of the mortar

| $\phi_{air}$ | **Compressive Strength, $\sigma_C$ (MPa)** | **Young's Modulus, $E$ (GPa)** |
|---|---|---|
| 0% | 70.88 | 30.03 |
| 12% | 39.45 | 27.90 |
| 16% | 36.92 | 26.68 |

### 4.4.2 Size Distribution and Spatial Arrangement

In typical engineering applications, aggregates are sized using sieve analysis, where the gradation curve is determined from the mass retained on each sieve used in the analysis. Sieves with increasingly smaller nominal openings will actually contain increasingly greater numbers of aggregate particles per unit mass of aggregate. Since the aggregates and ITZ are modeled as rectilinear slit flaws, the aggregate number density retained on each sieve may be obtained from cumulative gradation data obtained by mass through sieve analysis. For this calculation, sand particles are idealized as spheres, as has been done frequently in the literature [111, 112, 113, 114]. For sieve *i*, the number of slit flaw particles $\rho_{s,i}$ appearing on sieve *i* may be calculated from

$$\rho_{s,i} = \frac{6m_i}{\rho_{FA}\pi d_i^3} \qquad \text{Eq. 4.1}$$

where $m_i$ is the mass of fine aggregate retained on sieve *i*, $d_i$ is the mean opening of sieve *i* (*d* corresponds to 2*s* in Figure 4.3a), and $\rho_{FA}$ is the mass density of the fine aggregate. An orientation of $\varphi_0 = 62.4°$ is selected for the slit flaws because it is the most optimal orientation for wing crack growth under uniaxial compressive loading for a material with the coefficient of friction $\mu = 0.7$ [115]. The size distribution of the slit flaws is expressed as a probability density function and denoted as $f(s)$ in Figure 4.3a.

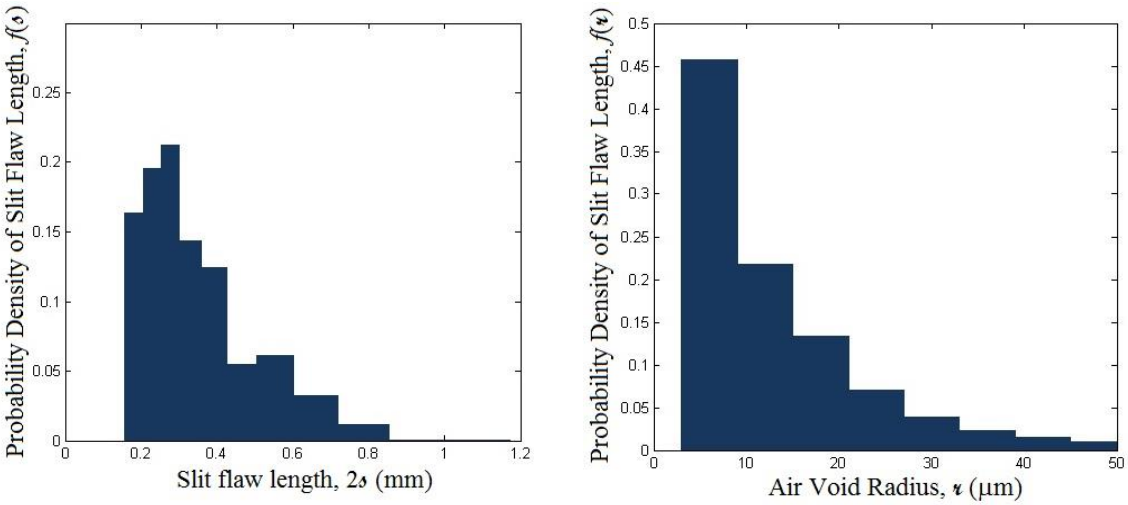


(a) (b)

**Figure 4.3:** Size distribution of (a) aggregates and (b) entrained air voids expressed as probability density functions

To investigate the characteristics of the entrained air void system in mortar, a sample mortar with *w*/*c* = 0.4 dosed with 2.00 fl.oz./cwt AEA to obtain a target air content of about 10% was cast for analysis using x-μCT. (An overview of x-μCT and its application to cement-based materials can be found in [104].) The mix design was the same as that used for the Kolsky bar tests. The sample was scanned at 100 kV and 60 μA using the "Ultratom" by RX Solutions at the Laboratoire Navier at École Nationale des Ponts et Chaussées (ENPC). The instrument used 1440 projections, with an average of 8 images per projection. Images were acquired every 0.5 seconds. A portion of the 3D reconstruction is shown in Figure 4.4a. Figure 4.4b shows a detail of a slice from the scan which measures 1.15 mm per side, where grayscale values range from 0 to 65535. To segment the voids from the surrounding paste and aggregate matrix, the image was binarized by automatic thresholding at grayscale values of 24158. Figure 4.4c demonstrates that simple thresholding accurately resolves the entrained air voids. The

section for analysis was a cube measuring 840 voxels per side, corresponding to a cube of material measuring 5 mm per side (this is equivalent to the through-thickness of the specimens for Kolsky bar testing and the edge dimensions of the simulated microstructures for the micromechanics modeling). The number density of these radial flaws $\rho_r$ was calculated on each image and averaged over the microstructure. To avoid edge effects, an unbiased counting frame was used to measure the number density [116].

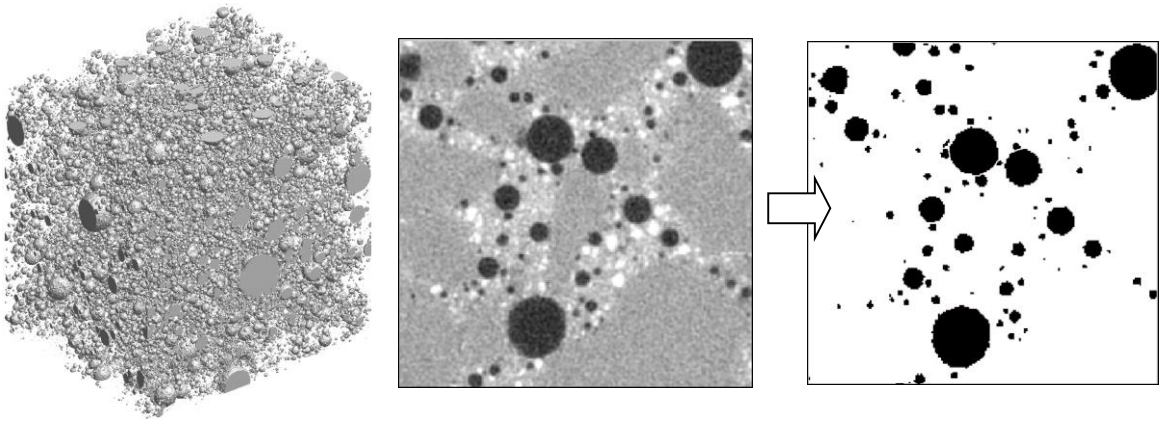

shown: 2.5 mm per edge

shown: 1.7 mm per side

shown: 1.7 mm per side

(a) (b) (c)

**Figure 4.4:** (a) A reconstruction of a cube of material measuring 2.5 mm per side from x-μCT. Image quality is demonstrated by (b), and binarization by (c). In order to better show detail, the images reproduced here are smaller than the actual field of view considered for analysis.

Since the micromechanics model is two-dimensional (see Section 4.5), a corresponding two-dimensional size distribution of entrained air voids was obtained by image analysis on the set of slices. In binary images of entrained air voids, only whole circles were considered in the analysis (i.e. entrained air voids which intersected the

boundary of the image were rejected). The radius of each air void was calculated from its area. The size distribution of these radii is shown as a probability density function expressed by $f(r)$ in Figure 4.3b.

The cluster radius discussed in Section 4.3.2 was obtained using the radial distribution function, $g_2(z)$. A radial distribution function is related to the probability of finding a particle centroid located a distance between $z$ and $z + dz$ from the centroid of a reference particle [81]. In Figure 4.5a, the reference particle is the center particle (shown in the darkest shade), particle centroids are in the range from $z$ and $z + dz$ are in a medium shade, and all other particles are the lightest shade. The system exhibits short range order for small values of $z$. As $z$ increases, amplitudes of oscillations dampen and eventually the system converges to unity. The point where $g_2(z)$ converges is taken to be related to the cluster radius. Function $g_2(z)$ was calculated on each of the 840 images in the stack considered for analysis and averaged to give the average radial distribution function $\hat{g}_2(z)$ as shown in Figure 4.5b. This gives a cluster radius $R_c$ of 240 μm.

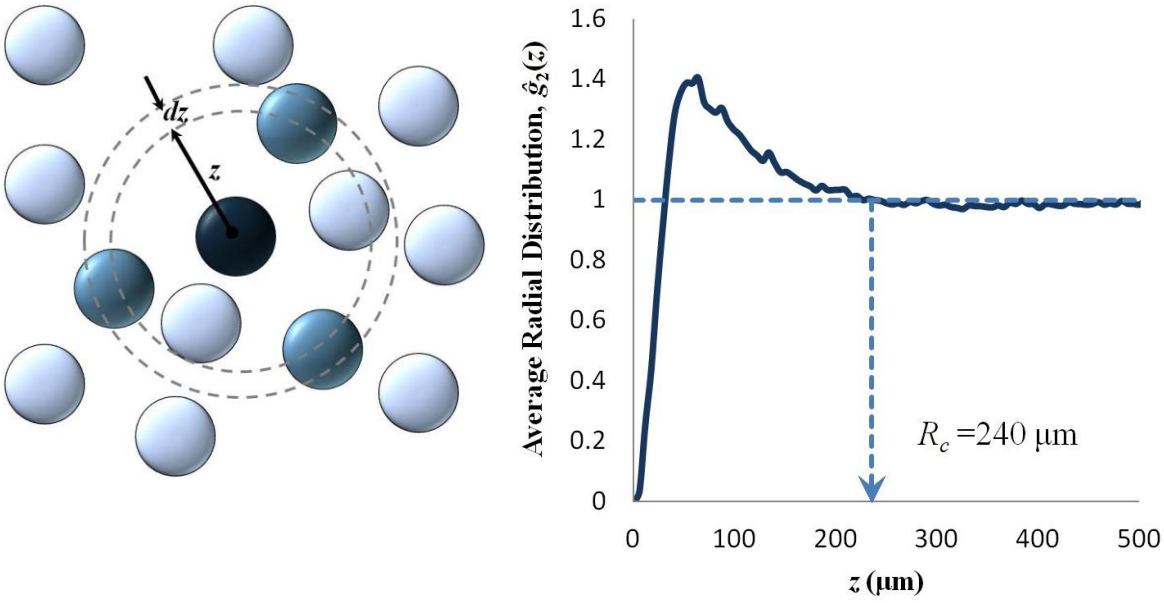


(a) (b)

**Figure 4.5:** (a) Demonstration of the radial distribution function. (b) Averaged radial distribution function for the centroids of entrained air voids in the x-ray microtomographic image

The microstructure shown in Figure 4.6a is a simulation of the entrained air void system using parameters of the Neyman Type A distribution, while Figure 4.6b is a binarized slice from an x-ray microtomographic image. The microstructures were compared using two-point correlation functions, and the results suggested that they were both statistically and visually comparable. This demonstrates that the Neyman Type A distribution may be used to generate statistically-similar virtual microstructures to be analyzed by the micromechanics model.

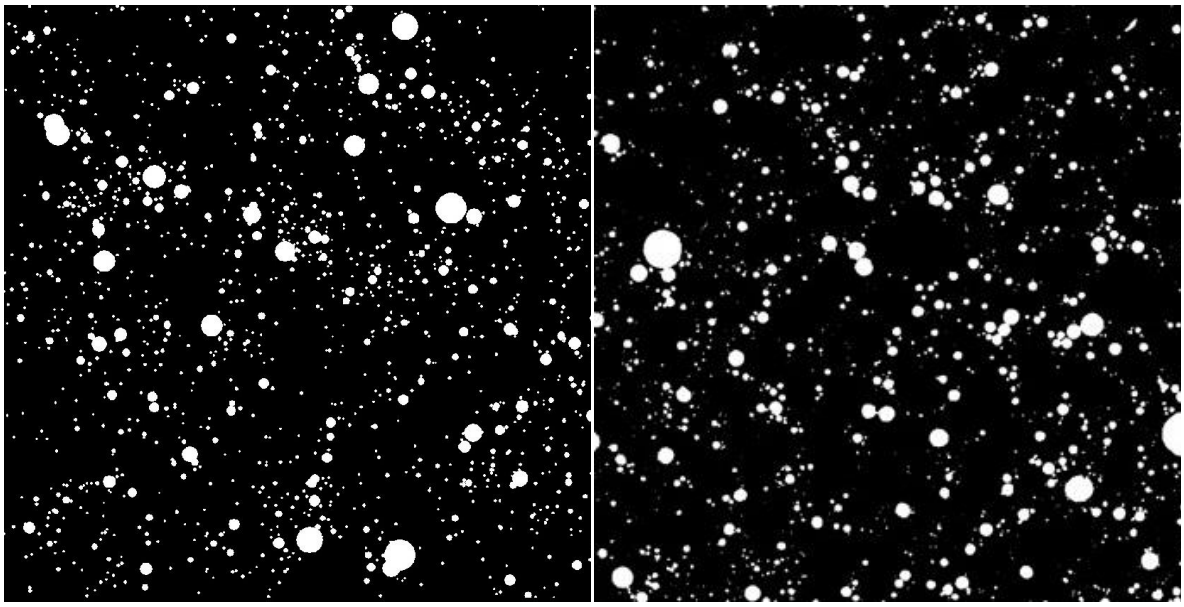

(a) (b)

**Figure 4.6: (**a) Simulation using parameters of the Neyman Type A distribution compared to (b) an actual image of mortar

## 4.5 Micromechanics: Self-consistent Model for Characterizing Dynamic Uniaxial Compressive Strength

The characterization, described in Section 4, gives quantitative information about the microstructure that may be mapped to the strain-rate dependent constitutive behavior. This work focuses on uniaxial compression at strain-rates between 150/s – 200/s. The modeling follows the analytical models of Paliwal and Ramesh [6] for slit flaws and Katcoff and Graham-Brady [97] for round flaws. Figure 4.7 presents an overview of the model. Two-dimensional slit flaws and circular flaws are initially dispersed in the material as described by the quantitative characterization as shown in Figure 4.7a (see [117] for a pseudo-three-dimensional application of this model). Under a uniaxial compressive load, wing cracks develop [50], as in Figure 4.7b. The model assumes that

each flaw is isolated from other flaws by an elliptical zone of undamaged material that is surrounded by a homogenous medium with the elastic properties of the damaged material. As shown by Figure 4.7c, the stress in the zone is calculated using the elasticity solution for an elliptical inclusion under far-field stresses. Local stresses in the elliptical inclusion ($\sigma_{11}^{local}$ and $\sigma_{22}^{local}$ ) are determined, and the stress concentrations at the tips of cracks of length $l_s$ (slit flaws) or $l_e$ (circular flaws) are determined. If the stress intensity factors do not exceed the critical stress intensity factor ($K_{Ic}$) for the mortar, the crack is assumed to grow according to the crack growth law. A thorough treatment of this model, including derivation and assumptions, may be found in [117].

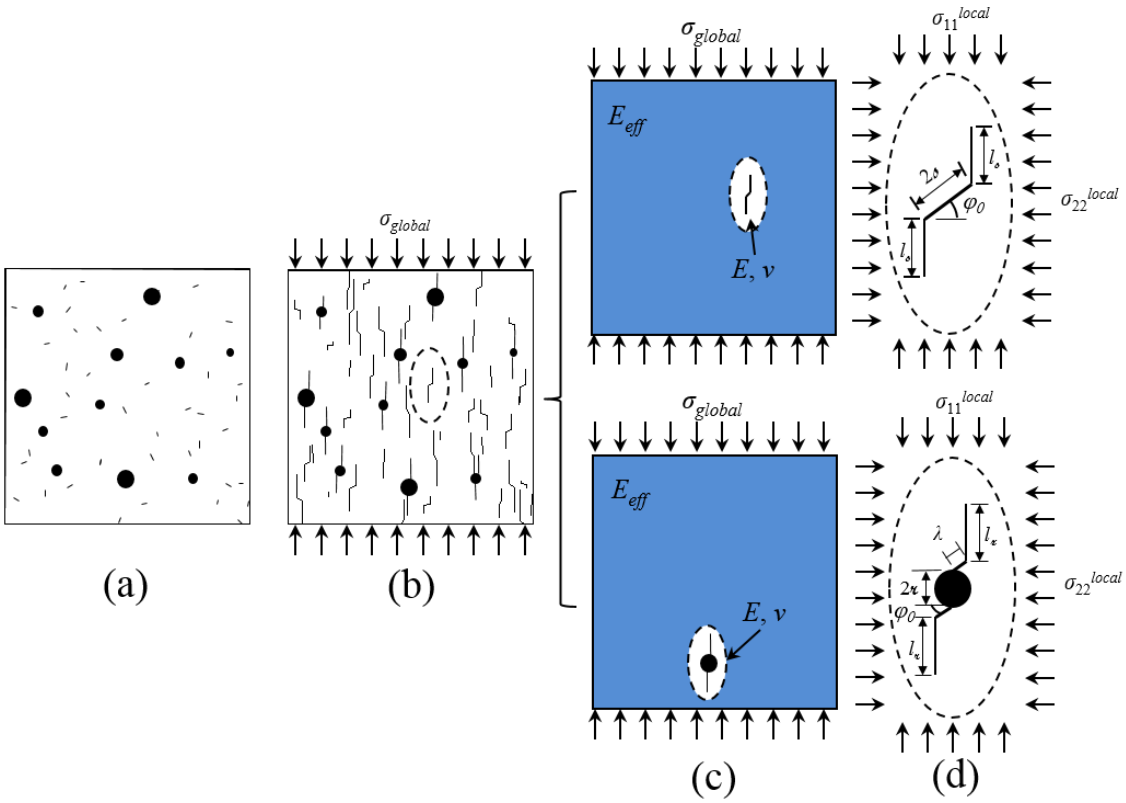


**Figure 4.7:** Schematic of self-consistent model: (a) undamaged microstructure consisting of slit-like and circular flaws; (b) damage develops in axially compressed material, cracks grow in direction of loading; (c) isolated undamaged region around a single flaw; (d)

local stresses around individual flaw used to calculate stress intensity factors at crack tip (after [47, 97])

The micromechanics model is outlined as a flow chart in Figure 4.8 [6, 47, 97]. The model requires as parameters: an undamaged Young's modulus $E$ and Poisson's ratio $v$, Rayleigh wave speed $C_R$, coefficient of friction of the flaw interface $\mu$, critical shear stress at the flaw interface $\tau$, and critical stress intensity $K_{Ic}$. Two additional crack growth parameters $\alpha$ and $\gamma$ may be used in future studies to calibrate the model to experiments, as discussed in [117]. In this study, these parameters have been set to unity to avoid overfitting the model and to focus on the effects of flaw geometry and spatial arrangement. Furthermore, the authors presently have no evidence in support of any particular value for either of these parameters. However, they may be of interest to future researchers and have been included for formalism. Input material properties and microstructural properties are listed in Table 4.3.

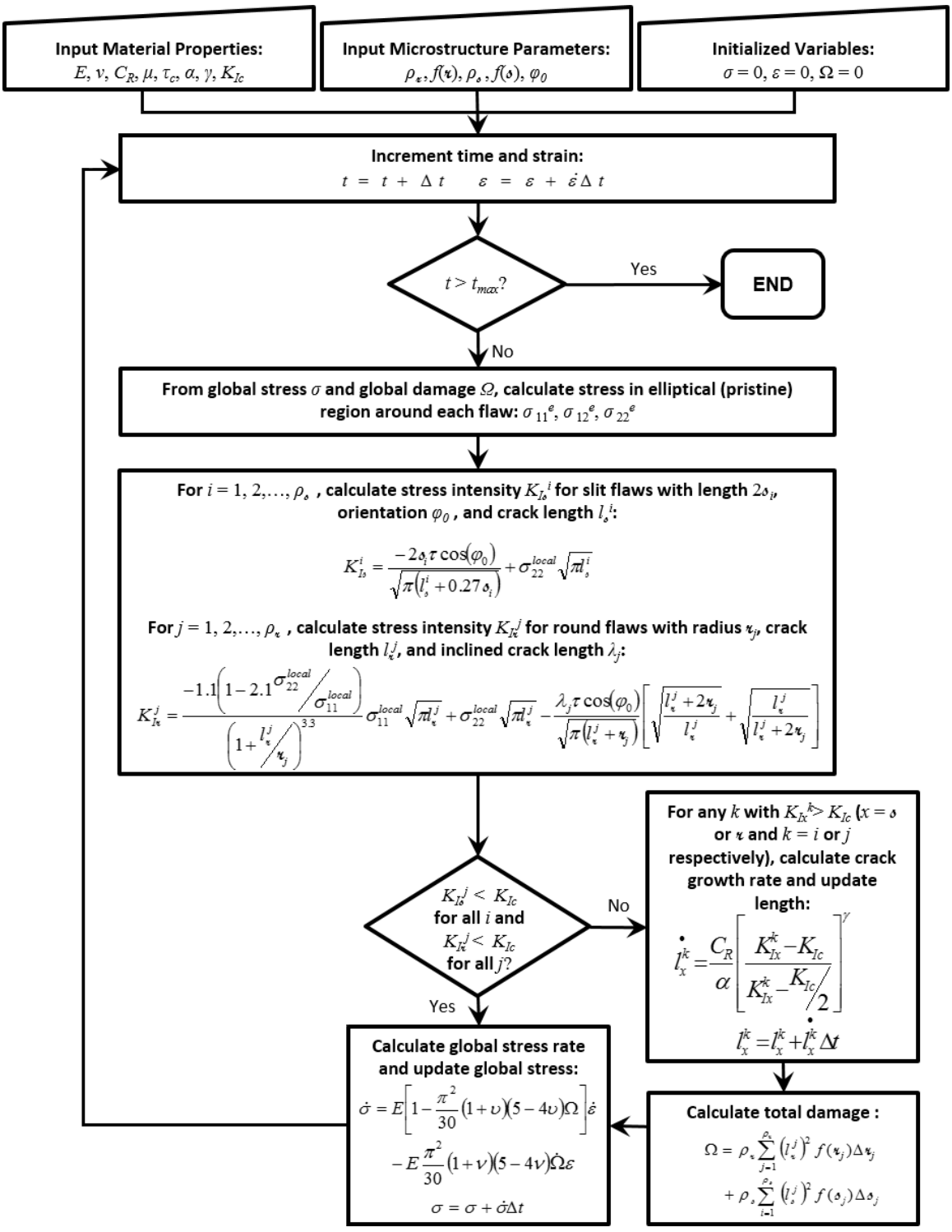


**Figure 4.8:** Flow chart for analysis of a dynamically loaded mortar specimen (see [6, 47, 97] for more details)

**Table 4.3:** List of model input parameters

| Parameter | Symbol | Model Input | Source |
|---|---|---|---|
| Young's Modulus | $E$ | 30 GPa | Simulation[1] |
| Poisson's ratio | $\nu$ | 0.27 | Simulation[1] |
| Rayleigh wave speed | $C_R$ | 2044 m/s | Laboratory[2] |
| coefficient of friction of the flaw interface | $\mu$ | 0.7 | Ref. [118][3] |
| critical shear stress at the flaw interface | $\tau$ | 0 | Ref. [6] |
| crack growth parameter | $\alpha$ | 1 | Ref. [6] |
| crack growth parameter | $\gamma$ | 1 | Ref. [6] |
| critical stress intensity | $K_{Ic}$ | 0.2 MPa $\sqrt{\text{m}}$ | Ref. [119][3] |
| round flaw number density | $\rho_r$ | 100 $mm^{-2}$ (12% air), 133 $mm^{-2}$ (16% air) | Image Analysis[4] |
| round flaw size distribution | $f(r)$ | see Figure 4.3b | Image Analysis[4] |
| parent flaw percentage | $\ell$ | 10% | Image Analysis[4] |
| cluster radius | $R_c$ | 40 μm | Image Analysis[4] |
| slit flaw number density | $\rho_s$ | 2 $mm^{-2}$ | Image Analysis[4] |
| slit flaw size distribution | $f(s)$ | see Figure 4.3a | Sieve Analysis[4] |

[1]Using VCCTL; see Section 4.1 and Ref [109]

[2]Calculated from measured density

[3]Conservative value

[4]See Section 4.2

The choice of window size is important to provide some measure of localized initial failure that would occur in the sample. If the window size is very small, then a window could potentially have zero flaws and "infinite" strength (since the micromechanics model is flaw-driven), which is not physically reasonable. Conversely, if the window size is too large, the model fails to capture localization and the moving window technique loses its usefulness. In this study, the window size was selected as a square measuring 1 mm per side. This length is over 400% of the cluster radius (see Section 4.3.2 and Figure 4.5b specifically). Since the cluster radius is interpreted as a

measure of the size of the bulk paste region where entrained air voids form, this window size is reasonable to capture the interaction between entrained air voids and aggregates without causing singularities. This window size is 118% of the nominal opening of the No. 20 sieve (nominal opening = 0.85 mm) for which $f(s) = 0.012$ (see Figure 4.5a for the aggregate size distribution). While it is noted that two size classes of aggregates exist which are larger than 0.85 mm (with nominal sizes of 1.00 mm and 1.18 mm respectively), the cumulative probability that slit flaws *belonging* to either of these size classes will be simulated in a sample microstructure (as in Figure 4.1b) is less than 0.015%. Therefore, it is unreasonable to base the window size on the MSA when doing so may compromise the effectiveness of the moving window approach. Further discussion of the effect of window size is provided in Section 4.6.

Figure 4.9 demonstrates the results of the moving window approach (detailed in Figure 4.1) for a representative test. A strength contour map has been superimposed over the microstructure image to highlight the influence of flaw geometry and clustering on the local strength at failure. In this particular microstructure (Figure 4.9), deep red corresponds to the highest dynamic strength of about 180 MPa, while dark blue corresponds to the minimum strength of 80 MPa. From this example, a fracture pattern through the darkest blue region can be envisioned.

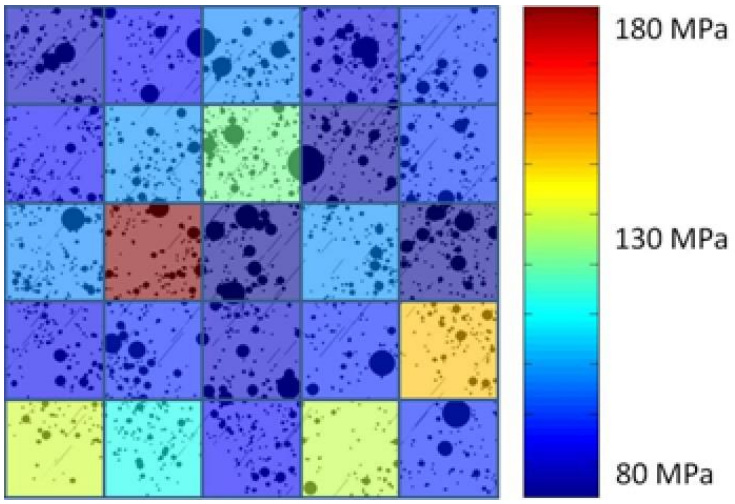


**Figure 4.9:** Strength contour map showing the dynamic strength of each window

## 4.6 Dynamic Testing

In order to observe the failure process experimentally and validate the micromechanics model, a compression Kolsky bar was used to load the samples in dynamic uniaxial compression. Originally developed to measure high strain-rate plastic response in metals [120], the Kolsky bar has been applied to a wide range of brittle materials [121, 122] including concrete and mortar [123, 124, 125]. The objective of these Kolsky bar tests was to obtain stress time histories ($\sigma(t)$) under uniaxial compression at strain-rates ($\dot{\varepsilon}$) between 150/s and 200/s. Strain-rates in that range are expected under hard impact or blast loads [93]. Figure 4.10 shows a schematic of the Kolsky bar test setup, consisting of a striker bar, incident bar, and a transmitter bar. The bars were made of aluminum with Young's modulus $E_b$ = 73 GPa and diameter $d_b$ = 12.7 mm. The specimen is placed between the incident and transmitter bars. In the apparatus used in this study, the sample was surrounded by an acrylic box (with holes for the incident and transmitter bars) to allow the remaining particles to be collected and analyzed after the tests. The striker bar, fired from a gas gun, imparts an elastic stress

wave into the incident bar with strain $\varepsilon_I(t)$. The incident wave travels to the specimen, which is held fast between the incident bar and the transmitter bar. After the incident wave reaches the specimen, it is partially reflected back into the incident bar with $\varepsilon_R(t)$ and partially transmitted into the transmitter bar with $\varepsilon_T(t)$ due to impedance mismatch between the bar and the sample. Strain gauges mounted on the incident and transmitter bar measure the stress waves in the bars and these are recorded by a high speed data acquisition system. Each test was imaged using a Photron Fastcam SA5 at a frame rate of approximately 262,500 frames per second. The stress in the specimen can be calculated from the strains in the bar (for a detailed discussion of Kolsky bar data analysis, see [121] and [126]).

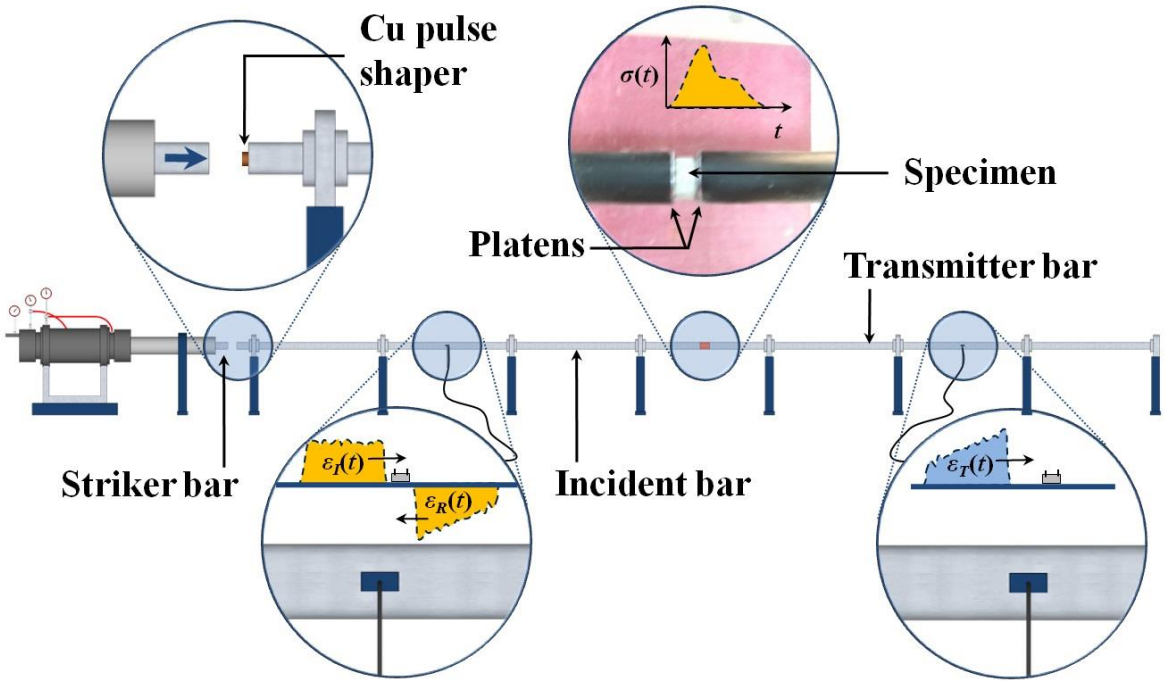


**Figure 4.10:** Schematic of a Kolsky bar apparatus. Inset of the specimen is a photo from the actual test.

For each time reading, the gage voltage is $V_G(t)$. Raw data from the strain gage should be centered at zero voltage when there is no load in the apparatus. However, this

may not be the case practically. A voltage correction, $V_{corr}$, is obtained by averaging $V_G(t)$ over a constant region before the application of the load (see Figure 4.11). This correction voltage is subtracted from the initial reading to give the voltage used in calculations, $V(t) = V_G(t) - V_{corr}$.

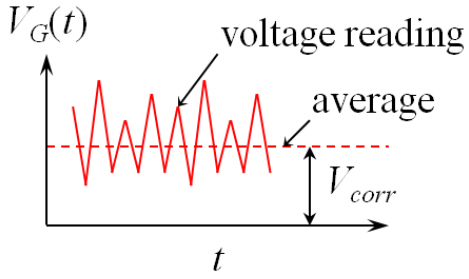


**Figure 4.11**: Voltage correction

The time readings from the transmitter gage, $t_G$, must also be corrected to reflect the time that the strain readings are occurring in the specimen, and not in the transmitter bar. Thus time $t$ is given by

$$t = t_G - \frac{d_{trans} + {}^{L_s}\!/_2}{C_b} \qquad \text{Eq. 4.2}$$

where $t_G$ is the time readings obtained from the strain gage, $d_{trans}$ is the distance from the specimen interface to the strain gage, $L_s$ is the length of the specimen, and $C_b$ is the wave speed of the transmitter bar (calculated from the bar's elastic modulus $E_b$ and density $\rho_b$ by the expression $C_b = \sqrt{E_b/\rho_b}$).

Once the corrections for voltage and time have been made, the time histories for strain and stress may be obtained. The strain history is

$$\varepsilon_t = \frac{2V(t)}{SGF \cdot v_{in}} \qquad \text{Eq. 4.3}$$

where $v_{in}$ is the input velocity of projectile used to load the incident bar and *SGF* is a gage factor intrinsic to the system. For this series of tests, *SGF* = 2.04.

The stress history in the specimen is

$$\sigma(t) = \frac{E_b A_b}{A_s} \varepsilon_T(t) \qquad \text{Eq. 4.4}$$

where $E_b$ and $A_b$ are the bars' elastic modulus and cross-sectional area, respectively, $A_s$ is the cross-sectional area of the specimen, and $\varepsilon_T(t)$ is the strain-history from the transmitter bar. The dynamic compressive strength of the specimen is denoted as $\sigma_{DYN} = \max(\sigma(t))$. Finally, the strain-rate $\dot{\varepsilon}$ is calculated from the slope of the linear portion of the stress/time history, $d\sigma/dt$. For consistency, the linear portion of the time history was taken to be the region between 10% and 90% of the peak stress on the loading side of the stress/time curve. As the specimen response is assumed to be linearly-elastic [30], the strain-rate is

$$\dot{\varepsilon} = \frac{1}{E_s} \cdot \left. \frac{d\sigma}{dt} \right|_{linear} \qquad \text{Eq. 4.5}$$

where $E_s$ is the elastic modulus of the specimen material (i.e., mortar).

## 4.7 Results and Discussion

Five mortar samples were cast for each of three different air contents (0%, 12%, and 16%), and each was tested in the Kolsky bar apparatus. Each mortar specimen was pulverized by the test, leaving behind fragments, ranging from approximately 20 μm to 2 mm in size. The fragments were sieved to obtain particle size distributions for each sample type.

Figure 4.12 is a micrograph showing fragments retained on a No. 18 sieve (1 mm nominal size) for one of the 12% air entrained samples. Cross sections of both entrained air voids and fine aggregate particles can be seen in the image (examples of both are indicated on the figure). The image suggests that cracks pass directly through the aggregate particles, which validates an important assumption used in the modeling (see Section 4.3.1). The wing crack geometry only makes sense if the crack can travel through both paste and aggregate without significant deviation. The observed cracks which pass through the aggregates indicate that this is not an unreasonable assumption.

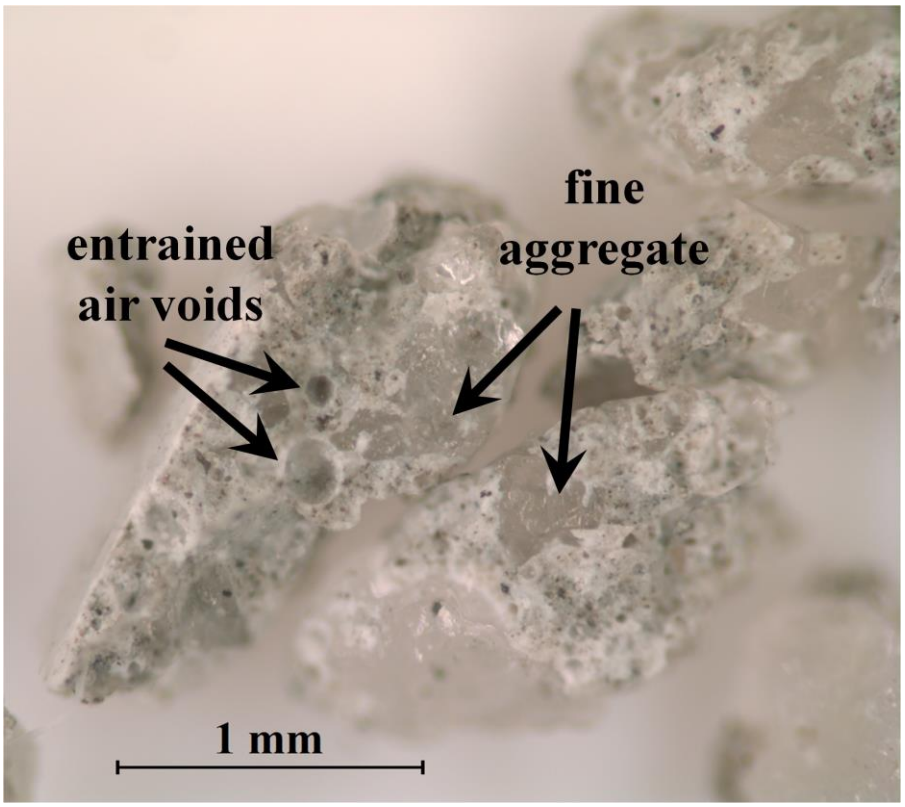


**Figure 4.12:** Mortar particles retained on a No. 18 sieve (1 mm) for an air entrained sample

Figure 4.13 shows the particle size distribution (expressed as a cumulative distribution function) for each of the three air contents (error bars denote standard

deviation). Increasing air content has the net effect of increasing the number of small particles relative to the non-air entrained sample. This behavior also supports the modeling assumption that failure in this range of loading rates is flaw driven. One may interpret the larger fragments left behind by non-air entrained samples to mean that cracks originate at the ITZ and traverse the hydrated cement paste phase before interacting with one another. When entrained air voids are present, then cracks may also initiate throughout the paste due to stress concentrations. In this case, a larger number of small fragments would be expected due to the close spacing of the entrained air voids, as shown in Figure 4.13.

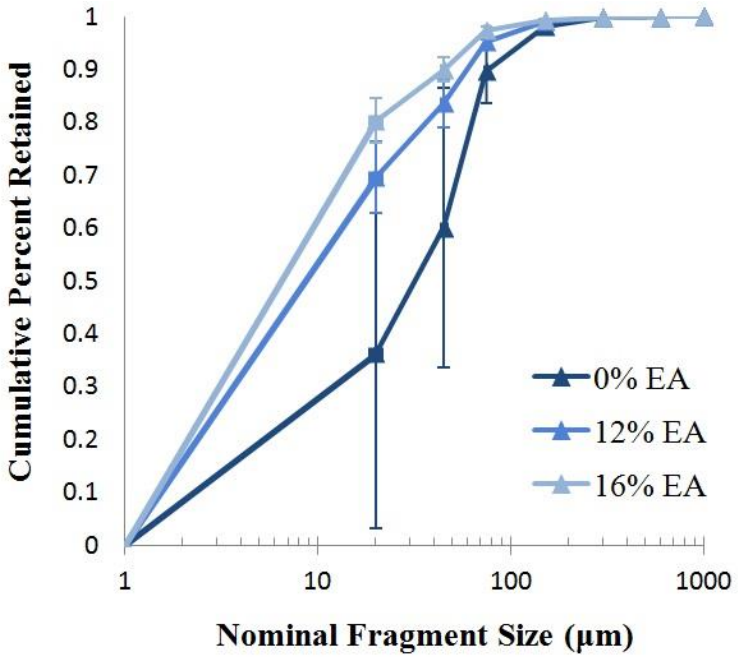


**Figure 4.13:** Particle size distribution of mortar fragments

A representative data set showing the stress-time history from each of the three sample types is shown in Figure 4.14. The numbers along the stress-time histories correspond to the image frames below the graphs, each of which shows a high speed image of the sample at the numbered points. The stress-time history for the non-air

entrained sample approaches the sample's dynamic strength and then decays to zero. This sample shows crack growth while the load is falling. Rectilinear cracks can be detected in image 5 (at the peak stress) and continue to become more distinguishable during unloading. A change in slope is observed between frames 8 and 9 in all three sample types. In the 12% EA and 16% EA samples, this change in slope is followed by a discernable post-peak "plateau" region before the stress-time history decays to zero. Both air entrained samples types appear to deform without axial cracking until after the peak stress, with visible cracks appearing just before the plateau regions (in image 7 for 12% EA and images 6 for 16% EA). In the higher air entrapped sample, the cracks are more distinguishable later in the plateau. In both air entrained mortars, the material fragments in the latter portion of the plateau and the particles begin to disperse, creating a "mushroom" effect. The final frames in the series of images along the 0% EA stress-time history indicate a lesser degree of fragmentation than the 0% EA sample. Based on these observations, it is concluded that the air entrained samples first exhibit signs of void consolidation, then hold a load plateau until the cracks fully form through the thickness and the mortar fails.

To facilitate comparison among the datasets and to investigate this post-peak plateau response further, all of the results of the Kolsky Bar tests are shown in Figure 4.15, where the stress-time histories have been normalized: the time has been normalized such that $t_{peak}$ is the time corresponding to the failure stress $\sigma_{DYN}$, and the stress has been normalized by $\sigma_{DYN}$. The loading portion of the curves exhibits the same qualitative behavior in all three cases. Notably, the post-peak response differs between sample sets. A clear post-peak plateau region arises as air content increases, which is indicated by the

dashed boxes in the 12% EA and 16% EA plots in Figure 4.15. This is likely due to entrained air voids collapsing on themselves, as this behavior is not observed in non air-entrained samples. In effect, as the voids collapse and develop new contact surfaces, the material carries more residual stiffness even as the damage level increases. The attenuation difference between air in the void space and the surrounding material may also contribute to this region, as the shock wave moves from solid to air [127]. Air flow between the voids has been identified as a contributing factor of the strain-rate effect in studies of foamed metals, for example [128] (although given the fine porespace connecting these entrained air voids, that may not be a major contributing factor). The variable post-peak curves in the samples containing no air entrainment may be due to similar phenomena, but occurring in large capillary pores. These plateau regions serve as an indicator of the presence of the air entrainment.

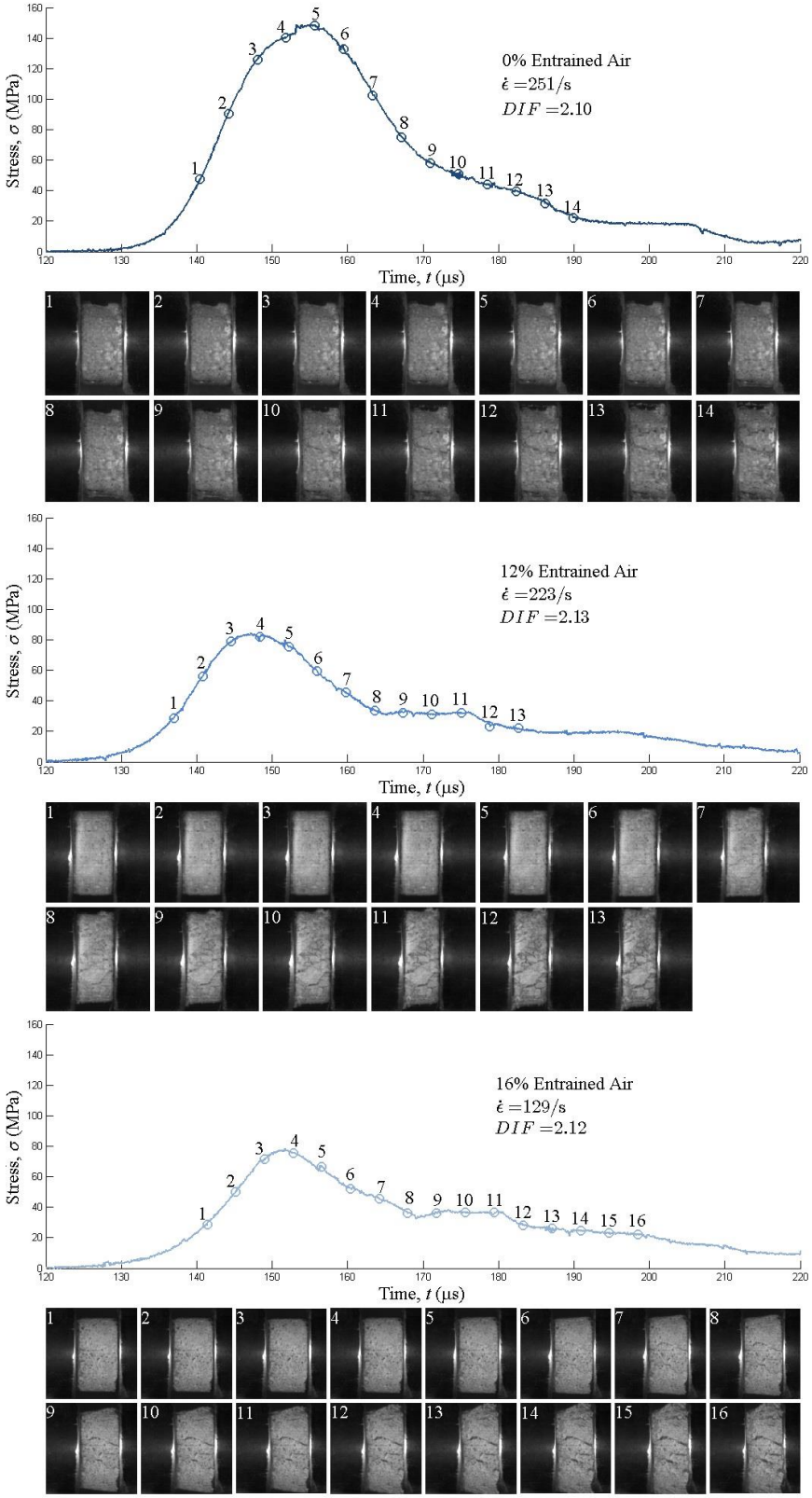


**Figure 4.14:** Representative Kolsky bar data for each sample type

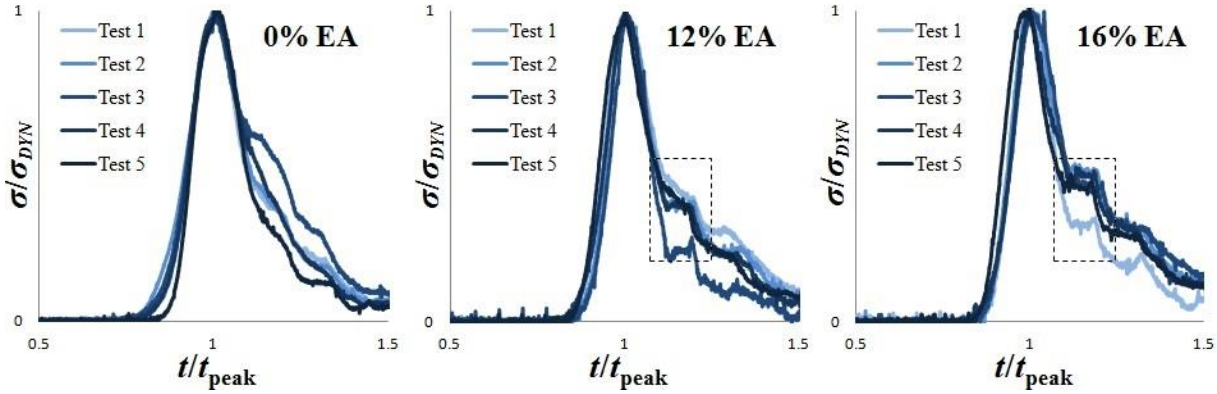


**Figure 4.15:** Normalized Kolsky Bar results. Dashed boxes in 12% and 16% EA indicate the plateau.

Table 4.4 shows the average dynamic strengths and standard deviations for each sample type obtained from both the Kolsky bar tests and the micromechanics model. The experimental and simulated average strengths are within 10% of one another for each sample type tested. The dynamic increase factor (DIF) is the ratio of average dynamic-to-static compressive strength (see Table 4.2). The DIF is also included Table 4.4. While air entrainment decreases the average dynamic strength to about 70±1% of the control samples, air entrained samples exhibit higher average DIFs than non-air entrained samples. The DIF for the 16% air entrained samples is also higher than the 12% air entrained samples for both the experimental strengths and the model strengths. The standard deviations of the experimental datasets decrease with increasing air content, while the standard deviations in the model are actually quite similar. The standard deviations of the experimental data are between 150% - 330% of the simulation data. However, due to the small sample size of the Kolsky bar datasets relative to the simulation datasets (5 samples versus 500), this is to be expected. The probability mass functions (PMFs) associated with the distribution of dynamic strengths in the control sample (0% entrained air) is shown in Figure 4.16, while the two air entrained specimens

are shown in Figure 4.17 and Figure 4.18, respectively. Open circles along the abscissae in Figure 4.16 – Figure 4.18 on the figures denote the failure strengths of the Kolsky bar test specimens. The model PMFs agree very well with the Kolsky bar data points in an average sense. Some of the experimental data points lay outside the boundaries of the simulation results, suggesting that the model may under-predict the variance. In future work, perhaps this could be rectified by calibrating the crack growth laws to the dataset. Since this calibration was not performed here, these results are considered to be in good agreement.

**Table 4.4:** Comparison of average dynamic strengths from the experiments and models

| | **0% EA** | | **12% EA** | | **16% EA** | |
|---|---|---|---|---|---|---|
| | **Strength (Std. Dev.)** | **DIF** | **Strength (Std. Dev.)** | **DIF** | **Strength (Std. Dev.)** | **DIF** |
| **Kolsky Bar Test** | 121 MPa (22 MPa) | 1.71 | 84 MPa (17 MPa) | 2.13 | 85 MPa (10 MPa) | 2.30 |
| **Micromechanics Model** | 113 MPa (6.6 MPa) | 1.59 | 81 MPa (6.8 MPa) | 2.05 | 80 MPa (6.5 MPa) | 2.17 |
| **Error in Mean** | 6.6% | | 3.6% | | 5.9% | |

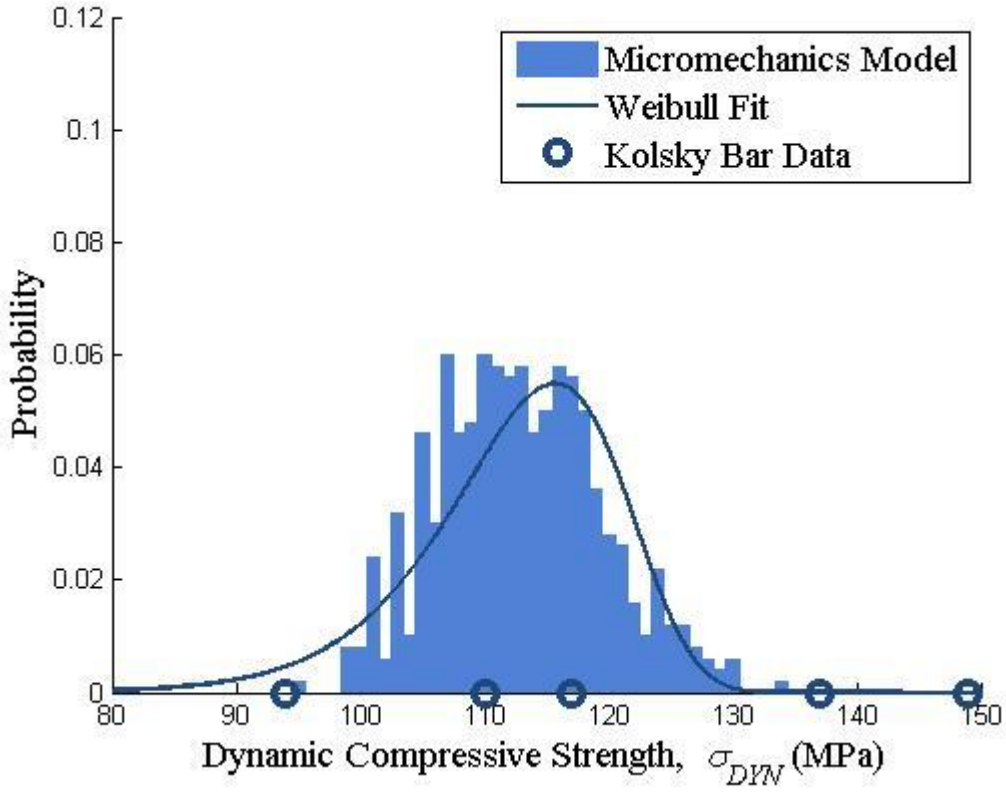


**Figure 4.16:** Unimodal Weibull distribution fit to micromechanics output for non-air entrained specimen. Kolsky bar test points are plotted as open circles.

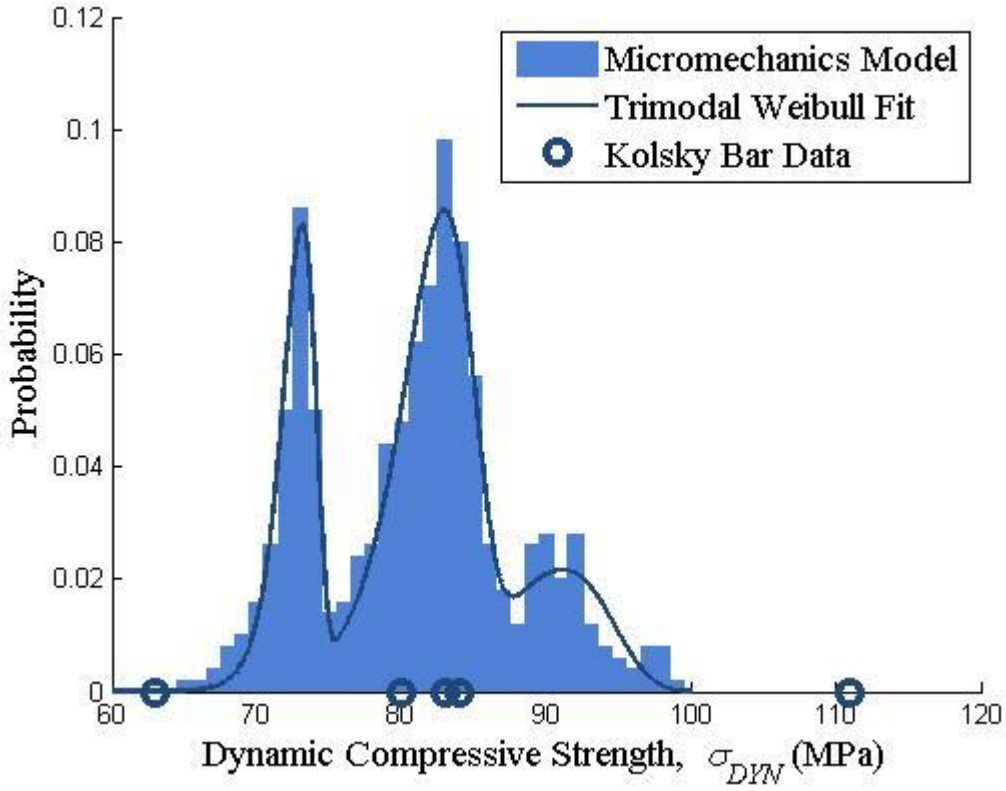


**Figure 4.17:** Trimodal Weibull distribution fit to micromechanics output for the 12% air entrained specimen. Kolsky bar test points are plotted as open circles.

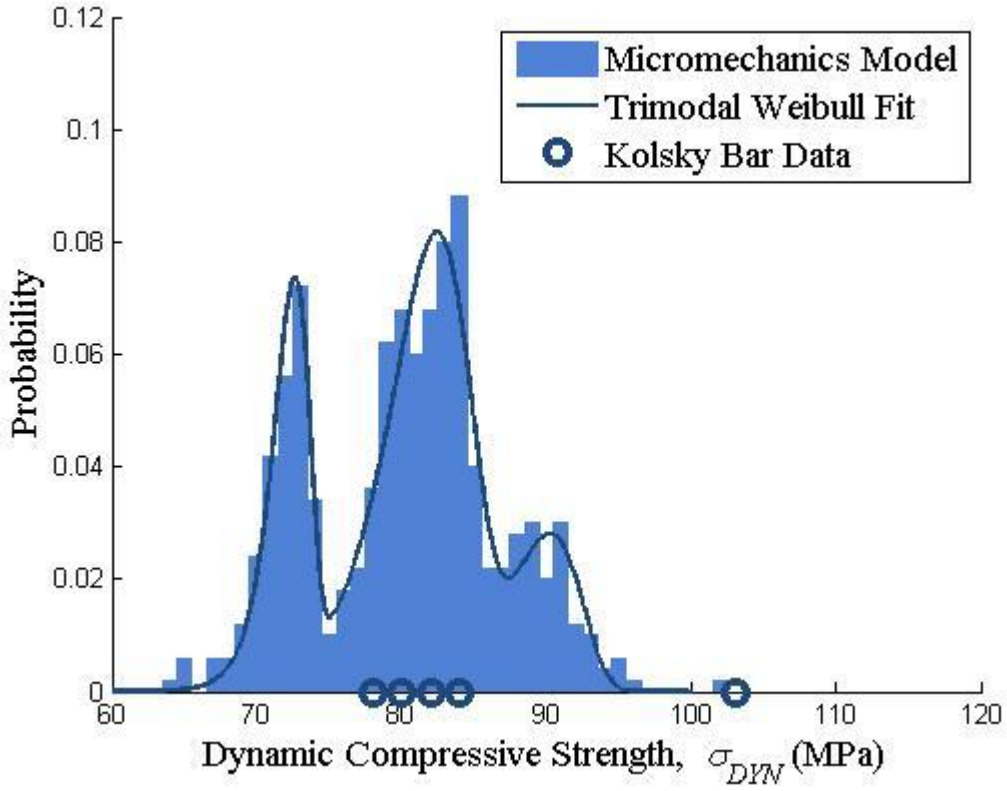


**Figure 4.18:** Trimodal Weibull distribution fit to micromechanics output for the 16% air entrained specimen. Kolsky bar test points are plotted as open circles.

The shapes of the probability mass functions suggest the distribution of strengths may be modeled using a Weibull distribution. The cumulative distribution function (CDF) of a general (unimodal) Weibull distribution is given by

$$F(\sigma_{DYN}) = 1 - \exp\left[-\left(\frac{\sigma_{DYN}}{\sigma_N}\right)^m\right] \qquad \text{Eq. 4.6}$$

where $\sigma_N$ is the normalizing stress and $m$ is the Weibull modulus. While the applicability of the Weibull to failure in ceramics is the subject of some debate [129, 130, 131], the distribution has been previously utilized to model mortar [132, 133]. While the PMF of dynamic strength corresponding to the control microstructure containing only slit flaws

appears to be unimodal, the PMFs of dynamic strengths corresponding to heterogeneous microstructure containing both slit and round flaws clearly are not. Mixed distributions arise in the study of engineering failure analysis when the population of interest contains two or more nonhomogenous subpopulations [134]. Weibull distributions are perhaps the most common multimodal distributions because of their flexibility. In this case, analyzing the output of the micromechanics model as a trimodal Weibull distribution helps analyze the confluence flaw types in a continuous probabilistic framework. The CDF of the trimodal Weibull distribution is given by

$$F(\sigma_{DYN}) = 1 - \beta_1 \exp\left[-\left(\frac{\sigma_{DYN}}{\sigma_{N1}}\right)^{m_1}\right] - \beta_2 \exp\left[-\left(\frac{\sigma_{DYN}}{\sigma_{N2}}\right)^{m_2}\right] - \beta_3 \exp\left[-\left(\frac{\sigma_{DYN}}{\sigma_{N3}}\right)^{m_3}\right] \quad \text{Eq. 4.7}$$

which differs from the general Weibull CDF by having Weibull moduli $m_k$, normalizing stresses $\sigma_{Nk}$, and a scale parameters $\beta_k$ ($k$ = 1,2,3). The $\beta_k$ terms must sum to unity. The fitted values for $m_k$, $\sigma_{Nk}$, and $\beta k$ are in Table 4.5 (note that 0% EA will have only one normalizing stress and Weibull modulus, and no scale parameter, per Eq. 4.6). Probability plots for the three cases are shown in Figure 4.19, which indicate the Weibull model is a good fit for the data. A method of assessing the validity of these results is to perform a $\chi^2$ goodness-of-fit test, which tests whether the experimental data could be drawn from the distribution explained by Eq. 4.6 and Eq. 4.7. In this case, the $\chi^2$ goodness-of-fit test investigates the null hypothesis $H_0$: the experimental data fits the distributions described by Eq. 4.6 (0% EA) or Eq. 4.7 (12% EA and 16% EA) versus $H_1$: the experimental data does not fit the aforementioned distribution. The *p*-values in Table 4.5 are results of the $\chi^2$ goodness-of-fit test and are interpreted as the probability of observing a test statistic as extreme as, or more extreme than, the observed value under

the null hypothesis. Small values of $p$ (i.e., $p < \alpha$) cast doubt on the validity of the null hypothesis. In all three cases, the $\chi^2$ goodness-of-fit test indicates that the null hypothesis cannot be rejected at the $\alpha = 0.05$ significance level. A broad interpretation of this finding would conclude that, despite variability in the experimental results, the data indicates that the dynamic strengths of the five specimens at each air-entrainment level, as obtained from the Kolsky bar tests, are statistically consistent with the micromechanics simulations.

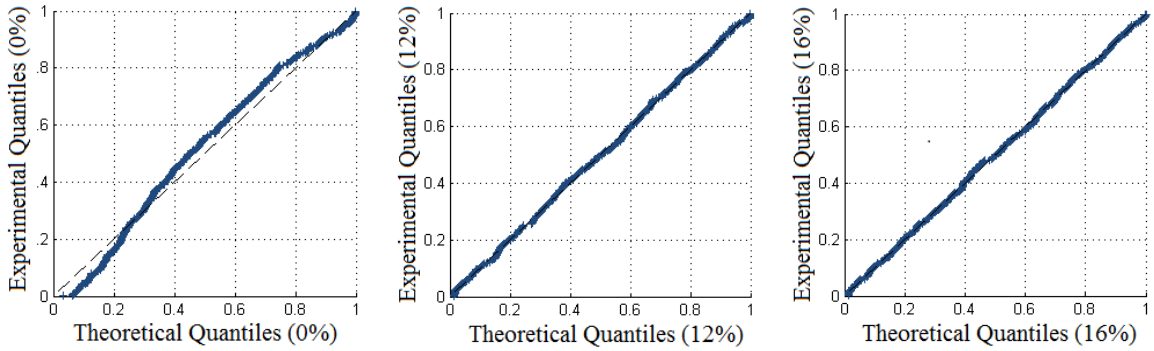


**Figure 4.19:** Probability plots for the three air contents

**Table 4.5:** Weibull parameters and $\chi^2$ goodness-of-fit results

| $\phi_{air}$ | Scale parameter | | | Normalizing stress | | | Weibull modulus | | | *p*-value |
|---|---|---|---|---|---|---|---|---|---|---|
| | $\beta_1$ | $\beta_2$ | $\beta_3$ | $\sigma_{N1}$ | $\sigma_{N2}$ | $\sigma_{N3}$ | $m_1$ | $m_2$ | $m_3$ | |
| 0% | N/A | | | 116.0 | | | 17.3 | | | 0.29 |
| 12% | 0.24 | 0.53 | 0.23 | 72.5 | 81.6 | 89.2 | 66.6 | 35.6 | 24.4 | 0.51 |
| 16% | 0.23 | 0.58 | 0.19 | 72.6 | 82.4 | 90.3 | 60.8 | 30.9 | 36.9 | 0.79 |

A sensitivity study was done in order to understand the effect that window size has on $\sigma_{DYN}$ and the number of modes in the PMF for the 12% EA sample. The number of windows was increased from 1 (i.e. no discretization) to 36 (i.e. a 6 × 6 grid). As discussed in Section 4.2, each microstructure is discretized into an $M \times M$ grid of $W_{tot}$ windows. $M$ was increased from unity until the mesh was fine enough to produce

singularities (i.e. the simulation failed because the window contained no flaws), which occurred at $M = 7$. Therefore $M$ ranged from $M = 1$ ($W_{tot} = 1$, window size = 5 mm) to $M = 6$ ($W_{tot} = 36$, window size = 0.83 mm). For each integer value of $M$, $\sigma_{DYN}$ was calculated, a PDF was obtained, and the number of modes were counted. Figure 4.20 shows the results of this sensitivity analysis. The size of the window is shown along the bottom horizontal axis, while the corresponding number of windows is shown across the top axis (note that both horizontal axes convey the same information). The square data points correspond to the dynamic strength, plotted along the left vertical axis. The triangular data points correspond to the number of modes. The coarsest microstructure produces the highest strength and the lowest number of modes. This is to be expected, because without discretization the model cannot account for clustering and the corresponding reduction in strength due to stress concentration. This also means that no heterogeneous subpopulations have a noticeable effect, resulting in a unimodal PMF. The number of modes converges to three rapidly and does not exceed three by the time the simulation failed. Any window size between 0.83 mm and 1.67 mm produces a trimodal distribution, transitioning between window sizes of 1.67 mm and 2.5 mm. Experimental results confirm that $M = 5$ reasonable. An argument could be made to choose $M = 6$, but this produces a window size which is smaller than the No. 20 sieve, for which the probability of occurrence is non-trivial. Future work could optimize the window size.

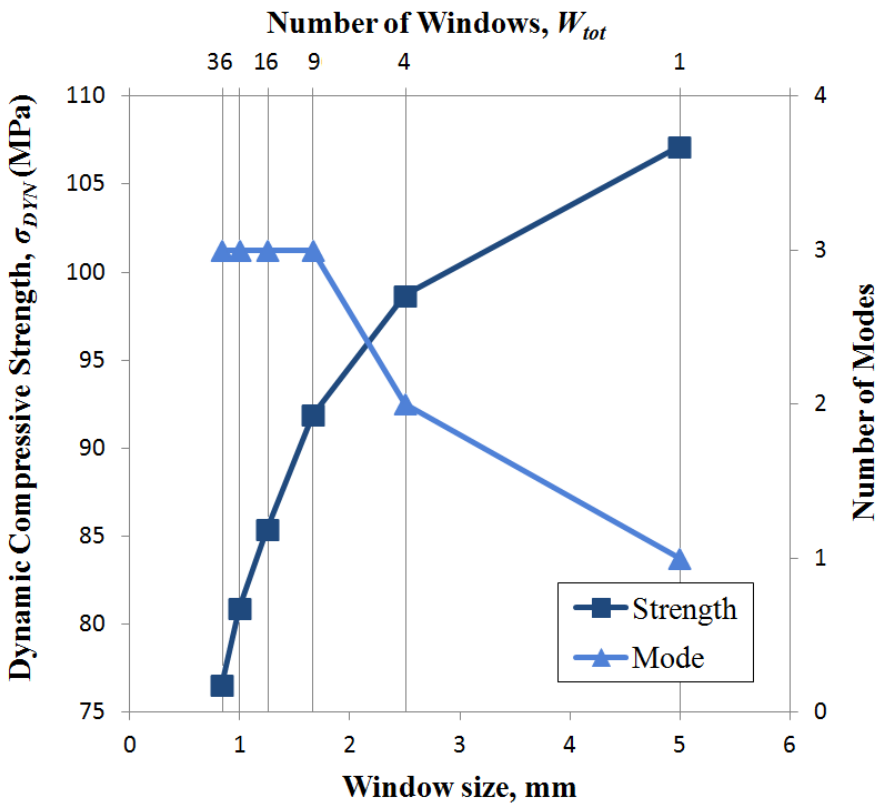


**Figure 4.20:** Effect of window size on strength and number of modes

In order to explain the three modes arising in the distribution of strengths in air entrained samples, the simulations results were sorted into one of three modes. In the interest of brevity, analysis will focus on the 12% air entrained dataset. Since the material properties were constant in all of the simulations, and since damage is driven by flaws in this model, it is justified to assume that the dynamic strength modes (and the underlying flaw statistics corresponding to each strength value) may be sorted based on damage. As was shown in the flow chart in Figure 4.8, the damage parameter $\Omega$ relates to the total number, size distribution, and crack growth associated with the flaws.

Figure 4.21a shows the dynamic strength plotted against the damage parameter. Three distinct regions can be discerned in the figure. The lightest blue datapoints are

assumed to belong to mode 1, the middle blue datapoints are assumed to belong to mode 2, and the darkest blue datapoints are assumed to belong to mode 3.

Figure 4.21b shows the dynamic strength PMF when the data are sorted into three modes by this method (compare to in Figure 4.17, showing the dynamic strength PMF of the entire dataset). The overlapping PMFs in

Figure 4.21b expose the need to separate the data into the constituent modes based on a metric other than simple thresholding using a local minimum (e.g. choosing a value of 87 MPa as the demarcation between mode 2 and mode 3). Mode 1 and mode 2 show a small degree of overlap. However, mode 2 and mode 3 show a high degree of overlap since mode 3 has a very wide distribution of strength values.

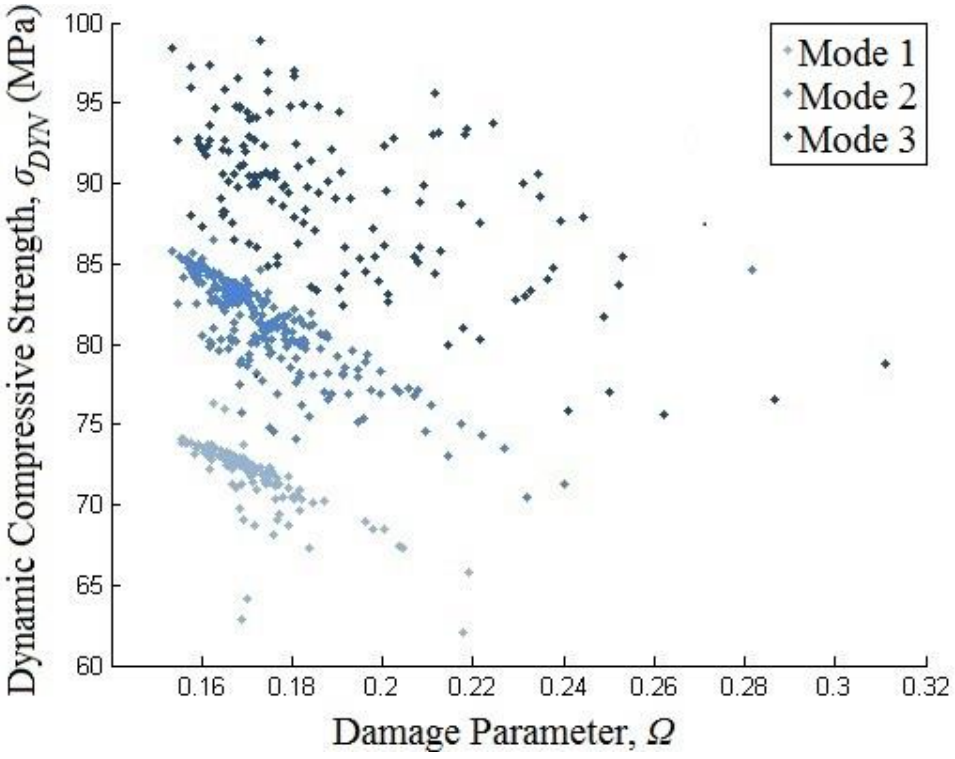


(a)

**Figure 4.21:** (a) dynamic strength versus damage parameter, showing clusters related to the three modes and (b) resulting histograms of the sorted strength data

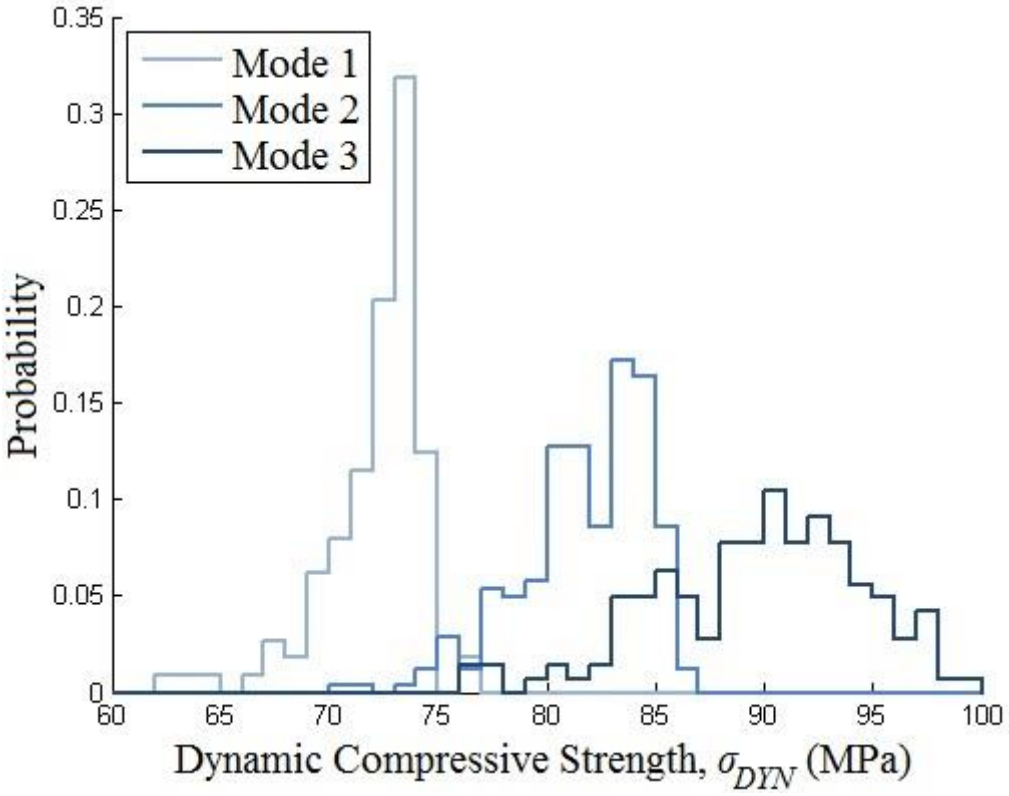


(b)

**Figure 4.21:** (Continued) (a) dynamic strength versus damage parameter, showing clusters related to the three modes and (b) resulting histograms of the sorted strength data

Next, stepwise multiple regression was carried out using R (this analysis still focuses on the 12% dataset). This analysis is necessary to study the flaw statistics (number and size distribution of flaws) in the window where failure initiated (i.e., the weakest link in the discretized microstructure). The number of flaws is easily described by local number densities $\rho_s$ and $\rho_r$. The effect of size distribution is considered by computing the expected value of the local flaw size distribution, E[$s$] and E[$r$]. The response variable is $\sigma_{DYN}$. The dataset for each of the three modal regions was sorted by considering the flaw statistics associated with each mode of $\sigma_{DYN}$ as shown in

Figure 4.21b. The parameters $\rho_s$, E[$\mathscr{s}$], $\rho_v$, and E[$\mathscr{v}$] were considered separately, along with interactions $\rho_s \cdot \rho_v$, $\rho_s \cdot$E[$\mathscr{s}$], $\rho_s \cdot$E[$\mathscr{v}$], $\rho_v \cdot$E[$\mathscr{s}$], $\rho_v \cdot$E[$\mathscr{v}$], and E[$\mathscr{s}$]·E[$\mathscr{v}$]. The threshold $p$-value was set to $p = 0.05$ throughout.

The results of the stepwise multiple regression are shown in Table 4.6. In mode 2, the mostly likely mode which accounts for the majority of the response data ($\beta_2 = 0.53$), the analysis suggests that $\rho_v$ and E[$\mathscr{v}$] contribute the most to the dynamic strength. This is interpreted to mean that failure is most *likely* to occur in the hydrated cement paste due to the interaction of microcracks which emanate from entrained air voids due to stress concentration. The mean of the second mode has approximately the same mean as the mean of the entire distribution (81.6 MPa in mode 2 versus 81 MPa for the entire data set). The two modes flanking mode 2 occur with similar probabilities ($\beta_1 = 0.24$ and $\beta_3 = 0.23$). Unlike mode 2, terms relating to presence of aggregates are shown to be statistically significant in the other modes. In both mode 1 and mode 2, aggregate size E[$\mathscr{s}$] and the interaction between aggregate size and air void size E[$\mathscr{s}$]E[$\mathscr{v}$] are significant. However, the number density of air voids $\rho_v$ is significant in mode 1, but the average void size E[$\mathscr{v}$] is significant in mode 3. This suggests that a *larger number* of air voids in the vicinity of an aggregate could cause the first spike in the histogram (see Figure 4.17), which is likely to occur in about 24% of specimens and will result in local failure with a mean dynamic strength of 72.5 MPa. Since E[$\mathscr{v}$] is significant in mode 3 but $\rho_v$ is not, the higher strengths associated with mode 3 (mean $\sigma_{DYN} = 89.2$ MPa) suggest that the sample will have the highest dynamic load capacity if the air voids are unclustered and are relatively larger air voids, on a length scale similar to entrained air.

**Table 4.6:** Regression analysis of 12% air entrained model output

| Mode | $B$ | Mean $\sigma_{DYN}$ (MPa) | Parameter | $p$-value |
|---|---|---|---|---|
| 1 | 0.24 | 72.5 | **E[$\mathcal{s}$]** | 0.034 |
| | | | **$\rho_{\mathcal{r}}$** | 0.017 |
| | | | **E[$\mathcal{s}$]E[$\mathcal{r}$]** | 0.031 |
| 2 | 0.53 | 81.6 | **$\rho_{\mathcal{r}}$** | 0.031 |
| | | | **E[$\mathcal{r}$]** | 0.008 |
| 3 | 0.23 | 89.2 | **E[$\mathcal{s}$]** | 0.024 |
| | | | **E[$\mathcal{r}$]** | 0.002 |
| | | | **E[$\mathcal{s}$]E[$\mathcal{r}$]** | 0.011 |

Further analysis was carried out using analysis of variance (ANOVA). While the stepwise multiple regression was useful for successively eliminating parameters and interactions which were not significant when all parameters were considered at once, ANOVA is useful for studying how means and variances of parameters and interactions change between modes. The hypothesis to be tested is that all the mean of a parameter is the same in each mode (i.e. for a parameter $x$, $H_0$ : $\mu_x^{(1)} = \mu_x^{(2)} = \mu_x^{(3)}$) versus the hypothesis that at least one mean is different. The same terms and interactions considered in the stepwise multiple regression analysis were considered for ANOVA, with the addition of two terms related to damage. The damage parameter $\Omega$ was decomposed into the contribution made by slit flaws $\Omega_{\mathcal{s}}$ and the contribution made by round flaws $\Omega_{\mathcal{r}}$ (see Figure 4.8). The results of the ANOVA are reported in Table 4.7, where $p$-values marked with an asterisk are significant at the 5% level. The means vary the most significantly for $\Omega_{\mathcal{s}}$, $\Omega_{\mathcal{r}}$, E[$\mathcal{s}$], and $\rho_{\mathcal{r}}$·E[$\mathcal{s}$].

**Table 4.7:** ANOVA results

| **Testing Null Hypothesis $H_0$** | *p*-value |
|---|---|
| $\mu_{\Omega_s}^{(1)} = \mu_{\Omega_s}^{(2)} = \mu_{\Omega_s}^{(3)}$ | $5.1\times10^{-24}$ * |
| $\mu_{\Omega_v}^{(1)} = \mu_{\Omega_v}^{(2)} = \mu_{\Omega_v}^{(3)}$ | $4.3\times10^{-22}$ * |
| $\mu_{\rho_s}^{(1)} = \mu_{\rho_s}^{(2)} = \mu_{\rho_s}^{(3)}$ | 0.70 |
| $\mu_{E[s]}^{(1)} = \mu_{E[s]}^{(2)} = \mu_{E[s]}^{(3)}$ | 0.05* |
| $\mu_{\rho_v}^{(1)} = \mu_{\rho_v}^{(2)} = \mu_{\rho_v}^{(3)}$ | 0.49 |
| $\mu_{E[v]}^{(1)} = \mu_{E[v]}^{(2)} = \mu_{E[v]}^{(3)}$ | 0.71 |
| $\mu_{\rho_s\rho_v}^{(1)} = \mu_{\rho_s\rho_v}^{(2)} = \mu_{\rho_s\rho_v}^{(3)}$ | 0.59 |
| $\mu_{\rho_s E[s]}^{(1)} = \mu_{\rho_s E[s]}^{(2)} = \mu_{\rho_s E[s]}^{(3)}$ | 0.28 |
| $\mu_{\rho_s E[v]}^{(1)} = \mu_{\rho_s E[v]}^{(2)} = \mu_{\rho_s E[v]}^{(3)}$ | 0.70 |
| $\mu_{\rho_v E[s]}^{(1)} = \mu_{\rho_v E[s]}^{(2)} = \mu_{\rho_v E[s]}^{(3)}$ | 0.04* |
| $\mu_{\rho_v E[v]}^{(1)} = \mu_{\rho_v E[v]}^{(2)} = \mu_{\rho_v E[v]}^{(3)}$ | 0.51 |
| $\mu_{E[s]E[v]}^{(1)} = \mu_{E[s]E[v]}^{(2)} = \mu_{E[s]E[v]}^{(3)}$ | 0.09 |

Figure 4.22a and Figure 4.22b shows the ANOVA plot comparing the means and quartiles of the distribution associated with $\Omega_s$ and $\Omega_v$, respectively. Comparison of Figure 4.22a to Figure 4.22b shows that the distributions exhibit opposite trends: $\Omega_s$ generally falls during the transition from mode 1 to mode 3, while $\Omega_s$ is rising. Therefore, the entrained air voids are playing a larger role in their contribution to damage in higher-

strength modes, while the aggregate/ITZ interaction is playing a diminished role. Since the control simulation (0% entrained air) effectively sets an upper boundary on dynamic strength at 113 MPa (see Table 4.4), and since the aggregate/ITZ flaw type is generally much larger in size than the entrained air void flaw type, it is reasonable that a locally-larger aggregate/ITZ flaw population would affect dynamic strength in this manner.

The ANOVAs of E[$\mathcal{S}$] and of $\rho_{\mathcal{S}}$·E[$\mathcal{S}$] shed some light on why terms related to E[$\mathcal{S}$] were significant in modes 1 and 3 when analyzed using stepwise regression. Figure 4.22c shows that the distribution of E[$\mathcal{S}$] varies starkly between the three modes. Meanwhile the spread of $\rho_{\mathcal{S}}$·E[$\mathcal{S}$] (see Figure 4.22d) gets progressively smaller, which reinforces the previously-drawn conclusion that the highest strength mode is more influenced by the *size* rather than *number* of entrained air voids.

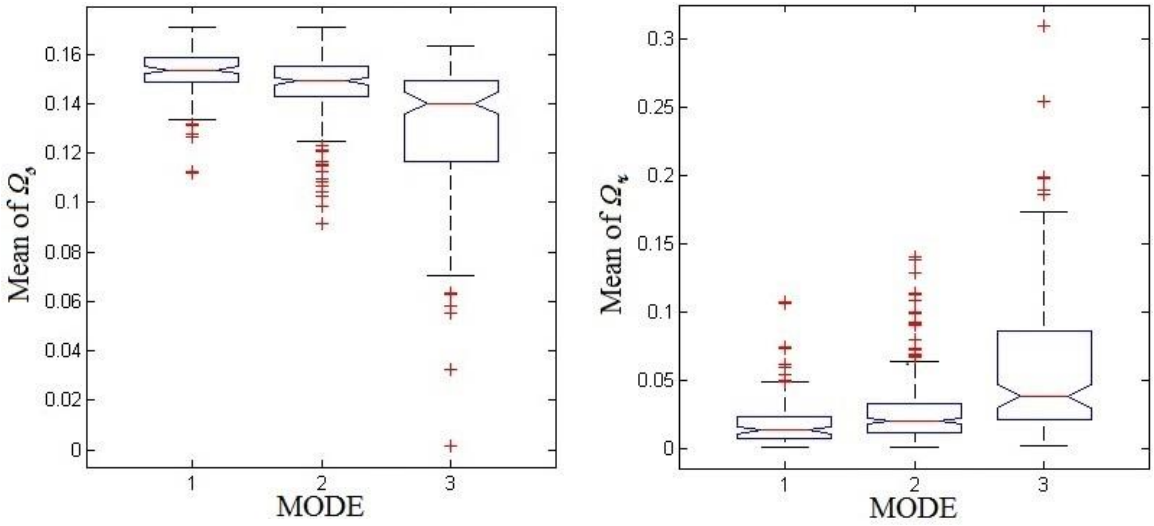


(a) (b)

**Figure 4.22:** ANOVA plots of (a) $\Omega_{\mathcal{S}}$, (b) $\Omega_{\mathcal{S}}$, (c) E[$\mathcal{S}$], and (d) $\rho_{\mathcal{S}}$·E[$\mathcal{S}$]

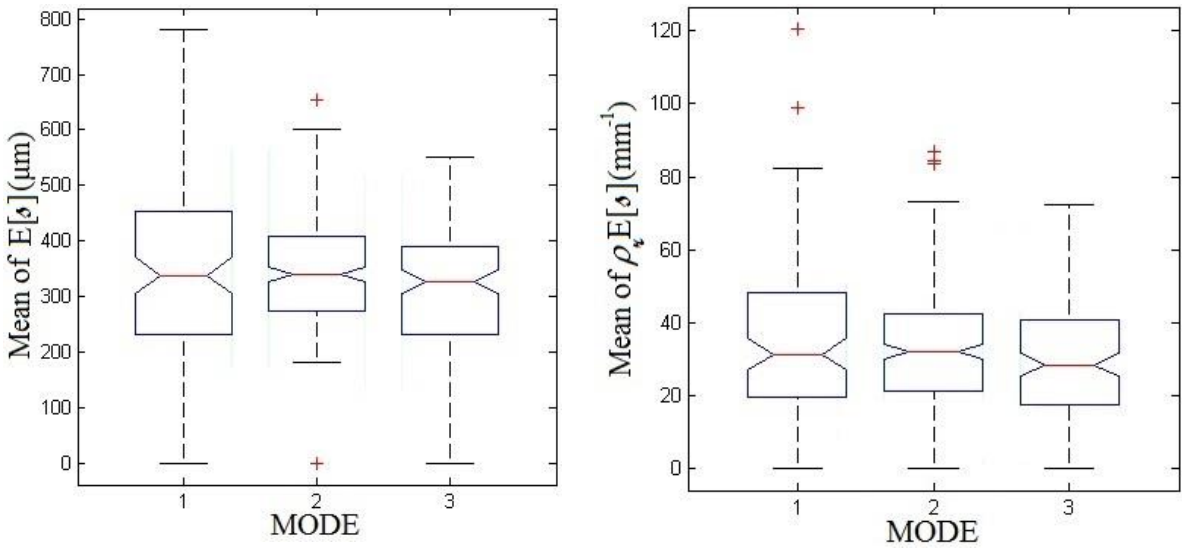


(c) (d)

**Figure 4.22:** (Continued) ANOVA plots of (a) $\Omega_{\mathfrak{d}}$, (b) $\Omega_{\mathfrak{r}}$, (c) E[ɔ], (d) $\rho_{\mathfrak{r}}$ ·E[ɔ]

The findings have several implications for engineering cementitious materials for blast resistance. For example, the Federal Emergency Management Administration (FEMA) issues design guidance to protect infrastructure from potential acts of terror, which includes hard impact and blast loads [135]. The classical approach has been to increase the standoff distance from the charge to the protected structure, because the blast overpressure decays exponentially with distance. When this additional space is either impractical or not readily available (such as bridge piers or buildings located in dense urban environments), concrete barriers are typically prescribed to impede vehicles and blast waves from impacting critical structural elements. While such design considerations may be successful in preventing primary damage (e.g. structural collapse), they do not address secondary effects such as injury from shrapnel created in the aftermath of the blast. The findings of this research suggest that air entrainment be included in materials-level considerations for engineering at-risk infrastructural elements.

Ultra-high-performance concrete (UHPC) panels have been investigated recently to stop projectile penetration, with a focus on the volume fraction and orientation of steel fibers [136]. This study suggests that the effect of entrained air should be investigated in these panels, since mode 3 confirms that an optimized air void system could increase the toughness without significantly decreasing the failure strength, although, certainly, the extension of this work to higher strength cementitious composites warrants further evaluation. Since air entrainment decreases the overall weight, it is particularly useful in reducing the strength-to-weight ratio of such panels.

To summarize, this approach combined materials characterization, mechanics, and experimentation. Mortars were characterized using a variety of techniques: fine aggregate was characterized using simple sieve analysis, while entrained air voids were characterized using advanced x-ray microtomography and statistical techniques. Static compressive strength was obtained using a hydraulic compression frame, while dynamic compressive strength was obtained using a Kolsky bar. Elastic properties were obtained using VCCTL for microstructure simulation. An interacting microcrack model was used to investigate the effects of slit flaws (i.e., fine aggregate) and spherical voids (i.e., entrained air voids) on dynamic strength. The model accounted for flaw shape and size. A moving window approach was used to account for localization of failure at locations with higher flaw concentrations. The dynamic strengths of mortars with varying air content were determined experimentally using a Kolsky bar and used for model validation. Based on these results, the following conclusions can be drawn:

1. The moving window approach was shown to be a useful tool for investigating the localization of failure that occurs in brittle materials such as mortar, with possible application to other brittle materials.
2. The good agreement in average dynamic strength in the control sample gives further credence to the theory that the dynamic strength increase in mortar and concrete may arise from crack propagation through rather than around aggregates. Post-failure microscopic analysis of fragments also supports this theory.
3. To the author's knowledge, the Neyman Type A distribution has been applied to entrained air voids for the first time. With further development, this approach could prove useful because it allows the distribution and clustering to be quantified in closed form. Cracks initiating from entrained air voids are shown to activate in tandem with cracks initiating from the ITZ, leading to a finer particle size distribution of fragments.
4. Experimental validation suggests the model is useful for predicting dynamic strength. The model is especially useful for determining quite rapidly the potential range in dynamic strengths among materials with varying microstructures. As a comparison, the 1500 simulations used in this paper could be obtained in one day of computer run time, while 15 Kolsky bar samples consumed two days of laboratory testing time. Obtaining the data for histograms shown in Figure 4.16 through Figure 4.18 would take several months if carried out experimentally rather than numerically. Therefore, the model helps interpret the variability of the Kolsky bar tests, and with further development and validation could reduce the need for very large, time-consuming datasets from experimental programs.

5. Air entrainment lowers the static compressive strength and the average dynamic compressive strength. However, the dynamic increase factor (the ratio of dynamic to static strength) increases with increasing air content. High speed images of the failure process suggests that the air entrained mortars first exhibit signs of void consolidation, then hold a load plateau until the cracks fully form through the mortar.
6. Flaws may interact in different ways, resulting in three failure modes. The analysis of the micromechanics model's strength data suggests that larger flaws shift the dynamic strength upwards into the third failure mode.
7. Furthermore, the post-peak plateau regions observed in the Kolsky bar stress-time histories suggest that the damaged material can bear some additional load after failure, possibly after void collapse. With further development, this model may allow the entrained air void system to be engineered to be beneficial to a concrete element subjected to blast or impact loading.

# CHAPTER 5

# POROELASTIC MODELING OF CYCLIC FREEZING AND THAWING IN PORTLAND CEMENT SYSTEMS

This chapter presents a poromechanical model to calculate the evolution of stresses that accumulate in a local "shell" of hydrated cement paste matrix surrounding entrained air voids (Task 3.A.). The objective is to use the model to study the stresses that develop around each entrained air void, where the shell's thickness $L$ is related to the spatial arrangement and capacity of the entrained air voids[5]. Furthermore, the model predicts the amount of water expelled into the entrained air void during freezing. The model can be used to simulate damage evolution in freeze/thaw tests, with the goal to understand the progression of damage in the samples presented in Chapter 3 under cyclic freezing and thawing. This model is anticipated to be a useful tool to isolate the effects of the porespace and the size distribution of entrained air voids when investigating freeze/thaw durability. Furthermore, it will give a theoretical basis rather than a purely experimental basis for the threshold of $\overline{M}$ reported in Chapter 3 (Task 3.B).

## 5.1 Introduction

ASTM C666 describes two relatively rapid laboratory procedures (procedures A and B) to determine a concrete's resistance to cyclic freezing and thawing [137]. In procedure A, the test is conducted on concrete prisms which are completely saturated in water and subjected to a number of freeze/thaw cycles (typically 300 cycles), while in

[5] Note the distinction between shell thickness $L$ and ASTM C457 spacing factor $\overline{L}$

procedure B, the samples are frozen in air and thawed in water. Procedure A has the advantages over procedure B of avoiding the displacement of water during cycles, ensuring a high degree of saturation, and reducing the minimum about of water to be cooled or heated. Therefore, procedure A tends to be more common than procedure B [138]. Both procedures specify that the dynamic Young's modulus should be measured periodically (not exceeding 36 cycles between measurements) throughout the test. A durability factor (DF) is calculated as the ratio between the current dynamic Young's modulus and the initial dynamic Young's modulus. The standard advises that measurement should terminate if the dynamic Young's modulus drops below 60% of its initial value (i.e., DF < 60%). Cyclic freeze/thaw failure is ill-defined by the ASTM C666 standard; however, admixture standards ASTM C260, ASTM C494/C494M, and ASTM C1017/C1017M-07 offer guidance, specifying that the ASTM C666 durability factor of a mixture with and without admixture should not differ by more than 20%. This suggests the critical durability factor should be between 70% or 80%. In this study, failure was determined in this test whenever a specimen's current dynamic Young' modulus decreased below 80% of its initial dynamic Young' modulus.

In this contribution, the damage evolution is hypothesized to arise from tensile stresses which develop due to crystallization pressures acting on the paste, which arise due to freezing, following theory developed by Coussy [139, 140]. As a volume of paste freezes, the liquid in the pore space reaches pressure above atmospheric pressure. Entrained air voids limit this pressure buildup in the still unfrozen pore solution during freezing by acting as expansion reservoirs. The pressure inside the entrained air void is assumed to remain at atmospheric pressure. Therefore, liquid water entering the entrained

air void is no longer confined and instantly freezes. Therefore, liquid in contact with the forming ice crystals must depressurize to satisfy equilibrium between the liquid water and the ice crystals. This causes liquid at a distance to be sucked towards the entrained air void. This suction will continue as long as the air void is not completely filled. It is noted that this suction causes the entrained air void to contract, as was discussed in [140] and observed experimentally in [141]. However, the magnitude of this contraction is considered a second-order effect when calculating the total volumes of entrained air voids after freezing, and has been neglected in this analysis.

However, it has been observed that water will continue to migrate to entrained air voids over time when the concrete is in saturated condition. Extensive work by Fagerlund [142] provides a framework in which to model this observation. The macropores (i.e., pores between 50-10,000 nm in throat diameter; see Table 1.1) will fill quickly due to capillary action. The entrained air voids in a concrete specimen submerged in water will not stay air-filled, but will take up water by a slow air dissolution-diffusion process. In this contribution, this process will be referred to as absorption (adsorption is neglected). Therefore, the entrained air voids in concretes undergoing ASTM C666 testing are likely to absorb water over time, particularly when using procedure A. This absorption may also contribute to damage as progressively larger entrained air voids absorb water, thereby losing their two-fold efficiency as expansion reservoirs and cyropumps and becoming ineffective. These two mechanisms are described in Section 5.2, where Section 5.2.1 describes the mass conservation and flow problem used to develop the evolution of stresses which develop in the periphery of entrained air voids during freezing, and Section 5.2.1.3 describes the absorption of water over time.

## 5.2 Mechanisms

This section presents and overview of the mechanism by which damage is assumed to accumulate in the "shell" surrounding entrained air voids.

### 5.2.1 Hydraulic Pressure

#### 5.2.1.1 Constitutive Relationships

The basic formulation of the problem involves conservation of the mass $m$ of water (in either liquid or crystalline solid state) in the system at every time $t$. A porous medium's initial (undeformed) porosity can be expressed by $\phi_0$. A *saturated* porous solid, wherein the pore space is wholly occupied by either a liquid phase ($L$), an ice crystal phase ($C$), or a combination of the two is considered. The partial porosity of the crystal or liquid phase is related to the initial porosity through the saturation, $S_J$, and the rate of change of phase $J$, $\varphi_J$ (Eq. 5.1). The saturations describe the percentage of the pore space occupied by liquid water or ice crystals, and therefore must sum to unity (Eq. 5.2).

$$\phi_{J=C,L} = S_J \phi_0 + \varphi_J \qquad \text{Eq. 5.1}$$

$$S_C + S_L = 1 \qquad \text{Eq. 5.2}$$

For a linear elastic solid with stress tensor $\boldsymbol{\sigma}$ and linearized strain tensor $\boldsymbol{\varepsilon}$, classical mechanics gives the relationship $\sigma = K\epsilon + 3\alpha\Delta T$, where $K$ is the bulk modulus, $\alpha$ is the coefficient of thermal expansion, $\sigma = \frac{1}{3}\,\mathrm{tr}(\boldsymbol{\sigma})$, and $\epsilon = \mathrm{tr}(\boldsymbol{\varepsilon})$. The $\Delta T$ reflects a temperature change from a reference temperature. In the analysis that follows, the reference temperature will be the melting point of water, $T_m$ (273.15 K).

Thermoporoelasticity extends the state equations by adding terms that account for pressure buildup by matter within the porespace. For a poroelastic solid with a porespace occupied by a combination of liquid water and crystal phases, the state equations are

$$\sigma = K\epsilon - b_C\, p_C - b_L\, p_L - 3\alpha_S K(T - T_m) \qquad \text{Eq. 5.3 a}$$

$$\varphi_C = b_C\, \epsilon + p_C / \mathrm{N}_{CC} + p_L / \mathrm{N}_{CL} - 3\alpha_{\varphi C}(T - T_m) \qquad \text{Eq. 5.3 b}$$

$$\varphi_L = b_L\, \epsilon + p_C / \mathrm{N}_{CL} + p_L / \mathrm{N}_{LL} - 3\alpha_{\varphi L}(T - T_m) \qquad \text{Eq. 5.3 c}$$

where $b_C$ and $b_L$ denote the liquid and crystal Biot coefficients, respectively, $p_C$ and $p_L$ denote the crystal and liquid pressures, respectively, $N_J$ terms denote the Biot moduli, and the subscript $S$ denotes the solid phase.

The mass in the system at any time is the sum of the current density of each phase multiplied by the volume fraction of each phase, expressed by

$$m = \phi_C \rho_C + \phi_L \rho_L \,. \qquad \text{Eq. 5.4}$$

The state equation which governs how the current density $\rho_J$ of phase $J$ ($J = C, L$) varies with liquid pressure $p_J$ and temperature $T$ is given by

$$\frac{1}{\rho_L} = \frac{1}{\rho_L^0}\left[1 - \left(p_L - p_{atm}\right)/ K_L + 3\alpha_S \left(T - T_m\right)\right] \qquad \text{Eq. 5.5}$$

where $\rho_J^0$ is the initial density of phase $J$, $p_L$ is the pressure of phase $J$, $p_{atm}$ is atmospheric pressure, $K_J$ is the bulk modulus of phase $J$, and $\alpha_S$ is the coefficient of thermal expansion for the solid phase. In the analysis that follows, atmospheric pressure will always be taken as the zero reference pressure.

For a certain pore throat radius $\varrho$, the chemical potentials of liquid water and ice can only equilibrate (e.g. $\mu_C = \mu_L$) when the water temperature supercools to some depressed degree $T - T_m$. As supercooling occurs, it is assumed that ice occupies all the

pores with radius greater than $\varrho$, but may not penetrate into smaller pores unless the temperature is further depressed and supercooling breaks the crystal-liquid equilibrium. Using the Gibbs-Duhem equation, one may derive the Thompson equation to relate pressure of a liquid with melting entropy $\Delta S_m$ and melting to the crystal pressure at a given temperature $T$ as

$$p_C - p_L\left(\frac{\rho_C^0}{\rho_L^0}\right) = \Delta S_m\left(T_m - T\right). \qquad \text{Eq. 5.6}$$

The retention curve describes the fraction of the pore space which is saturated by liquid water is $S_L$, and it is dependent on the size distribution of pores. Let the size distribution of pores be described by $F(\varrho)$, which gives the percentage pores with entry radii greater than or equal to $\varrho$. Studies of cement-based materials typically obtain $F(\varrho)$ through porosimetry, a pressure technique whereby the pore size distribution is obtained by injecting a non-wetting fluid into the porous solid saturated with a wetting fluid. In the common case of mercury intrusion porosimetry (MIP), the non-wetting fluid is liquid mercury and the wetting fluid is mercury vapor. It should be noted that the pore structure refines (i.e. less interconnectivity, smaller average pore throat diameter) as water-to-cement ratio decreases [143]. More well-hydrated or mature specimens will also show finer pore structures than their insufficiently cured or earlier age counterparts, although beyond 28 days the MIP curve stabilizes in much the same way that compressive strength approaches its maximum value at around 28 days [143]. The entry radius of the pores, $\varrho$, is related to the capillary pressure, $p_{cap}$, by the Young-Laplace equation:

$$p_{cap} = p_{nW} - p_W = 2\gamma_{nWW}\cos(\theta) / \varrho \qquad \text{Eq. 5.7}$$

where the subscripts $nW$ and $W$ denote the non-wetting and wetting phases, respectively, with known interface energy $\gamma_{nWW}$ and contact angle $\theta$. In the case of ice crystal intrusion

into the saturated hydrated cement paste matrix, the crystal phase is the non-wetting fluid and the liquid water is the wetting phase. The liquid saturation is related to the porosity function by $S_L = 1 - F(\varrho)$. As $F(\varrho)$ is a tail distribution, $S_L$ may be given a probabilistic interpretation as the cumulative distribution function of the pore entry radii. As Eq. 5.7 links the pore radii to the capillary pressure, the size distribution may be expressed as $S_L(p_{cap})$. A well-accepted analytical expression for $S_L$ is based on the work of van Genuchten [144], and is given by

$$S_L = S_r + (1 - S_r)\left[1 + \left(\frac{p_{cap}}{\pi_0}\right)^{\frac{1}{1-m_v}}\right]^{-m_v} \qquad \text{Eq. 5.8}$$

where $S_L$, $m_v$, and $\pi_0$ are adjustable constants related to the material pore structure. Parameter $S_r$ takes into account that as water crystallizes in pores, a liquid like layer of unfrozen water still exists between the ice crystals and the pore wall [145]. Experimental work by Powers and Brownyard [146] showed that liquid water continues to exist in concrete until -78 °C. Since this is far below the maximum freezing temperature of -18 °C used in ASTM C666 tests on hardened concrete, Eq. 5.8 is valid in the range of temperatures explored in this study. The parameters $S_r = 0.085$, $\pi_0 = 0.45$ MPa, and $m_v = 0.41$ will be used for Eq. 5.8, based on [147].

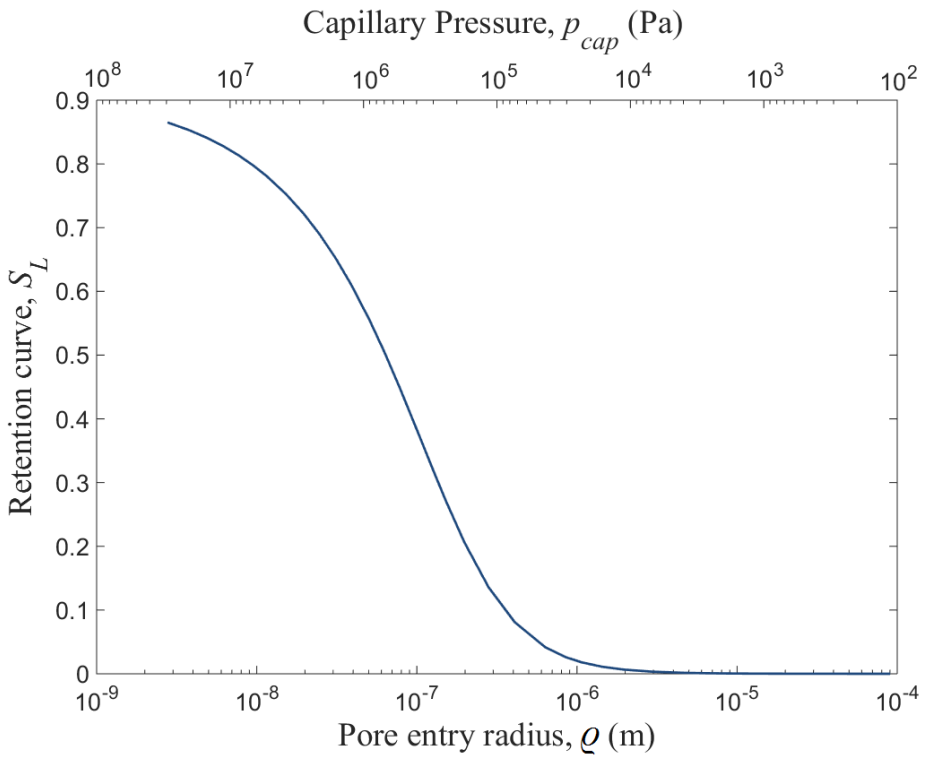


**Figure 5.1**: Retention curve utilized in this study versus pore entry radius (bottom) and capillary pressure (top)

From Eq. 5.7, the size distribution may be expressed as $F(p_{cap})$. Since the size distribution is an intrinsic property of the porous solid, the capillary pressure arising from Eq. 5.7 is a property of the morphology of the pore space, and may be calculated for any $\gamma_{nww}$ and $\theta$. By utilizing the Thompson equation (Eq. 5.6) one obtains the retention curve as, $S_L(p_L)$, with

$$p_{cap} + p_L\left(1-\frac{\rho_C^0}{\rho_L^0}\right) = \Delta S_m\left(T_m - T\right). \qquad \text{Eq. 5.9}$$

At a given temperature $T$, $p_{cap}$ can be related to pore radii by Eq. 5.7. Since the intruding ice crystal is assumed to be hemispherical, $\theta$ is taken to be zero [148].

5.2.1.2 Simplifying Assumptions

In order to proceed, the following assumptions are made:

(I) Using the approximation that $1/(1 + x) \approx 1 - x$ for $x \ll 1$, Eq. 5.5 may be inverted:

$$\rho_J = \rho_J^0\left[1+\frac{p_J}{K_J}-3\alpha_J\left(T_m-T\right)\right]$$

under the condition that $p_J/K_J \ll 1$ and $\alpha_J(T - T_m) \ll 1$.

(II) Restricting analysis to water, bulk moduli $K_L$ = 2200 MPa and $K_C$ = 8800 MPa. Since the melting entropy of water is $\Delta S_m$ = 1.2 MPa $K^{-1}$, the contributions of any term weighted by $\Delta S_m(T - T_m)$ divided by a bulk modulus may be discarded.

(III) The orders of magnitude of coefficients of thermal expansion $\alpha_J$ are $10^{-5}$ $K^{-1}$, so terms weighted by $\alpha_J(T - T_m)$ may be discarded.

(IV) Similar order of magnitude analysis may allow any term weighted by $b_J\sigma\rho_J^0/K_J$ to be neglected

Combining the mass in the system described by Eq. 5.4 with the saturation terms in Eq. 5.1 and Eq. 5.2 yields

$$m = \sum_{J=C,L}\left[\phi_0 S_J\rho_J + \varphi_J\rho_J\right]. \qquad \text{Eq. 5.10}$$

From assumption (I), Eq. 5.10 can be written as

$$m = \sum_{J=C,L}\left[\phi_0 S_J\rho_J^0 + \phi_0 S_J\rho_J^0\left(\frac{p_J}{K_J}-3\alpha_J\left(T-T_m\right)\right)+\varphi_J\rho_J\right]. \qquad \text{Eq. 5.11}$$

Neglecting thermal terms per assumption (III),

$$m = \sum_{J=C,L}\left[\phi_0 S_J\rho_J^0 + \phi_0 S_J\rho_J^0\left(\frac{p_J}{K_J}\right)+\varphi_J\rho_J\right]. \qquad \text{Eq. 5.12}$$

Substituting Eq. 5.1 into Eq. 5.12 gives

$$m = \phi_0 \rho_L^0 + \phi_0 S_C \left( \rho_C^0 - \rho_L^0 \right) + \sum_{J=C,L} \left[ \phi_0 S_J \rho_J^0 \left( \frac{p_J}{K_J} \right) + \varphi_J \rho_J \right]. \qquad \text{Eq. 5.13}$$

Directing attention to the $\varphi_J \rho_J$ terms, assumption (III) allows state equation Eq. 5.3 a to be written as

$$\epsilon = \sigma / K - b_C \, p_C / K - b_L \, p_L / K \, . \qquad \text{Eq. 5.14}$$

Substituting Eq. 5.14 into the state equations gives

$$\varphi_J = \frac{b_J \sigma}{K} + p_J \left( \frac{b_J^2}{K} + \frac{1}{N_{JJ}} \right) + p_I \left( \frac{b_J b_I}{K} + \frac{1}{N_{JI}} \right), \; I \neq J \qquad \text{Eq. 5.15}$$

Noting the relative order of magnitude of the Biot terms and the solid bulk modulus ($K >$ 20,000 MPa for cement paste), all but the leading term may be neglected. Assumption (I) and (III) give

$$\varphi_J \rho_J = \frac{b_J \sigma \rho_J^0}{K} \left( 1 + \frac{p_J}{K_J} \right). \qquad \text{Eq. 5.16}$$

Therefore, assumption (IV) allows terms in the form $\varphi_J \rho_J$ to be neglected, a reasonable assumption in light of the poor compressibility of the porous solid compared with that of water. Substituting Eq. 5.6 into Eq. 5.14 gives

$$m = \phi_0 \rho_L^0 + \phi_0 S_C \left( \rho_C^0 - \rho_L^0 \right) + \phi_0 S_C \rho_C^0 \frac{(\rho_C^0 / \rho_L^0) p_L - \Delta S_m (T_m - T)}{K_C} + \frac{\phi_0 S_L \rho_L^0}{K_L} p_L \, . \qquad \text{Eq. 5.17}$$

From assumption (II), the $\Delta S_m (T - T_m) / K_C$ term is eliminated to form

$$m = \phi_0 \rho_L^0 + p_L \phi_0 \rho_L^0 \left( \frac{S_C}{K_C} \left( \frac{\rho_C^0}{\rho_L^0} \right)^2 + \frac{S_L}{K_L} \right) - S_C \phi_0 \left( \rho_L^0 - \rho_C^0 \right) + \phi_0 \rho_L^0 \, . \qquad \text{Eq. 5.18}$$

Noting that $(\rho_C^0 / \rho_L^0)^2 \approx 1$, the mass in the system may finally be expressed as

$$m = p_L \phi_0 \rho_L^0 \left( \frac{S_C}{K_C} + \frac{S_L}{K_L} \right) - S_C \phi_0 \left( \rho_L^0 - \rho_C^0 \right) + \phi_0 \rho_L^0 . \qquad \text{Eq. 5.19}$$

Darcy's law provides the relationship between the spatial variable $r$ and time variable $t$. The water continuity equation, which expresses the mass conservation of water in the system is

$$\frac{dm}{dt} = -\rho_L^0 \nabla \cdot \underline{q}_L = \phi_0 \rho_L^0 \frac{\kappa}{\eta_L} \frac{1}{r^2} \frac{\partial}{\partial r} \left( k_{rL}(S_L) r^2 \frac{\partial p_L}{\partial r} \right) \qquad \text{Eq. 5.20}$$

Where $\kappa$ is the intrinsic permeability and $\eta_L$, is the viscosity of the liquid. The relative permeability, $k_{rL}(S_L)$, is a function that relates accounts for decreased permeability as the solids nucleate in the porespace. Using the expression by van Genuchten, the relative permeability is

$$k_{rL}(S_L) = \sqrt{S_L} \left[ 1 - \left( 1 - S_L^{\frac{1}{m_v}} \right)^{m_v} \right]^2 \qquad \text{Eq. 5.21}$$

where $m_v$ is the same parameter used in Eq. 5.8. Substitution of Eq. 5.19 into Eq. 5.20 yields

$$\frac{\partial}{\partial t} \left[ S_C \left( \rho_C^0 - \rho_L^0 \right) \right] + \frac{\partial}{\partial t} \left[ \left( \frac{S_C}{K_C} + \frac{S_L}{K_L} \right) p_L \rho_L^0 \right] = \rho_L^0 \frac{\kappa}{\phi_0 \eta_L} \frac{1}{r^2} \frac{\partial}{\partial r} \left( k_{rL}(S_L) r^2 \frac{\partial p_L}{\partial r} \right) \qquad \text{Eq. 5.22}$$

where relationships between $S_C$ and $S_L$ are established in Eq. 5.2. and between $p_L$, $p_{cap}$, and $S_L$ by Eq. 5.8 and Eq. 5.9. The temperature is related to time by $T = T_m - \mathring{T}t$, where $\mathring{T}$ is a constant cooling rate. The cooling rate was adapted from ASTM C666, which prescribes that lowering the temperature from 4 to -18°C should be conducted in not less than 2 hours and not more than 5 hours [137]. For this study, $\mathring{T}$ = 5 K/hr. After obtaining a solution to Eq. 5.22, the mean pore pressure in the shell is calculated using

$$p_M = \langle S_L p_L + S_L p_C \rangle = \frac{3}{4\pi\left((\mathcal{R}+L)^2 - \mathcal{R}^2\right)} \int_{\mathcal{R}}^{\mathcal{R}+L} 4\pi\xi^2 \left(S_L p_L + S_L p_C\right) d\xi \qquad \text{Eq. 5.23}$$

5.2.1.3 Boundary Conditions

Consider an entrained air void with radius $\mathcal{R}$ (see Figure 5.2a). Air void radii may be derived from a size distribution $f(\mathcal{R})$, as discussed in Chapter 3. The poroelastic problem is approached by calculating the evolution of stresses within a shell of thickness $L$ around an air void. Consider an element of porous solid at a distance $r$ from the center of the air void, where $\mathcal{R} \leq r \leq (\mathcal{R} + L)$. At the surface of the air void, the liquid is in contact with ice that has crystallized where $p_C = 0$. According to the Thompson equation, the liquid must therefore depressurize to meet liquid-crystal equilibrium. At distance $L$ from the air void's surface the liquid pressure is constant. Formally, these boundary conditions are

$$p_L\big|_{r=\mathcal{R}} = -\left(\frac{\rho_L^0}{\rho_C^0}\right)\Delta S_m (T_m - T) \quad \text{and} \quad \left.\frac{\partial p_L}{\partial r}\right|_{r=\mathcal{R}+L} = 0\,. \qquad \text{Eq. 5.24}$$

The maximum pressure will occur at the edge of the shell, or at $r = (\mathcal{R}+L)$, so $p_{max}$ is obtained by evaluating the saturation and pressure terms at the boundy of the shell:

$$p_{\max} = \left(S_L p_L + S_L p_C\right|_{\mathrm{R}+L}\,. \qquad \text{Eq. 5.25}$$

The porous solid surrounding the entrained air void consists of a solid matrix and porespace that is completely saturated with liquid water at time $t_0$, as in Figure 5.2b. As time increases and temperature decreases at a constant cooling rate, ice crystals begin to form in larger pores, as depicted in Figure 5.2c. The parameters necessary to solve the mass conservation problem in Eq. 5.22 in conjunction with Eq. 5.8 and Eq. 5.9 are listed in Table 5.1.

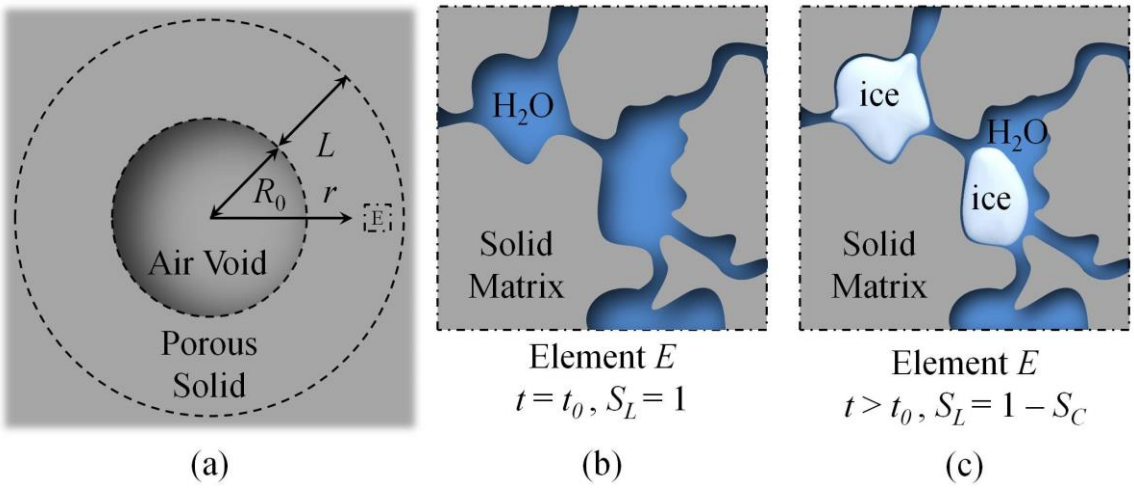


**Figure 5.2:** (a) Environment around an entrained air void with radius $\mathcal{R}$. Element *E*, at a distance *r* from the void's centroid, is shown (b) at the initial time and (c) at a time after ice nucleation has commenced.

**Table 5.1:** Parameters for poroelastic model

| Variable | Value | Unit | Significance | Source |
|---|---|---|---|---|
| $\kappa$ | $10^{-20}$ | $m^2$ | Intrinsic permeability | Ref. [3] |
| $\phi_0$ | 0.22 | - | Porosity | VCCTL |
| $K_C$ | 8.8 | MPa | Bulk modulus of ice | Ref. [140] |
| $K_L$ | 2.2 | MPa | Bulk modulus of liquid | Ref. [140] |
| $m_v$ | 0.41 | - | Van Genuchten parameter | Ref. [147] |
| $S_r$ | 0.085 | - | Van Genuchten parameter | Ref. [147] |
| $\pi_0$ | 0.45 | MPa | Van Genuchten parameter | Ref. [147] |
| $\rho_C^0$ | 916.7 | kg/ $m^3$ | Initial mass density, ice crystals | Ref. [149] |
| $\rho_L^0$ | 998.2 | kg/ $m^3$ | Initial mass density, liquid water | Ref. [149] |
| $\Delta S_m$ | 1.2 | MPa/K | Melting entropy of ice | Ref. [140] |
| $T_m$ | 273.15 | K | Melting point of water | Ref. [140] |
| $\mathring{T}$ | 5 | K/hr | Cooling rate | N/A |
| $\eta$ | $1.79 \times 10^{-3}$ | Pa/s | Viscosity of water | Ref. [140] |

* For a *w*/*c* = 0.45 cement paste hydrated under saturated, sealed conditions for 28 days

5.2.1.4 Mass Expelled Due to Flow

As freezing occurs, a mass of water is expelled into the shell. The mass of liquid in the shell initially $m_s$ is

$$m_s = \phi_0 \rho_L^0 V_s . \quad \text{Eq. 5.26}$$

where $V_s$ is the volume of the shell of thickness $L$ surrounding and air void of radius $\mathcal{R}$. As freezing occurs, the mass of fluid in the shell is

$$m_s = \phi_0 \rho_C^0 S_C V_s + \phi_0 \rho_L^0 (1 - S_C) V_s . \quad \text{Eq. 5.27}$$

which accounts for the presence of ice in the shell. The mass of liquid water expelled into the shell $m_{exp}$ is

$$m_{exp} = \left(\rho_L^0 - \rho_C^0\right) \phi_0 S_C V_s . \quad \text{Eq. 5.28}$$

The volume that this expelled water occupies (as ice) is

$$V_{exp} = \left( \left( \frac{\rho_L^0}{\rho_C^0} \right) - 1 \right) \phi_0 S_C V_s . \quad \text{Eq. 5.29}$$

Clearly, it is important that the volume of an entrained air void $V_{void}$ exceeds the volume expelled (i.e., $V_{void} > V_{exp}$), or else the air void has become full of ice and loses its effectiveness.

### 5.2.2 Absorption

In [142], Fagerlund explains that although the capillary porosity (i.e., pores smaller than roughly 10,000 nm or 10 μm) of cement paste fills relatively quickly due to capillary action, the entrained air voids will slowly become water-filled as the air in the entrained air void diffuses into the water in the pore space by

$$V_{abs} = \left( \frac{q'}{\rho_{air}^{0}} \right) t \qquad \text{Eq. 5.30}$$

where $\rho_{air}^{0}$ is the mass density of air (1.25 kg/m$^3$) and $q'$ is the flux of air, with units of mass per unit time. Fagerlund used the term "absorption" to describe this phenomenon, although it is acknowledged that the mechanism is different than the manner in which the term absorption is classically defined in the literature pertaining to cement-based materials. Herein, the term "absorption" will be used to describe the phenomena described by Eq. 5.30. The value of $q'$ is dependent on the bulk diffusivity of air in pore water, the solubility of air, the surface tension of water, and the general size of the system. Many of these factors are poorly defined for air in pore water. In these studies, is on the order of $10^{-18}$ – $10^{-22}$ kg/s, due to the fact that the diffusivity of air in pore water is probably much higher than the bulk diffusivity of air in water, and that all of these factors are temperature dependent, meaning the entire flux will slow as temperature approaches -18°C for the simulations of cyclic freeze/thaw tests.

The preceding discussion of absorption is described schematically in Figure 5.3. The initial system is described in Figure 5.3a. Before a specimen of air entrained concrete is submersed in water, the system is idealized as being empty of water (although, in reality, the capillary pores are likely to contain some level of residual pore water). Solid space is denoted by the light gray region, while the voidspace consisting of the capillary pores and the entrained air void are represented by a dark gray region. Note that the pore space is not intended to be drawn to scale relative to the entrained air void itself. After the sample has been submerged in water, the system is represented by Figure 5.3b, where the pore space will fill with water rather quickly due to capillary action. The saturated pores

are represented in blue. Note that the schematic in Figure 5.3b recalls the assumption that the pore space is saturated, as detailed in Figure 5.2b. As air slowly departs the entrained air void according to Eq. 5.30, it is replaced by water, which is referred to as the "absorbed" water in Figure 5.2c. The volume represented as dark gray in Figure 5.2c is still available as an expansion reservoir for freeze/thaw action until such a time as the entire air void becomes full of absorbed water.

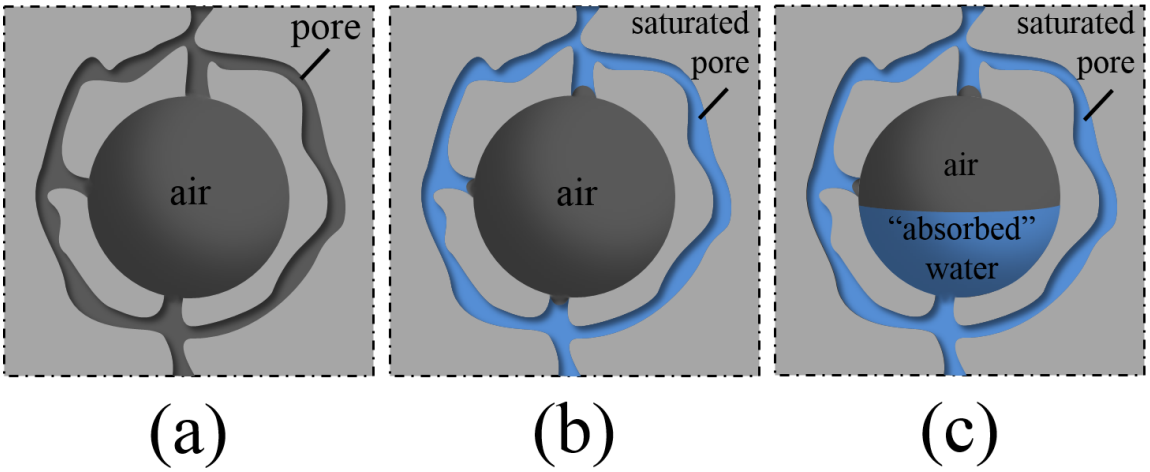


**Figure 5.3:** Schematic depecting capillarity and diffusion

Fagerlund proposed two models for absorption of water by air voids. In Model 1, all of the entrained air voids were assumed to immediately take in water at the same rate. In Model 2, entrained air voids were assumed to absorb water in order of size, such that a size class of entrained air voids saturates completely before the next largest size class of entrained air voids begin absorbing water. Model 2 was argued to be more thermodynamically feasible, and both numerical and experimental results in [142] confirmed that Model 2 better reflects the time scale in which a typical entrained air void system in a submerged concrete specimen absorbs water. Therefore, Model 2 has been

adopted herein, where $V_{abs}$ is distributed to the entrained air voids in order of increasing size.

## 5.3 Model System

For simplicity, four classes of entrained air voids are chosen to model the entrained air void systems of Chapter 3. Since this investigation constitutes a rather first-order analysis of a complex physical problem, it is reasonable to reduce the system to be manageable. A unique size distribution $f(\mathcal{R}_i)$ for this system of four size classes can be chosen to be representative of the material systems in Chapter 3. Each probability $f(\mathcal{R}_i)$ can be calculated such that each distribution of voids preserves the moments of the actual size distribution calculated for the concretes in Chapter 3 by the following equation:

$$\begin{bmatrix} 1 & 1 & 1 & 1 \\ \mathcal{R}_1 & \mathcal{R}_2 & \mathcal{R}_2 & \mathcal{R}_4 \\ \mathcal{R}_1^2 & \mathcal{R}_2^2 & \mathcal{R}_3^2 & \mathcal{R}_4^2 \\ \mathcal{R}_1^3 & \mathcal{R}_2^3 & \mathcal{R}_3^3 & \mathcal{R}_4^3 \end{bmatrix} \begin{Bmatrix} f(\mathcal{R}_1) \\ f(\mathcal{R}_2) \\ f(\mathcal{R}_3) \\ f(\mathcal{R}_4) \end{Bmatrix} = \begin{Bmatrix} 1 \\ \langle \mathcal{R} \rangle \\ \langle \mathcal{R}^2 \rangle \\ \langle \mathcal{R}^3 \rangle \end{Bmatrix} \qquad \text{Eq. 5.31}$$

where $\langle \mathcal{R}^k \rangle$ ($k$ = 1,2,3) are the target moments from the actual size distributions calculated in Chapter 3, $\mathcal{R}_i$ ($i$ = 1,2,3,4) are the size classes of air voids included in this chapter, and $f(\mathcal{R}_i)$ are their respective probabilities of occurrence. From equation Eq. 5.31, it is evident that four sizes classes of entrained air voids are the minimum required to preserve the three moments and enforce that the sum of $f(\mathcal{R}_i)$ is equal to unity. The four size classes were chosen to be representative of the size classes observed in an actual distribution of entrained air voids. The sizes are listed in Table 5.2. The smallest void class is 10 μm. This lower limit is justified because it approximately corresponds to the smallest size class of entrained air voids that can be resolved by the image analysis

technique outlined in Chapter 3. Intermediate size classes of 25 μm and 65 μm were chosen to be representative of the majority of the size distributions without over representing the smallest classes of voids. Figure 5.4 shows the size distributions of all the entrained air void systems investigated in Chapter 3. While the percentile value for each entrained air void class varies slightly between distributions, on average, entrained air voids of radii sizes 10 μm, 25 μm, and 65 μm approximately correspond to the 30$^{th}$, 80$^{th}$, and 99$^{th}$ percentiles of each distribution, respectively. Finally, the fourth size class was chosen such that Eq. 5.31 yielded strictly non-negative values of $f(\mathcal{R}_i)$ since a negative probability of occurrence for any particular size class is unrealistic and meaningless. While it is evident from Figure 5.4 that voids with radii larger than 65 μm occur with quite small probability, they do indeed occur. Since the volume that an entrained air void occupies scales cubically with its radius, these larger classes of voids contribute to the total volume fraction of air in the paste even though they occur relatively infrequently compared to the smaller entrained air voids. Furthermore, the absolute largest entrained air voids observed in every system exceeded 1.5 mm in radius.

**Table 5.2:** Size classes of air voids for investigation

| Radius | Size (μm) |
|---|---|
| $\mathcal{R}_1$ | 10 |
| $\mathcal{R}_2$ | 25 |
| $\mathcal{R}_3$ | 65 |
| $\mathcal{R}_4$ | 240 |

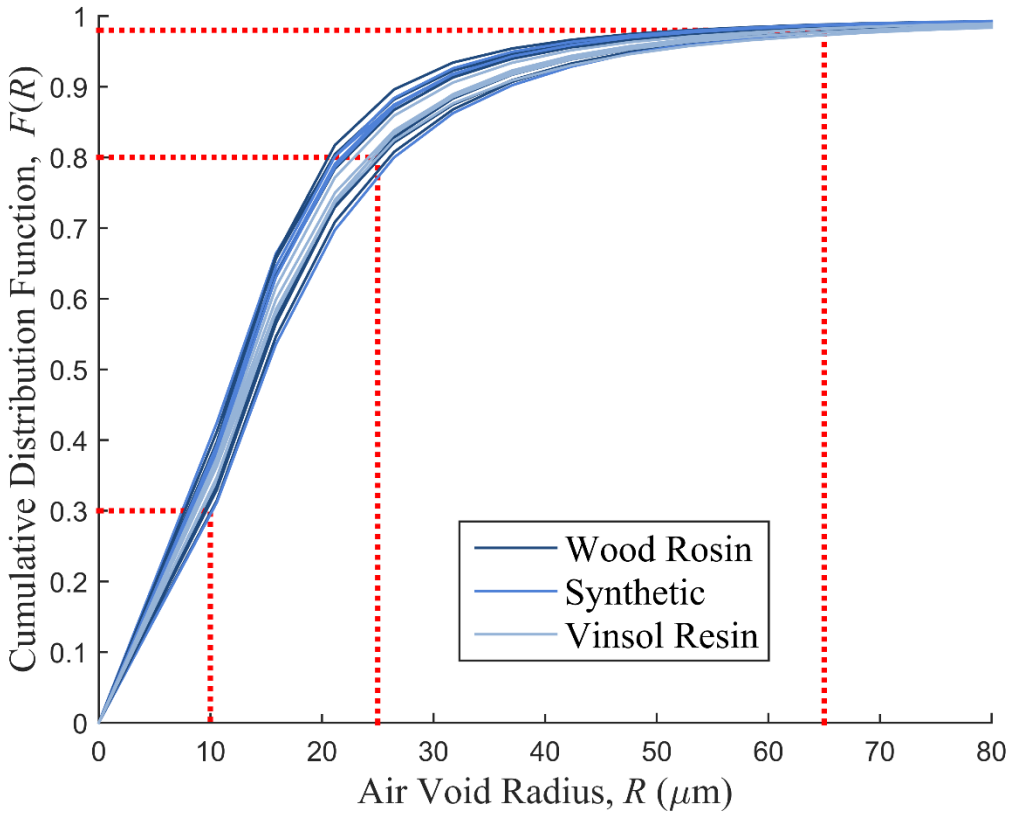


**Figure 5.4:** Full cumulative distribution functions of entrained air void systems, with corresponding probabilities for size classes 1, 2, and 3.

Because these simplified systems of four air voids have the same moments as the actual systems investigated previously, they will have the same paste volume fraction $\hat{\phi}_{air}$ and paste number density $\hat{\rho}_{air}$ as those systems because

$$\hat{\phi}_{air} = \frac{4}{3}\pi\hat{\rho}_{air}\left\langle \mathcal{R}^3 \right\rangle . \qquad \text{Eq. 5.32}$$

Since the surface area of entrained air voids per unit volume of paste $\hat{s}_{air}$ is described by

$$\hat{s}_{air} = 4\pi\hat{\rho}_{air}\left\langle \mathcal{R}^2 \right\rangle , \qquad \text{Eq. 5.33}$$

these simplified systems have the same surface area per unit volume as the systems in Chapter 3 as well. Finally, since $\hat{\phi}_{air}$, $\hat{\rho}_{air}$, and $\left\langle \mathcal{R}^k \right\rangle$ ($k$ = 1,2,3) are necessary to define $\overline{M}$ and $\hat{\phi}_{air}$ and $\hat{s}_{air}$ are necessary to define $\overline{L}$, both spacing factors $\overline{M}$ and $\overline{L}$ are preserved as well. Therefore, these simplified systems can be directly compared to the experimental results.

The initial values for shell thickness $L$ are determined such that the volume fraction is preserved. Assuming that the shrinkage in the system is a higher-order effect, the volume fraction of the hydrated cement paste in the matrix is

$$\hat{\phi}_{HCP} = \frac{4}{3}\pi\hat{\rho}_{air}\left\langle \left(\mathcal{R}+L\right)^3 - \mathcal{R}^3 \right\rangle = \frac{\left\langle \left(\mathcal{R}+L\right)^3 - \mathcal{R}^3 \right\rangle}{\left\langle \left(\mathcal{R}+L\right)^3 \right\rangle}. \qquad \text{Eq. 5.34}$$

The initial value of for the shell thickness $L_{init}$ is chosen such that the volume fraction of air voids is preserved by the following expression:

$$\hat{\phi}_{air} = \frac{\left\langle \mathcal{R}^3 \right\rangle}{\left\langle \left(\mathcal{R}+L_{init}\right)^3 \right\rangle}. \qquad \text{Eq. 5.35}$$

Figure 5.5 compares the value of the shell thickness two the two spacing factors. From Figure 5.5a, it appears that $L$ scales fairly linearly with $\overline{M}$, and is on the same order of magnitude. From Figure 5.5b, a general linear trend is observed as $L$ varies with $\overline{L}$. However, the scatter is much greater, and $\overline{L}$ is on a different order of magnitude than the shell thickness.

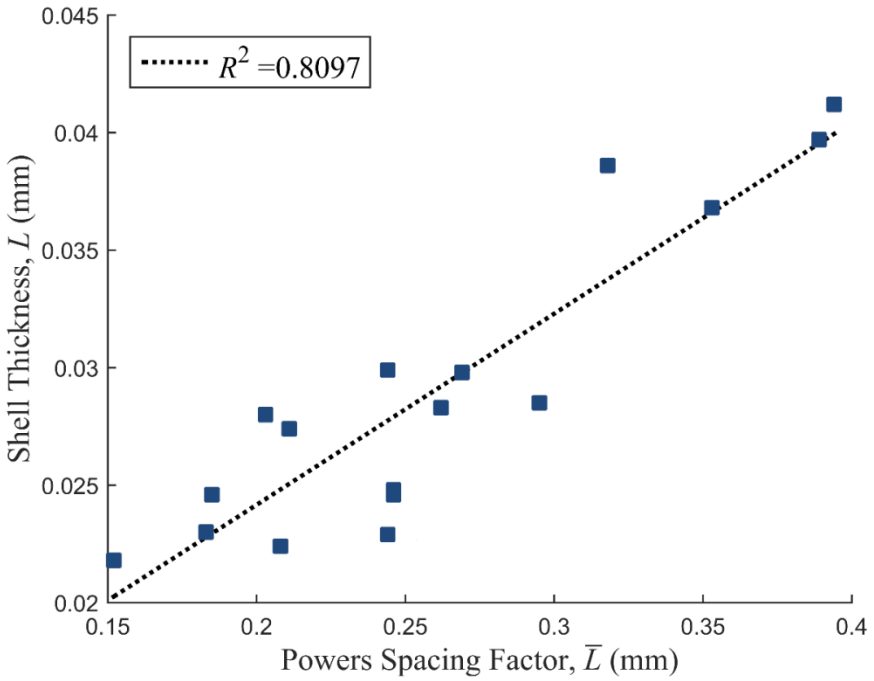


(a)

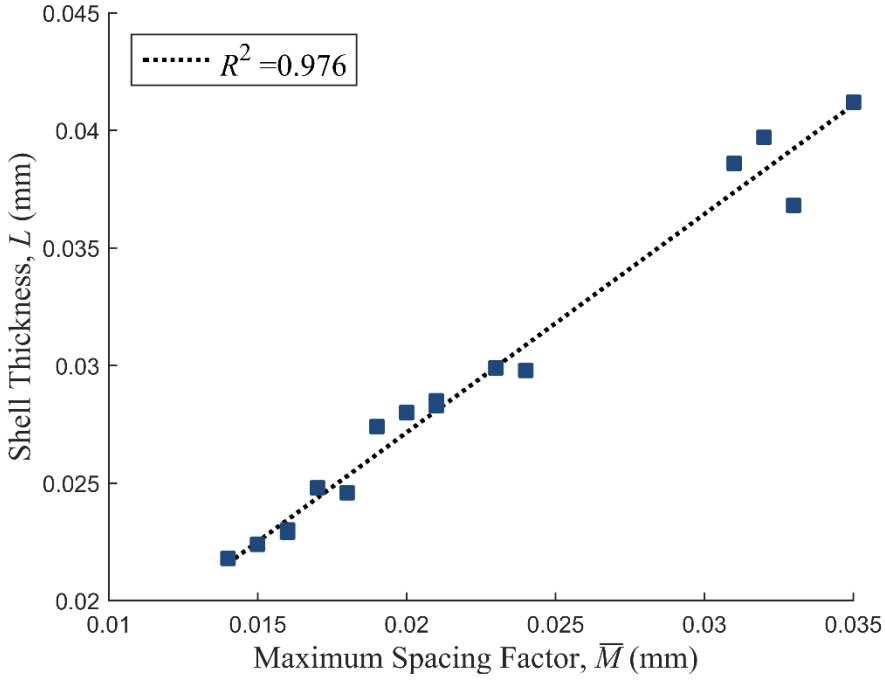


(b)

**Figure 5.5:** Shell thickness versus (a) Powers spacing factor and (b) maximum spacing factor

As water is expelled from the pore space in the shells surrounding entrained air voids due to freezing, it is conceivable that some entrained air voids may completely saturate. This is especially true if time-dependent absorption is considered. If this is the case, then using the central differential equation for the saturations and pressures in the shells (Eq. 5.22) for such saturated entrained air voids is unphysical. Therefore, the shell thicknesses must redistribute. In this first-order treatment, the shell thickness is assumed to be redistributed based on the proportion of the mass of water in the entrained air void which is in excess of the mass of water which is expelled from the shell during freezing. The initial volume of hydrated cement paste associated with voids of size class *i* is

$$\hat{\phi}_{HCP,init}^{(i)} = \frac{f(\mathcal{R}_i)\left(\left(\mathcal{R}_i + L_{init}\right)^3 - \mathcal{R}_i^3\right)}{\left\langle\left(\mathcal{R} + L_{init}\right)^3\right\rangle}. \qquad \text{Eq. 5.36}$$

At each point in time, the volume of water $V_W$ in entrained air voids of class *i* is

$$V_W^{(i)} = V_{abs}^{(i)} + V_{exp}^{(i)}. \qquad \text{Eq. 5.37}$$

where $V_{exp}$ is determined by Eq. 5.29 and $V_{abs}$ is determined by Eq. 5.30. If the volume of water entering an entrained air void does not exceed the volume of the entrained air void, then there is no need to redistribute the shell thicknesses. However, if the volume of water entering an entrained air void exceeds the capacity of the entrained air void, it becomes necessary to redistribute the shell thicknesses. The volume of water in excess of what entrained air voids of size class *i* can accommodate is

$$V_{exc}^{(i)} = \left\{V_W^{(i)} - V_{void}^{(i)}\right\}, \qquad \text{Eq. 5.38}$$

where $V_{void}^{(i)}$ is the volume of an entrained air void with radius $\mathcal{R}_i$ and $\{\cdot\}$ are the Macaulay brackets. If $V_{exc}^{(i)}$ greater than zero for any entrained air void size classes *i*, the shell

thicknesses must decrease. Therefore, the volume fraction of paste occupied by these shells $\hat{\phi}_{HCP}^{(i)}$ must also decrease according to

$$\hat{\phi}_{HCP}^{(i)} = \left\{ \hat{\phi}_{HCP,init}^{(i)} - \hat{\phi}_{HCP,init}^{(i)} \frac{V_{exc}^{(i)}}{V_{exp}^{(i)}} \right\} \qquad \text{Eq. 5.39}$$

where the Macaulay brackets enforce that the shell volume fraction is non-negative. The other shell thicknesses of the larger voids for which $V_{exc}$ is still equal to zero must increase to offset the fact that the shells surrounding smaller entrained air voids have decreased in thickness. Therefore, the volume fraction of HCP is preserved. This is expressed by

$$\hat{\phi}_{HCP}^{(i)} = \hat{\phi}_{HCP,init}^{(i)} + \sum_{j=1}^{i-1} \hat{\phi}_{HCP,init}^{(j)} \frac{V_{exc}^{(i)}}{V_{exp}^{(i)}} \frac{\hat{\phi}_{HCP,init}^{(i)}}{\sum_{k=j}^{4} \hat{\phi}_{HCP,init}^{(k)}} \qquad \text{Eq. 5.40}$$

where $\hat{\phi}_{HCP,init}^{(i)}$ is calculated by Eq. 5.36 and water volumes $V_{exp}^{(i)}$ and $V_{exc}^{(i)}$ are determined by Eq. 5.29 and Eq. 5.38, respectively. Finally, the new shell thicknesses surrounding entrained air voids of size class *i* can be calculated by

$$L_{new}^{(i)} = \sqrt[3]{\frac{3\hat{\phi}_{HCP}^{(i)}}{4\pi\hat{\rho}_{air}} + \mathcal{R}_i^3} - \mathcal{R}_i \,. \qquad \text{Eq. 5.41}$$

Figure 5.6 describes the process of shell redistribution and ice ingress into the entrained air voids schematically. In Figure 5.6a, the porous solid space is denoted by the light gray region, and the entrained air voids are denoted by the dark gray spheres. Three types of entrained air voids are shown for simplicity, with radii $\mathcal{R}_1$, $\mathcal{R}_2$, and $\mathcal{R}_3$. The shell thickness *L* in Figure 5.6a is exactly equal to the shell thickness *Linit* described in Eq. 5.35, and is constant for all three sizes of air voids in the figure. Figure 5.6b represents the effects of freezing, where water has been expelled into the entrained air voids by

freezing and has become ice (the ice crystals forming inside entrained air voids are represented by white ellipsoids). At freezing temperatures, any water that has been absorbed by the mechanism described in Section 5.2.2 also crystallizes into ice, so the mechanism described by Figure 5.6 holds true whether or not absorption is considered in the model. In Figure 5.6b, the shell thicknesses have redistributed according to Eq. 5.41, and are denoted by $L_1$, $L_2$, and $L_3$ corresponding to entrained air voids with radii $\mathcal{R}_1$, $\mathcal{R}_2$, and $\mathcal{R}_3$, respectively. As long as no size class of entrained air voids becomes completely ice-filled, the system represented by Figure 5.6b will continue for the duration of the simulation of the ASTM C666 test (i.e., for as many freeze/thaw cycles considered by the model). However, if a size class of entrained air voids becomes completely filled with ice (e.g., due to the slow absorption phenomenon), then the shells surrounding larger air voids will enlarge and will serve as expansion reservoirs for a larger volume of hydrated cement paste. In Figure 5.6c, the size class of entrained air voids with radius $\mathcal{R}_1$ have become filled with ice, and therefore can no longer serve as expansion reservoirs. Thus, shell thickness $L_1$ goes to zero, and $L_2$ and $L_3$ continue to grow according to equation Eq. 5.41.

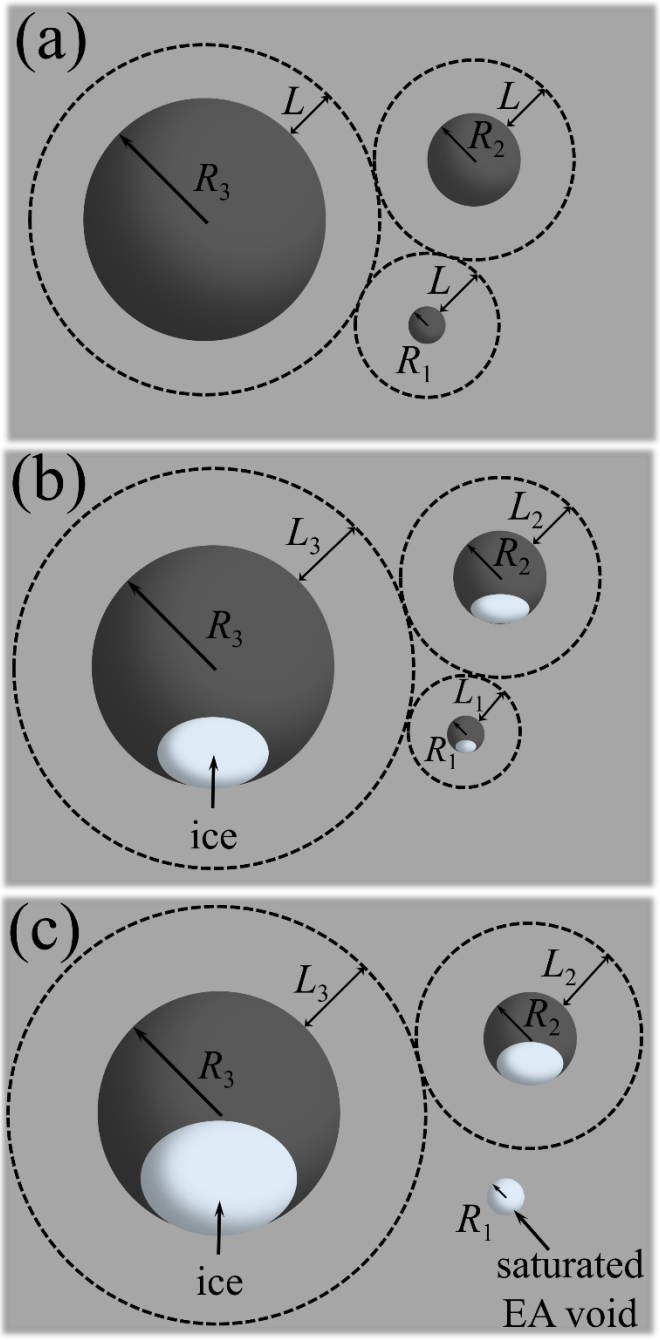


**Figure 5.6:** Schematic describing shell redistribution. In (a), shell thickness $L = L_{init}$ is constant for all voids, according to Eq. 5.35. In (b), freezing begins, ice forms in air voids, and shell thicknesses redistribute according to Eq. 5.41. In (c), some air void classes saturate completely with ice, resulting in zero shell thickness

## 5.4 Results and Discussion

The mass conservation problem (Eq. 5.22 in conjunction with Eq. 5.8 and Eq. 5.9) was solved using the parameters listed in Table 5.1. The temperature is related to time by $T = T_m - \mathring{T}t$, where $\mathring{T}$ is a constant cooling rate. The cooling rate was adapted from ASTM C666, which prescribes that lowering the temperature from 4 to -18°C should be conducted in not less than 2 hours and not more than 5 hours [136]. For this study, $\mathring{T} = 5$ K/hr. After obtaining a solution to Eq. 5.22, the mean pressure $p_M$ from Eq. 5.23 can be evaluated. First, the results of Eq. 5.23 will be presented for arbitrary shell thicknesses surrounding a single entrained air void for each air void radius listed in Table 5.2. Next, the results are presented for entire systems of entrained air voids, where the shells are distributed according to the theory described by Eq. 5.39 – Eq. 5.41. In Section 5.4.1, the results are presented assuming *no absorption* is occurring (i.e., the flux of air in Eq. 5.30 is assumed to be zero). In Section 5.4.2, the results are presented for varying rates of air flux, representing progressively faster rates of air movement away from the entrained air voids. In Section 5.4.3, theoretical entrained air void systems are generated for varying paste air contents and size distributions. Section 5.4.3 allows for a direct comparison between $\overline{M}$ and $\overline{L}$ as indicators of freeze/thaw durability. Additionally, it provides a framework toward engineering an optimum entrained air void system for adequate freeze/thaw resistance. In Section 5.4.4, an example of this potential to optimize an entrained air void system is presented based on the recommendations Chapter 4 for optimizing dynamic compressive strength of air entrained concretes.

In Figure 5.7, the mean pressure is plotted as a function of shell thickness for each of the four size classes of air voids. The curves have been truncated at whichever

thickness causes the volume of water expelled as ice during freezing to fill the shell completely (e.g., for void class $\mathcal{R}$ = 65 μm, a shell thickness in excess of 191 μm will theoretically saturate the void entirely with ice). It is noted that Figure 5.7 shows the analytical results of the flow equations, which assume the solid material is stiffer than the water in the pore space. As the shell thickness surrounding void with radii $\mathcal{R}$ = 65 μm and $\mathcal{R}$ = 240 μm increases, the pressures calculated by E. 5.23 are large, well in excess of the material's static compressive strength. As will be detailed later in the discussion, the large theoretical pressures in Figure 5.7 are not used in practice.

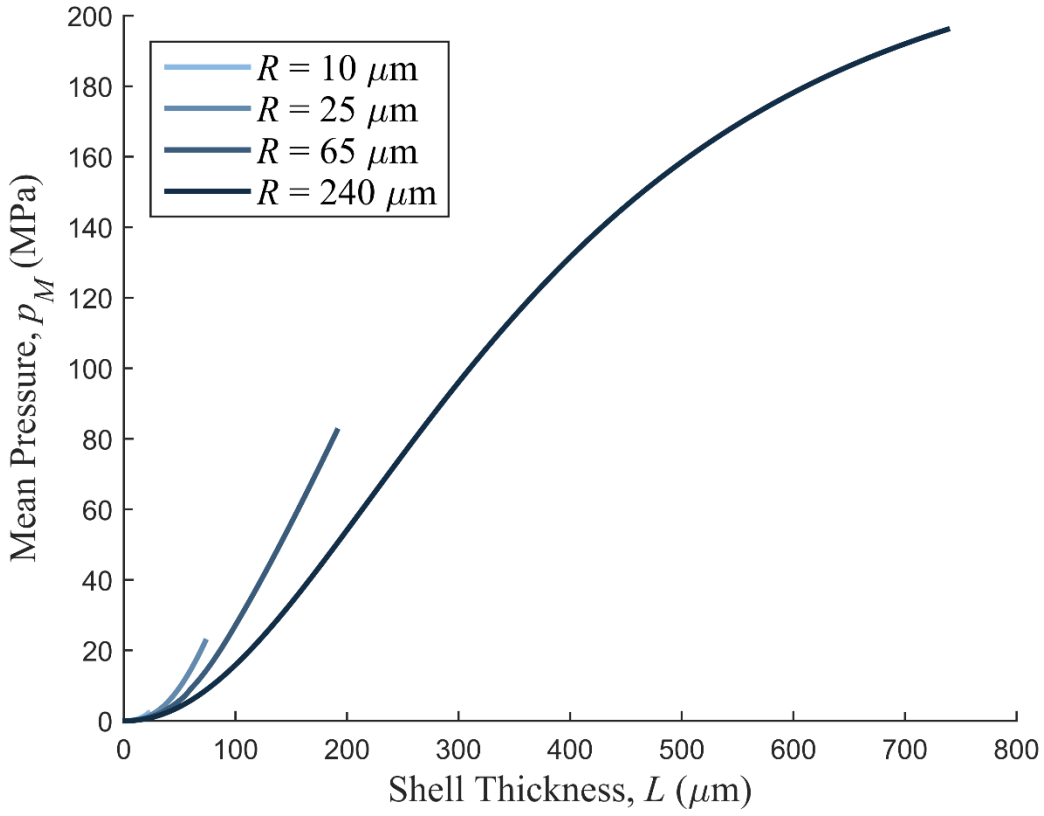


**Figure 5.7:** Mean pressure versus shell thickness for the four classes of air void radii. Curves have been truncated at such a shell thickness as to completely saturate the entrained air void

Figure 5.8 shows the volume of water expelled during freezing for each class of entrained air void as a function of the shell thickness. The volumes have been normalized by the volume of the entrained air void, such that when $V_{exp}/V_{void}$ is unity, the void is saturated with ice and loses its functionality as an expansion reservoir. While it is clear that the relatively larger classes of entrained air voids can draw from quite large shells of influence without saturating with ice, the mean pressures in Figure 5.7 is a reminder that shells with a thickness greater than 100 μm would result in mean pore pressures that would certainly fail the material locally.

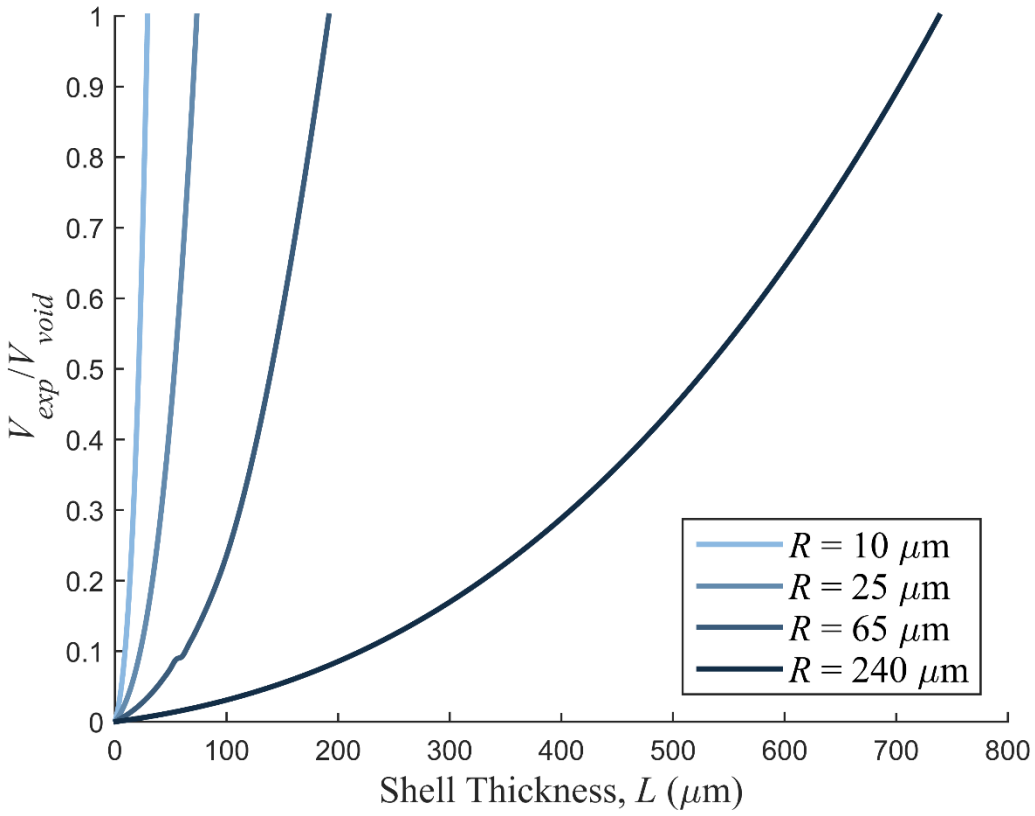


**Figure 5.8:** Volume of liquid expelled from the shell versus shell thickness for the four classes of entrained air void radii. Volumes have been normalized by entrained air void capacity.

### 5.4.1 Case I: No Absorption

As a baseline, the model air void systems based on the concretes from Chapter 3 were simulated assuming no absorption is taking place. Under this assumption, the entrained air voids within the concretes subjected to ASTM C666 would remain air-filled throughout the duration of the test. In Figure 5.9, the mean pore pressure in each concrete is plotted against the number of cycles (dashed lines denote failed samples). In this case, the shell thicknesses redistribute only once (recall that the shell consists of HCP alone). The only source of water entering the shells comes from the mechanics of freezing.

Therefore, the mean pressure calculation should not change between the first and three-hundredth cycle. Figure 5.9 shows that all the microstructures which simulate failed specimens experience positive mean pore pressures during the test, while microstructures which simulate specimens which did not fail experience negative mean pore pressures, even in this baseline case where absorption is neglected. This first-order model of the ASTM C666 test does not calculate damage explicitly. However, it is reasonable to postulate that once the mean pore pressures become positive, microcracking begins to occur locally due to the inherently low tensile capacity and brittleness of the material. It is noted that if such cracking did occur, the underlying retention curve (Figure 5.1, Eq. 5.8) is likely to change as well. However, the retention curve remains constant in all the calculations in this contribution, due to the highly-coupled complexity of the problem and the lack of a theoretical basis or an experimental dataset which could update the shape of the retention curve after cracking. Figure 5.10a plots mean pore pressure versus $\overline{L}$, and Figure 5.10b does the same for $\overline{M}$. While both plots exhibit a general linear trend when plotting mean pressure with spacing factor, it is evident that the linear relationship between spacing factor and mean pore pressure is stronger for $\overline{M}$ ($R^2$ = 0.98) than for $\overline{L}$ ($R^2$ = 0.83). Notably, the linear trend in Figure 5.10b suggests that samples with $\overline{M}$ > 0.023 mm will experience tensile pressures from very first freeze/thaw cycle. This cutoff corresponds to the value obtained empirically from freeze/thaw tests in Chapter 3.

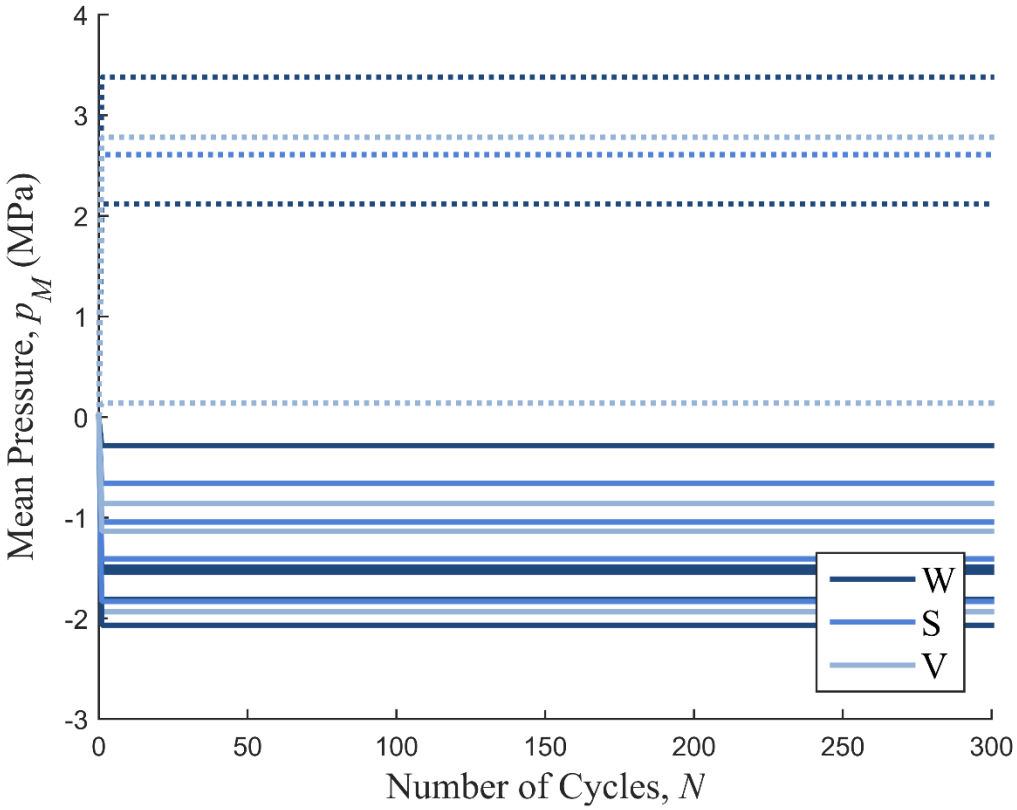


**Figure 5.9:** Mean pressure versus number of cycles for the concretes in Chapter 3 for the case of no absoption. Dashed lines denote failed samples.

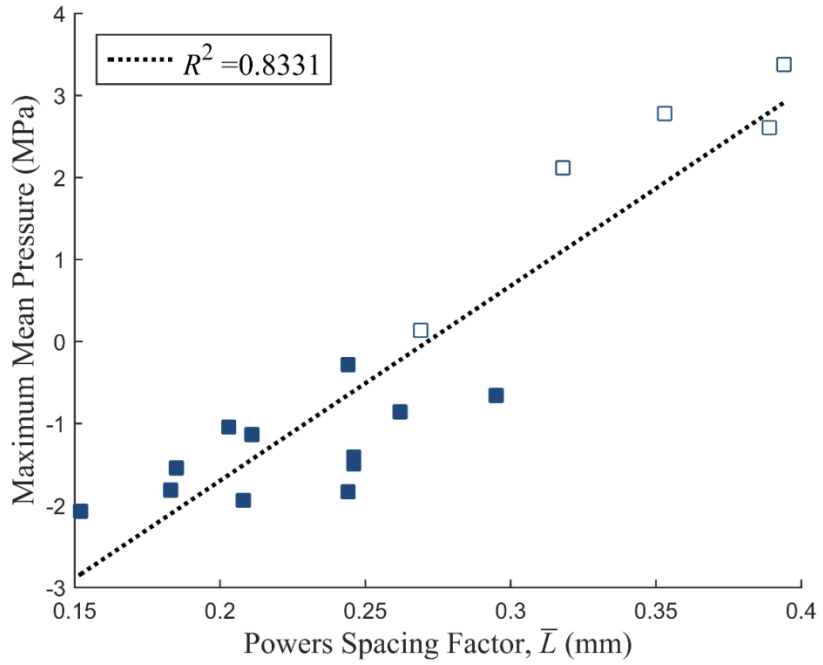


(a)

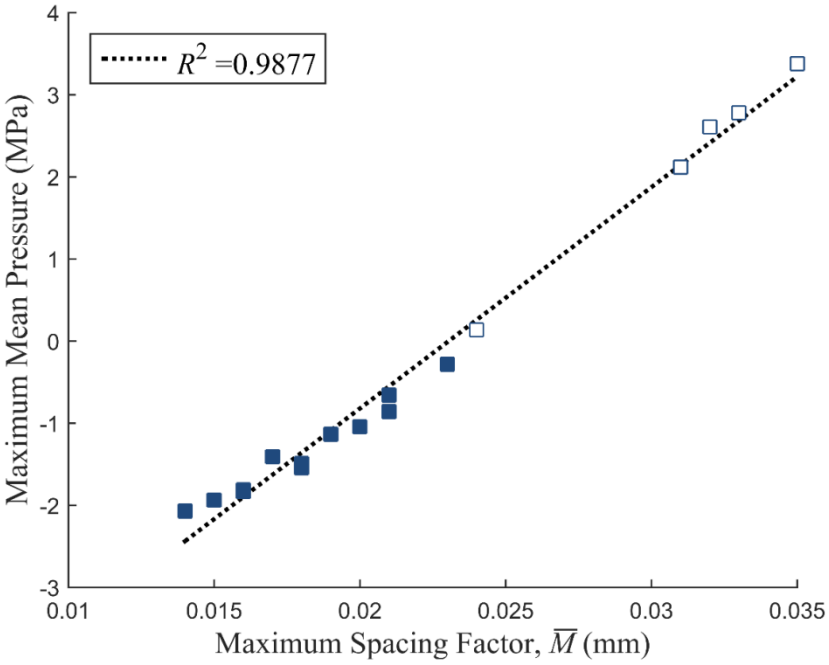


(b)

**Figure 5.10:** Maximum mean pressure versus (a) Powers spacing factor and (b) maximum spacing factor for the case of no absorption

### 5.4.2 Case II: Varying Absorption

In this section, the effect of absorption is investigated by varying the value of flux of air $q'$ (see Eq. 5.30) from a 'low' to a 'high' value. In this investigation, a "low" rate of absorption will be signified by $q' = 10^{-22}$ kg/s, an "intermediate" rate of absorption will be signified by $q' = 10^{-21}$ kg/s, and a "high" rate of absorption will be signified by $q' = 10^{-20}$ kg/s. The reason for varying $q'$ in such a manner is twofold. First, the theory upon which Eq. 5.30 is based assumes absorption is happening at 20 °C [141]. It is likely that the absorption rates observed in [141] for saturated air-entrained concrete specimens at room temperature will be slower at the freezing temperatures experienced during the ASTM C666 test [149]. Second, the bulk diffusivity of air in pore solution is not well understood, and Fagerlund only speculates at its order of magnitude [141]. For these reasons, the flux of air is increased until such a point as the results of the analysis are no longer physically reasonable in order to draw some conclusions about the effect of absorption.

The results for an "intermediate" rate of absorption ($q' = 10^{-22}$ kg/s) are shown in Figure 5.11, and the comparisons between the spacing factors and maximum pressures are shown in Figure 5.12. This low absorption rate causes a change in the mean pore pressure over time; it is no longer constant as in the preceding section. In this case of a "low" rate of absorption, the nonlinearity in the curves is attributed to the 10 μm voids slowly filling with water. The excess water volume in the 10 μm voids continues to increase after ever cycle. The volume fraction of the shells surrounding the 10 μm voids must decrease according to Eq. 5.39, and the volume fraction of the shells surrounding the larger voids must increase according to Eq. 5.40. For the samples which failed the

ASTM C666 test (dashed lines), this nonlinearity begins immediately, suggesting that the higher-pressure systems do not contain enough small entrained air voids to endure the first cycle without the need to redistribute the shell thicknesses towards the larger classes of entrained air voids. However, for some of the samples with very good freeze/thaw resistance (e.g., those which maintain negative pore pressures below -1 MPa for the duration of the freeze/thaw cycling), the shell thicknesses do not need to redistribute immediately. Therefore, some show constant mean pore pressures for up to 150 freeze/thaw cycles before the influence of the 10 μm voids begins to wane. By comparing Figure 5.10 to Figure 5.12, it is evident that the correlation between the spacing factors and mean pore pressures is relatively unchanged if absorption is slow.

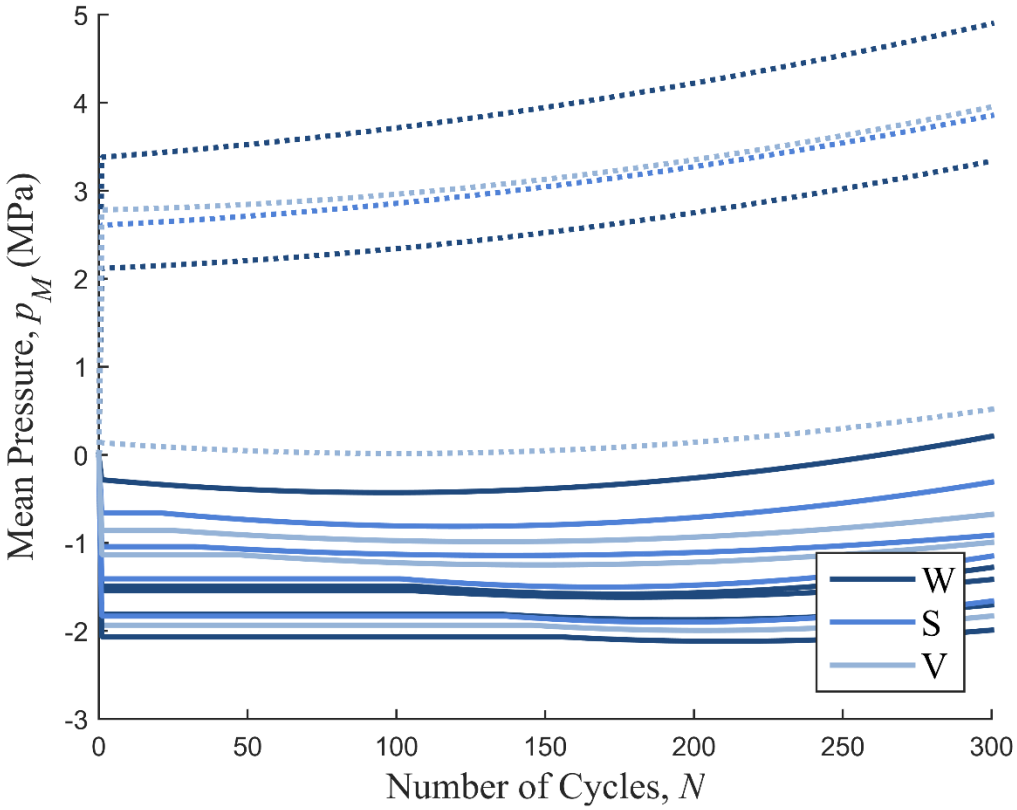


**Figure 5.11:** Mean pressure versus number of cycles for the concretes in Chapter 3 for the case of low absorption ($q' = 10^{-22}$). Dashed lines denote failed samples.

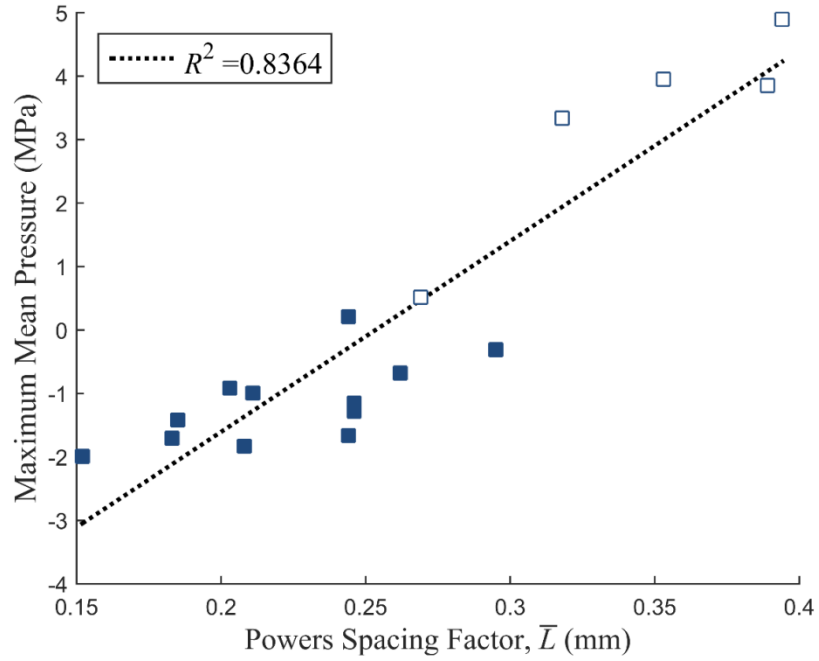


(a)

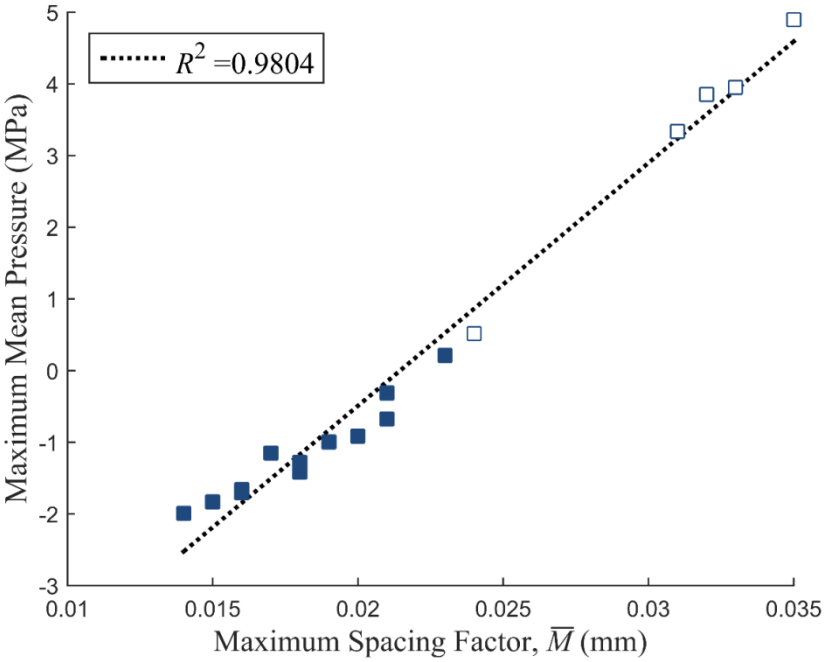


(b)

**Figure 5.12:** Maximum mean pressure versus (a) Powers spacing factor and (b) maximum spacing factor for the case of low absorption ($q' = 10^{-22}$)

The results for an "intermediate" rate of absorption ($q' = 10^{-21}$ kg/s) are shown in Figure 5.13, and the comparisons between the spacing factors and maximum pressures are shown in Figure 5.14. The nonlinear portion in the leftmost portions of Figure 5.13 show the 10 μm entrained air voids slowly saturate with water. The curves become constant again at approximately 40 cycles. At this point, the 10 μm entrained air voids have absorbed so much water that they cannot accommodate any liquid expelled due to freezing from a shell of any thickness, and therefore become ineffective. At this point, freeze/thaw resistance depends on the other size classes of entrained air voids. However, the constant pressure regions of Figure 5.13 suggest that although the 25 μm effectively take over as the smallest size class of entrained air voids in the system, they do not come close to saturating at this level of absorption, and therefore their shell thicknesses do not need to redistribute to the 65 μm and 240 μm size classes of entrained air voids. At this intermediate rate of absorption, only one of the samples which did not fail the ASTM C666 test experiences positive mean pore pressures. Figure 5.14b shows that the correlation between $\overline{M}$ and the maximum mean pore pressure is still very strongly linear at this rate of absorption with $R^2 = 0.98$.

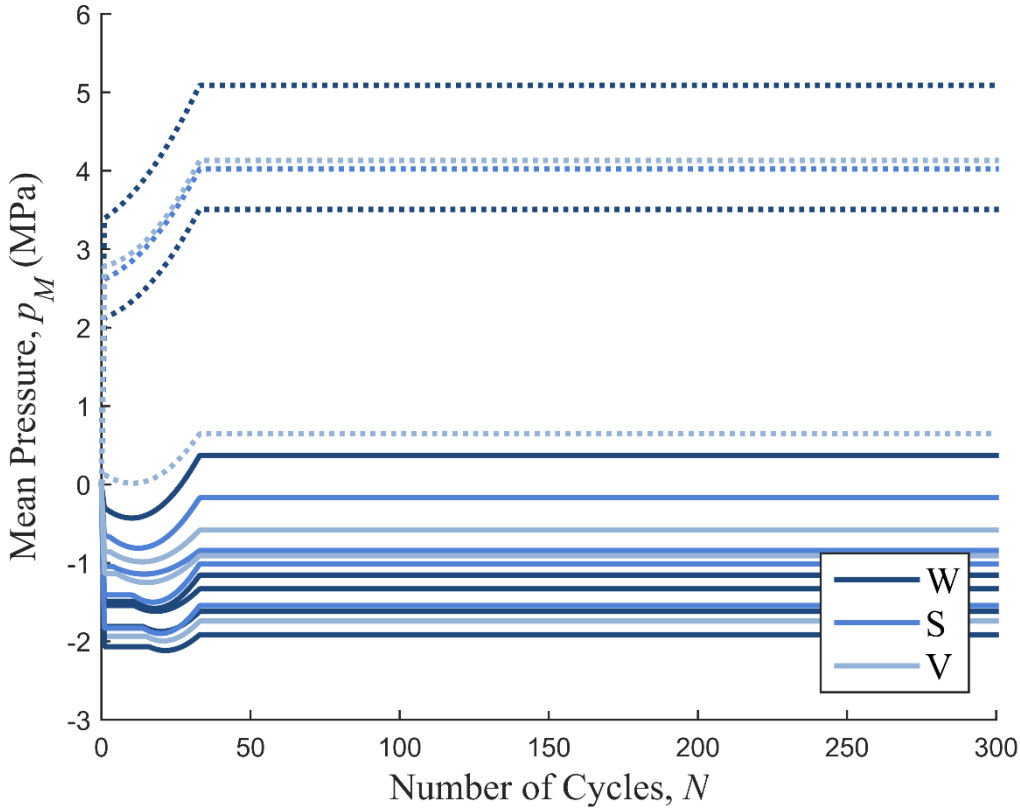


**Figure 5.13:** Mean pressure versus number of cycles for the concretes in Chapter 3 for the case of intermediate absorption ($q' = 10^{-21}$). Dashed lines denote failed samples.

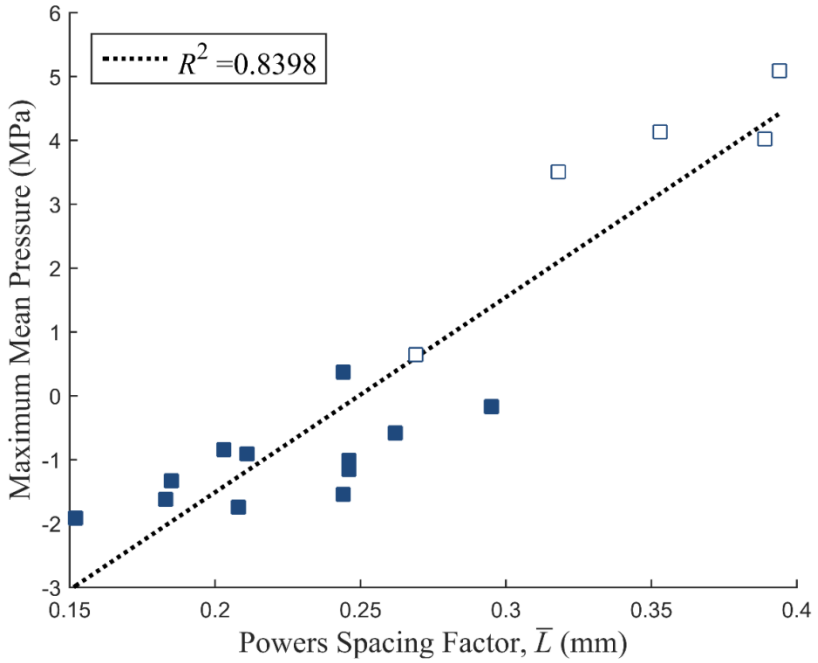


(a)

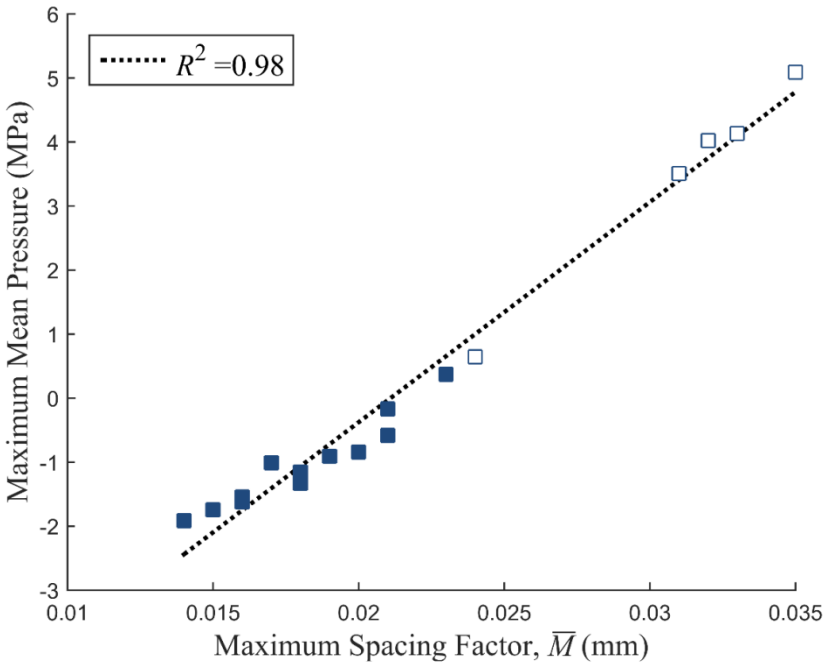


(b)

**Figure 5.14:** Maximum mean pressure versus (a) Powers spacing factor and (b) maximum spacing factor for the case of intermediate absorption ($q' = 10^{-21}$)

The results for a "high" rate of absorption ($q' = 10^{-20}$ kg/s) are shown in Figure 5.15, and the comparisons between the spacing factors and maximum pressures are shown in Figure 5.16. Even samples which did not fail ASTM C666 testing experimentally exhibit positive mean pore pressures at this rate of absorption. At this rate of absorption, the 10 μm entrained air voids saturate immediately, and the first slope in Figure 5.15 corresponds to saturation of the 25 μm entrained air voids. By approximately 5 cycles, 25 μm entrained air voids have saturated in all cases. This leads to a constant region between approximately 5 and 45-50 cycles, during which time the 25 μm entrained air voids have saturated but the 65 μm entrained air oids are not yet at capacity. Finally, the 65 μm entrained air voids saturate between approximately 45 and 55 cycles, at which point only the 25 μm entrained air voids are left as functioning expansion reservoirs. At this point, shell thicknesses are very large and the theoretical mean pressures are very high. For the samples which failed, the model predicts mean pore pressures as high as 43 MPa, which is on the order of the *compressive* strength rather than the *tensile* strength of the material. For these high pressures, the results of the flow model are unreasonable, as the solid phase has certainly failed locally and pressures redistribute. Therefore, it is entirely unreasonable to assume rates of $q' > 10^{-20}$ kg/s. Figure 5.16 shows that both spacing factors are relatively similar indicators of maximum mean pore pressure in this case. While $\overline{M}$ seemed more linearly correlated to mean pore pressure than $\overline{L}$ for the cases of no absorption, low absorption, and intermediate absorption, it appears to become markedly less correlated once the rate of absorption is unphysically high.

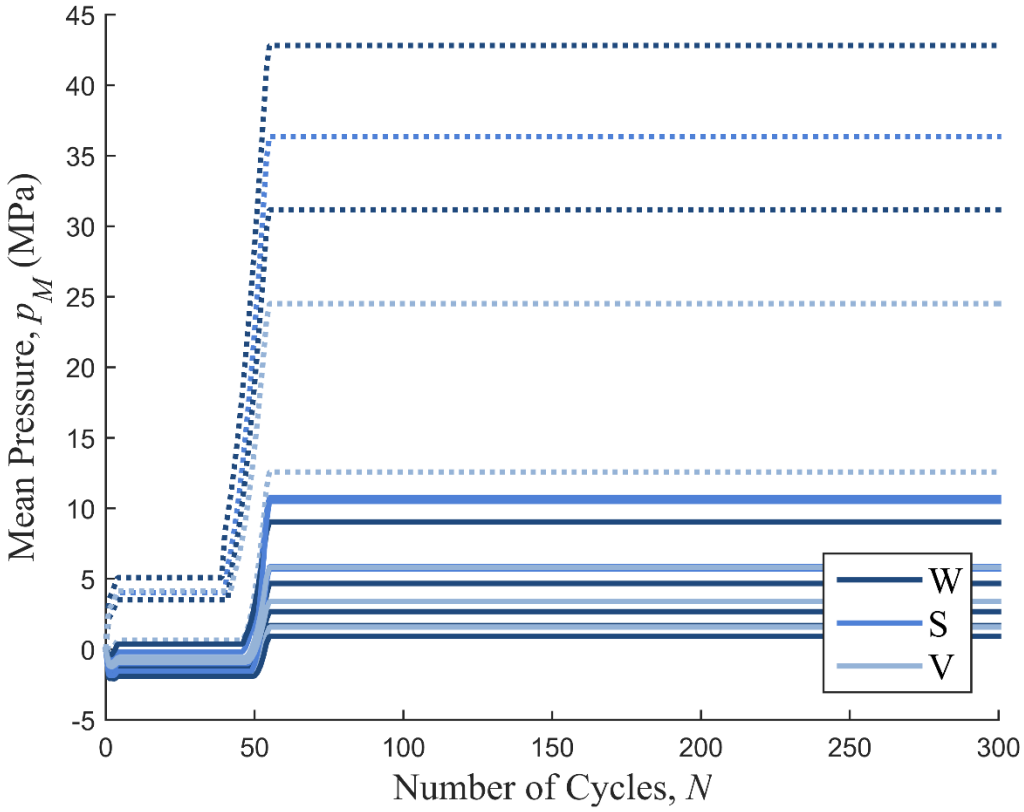


**Figure 5.15:** Mean pressure versus number of cycles for the concretes in Chapter 3 for the case of high absorption ($q' = 10^{-20}$). Dashed lines denote failed samples.

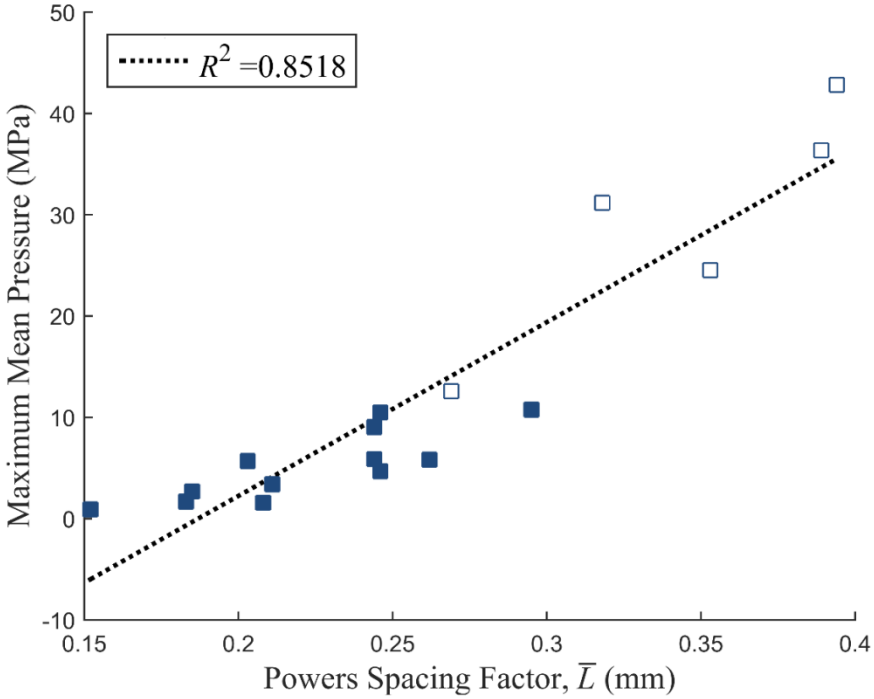


(a)

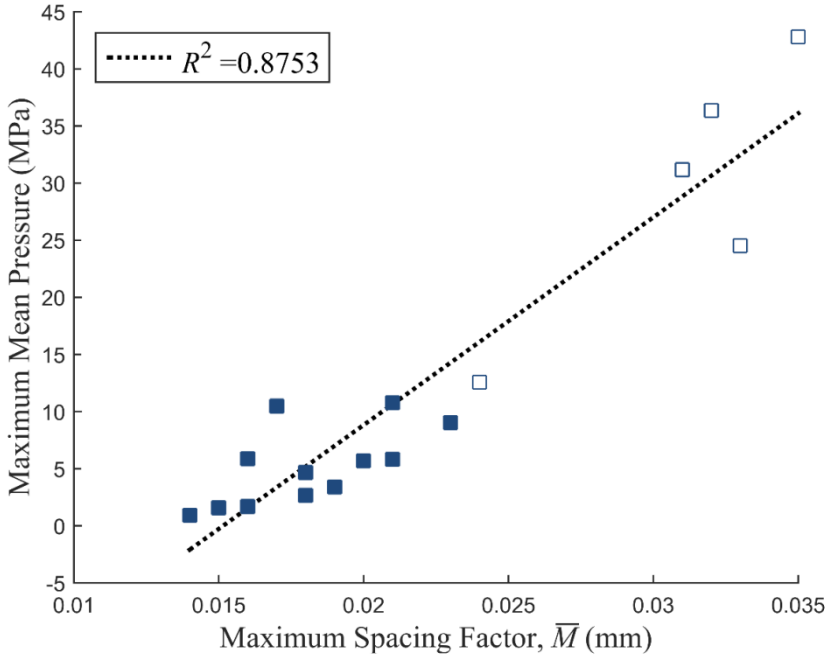


(b)

**Figure 5.16:** Maximum mean pressure versus (a) Powers spacing factor and (b) maximum spacing factor for the case of high absorption ($q' = 10^{-20}$)

### 5.4.3 Theoretical Results for Arbitrary Entrained Air Void Size Distributions

In order to examine the potential applications of the modeling technique in this chapter, as well as to determine boundaries on $\overline{M}$ for arbitrary systems outside of the experimental dataset, some theoretical size distributions of air voids were generated and analyzed. For simplicity, the size distributions were assumed to be lognormal. A lognormal distribution can be defined by its first two moments. To generate these air void systems, paste air contents $\hat{\phi}_{air}$ were varied systematically from $\hat{\phi}_{air}$ = 0.10 to $\hat{\phi}_{air}$ = 0.50. For each air content, the mean air void size $\langle \mathcal{R} \rangle$ varied from 0.01 mm to 0.05 mm. For each value of $\langle \mathcal{R} \rangle$, the second moment $\langle \mathcal{R}^2 \rangle$ was varied from 0.0001 mm$^2$ to 0.001 mm$^2$. A lognormal distribution with location parameter $\xi$ and scale parameter $\varsigma$ is given by

$$f(\mathcal{R}) = \frac{1}{\mathcal{R}\varsigma\sqrt{2\pi}} \exp\left[ -\frac{(\ln(\mathcal{R}) - \xi)^2}{2\varsigma^2} \right], \qquad \text{Eq. 5.42}$$

where location parameter $\xi$ is calculated from $\langle \mathcal{R} \rangle$ and $\langle \mathcal{R}^2 \rangle$ by

$$\xi = \ln\left( \frac{\langle \mathcal{R} \rangle}{\sqrt{1 + \frac{\langle \mathcal{R}^2 \rangle - \langle \mathcal{R} \rangle^2}{\langle \mathcal{R} \rangle^2}}} \right) \qquad \text{Eq. 5.43}$$

and scale parameter $\varsigma$ is calculated by

$$\varsigma = \sqrt{\ln\left( 1 + \frac{\langle \mathcal{R}^2 \rangle - \langle \mathcal{R} \rangle^2}{\langle \mathcal{R} \rangle^2} \right)}. \qquad \text{Eq. 5.44}$$

The simulated entrained air void size distributions are shown in Figure 5.17. The inset helps to provide interpretation of the figure, where the curve transitioning in shape from red to blue signifies an increase in the mean void size (top inset figure) or variance of the distribution (bottom inset figure). In general, the shade of the curves in Figure 5.17 correspond to the mean size $\langle \mathcal{R} \rangle$, with lighter curves signifying lower values towards $\langle \mathcal{R} \rangle$ = 0.01 mm and darker curves signifying higher values towards $\langle \mathcal{R} \rangle$ = 0.05 mm. Increasing $\langle \mathcal{R} \rangle$ has the net effect of shifting the distribution to the right, while shifting the variance has the effect of changing the curvature of the distribution, where lower variances correspond to steeper curves. From these size distributions, the systems can still be modeled using four size classes of air voids described by $f(\mathcal{R}_i)$ according to the procedure described in Section 5.3.

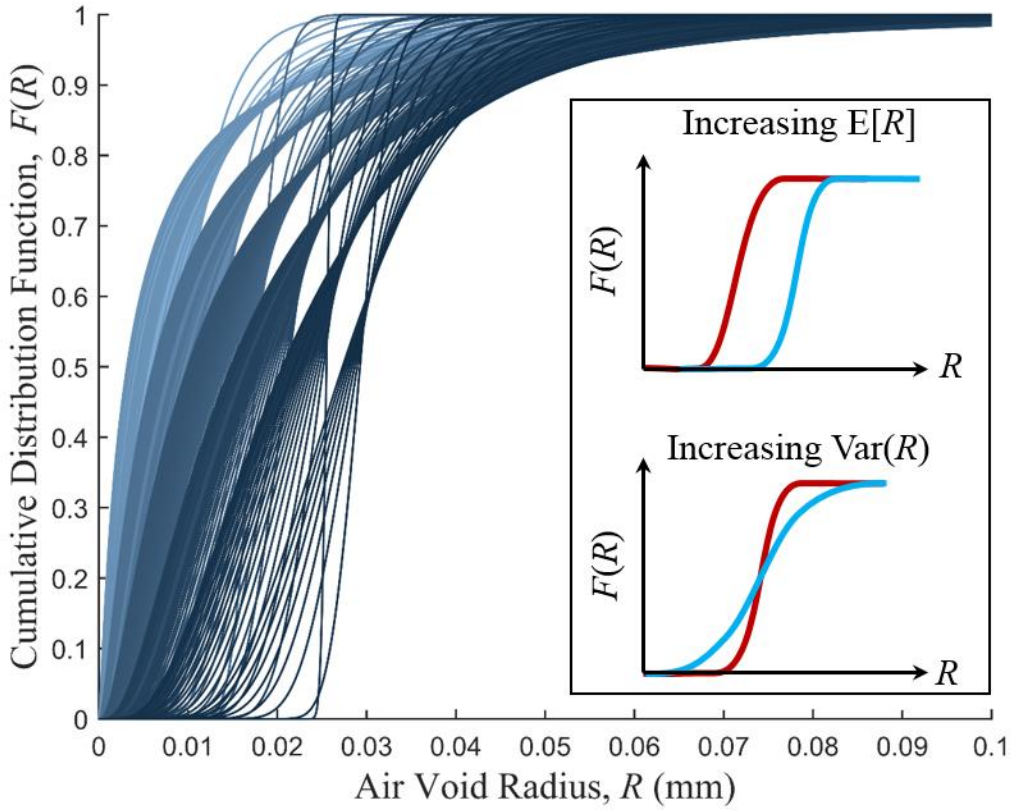


**Figure 5.17:** Theoretical size distributions of air voids. Inset describes the effect of shifting the mean and/or the variance.

Figure 5.18 presents the results of simulating freezing in arbitrary air void systems. In this system, absorption was neglected as in Section 5.4.1. In the figure, $\overline{M}$ is plotted against $\overline{L}$ as in Figure 3.8. The experimental data are denoted with black triangular markers in Figure 5.18, where open triangles denote the samples which failed the ASTM C666 test. The arbitrary air void systems which were generated for this study (i.e., those in Figure 5.17) are denoted by the circular datapoints. In a very broad sense, the same trends between $\overline{M}$ and $\overline{L}$ exists for the simulated entrained air void systems (described by Figure 5.17) as for the experimental air void systems. However, the vast cloud of circular data points helps to establish the range of sample space which is likely

to occur for lognormal distributions of entrained air voids. The color of the circular datapoints in Figure 5.18 corresponds to the range of mean pore pressure. Blue and green datapoints experience overall negative mean pore pressures, while yellow, orange, and red datapoints experience positive pore pressures. It is notable that all but one of the failed samples exist within the range of yellow datapoints (e.g., those experiencing tensile stresses). It is clear from the figure that given a particular configuration of entrained air voids, the mean pore pressure may be either negative for $\overline{M}$ as high as 0.035 mm or it may be positive for $\overline{M}$ as low as 0.029 mm. While this suggests that the value of $\overline{M}$ alone does not provide a definitive demarcation between compressive and tensile pore pressures for arbitrary entrained air void systems, the trends in Figure 5.18 nevertheless point to $\overline{M}$ as a more appropriate indicator of mean pore pressure than $\overline{L}$. Most notably, the clusters of color for each pressure regime are almost completely stratified vertically (i.e., mean pore pressure increases with increasing $\overline{M}$), as opposed to horizontally (i.e, with increasing $\overline{L}$). Strikingly, values of $\overline{L}$ greater than 0.35 mm can experience very negative or very positive pore pressures, while such disparities are not observed in $\overline{M}$.

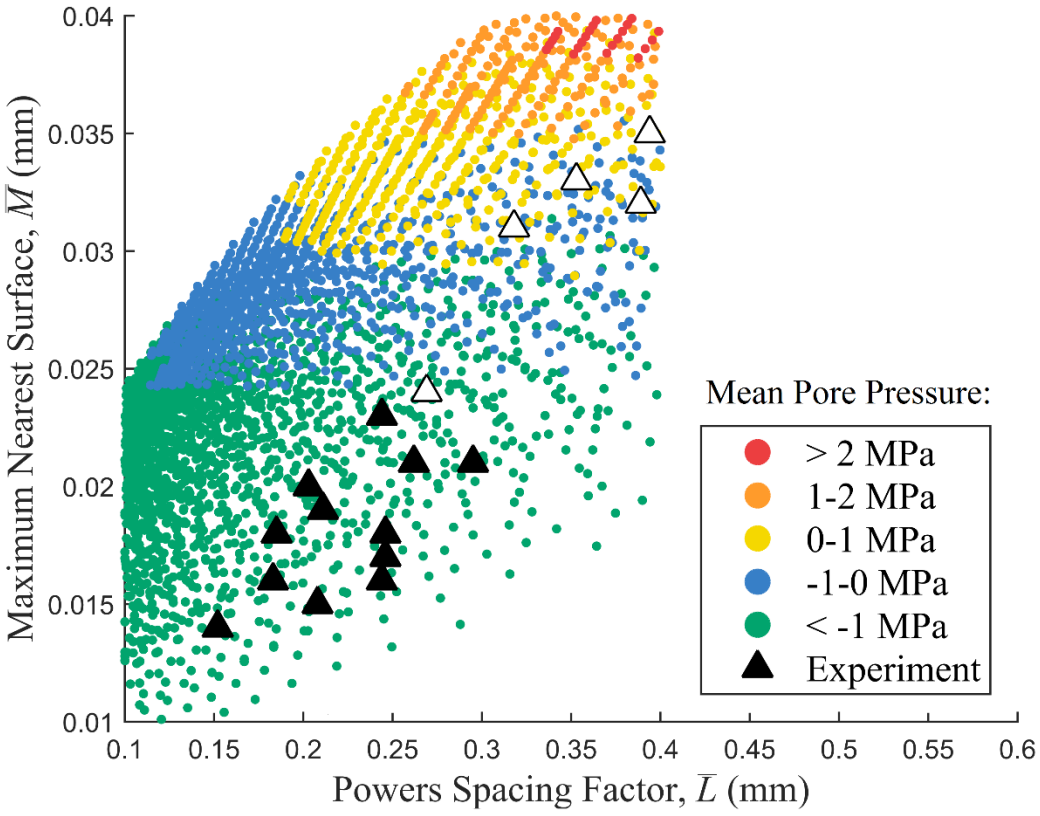


**Figure 5.18:** Maximum spacing factor versus Powers spacing factor for arbitrary air void systems. Color corresponds to mean pore pressure.

Figure 5.19 is similar to Figure 5.18. In Figure 5.19, the color of the datapoint corresponds to the *maximum* pore pressure felt anywhere in the system, as opposed to the mean pore pressure. This is an indication of which samples will begin to experience high pressures which could initiate degradation locally. It is notable that the yellow datapoints (indicating positive pore pressures) begin to cross the ordinate at $\overline{M}$ = 0.023 mm, the same demarcation between samples with adequate and inadequate durability factors determined purely experimentally in Chapter 3. In the same manner as Figure 5.18, maximum pore pressures are stratified to align with $\overline{M}$ rather than $\overline{L}$. Figure 5.19 sheds

some light on the open triangle at coordinates (0.269,0.024), which is referenced as V45-1 in Chapter 3. This data point is at the borderline of a cluster of yellow data points (positive pressures) and blue data points (negative pressures). Given this failed sample's proximity to some of the other unfailed samples, it is likely that it belongs to the family of data points with *positive* maximum pore pressure rather than *negative* maximum pore pressures.

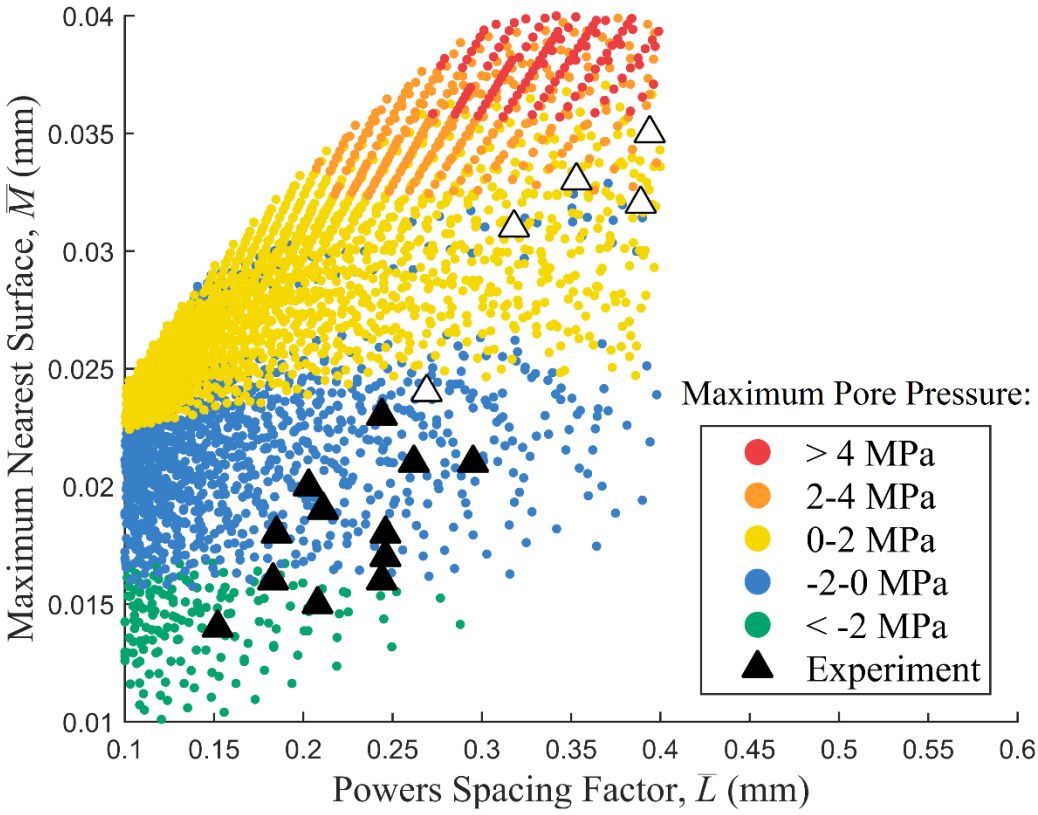


**Figure 5.19:** Maximum spacing factor versus Powers spacing factor for arbitrary air void systems. Color corresponds to maximum pore pressure.

### 5.4.4 Theoretical Optimized Entrained Air Void System for Dynamic Loading

The results from Section 5.4.3 have a potential to allow engineers speculate about theoretical optimum entrained air void systems which have been tailored to particular

durability concerns. This is particularly useful in circumstances where an entrained air void system that is "optimum" for a particular durability concern is not "optimum" for another, competing durability concern. In the simplest example, the classical philosophy of adding air entrainment to concrete has always highlighted the competition between adding enough air to allow for adequate freeze/thaw resistance without adding too much air which compromises static compressive strength. In a more complex example, consider the case of high strain-rate loading. Recall that it was concluded in Chapter 4 that mortars containing relatively larger entrained air voids exhibited higher dynamic strengths than mortars with relatively smaller entrained air voids. For the samples in Chapter 4, this ultimately suggested the dynamic strength failure mode could shift from mode 1 (with an average strength of about 72 MPa) to mode 3 (with an average strength of about 90 MPa). The results from Section 5.4.3 allow engineers to speculate about an optimized entrained air void system which considers static strength, freeze/thaw resistance, and high strain-rate response. Figure 5.20 shows such an optimized size distribution in red. To determine the system, $\overline{M}$ was limited to 0.023 mm to allow for adequate freeze.thaw resistance. The datapoints with $\overline{M}$ < 0.023 mm were then probed to find the lowest paste air content $\hat{\phi}_{air}$ to minimize the impact on quasistatic compressive strength. Finally, the theoretical optimum size distribution can be calculated from the mean and variance of the distribution used to generate the CDFs which were used to create Figure 5.18 and Figure 5.19. The results suggest that an adequate $\overline{M}$ for frost resistance can be obtained at a paste air content of $\hat{\phi}_{air}$ = 15% (note that the lowest paste air content of the experimental samples in Chapter 3 was 18%). This allows for entrained air voids with an average size of about 30 μm (note that the average size of air voids in Chapter 3 varied from about 16

μm to 22 μm). In Figure 5.20, the size distributions of entrained air voids for the concretes in Chapter 3 are shown in shades of blue. It is clear from the figure that an "optimum" entrained air void size distribution has a vastly different shape than the air void systems obtained experimentally.

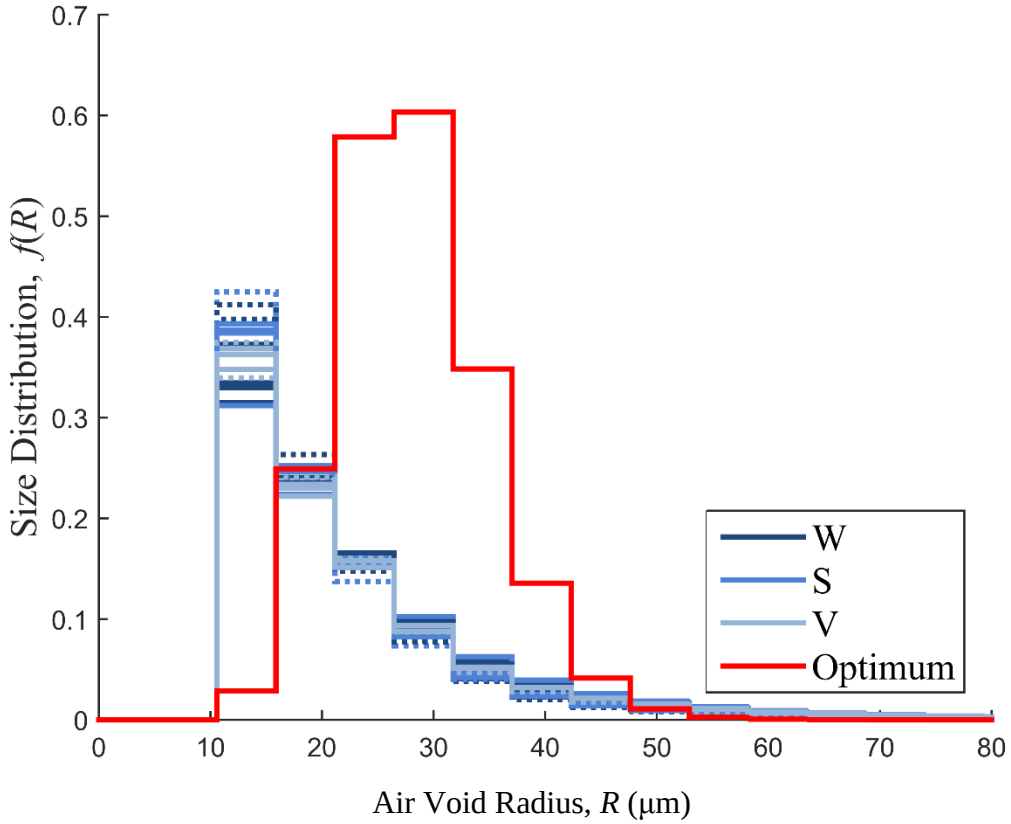


**Figure 5.20:** Theoretical optimum air void size distribution for cyclic freezing and thawing and high strain-rate loading.

## 5.5 Conclusions

In Section 5.2, the origins of the of the pore pressure build-up leading to damage during the ASTM C666 freeze/thaw test were described. Linear elastic poromechanics was used as a framework to determine the pressure profile in a shell surrounding a single entrained air void in Section 5.2.1. The concept of absorption was introduced in Section

5.2.2, which has the overall effect of slowly decreasing the effectiveness of entrained air voids as they become filled with water. In Section 5.3, a framework was outlined to model systems of entrained air voids. The systems of entrained air voids investigated in Chapter 3 were reduced to simplified systems consisting of four size classes of entrained air voids. The thickness of the shell of influence around each entrained air void is distributed in such a way that entrained air voids do not draw in more water during freezing than the voids are capable of accommodating. Simulation of the ASTM C666 test was carried out in Section 5.4. In Section 5.4.1, the concretes from Chapter 3 were investigated analytically for the case where absorption was negligible in order to provide a baseline for analysis. In Section 5.4.2, the rate of absorption was gradually increased. In Section 5.4.3, arbitrary theoretical systems of entrained air voids with varying air contents were generated to explore trends in the spacing factors outside that of the experimental data. In Section 5.4.4, the findings of this chapter used with the insights from Chapter 4 to optimize the entrained air void system for both resistance to high strain-rate loading and cyclic freezing and thawing. The following conclusions can be drawn:

1. A stronger linear correlation was found between the thickness of the shell of influence surrounding entrained air voids and $\overline{M}$ than between the shell thickness and $\overline{L}$. Furthermore, the shell thickness and $\overline{M}$ were very relatively close to the same numeric value, while $\overline{L}$ was an order of magnitude higher than the shell thickness in all cases.

2. Since shell thickness is an important factor in determining the ultimate mean pore pressure, $\overline{M}$ and not $\overline{L}$ is a more appropriate indicator of the evolution of pressures that will develop during freezing.
3. A conservative lower bound for $\overline{M}$ for arbitrary systems is likely in the range of 20 μm – 25 μm.
4. While it is likely that entrained air voids are slowly absorb water as the air within the void dissolves into the pore water, the poroelastic model alone can yield reasonable predictions of freeze/thaw durability without accounting for absorption. The rate of absorption warrants further study.
5. The results provide a framework for tailoring systems of entrained air voids for specific durability concerns, or optimizing the system when two or more durability concerns each require disjoint entrained air void configurations. This has the potential to allow admixture chemists to engineer novel systems of entrained air voids.

# CHAPTER 6

# CONCLUSIONS AND FUTURE WORK

## 6.1 Conclusions

The main objective of this research was to probabilistically quantify the size distribution and spatial arrangement of voidspace in cementitious composites across length scales, and use this information to predict mechanical behavior of cementitious material systems under different extremes in loading and exposure conditions. These extremes occur on different time scales. The following sections present the key findings of this research.

### 6.1.1 Characterization of Entrained Air Voids in Hardened Concrete

A novel technique for quantitative characterization of entrained air voids in hardened concrete was developed. The method calculates the 3D size distribution from 2D images directly, rather than assuming a size distribution, as has been done previously. A comparison study of the new spacing factor, $\overline{M}$, with the ASTM spacing factor, $\overline{L}$, suggested the new spacing factor is more sensitive to microstructural changes than $\overline{L}$. No clear clear delineation was observed in $\overline{L}$ between those concretes that perform adequately in ASTM C666 and those which fail. Experimental data suggested suggests two distinct regions in $\overline{M}$: those which failed (all with $\overline{M}$ > 0.024 mm) and those which did not (specifically, those below $\overline{M}$ $\leq$ 0.023 mm). Some interplay may also exist between entrained air void number density and spacing. A spacing factor which is sensitive to changes in the microstructure has the potential to improve the economy in

petrographic analysis of concretes, especially if it could limit specimens which fail the requirements of ASTM C457 and necessitate more expensive testing per ASTM C666.

### 6.1.2 Analysis and Modeling of Portland Cement Mortar Under Impact

The moving window approach was shown to be a useful tool for investigating the localization of failure that occurs in brittle materials such as mortar. Specifically, a sensitivity study on window size suggested that flaws may be multimodal and helped identify the representative volume element for air entrained mortar. Flaws may interact in different ways, resulting in three failure modes. The analysis of the micromechanics model's strength data suggests that larger flaws shift the dynamic strength upwards into the third (i.e., highest strength) failure mode.

The good agreement in average dynamic strength in the control sample gives further credence to the theory that the dynamic strength increase in mortar and concrete may arise from crack propagation through rather than around aggregates. Post-failure microscopic analysis of fragments also supports this theory.

Experimental validation suggests the model is useful for predicting dynamic strength. The model is especially useful for determining quite rapidly the potential range in dynamic strengths among materials with varying microstructures. Therefore, the model helps interpret the variability of the Kolsky bar tests, and with further development and validation could reduce the need for very large, time-consuming datasets from experimental programs.

Air entrainment lowers the static compressive strength and the average dynamic compressive strength. However, the dynamic increase factor (the ratio of dynamic to static strength) increases with increasing air content. High speed images of the failure

process suggests that the air entrained mortars first exhibit signs of void consolidation, then hold a load plateau until the cracks fully form through the mortar.

### 6.1.3 Modeling of Cyclic Freeze/Thaw Damage to Cementitious Materials

A stronger linear correlation was found between the thickness of the shell of influence surrounding entrained air voids and $\overline{M}$ than between the shell thickness and $\overline{L}$ . Since shell thickness is an important factor in determining the ultimate mean pore pressure, $\overline{M}$ and not $\overline{L}$ is a more appropriate indicator of the evolution of pressures that will develop during freezing. Results suggest that a conservative lower bound for $\overline{M}$ for arbitrary systems is likely in the range of 20 μm – 25 μm.

While it is likely that entrained air voids are slowly absorb water as the air within the void dissolves into the pore water, the poroelastic model alone can yield reasonable predictions of freeze/thaw durability without accounting for absorption. The rate of absorption warrants further study. Nevertheless, the results provide a framework for tailoring systems of entrained air voids for specific durability concerns, or optimizing the system when two or more durability concerns each require disjoint entrained air void configurations. This has the potential to allow admixture chemists to engineer novel systems of entrained air voids.

## 6.2 Recommendations

The following sections present recommendations based on the current research into quantitative characterization and mechanical modeling of cementitious composites.

### 6.2.1 Characterization Techniques for Entrained Air Voids in Hardened Concrete

The advent of high quality, low cost image acquisition techniques such as desktop scanners has created an opportunity to improve the characterization of entrained air voids by image analysis. It is recommended that the community adopt a more advanced underlying theory of microstructure to compliment today's advanced image acquisition and processing techniques. Chapter 3 outlines a detailed model of entrained air voids in concrete. As microstructures are stochastic, they are more appropriately approached with a probabilistic framework rather than a purely deterministic one.

### 6.2.2 Analysis and Modeling of Portland Cement Mortar Under Impact

The data accumulated on the dynamic behavior of mortars is not yet so extensive and conclusive as to warrant recommendations for engineering vital concrete elements which are thought to have an elevated risk of experiencing blast or impact loads (e.g. bridge piers, load bearing elements in strategic structures or government buildings, etc.). However, this work does suggest that materials-level considerations could help inform the design philosophy when engineering the infrastructure surrounding these types of strategic structures (e.g. concrete barriers, concrete pavements, etc.). Since mode 3, the highest strength mode, is characterized by larger, unclustered air voids, a coarser entrained air void system may be beneficial when blast resistance is a concern (e.g., a Vinsol Resin admixture may be a good candidate for this scenario based on the conclusions drawn in Chapter 3).

The analysis outlined in Chapter 4 could serve as a forensic technique for assessing the susceptibility of concrete elements to damage (particular spalling which creates shrapnel) in the wake of a blast-loading scenario. Though coring is not entirely non-destructive, micromechanical modeling based on image analysis of cores has the

potential to create a large dataset of potential boundaries on dynamic strength without the need to subject a large number of cores to dynamic mechanical (i.e., completely destructive, expensive) testing.

### 6.2.3 Modeling of Cyclic Freeze/Thawing Damage to Cementitious Materials

The poroelastic model developed in Chapter 5 shows promise as a predictive tool to model the pore pressure profile in air entrained concretes subjected to the ASTM C666 test. Researchers acknowledge there still seems a potential opportunity to improve or at least refine methods for assessing the quality of air entrainment in concrete [151]. However, while some research has focused on new ways to characterize the entrained air void system (e.g., [60, 57, 59]) or improved understanding of the mechanics of freezing and thawing in cementitious materials (e.g., [139, 147]), this research constitutes the first attempt to develop a model for quantitative characterization of the entrained a void system in tandem with a mechanics-based model to describe the physics of cyclic freeze/thaw. Towards the development of optimized entrained air void systems, it is recommended that the spatial model in Chapter 3 be used alongside the poromechanical model in Chapter 5. Additionally, the model could be used as a forensic tool. If freeze/thaw is suspected as a damage mechanism, the necessary model inputs could be obtained from a relatively small core of material using image analysis and porosimetry.

## 6.3 Future Research

This dissertation research has contributed to the body of knowledge on quantitative characterization of cementitious composites. This research utilized quantitative characterization across size scales to predict mechanical behavior of cement-based materials across time scales; specifically, high strain-rate (i.e. “rapid”) loading and

freeze/thaw (i.e. "slow") loading. However, additional research will be necessary to develop guidelines to aid in engineering concrete to combat the durability concerns studied as part of this research.

- Chapter 3 presents experimental data which suggests $\overline{M}$ outperforms $\overline{L}$. While encouraging as a proof-of-concept, the dataset is relatively small, encompassing 17 samples. These samples vary admixture dosage, type, and *w*/*c*. However, further research is necessary to set limits on $\overline{M}$. The concretes in Chapter 3 were relatively "typical," containing no supplementary cementitious materials (SCMs) or admixtures beyond AEA. Modern construction materials contain a variety of chemical and mineral admixtures, and may use alternative cementing materials as well. Future research should explore the susceptibility of these materials to freeze/thaw damage and set appropriate limits on $\overline{M}$.
- Chapter 3 presents a relatively concise set of equations to model the entrained air void system. In light of empirical evidence and analytical modeling (e.g., the work in Chapter 5) suggesting a critical spacing, the next step towards engineering better cementitious composites for freeze/thaw durability would be to optimize the size distribution of entrained air voids. Specifically, this "optimum" system would entrain as little air as possible to limit the entrained air void system's deleterious effect on quasistatic compressive strength while providing adequate spacing in between voids to ensure freeze/thaw durability. Furthermore, the size distribution of multiscale voidspace could be optimized to control the flow rate. This research would present an opportunity to collaborate with chemists

towards the development of a chemical admixture capable of entraining such an optimum entrained air void system in concrete.

- The detailed statistical analysis in Chapter 4 underscores the complexity of modeling heterogeneous, clustered systems under high strain-rate loading with two flaw types. This analysis provides a framework for analyzing this complexity and studying localization effects. However, many more flaw types exist in geomaterials like concrete. Research should continue to developing a library of flaw types to capture the heterogeneity in cementitious composities. While the round flaws capture empty porosity or very soft inclusions, a better model for aggregate may be a round flaw with local stiffness properties (i.e., a hard inclusion). Furthermore, more research is necessary to investigate how this work performed on mortar might scale to concrete or concrete elements.
- The procedure in Chapter 4 considers a two-dimensional microstructure. Since actual microstructures are three-dimensional, this work could be extended. Preliminary work has been done by [117] to show the usefulness of this model in the quasi-three-dimensional case.
- Despite advances in modeling porous media, many idealizations are still made. For example, the "solid" has been considered as a homogenous continuum, and the porespace itself was assumed to be saturated by two phases (crystal/liquid) rather than as a more complicated mixture of crystal, liquid, and gas. The concrete "solid" is of course a complex composite, and consists of heterogeneities over several orders of magnitude. This approach necessitates a complex computational framework to simulate such systems. Image based techniques, such as x-ray nano-

and microtomography could also be used to improve the theory of the pore space over that of conventional mercury intrusion porosimetry.

- The phenomenon of “absorption” in Chapter 5 uses a relatively crude linear model relative to the relatively more robust mass conservation equations used to model flow. Future research could explore the problem in more detail, and amend the model with a more suitable set of constitutive equations.
- Chapter 5 does not calculate damage directly; rather, damage is inferred from positive mean or maximum pore pressures. Continuum damage mechanics or plasticity could be applied to this model to better quantify the damage accumulation during cyclic freeze/thaw.

# APPENDIX A

# SCALE INDEPENDENCE IN THE RECOVERY OF 3D INFORMATION USING 2D IMAGES

Advances in digital image analysis have allowed for rapid and detailed investigations of the microstructural topography of cementitious materials, and recent theoretical and analytical work have allowed for recovery of 3D information from 2D analyses. However, measurements of parameters such as the entrained air void size distribution and number density obtained from digital images of concrete are quite sensitive to the resolution of the image. To address this, an analytical model for recovering 3D information from 2D sections was applied to images of mortar at different resolutions, and the results were interpreted in terms of fractal geometry. Results suggest there exists a "critical" or "cutoff" resolution and correction factor for scale independence, which is crucial for viewing stereological measurements in an absolute sense rather than relative to the resolution of the instrument. Furthermore, the same analytical model was validated against full 3D x-ray microtomographic images.

## A.1 Introduction

It is well known that geometric measurements depend on the fineness of the measurement device. Mandelbrot famously illustrated this concept in 1967 by studying the length of the coastline of Great Britain [152]. Measuring the coastline with a series of successively finer measurement lengths – called yardstick lengths – yielded successively larger values for the total length of the coastline. Mandelbrot later coined the term "fractal" to describe the complex geometries of rough surfaces and self-similarity [153].

This dependency of magnification or image resolution on stereological measurements poses a challenge in the field of quantitative stereology [154, 155, 156], and fractal geometry has been applied to address this problem in diverse fields such as metallurgy [157], cell biology [158], and hydrology [159].

When discussing digital images, the yardstick length is controlled by the image resolution or pixel size. In Chapter 3, an analytical model was introduced for analyzing the distribution of spherical voids or inclusions in a solid. The approach was applied to the entrained air (EA) void system in hardened concrete, where measurements of the system's morphology are performed on digital images typically acquired by optical microscopy. The method offered two major contributions: (1) it offered a technique to reconstruct the three-dimensional (3D) size distribution of inclusions or voids from two-dimensional (2D) measurements, and (2) it used the size distribution and number data to produce a new spacing factor, $\overline{M}$. Using equations originally derived by Lu and Torquato [79], $\overline{M}$ can be calculated in closed form. It was concluded in Chapter 3 that $\overline{M}$ is more sensitive to changes in the EA void system's morphology than the ASTM C457 spacing factor, $\bar{L}$, which is currently used as a measure of concrete's resistance against damage caused by cyclic freezing and thawing [54]. Experimental freeze/thaw data also suggested that $\overline{M}$ may out-perform $\bar{L}$. In Chapter 5, a poroelastic model was developed to show how $\overline{M}$ and not $\bar{L}$ is a better indicator of the mean and maximum pore pressures felt by the hydrated cement paste matrix during freezing. Further explanation of the method is detailed in Section A.2. While the approach was applied to EA voids in cement-based material, the technique could be applied to any range of

materials systems which has been modeled using polydispersed spherical inclusions or voids, e.g., soft matter [160], semiconductors [161], and food microstructure [162].

However, validation of each of these two major contributions in Chapter 3 presents its own challenge. Since the size distribution parameters are obtained from digital images, they too will be influenced by the image resolution. The first objective of this study was to understand the effect of image resolution on quantitative characterization of the microstructure. This is of critical importance to prevent discrepancies from arising between measured values of $\overline{M}$. In [158], researchers addressed the discrepancies in the literature regarding measurements of the surface density of inner mitochondrial membranes obtained from micrographs by studying the effect that magnification had on their measurements. In so doing, they interpreted their findings in terms of a fractal dimension, identified a "critical" magnification, and produced a correction factor which depends only on the fractal dimension. A similar approach has been undertaken on digital images of air entrained portland cement mortar with varying image resolutions, which is detailed in Section A.3.

The second challenge is related to the spatial arrangement of entrained air voids, not the size distribution parameters. $\overline{M}$ is obtained from closed-form equations describing the nearest-surface distance from a random point in the hydrated cement paste to the periphery of an entrained air void. Calculating $\overline{M}$ in closed form requires that the spatial arrangement of the entrained air voids is homogeneous; that is, they are not clustered at the mesoscale. The method outlined in Chapter 3 is advantageous because full 3D measurements of the spatial arrangement are very difficult to obtain without x-ray imaging methods. Cement-based materials are relatively opaque to x-rays, and therefore

the sample dimensions for x-ray imaging is limited. Furthermore, x-ray imaging is cost-prohibitive for most structural engineering applications. However, it is a useful tool for research and model validation. In this contribution, x-ray microtomography (x-μCT) is used to validate the unclustered assumption used to calculate $\overline{M}$. Furthermore, the x-μCT analysis serves to validate the 2D analysis carried out in Section A.3. These results are presented in Section A.4.

## A.2 Analytical Modeling Applied to the Entrained Air Void System

While a thorough treatment of the analytical model used to characterize the entrained air void system may be found in Chapter 3, it is convenient to provide a concise summary of the modeling technique and assumptions. This section begins with an overview of the analytical model and its application to for the EA void system proposed in Chapter 3. In the discussion of the analytical model, the important areas for study are identified.

In Chapter 3, a technique was introduced to reconstruct the 3D size distribution of entrained air voids in hardened concrete from 2D digital images, and to interpret that size distribution in terms of a probabilistic maximum spacing between a random point in the hydrated cement paste and the periphery of the nearest entrained air void. First, samples of mortar or concrete are prepared for analysis. The sample preparation technique has been extensively studied in [84] and is often used to measure air content in hardened concrete, but an overview of the technique will be discussed briefly. Samples are lapped with a diamond saw and polished with successively finer polishing papers. Next, samples are lacquered with a black permanent marker, and a white calcium carbonate powder is forced into the entrained air voids. This facilitates converting digital grayscale images of

the concrete's surface to binary images, since black pixels will correspond to the solid phase (hydrated cement paste and aggregates) and white pixels will correspond to entrained air voids. To acquire the images, samples are scanned with a flatbed scanner. A threshold is typically selected from the histogram of gray values to demarcate air voids from solids.

The analysis technique first measures the lineal-path function, $L_{air}(z)$. The lineal-path function is the probability that a line of length $z$ lies entirely within the phase of interest (in this case, entrained air voids). For any statistically homogeneous and isotropic random media, $L_{air}(z)$ does not depend on the orientation of the line $z$. Furthermore – and of interest in Section A.3 – the (3D) lineal-path function can be obtained from (2D) digital images. The lineal-path function can be used to calculate three important system parameters: the size distribution probability density function (PDF) of EA voids $f(\mathcal{R})$, the number density (per unit volume) of entrained air voids $\rho_{air}$, and the cement paste air content $\phi_{air}$. Note that by its definition, it follows that $L_{air}(0) = \phi_{air}$, which gives the probability that a point (a line of zero length) lies in the entrained air void phase. The lineal-path function is related to $\rho_{air}$ by the differential relationship

$$\rho_{air} = \int_{\Re} \frac{2}{\pi}\left(\frac{1}{z^2}\frac{d^2 L_{air}(z)}{dz^2} - \frac{1}{z}\frac{d^3 L_{air}(z)}{dz^3}\right)dz \qquad \text{Eq. A.1}$$

which depends only on $L(z)$. The lineal-path function and $\rho_{air}$ are used to obtain the size distribution by

$$f(z) = \frac{2}{\pi\rho_{air}}\left(\frac{1}{z^2}\frac{d^2 L_{air}(z)}{dz^2} - \frac{1}{z}\frac{d^3 L_{air}(z)}{dz^3}\right) \qquad \text{Eq. A.2}$$

where variable $z$ corresponds to the diameter of a sphere. Therefore, $f(\mathcal{R})$ is obtained by the definition $\mathcal{D} = 2\mathcal{R}$.

Since the entrained air voids only exist within the matrix of hydration products, or hydrated cement paste, it is important to use parameters normalized by unit volume of hydrated cement paste and not per unit volume of mortar in the calculation of the nearest-surface cumulative distribution function (CDF) $H_V(y)$. Both the entrained air volume fraction $\phi_{air}$ and the entrained air void number density $\rho_{air}$ must be scaled according to

$$\hat{\phi}_{air} = \frac{\phi_{air}}{1-\phi_{agg}} \text{ and } \hat{\rho}_{air} = \frac{\rho_{air}}{1-\phi_{agg}}, \qquad \text{Eq. A.3}$$

where $\phi_{agg}$ is the volume fraction of aggregates, $\hat{\phi}_{air}$ is the volume fraction of entrained air voids in the hydrated cement paste, and $\hat{\rho}_{air}$ is the number density of entrained air voids per unit volume of hydrated cement paste. The function $H_V(y)$ gives the probability that the periphery of the nearest entrained air void has been reached at a distance $\leq y$ from a random point in the paste. Lu and Torquato performed the first study of nearest-surface distribution functions for polydispersed sphere systems and obtained closed-form results [79]. Exact representation of the nearest-surface functions in two- or three-dimensions would require knowledge of the positions of each particle in the system (the *n*-particle probability density), which is unknown. However, a Percus-Yevick approximation for the nearest-surface cumulative distribution function in closed form is given by

$$H_V(y) = 1-\left(1-\hat{\phi}_{air}\right)\exp\left[-\pi\hat{\rho}_{air}\left(cy+dy^2+gy^3\right)\right], \quad y>0 \qquad \text{Eq. A.4}$$

where *c*, *d*, and *g* are

$$c = \frac{4\left\langle \mathcal{R}^2 \right\rangle}{1-\hat{\phi}_{air}},\ d = \frac{72\pi\hat{\rho}_{air}\left\langle \mathcal{R}^2 \right\rangle^2 - \hat{\phi}_{air}+1}{(4\pi\hat{\rho}_{air}\left\langle \mathcal{R}^3 \right\rangle - 3)^2} + \frac{4\left\langle \mathcal{R} \right\rangle}{(1-\hat{\phi}_{air})}, \text{ and} \qquad \text{Eq. 6.5}$$

$$g = \frac{4(2\pi\left\langle \boldsymbol{\mathcal{R}}^2 \right\rangle \hat{\rho}_{air} - \hat{\phi}_{air} + 1)}{2(1-\hat{\phi}_{air})^2}.$$

Though cumbersome, it is evident that $H_V(y)$ is dependent on $\hat{\phi}_{air}$, $\hat{\rho}_{air}$, and the first three moments of the size distribution, defined as

$$\left\langle \boldsymbol{\mathcal{R}}^k \right\rangle = \int \boldsymbol{\mathcal{R}}^k f(\boldsymbol{\mathcal{R}}) d\boldsymbol{\mathcal{R}}. \qquad \text{Eq. A.6}$$

Section A.4 provides an assessment of this closed-form technique by comparing its performance to a full 3D analysis of the entrained air void spatial arrangement by x-μCT.

The definition of $\overline{M}$ was set at the 95$^{th}$ percentile value of $H_V(y)$, or

$$\overline{M} = H_V^{-1}(0.95) \qquad \text{Eq. A.7}$$

In theory, the maximum spacing between a point in the paste and the periphery of the nearest air void is infinity (though in practice, it is the size of the system). Since $\overline{M}$ is probabilistic, it is simply defined at a reasonably high confidence level. For a more detailed treatment of the model and discussion of Eq. A.1 through Eq. A.7, refer to Chapter 3.

## A.3 Two-dimensional Analysis

As was discussed in Section A.1, measurements obtained from images are sensitive to the resolution of the image. Beginning with Eq. A.1, it is evident that all system parameters – and as a consequence, $\overline{M}$ itself – are dependent on $L_{air}(z)$, which is obtained by digital image analysis. The lineal-path function is computed by analyzing connected pixels along a line in two orthogonal directions, as explained in [163]. Therefore, the yardstick length $\varepsilon$ is the length of a single pixel. The yardstick length is the inverse of the scanning resolution. For example, if a sample is imaged at 1200 DPI, then

the yardstick length $\varepsilon$ = 1/1200 inches (21 μm). The values obtained for each parameter that contributes to $\overline{M}$ will change as the yardstick length underlying $L_{air}(z)$ becomes finer.

In order to understand this phenomenon toward controlling it, 2D images of air entrained mortar were obtained at various resolutions (Section A.3.1). The lineal-path function was obtained for each image, and the size distribution and spatial arrangement were determined by Eq. A.1 through Eq. A.7 (Section A.3.2). Finally, the self-similarity between successively finer images is studied and a critical or cutoff resolution is proposed.

### A.3.1 Image Acquisition and Thresholding

The mortar used in this study was designed to be representative of the mortar phase of a standard concrete. The mortar was prepared using an ASTM C 150 Type I/II ordinary portland cement and the fine aggregate was a locally-available concrete sand sourced from Shorter, Alabama, with a specific gravity of 2.65. The water-to-cement (*w*/*c*) ratio was 0.40 and the cement-to-sand ratio for all mixtures was 1:1.3. The mix designs as batched for testing are reported in Table A.1, which reflect adjustment for a fine aggregate adsorption capacity of 0.5%. Samples were cast in cylindrical molds with a diameter of 32 mm and demolded after 24 hours. The chemical admixture used to entrain air was a commercially-available wood rosin air entraining admixture (AEA). The dosage of AEA was within the manufacturer's recommendations.

**Table A.1**: As-batched mortar mix designs

| Constituent | Content |
|---|---|
| Water | 442 g |
| Cement | 1088 g |
| Fine Aggregate | 1426 g |
| AEA | 2.00 mL |

After moist-curing in lime water for 4 days, the samples were lapped with a diamond saw to expose a plane section for analysis. The samples were polished with successively finer polishing papers. To facilitate binarizing the images, the polished mortar surface was darkened with a black permanent marker and calcium carbonate powder was forced into the entrained air voids, similar to the method originally described in [84]. This technique allows the solid phase to appear black, while the entrained air void phase appears white. Images were acquired using a flatbed scanner at resolutions of 1200 DPI, 2400 DPI, 3200 DPI, and 4800 DPI.

For 8-bit grayscale images, each pixel is assigned a gray value ranging from 0 (purely black) to 255 (purely white). Thresholding the images involves selecting a gray value which demarcates the solid phases from the air void phase. In order to threshold each image in a consistent manner, the following thresholding technique was adopted. Each image was thresholded at every value from 0 to 255. At each threshold, the number of features per area $\rho_A$ was calculated. A threshold of 0 yields $\rho_A = 0$ (i.e. an image with no features) and a threshold of 255 yields $\rho_A = 1$ (i.e. an image with one large feature). The derivative of $\rho_A$ with respect to the gray threshold $d\rho_A/dT$ essentially gives the rate at which new features are resolved.

Figure A.1 is a plot of $d\rho_A/dT$ for a representative sample. Two peaks – one positive, one negative – are distinguishable on the figure. The first peak arises at

relatively low gray values and corresponds to the fine aggregate. These features resolve themselves at a faster rate due to the way the sand particles absorb the lacquer. The next peak lies at relatively higher gray values and corresponds to entrained air voids. The curve shown in Figure A.1 suggests that gray values ranging from 0 to 48 correspond to fine aggregate particles; gray values from 49 to 99 correspond to hydrated cement paste, and values from 100 to 255 correspond to entrained air voids.

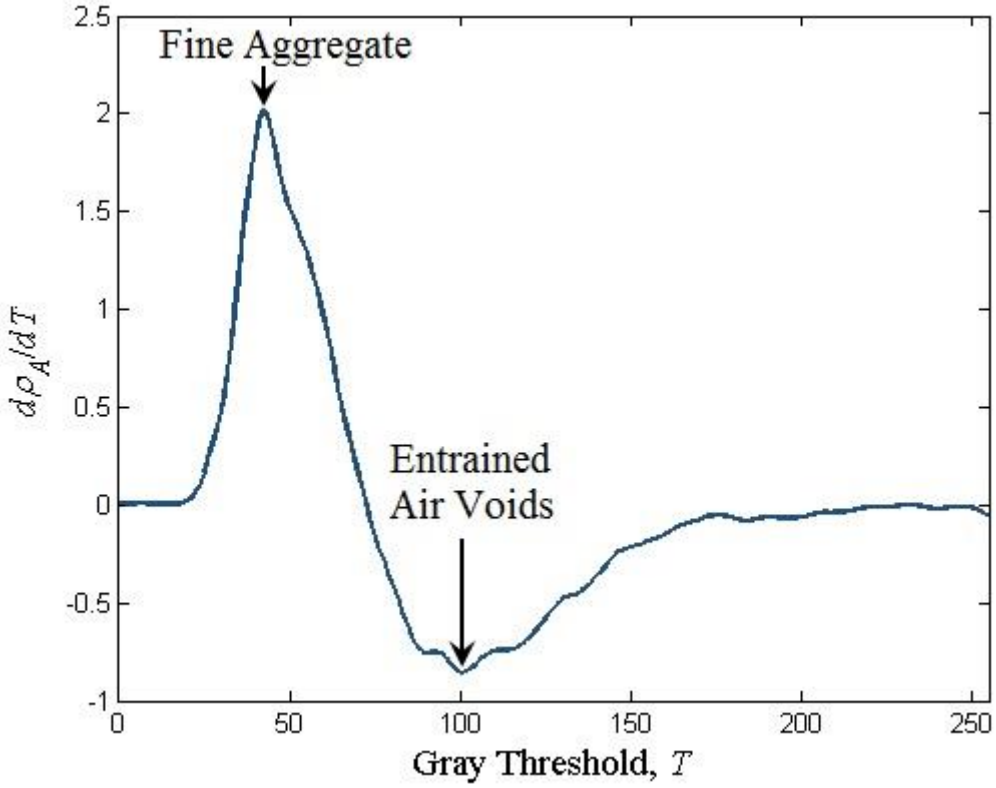


**Figure A.1:** Consistent thresholding technique used for image binarization

The sequential process of polishing, lacquering, and thresholding is illustrated in Figure A.2. The first image (Figure A.2a) shows a plane polished mortar specimen. Figure A.**2**b is a prepared specimen, in which the solids appear black due to black lacquering and the voids appear white due to calcium carbonate impregnation. The last image reflects the thresholding as prescribed by $d\rho_A/dT$ in Figure A.1. The gray phase

represents the hydrated cement paste phase, the light blue represents the fine aggregate particles, and the dark blue represents the entrained air voids. Inspection of Figure A.2a – Figure A.2c shows the appropriateness of the technique.

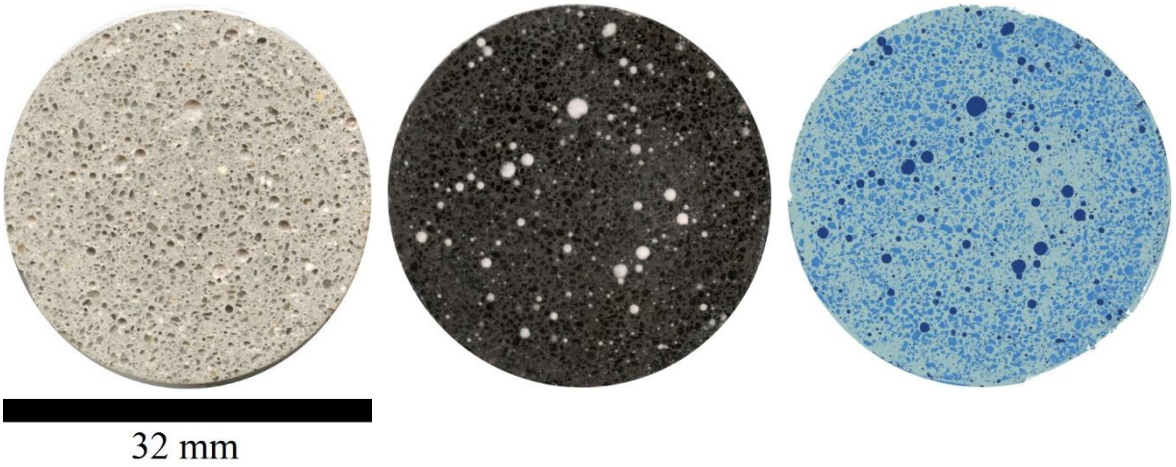


(a) (b) (c)

**Figure A.2:** (a) Plane polished mortar section; (b) black lacquered section impregnated with white calcium carbonate powder; (c) final thresholded image

### A.3.2 Size Distribution Analysis and Fractal Interpretation

In Figure A.2c, the mortar is idealized as a three phase material, where $\phi_{FA}$ represents the volume fraction of fine aggregate, $\phi_{HCP}$ represents the volume fraction of hydrated cement paste, and $\phi_{air}$ represents the volume fraction of entrained air voids, where $\phi_{air} + \phi_{HCP} + \phi_{EA} = 1$.

The size distribution PDFs for each resolution are shown in Figure A.3, where progressively lighter curves signal progressively finer resolutions and therefore progressively smaller yardstick lengths. The distributions all exhibit the approximately lognormal behavior which is typically observed in air-entrained concrete [15]. While all the distributions have a positive skew, the skew increases as resolution increases and as

the yardstick length decreases. This is partially attributed to the fact that finer features will resolve themselves at a rate governed by $\varepsilon$.

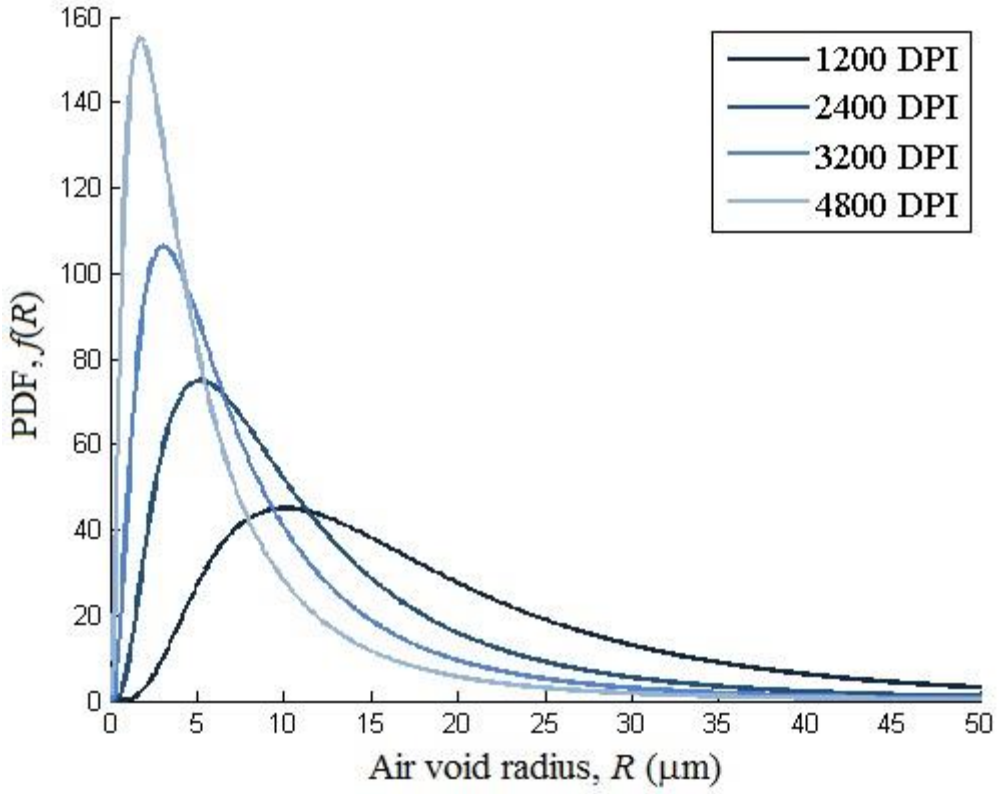


**Figure A.3**: Entrained air void size distribution at each resolution

Per Mandelbrot [153], the fractal dimension $D$ is related to the number $N_f$ of features resolved at a yardstick length $\varepsilon$ by the expression

$$N_f = \psi \varepsilon^{-D} \qquad \text{Eq. A.8}$$

where $\psi$ is a constant providing dimensional consistency. From Eq. A.9, it follows that

$$D = -\frac{\log N_f}{\log \varepsilon} \qquad \text{Eq. A.9}$$

The classical approach to calculating $D$ is to count the features resolved at successively finer yardstick lengths. In this study, $N_f$ is the number density $\hat{\rho}_{air}$ and $\varepsilon$ is the pixel size.

A log-log plot (Figure A.4) reveals $-D$ simply to be the fitted slope through $\log(\rho_{air})$ versus $\log(\varepsilon)$, and $\psi$ is the intercept with the ordinate axis. In this case, $D = 1.43$ and $\psi = 39790$.

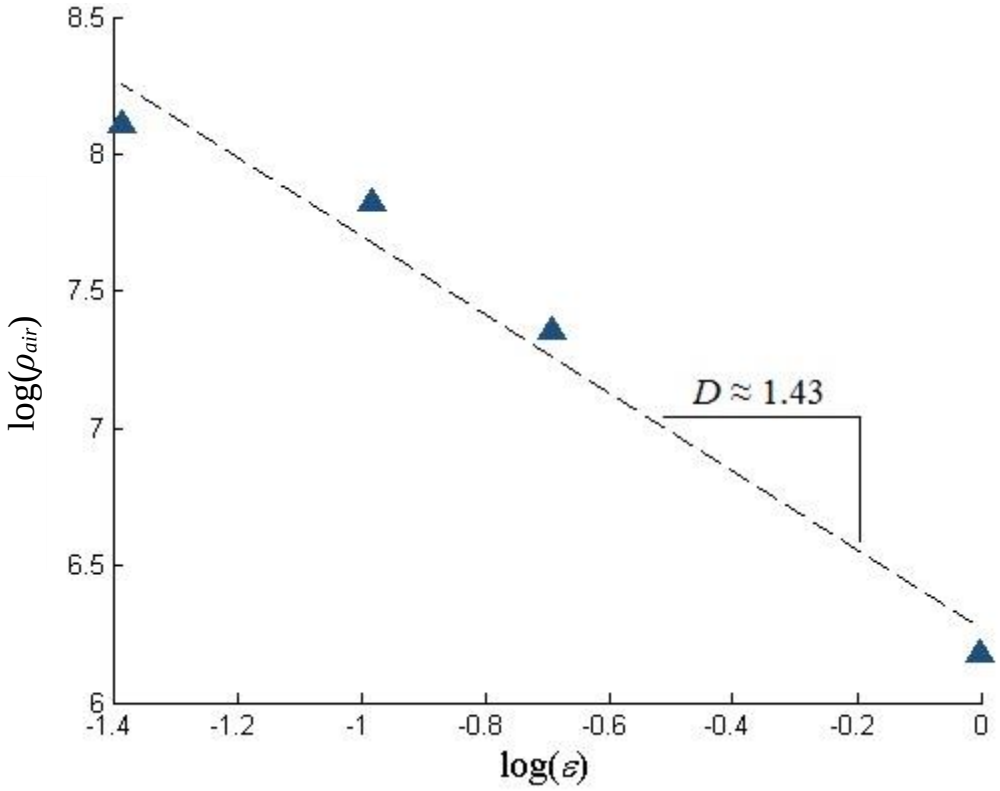


**Figure A.4:** Double logarithmic plot used to estimate $D$

To illustrate how $D$ may be used in this complex problem, imagine if entrained air voids were selected randomly from a volume of mortar. The probability of selecting $\hat{\rho}_{air}$ air voids with replacement with radius less than $\mathcal{R}$ is

$$P(\hat{\rho}_{air} \text{ with radius} \le \mathcal{R}) = F(\mathcal{R})^{\hat{\rho}_{air}} \qquad \text{Eq. A.10}$$

which is simply the CDF raised to the power $\hat{\rho}_{air}$. (Note that for any CDF $G(x)$, it is true that $G(x)^{\alpha}$ is also a CDF.) Let $F(\mathcal{R}|\varepsilon_a)$ denote a size distribution CDF measured from a

digital image with yardstick length $\varepsilon_a$, and $F(\boldsymbol{\mathcal{R}}\ \varepsilon_b)$ denote a size distribution CDF measured from a digital image with yardstick length $\varepsilon_b$. The two CDFs are related by

$$F(\boldsymbol{\mathcal{R}} \mid \varepsilon_a)^{\hat{\rho}_{air,a}} = F(\boldsymbol{\mathcal{R}} \mid \varepsilon_b)^{\hat{\rho}_{air,a}} \qquad \text{Eq. A.11}$$

Where $\rho_{v,a}$ and $\rho_{v,b}$ denote number densities obtained from digital images with yardstick lengths $\varepsilon_a$ and $\varepsilon_b$, respectively. Figure A.5 illustrates Eq. A.11 empirically, where $F(\boldsymbol{\mathcal{R}} \mid \varepsilon_{1200})^{\hat{\rho}_{air,1200}}$, $F(\boldsymbol{\mathcal{R}} \mid \varepsilon_{2400})^{\hat{\rho}_{air,2400}}$, and $F(\boldsymbol{\mathcal{R}} \mid \varepsilon_{3200})^{\hat{\rho}_{air,3200}}$ are plotted against $F(\boldsymbol{\mathcal{R}} \mid \varepsilon_{4800})^{\hat{\rho}_{air,4800}}$. A dotted line represents the line of equality.

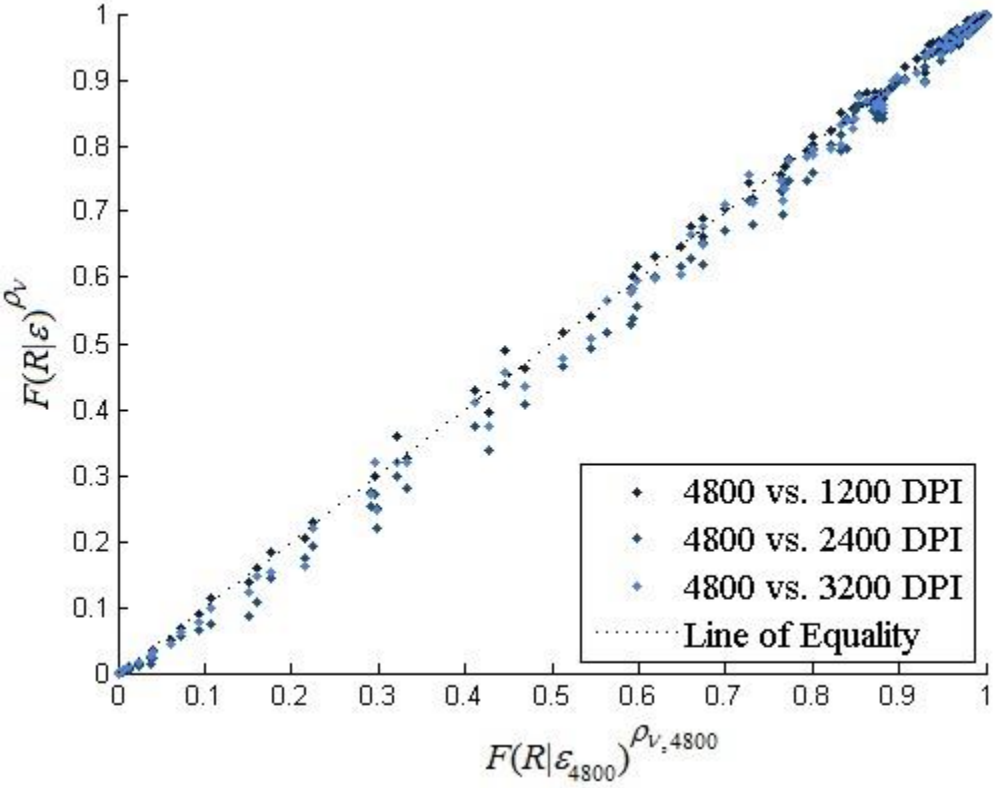


**Figure A.5:** Example of the linear relationship of $F(R|\varepsilon)^{\rho V}$ between digital images

Using the relationship that $\hat{\rho}_{air} = \psi\varepsilon^{-D}$ (i.e., Eq. A.8), Eq. A.11 may be rewritten as

$$F(\mathcal{R} \mid \varepsilon_a) = F(\mathcal{R} \mid \varepsilon_b)^{\left(\frac{\varepsilon_b}{\varepsilon_a}\right)^{-D}} \qquad \text{Eq. A.12}$$

which shows that the size distribution CDFs between any two resolutions may be equated with knowledge of ratio between their yardstick lengths $\varepsilon_a/\varepsilon_b$ and the fractal dimension *D*. Eq. A.12 also implies that the CDFs obtained in this study at one resolution may be "scaled" to the resolution of another image. For example, let $F(\mathcal{R} \mid \varepsilon_{1200})$ denote the EA void size distribution CDF obtained from the 1200 DPI image, and let $F(\mathcal{R} \mid \varepsilon_{2400})$ denote the EA void size distribution CDF obtained from the 2400 DPI image. Yardstick lengths $\varepsilon_{1200}$ = 20.4 μm and $\varepsilon_{2400}$ = 10.2 μm. Eq. A.13 shows that $F(\mathcal{R} \mid \varepsilon_{2400})$ is equivalent to a CDF obtained by scaling $F(R \mid \varepsilon_{1200})$ to a finer resolution of 2400 DPI, denoted by $F(\mathcal{R} \mid \varepsilon_{1200} \rightarrow \varepsilon_{2400})$. Therefore,

$$F(\mathcal{R} \mid \varepsilon_{2400}) = F(\mathcal{R} \mid \varepsilon_{1200} \rightarrow \varepsilon_{2400}) = F(\mathcal{R} \mid \varepsilon_{1200})^{\left(\frac{\varepsilon_{1200}}{\varepsilon_{2400}}\right)^{-D}} \qquad \text{Eq. A.13}$$

Figure A.6a – Figure A.6d show examples of this scaling between all of the CDFs in this study. In Figure A.6a, the dotted line represents the original size distribution CDF obtained from the 1200 DPI image. The colored solid lines represent the original CDFs for the other resolutions, where lighter colors correspond to finer resolutions (i.e., the lightest curve is 4800 DPI and the darkest is 2400 DPI). The dashed lines represent the results of scaling the 1200 DPI CDF to the other resolutions in the same fashion as the example in Eq. A.13. The scaled curves show very good agreement with the original curves, which is quite remarkable given the difference in resolutions. For example, the 4800 DPI image is 16 times as large as the 1200 DPI image and can resolve features which are ¼ of the size of a pixel in the 1200 DPI image. However,

Figure A.6a shows that a reasonably good fit to $F(\mathcal{R}|\varepsilon_{4800})$ can be obtained using only $F(\mathcal{R}|\varepsilon_{1200})$, the ratio of their yardstick lengths, and *D*. Figure A.6b, Figure A.6c, and Figure A.6d show the results of scaling $F(\mathcal{R}|\varepsilon_{2400}), F(\mathcal{R}|\varepsilon_{3200})$, and $F(\mathcal{R}|\varepsilon_{4800})$, respectively, following the same procedure as was done with $F(\mathcal{R}|\varepsilon_{1200})$ in Figure A.6a.

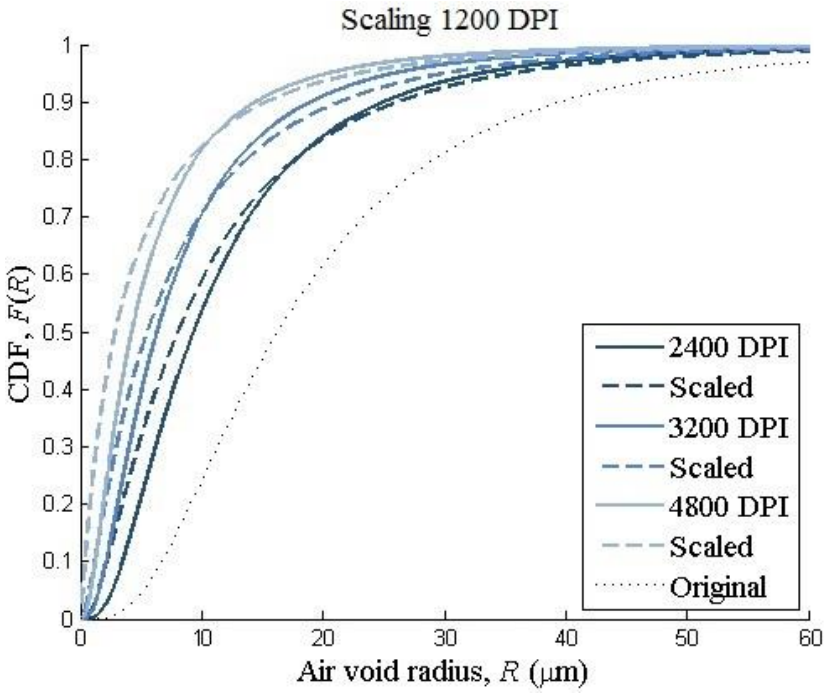


(a)

**Figure A.6:** Results of scaling CDFs of (a) 1200 DPI, (b) 2400 DPI, (c) 3200 DPI, and (d) 4800 DPI to the other resolutions

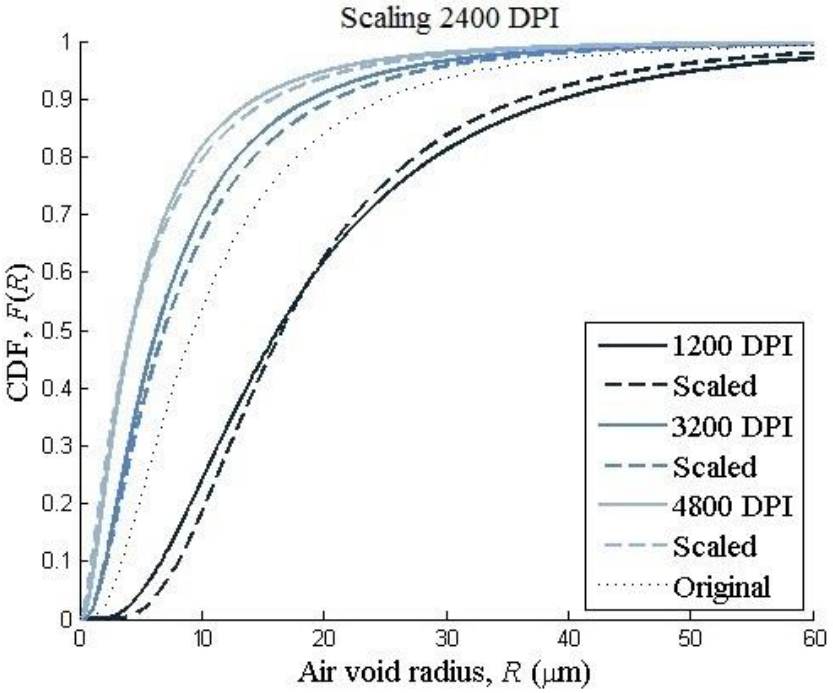


(b)

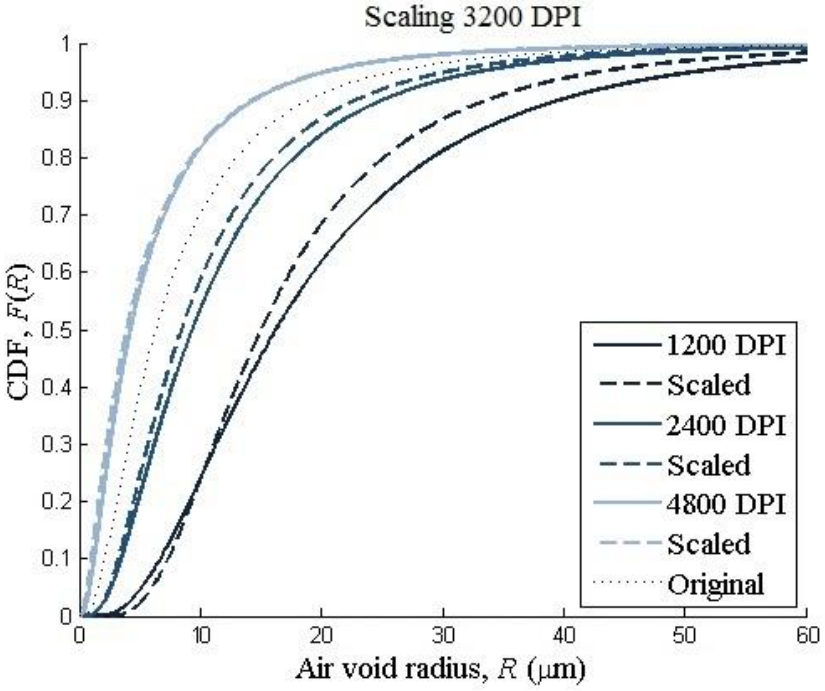


(c)

**Figure A.6:** (Continued) Results of scaling CDFs of (a) 1200 DPI, (b) 2400 DPI, (c) 3200 DPI, and (d) 4800 DPI to the other resolutions

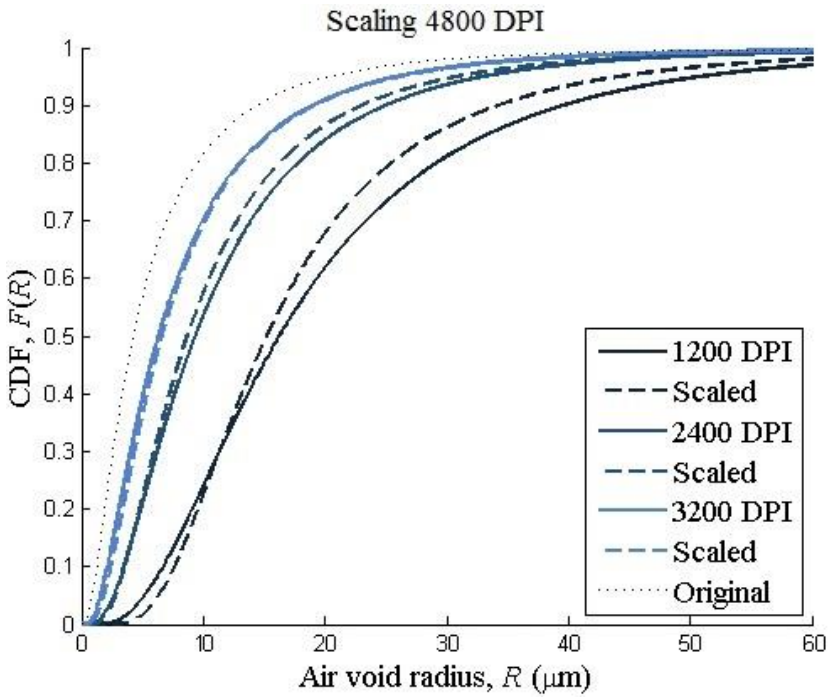


(d)

**Figure A.6:** (Continued) Results of scaling CDFs of (a) 1200 DPI, (b) 2400 DPI, (c) 3200 DPI, and (d) 4800 DPI to the other resolutions

Since the PDF is the first derivative of the CDF, then any size distribution $f(\mathcal{R} \mid \varepsilon_a)$ may be obtained from any size distribution $f(\mathcal{R} \mid \varepsilon_b)$ by

$$f(\mathcal{R} \mid \varepsilon_a) = \left(\frac{\varepsilon_b}{\varepsilon_a}\right)^{-D} f(\mathcal{R} \mid \varepsilon_b) F(\mathcal{R} \mid \varepsilon_b)^{\left(\frac{\varepsilon_b}{\varepsilon_a}\right)^{-D}-1} \qquad \text{Eq. A.14}$$

As mentioned previously, $\hat{\rho}_{air} = \psi \varepsilon^{-D}$. The volume fraction for a spherical void or inclusion may be calculated from the number density and size distribution by $\hat{\phi}_{air} = (4/3)\pi \langle \mathcal{R}^3 \rangle \hat{\rho}_{air}$. Therefore, if $\hat{\rho}_{air}$ is obtained by Eq. A.1 and $f(\mathcal{R})$ is obtained Eq. A.2 from an image with yardstick length $\varepsilon$, the parameters can be scaled to approximate the same parameters obtained from an image with a different resolution. Those scaled parameters may be used Eq. A.4 through Eq. A.6 in the calculation of $\overline{M}$. This has been

done for the four images (i.e., those with resolutions of 1200 DPI, 2400 DPI, 3200 DPI, and 4800 DPI) under investigation, and the results are reported in Table A.2. The shaded values on the diagonal represent the original (i.e., unscaled) values of $\overline{M}$ obtained from image analysis. The table shows that raw values of $\overline{M}$ range from 58.69 μm in the coarsest image (1200 DPI) to 36.36 μm in the finest image (4800 DPI) – an error of 61 percent. Rows of the table reflect pseudo-values of $\overline{M}$ obtained from scaling the size distribution parameters. For example, the first row, second column cell represents scaling the parameters from the 2400 DPI image to the 1200 DPI image (downscaling), while the second row, first column cell represents scaling the parameters of the 1200 DPI image to the 2400 DPI image (upscaling). The maximum error between two scaled and original values of $\overline{M}$ is 7.5% (specifically, scaling 2400 DPI to 4800 DPI), while the average absolute value of the error between the scaled $\overline{M}$ and original $\overline{M}$ is 4.4%. Scaling measurements from finer resolutions down to coarser resolutions is apparently more accurate than the reverse. For example, all resolutions finer than 1200 DPI are able to yield the value of 58.69 μm for $\overline{M}$ when scaled downwards.

**Table A.2:** Measurements of $\overline{M}$ at differing resolutions and cross-resolution scaling

| | **1200 DPI** | **2400 DPI** | **3200 DPI** | **4800 DPI** |
|---|---|---|---|---|
| **1200 DPI** | 58.69 μm | 58.69 μm | 58.69 μm | 58.69 μm |
| **2400 DPI** | 43.77 μm | 41.45 μm | 44.40 μm | 44.17 μm |
| **3200 DPI** | 39.72 μm | 39.02 μm | 37.54 μm | 39.78 μm |
| **4800 DPI** | 34.44 μm | 33.65 μm | 34.40 μm | 36.36 μm |

The good agreement between the values in Table A.2 suggests that this resolution dependence in measurements can be understood and harnessed. For example, recent studies on the topic of automated EA void analysis in concrete have been carried out at

pixel resolutions ranging from 1.7 μm [164] to 16.9 μm [84], with many resolutions in between [165, 166, 167, 168]. Interpreting these studies is challenging in light of the behavior observed in Table A.2, where large discrepancies are observed for the *same image* at pixel resolutions varying from 5.1 μm (4800 DPI) to 20.4 μm (1200 DPI). The technique presented herein has the potential to scale these measurements to a benchmark resolution and discern whether differences are the result of different system morphologies or merely image resolution.

However, the question of a critical resolution is still unanswered. In [158], researchers rectified this problem by identifying a critical magnification below which their measurements of outer mitochondrial membrane surface areas no longer exhibited a log-linear relationship. Essentially, if the entrained air void system were perfectly fractal, then fractal theory suggests that the voids would become infinitely small as $\varepsilon \rightarrow 0$. However, Mandelbrot observed that this is impossible for natural structures [153]. For example, the entrained air voids cannot be infinitely small; they must be large enough to stabilize during mixing and cement hydration. Furthermore, the anticipated low end entrained air void diameters overlap with the anticipated high end capillary pores (macropores), thus obfuscating the difference between the two types of voidspace. It was observed in this study that the relationship between number density and yardstick length ceases to be perfectly log-linear below 7.6 μm, or 3200 DPI. Figure A.7 is a new representation of Figure A.4 where the log-linear fit used to obtain $D$ was truncated at 3200 DPI (the vertical dashed line). A single dashed line now connects all data points which are coarser than 4800 DPI, producing a critical dimension $D_{crit} = 1.68$.

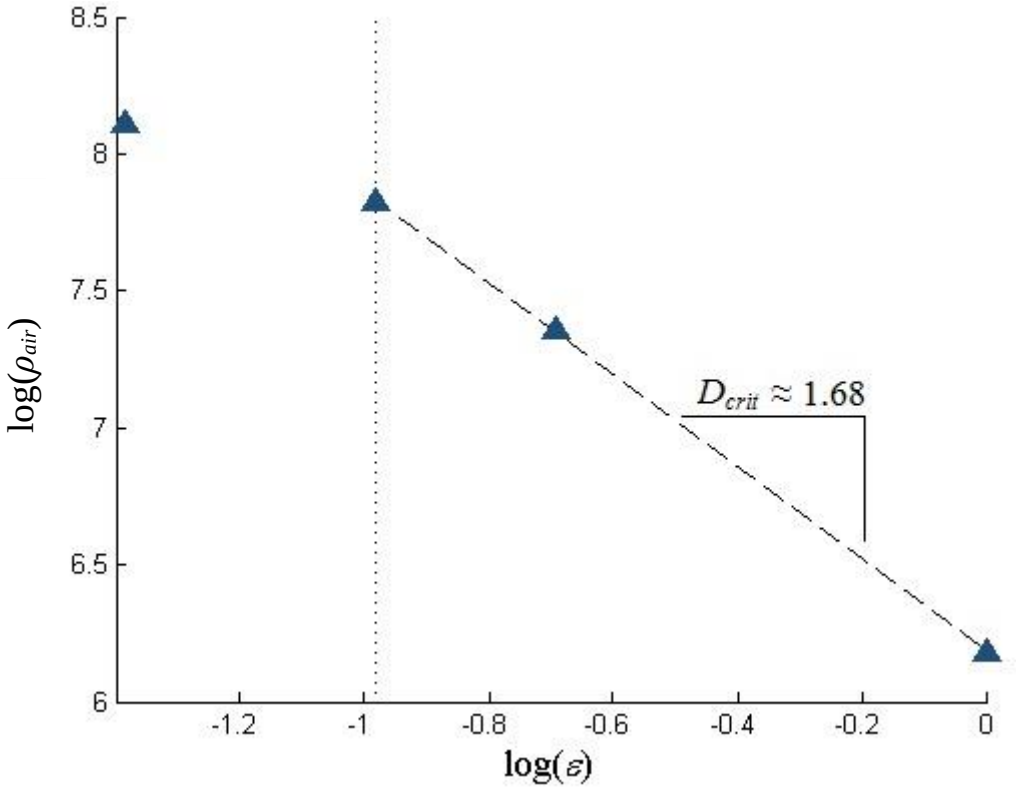


**Figure A.7:** Fractal dimension assuming a critical resolution

The analysis summarized in Table A.2 was repeated using $D_{crit}$, and the results are shown in Table A.3. This modification reduces the error in scaled values of $\overline{M}$ for every resolution save for 4800 DPI, which is past the critical resolution of 3200 DPI. If values related to 4800 DPI are disregarded because they surpass the critical resolution, the average error drops below 2%. For this reason, this study concludes that 3200 DPI – where each pixel is 7.6 μm – may be a useful benchmark for this type of analysis. This has the potential to reconcile discrepancies in the literature on the topic of air void analysis using digital images because it relies only on the ratio of image resolutions and $D_{crit}$. In the next section, a 3D image was scanned at an approximately-similar resolution of 6 μm per voxel to reflect this finding.

**Table A.3:** Cross-resolution scaling using the critical resolution

| | **1200 DPI** | **2400 DPI** | **3200 DPI** | **4800 DPI** |
|---|---|---|---|---|
| **1200 DPI** | 58.69 μm | 57.80 μm | 58.69 μm | 57.97 μm |
| **2400 DPI** | 41.76 μm | 41.45 μm | 40.74 μm | 39.85 μm |
| **3200 DPI** | 37.22 μm | 35.44 μm | 37.54 μm | 35.19 μm |
| **4800 DPI** | 31.45 μm | 29.45 μm | 30.23 μm | 36.36 μm |

## A.4 Three-dimensional Analysis

This section presents a full 3D analysis of air entrained mortar using x-μCT. The approach allows for a comprehensive analysis of the efficacy of the 2D reconstruction and analysis method discussed in the previous section, and also provides a frame of reference for assessing the closed-form expression used to calculate $\overline{M}$ .

An overview of x-μCT and its application to cement-based materials can be found in [104]. A cylindrical sample measuring 1 cm in diameter and 1 cm in length was cast from the same mortar mix that was used to cast the specimens for the 2D analysis in the preceding section (see Table 4.1). The sample was scanned at 100 kV and 60 μA using the "Ultratom" by RX Solutions at the Laboratoire Navier at École Nationale des Ponts et Chaussées (ENPC). The instrument used 1440 projections, with an average of 8 images per projection. Images were acquired every 0.5 seconds. Figure A.8a shows a 5 mm square area from the middle of a representative slice from the scan. The image was separated into fine aggregates, cement paste, and air voids by automatic thresholding. Figure A.8b shows a false-color 3D reconstruction of the scan, where fine aggregate particles are gold and entrained air voids are blue. The empty space in Figure A.8b corresponds to the hydrated cement paste. The section for analysis was a cube measuring 840 voxels per side, representing a cube of material measuring 5 mm per side (note that Figure A.8b only shows 2.5 mm per side to show detail).

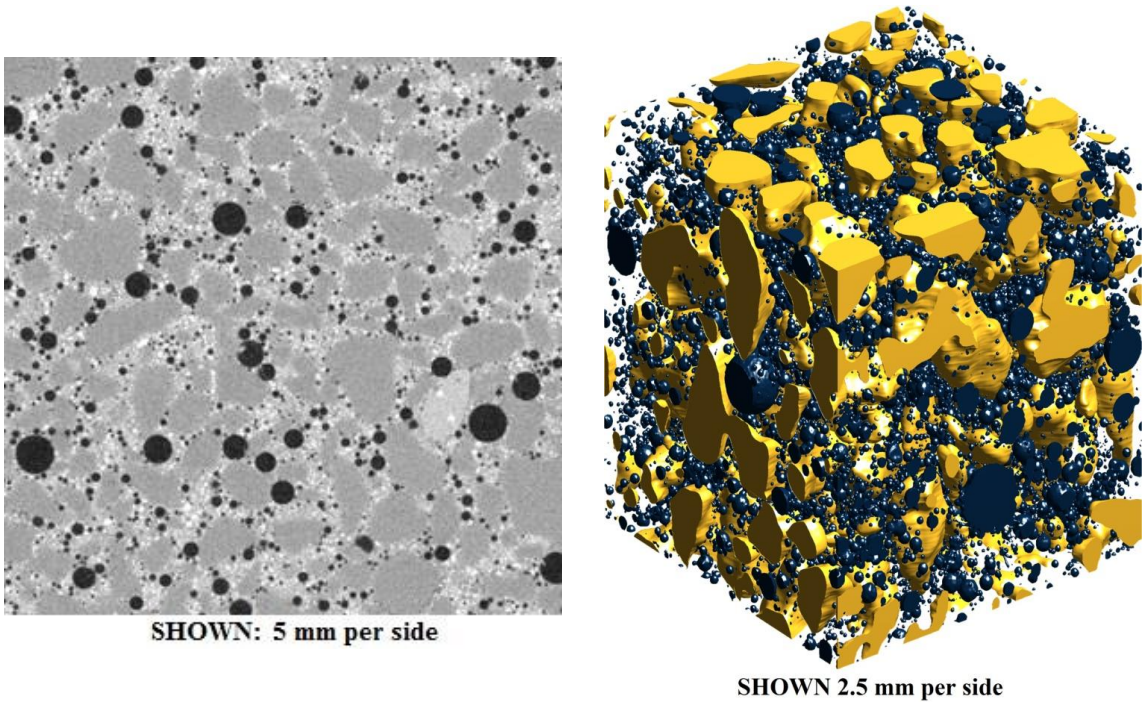


(a) (b)

**Figure A.8:** (a) A 5-mm square representative sample slice from x-μCT and (b) a 2.5-mm cubic reconstruction of the aggregates in gold and entrained air voids in blue.

The 3D image (from which Figure A.8b is obtained) allows the closed-form nearest-surface equations to be tested because the microstructure at any point in space is known. The strategy is as follows: first, obtain the size distribution parameters ($\hat{\phi}_{air}$, $\hat{\rho}_{air}$, $f(\mathcal{R})$) directly and substitute them into the closed-form expressions for $\overline{M}$ (Eq. A.4 – Eq. A.7), which is denoted by $\overline{M}_{CF}$. This removes the uncertainty in these 3D parameters because the x-μCT scan allows them to be found directly without the need for probabilistic reconstruction from 2D images. The second step is to obtain the discrete distribution of $H_V(y)$ directly from the x-μCT image, thereby allowing $\overline{M}$ to be observed directly, which is denoted by $\overline{M}_D$. The value of $\overline{M}_D$ provides a frame of reference for interpreting $\overline{M}_{CF}$. The third and final step is to compare the value of $\overline{M}_{CF}$ obtained in 3D

at the resolution of the x-μCT equipment to the trend in $\overline{M}$ which was observed in Section A.3 ($\overline{M}_D$ is not used as a basis for comparison because the closed-form expression for $H_V(y)$ was used for all of Section A.3).

The volume fraction of entrained air voids in the cement paste is simply equal to the sum of pixels corresponding to entrained air voids normalized by the sum of entrained air void pixels and hydrated cement paste pixels. This statistic is not sensitive to edge effects. However, an unbiased counting frame was used to calculate the number density to control for edge effects [116]. Three orthogonal faces of the mortar volume were chosen. Entrained air voids which intersected these three faces and voids which intersected no edges were considered to be inside the volume, while voids which intersected the opposite three orthogonal faces were considered to be outside the volume. This accounts for the physical reality that the centroids of some peripheral voids actually lay outside the mortar volume, while some lay inside. The size distribution was determined by back-calculating the radius of each entrained air void from its volume. Only voids which lay entirely within the volume were considered when calculating the size distribution because considering only partial volumes would result in artificially small radii. With these parameters known, $\overline{M}_{CF}$ was determined by direct application of Eq. A.4 – Eq. A.7.

The true 3D spatial arrangement was determined by first finding the discrete nearest-surface probability mass function $h_V(y_i)$, and then obtaining the discrete CDF from $H_V(y_j) = \sum_{i=1}^{j} h_V(y_i)$. This is easily accomplished using a distance transform, which is an image processing technique that gives the Euclidean distance $y_i$ from each

cement paste voxel to the nearest entrained air void voxel. A histogram of these lengths $y_i$ yields $h_V(y_i)$. $\overline{M}_D$ was then determined by its definition in Eq. A.7.

Figure A.9 shows the discrete CDF $H_V(y_i)$ in light blue. The continuous CDF $H_V(y)$ which uses a Percus-Yevick approximation is shown as a dark blue line. Calculating the spacing factor directly gives $\overline{M}_D$ = 42.0 μm, while calculating the spacing factor in closed-form gives $\overline{M}_{CF}$ = 37.2 μm. In this case, $\overline{M}_{CF}$ is about 11% lower than $\overline{M}_D$. Despite this, the two behaviors are in very good agreement. $\overline{M}_D$ may be influenced by the fact that a "point" or "surface" is ill-defined in a 3D voxellated image. For example, two adjacent voxels are considered to be one voxel apart, which is the distance from the *center* of one voxel to the *center* of the next. The saw-tooth edges of the digitized entrained air voids and the imperfect representation of a surface in a discrete microstructure may result in an artificially high value of $\overline{M}_D$. Because of this, the error between $\overline{M}_{CF}$ and $\overline{M}_D$ may be lower than reported.

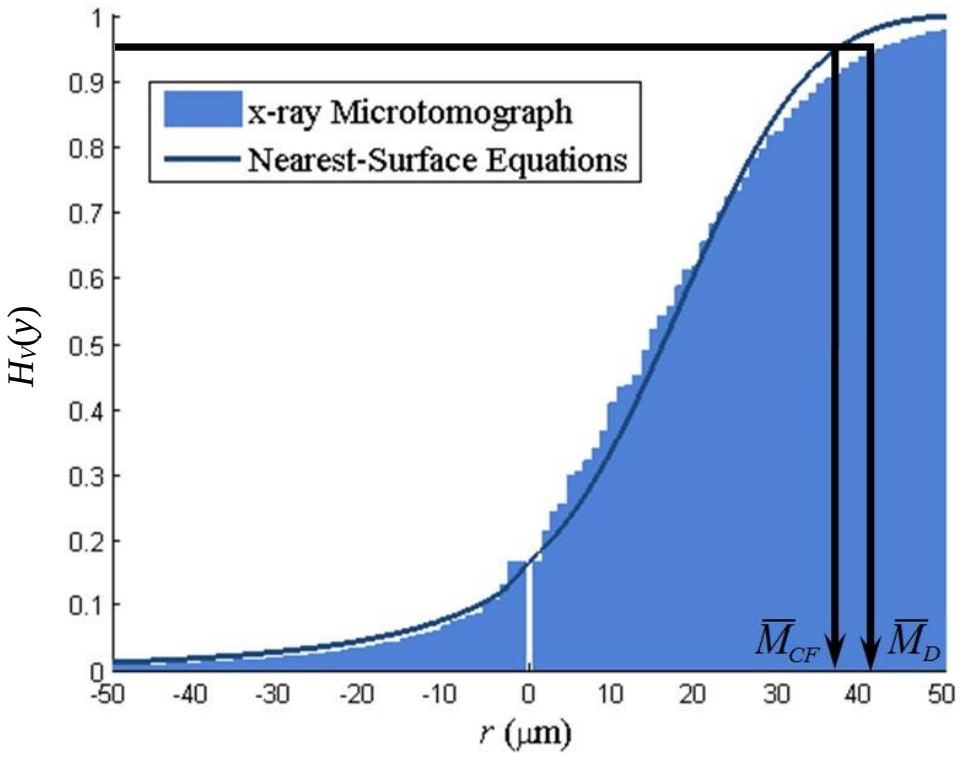


**Figure A.9:** Comparison of the nearest-surface equations to direct measurement of air void spacing

Figure A.10 shows the behavior observed in Section A.3 by plotting $\overline{M}$ versus in $\varepsilon$. (Note that these are the same values of $\overline{M}$ from the diagonal of Table A.2 and Table A.3) The analytical value of $\overline{M}$ from Section A.4 is denoted by an open data point. The 2D and 3D analytical values are in good agreement with each other. This is rather remarkable when one considers different approaches for calculating $\overline{M}$ in Sections A.3 and A.4. The 2D analysis required a high degree of preparation to ready the sample's surface for analysis, where the phases are separated by color (i.e. using an optical technique) rather than by their composition. The 2D technique also rests on a robust underlying analytical and probabilistic framework to obtain 3D statistics. By contrast, the phases were demarcated by x-ray analysis in Sections A.4 due to differences in density

between phases. The 3D measurements were rather straightforward and did not rely on an underlying theory of random heterogenous materials. However, if $\overline{M}$ were to be calculated from a 2D image with the same yardstick length as the x-ray microtomographic image ($\varepsilon$ = 6 μm for a resolution of about 4200 DPI) , one would expect to calculate a data point for $\overline{M}$ that would lie at the same location as the open square in Figure A.10. The differences in equipment acquisition and operating costs between 2D and 3D imaging techniques are staggering. From the standpoint of quality control and quality assurance, the 2D analytical technique recovers a great deal of information while demanding far less capital.

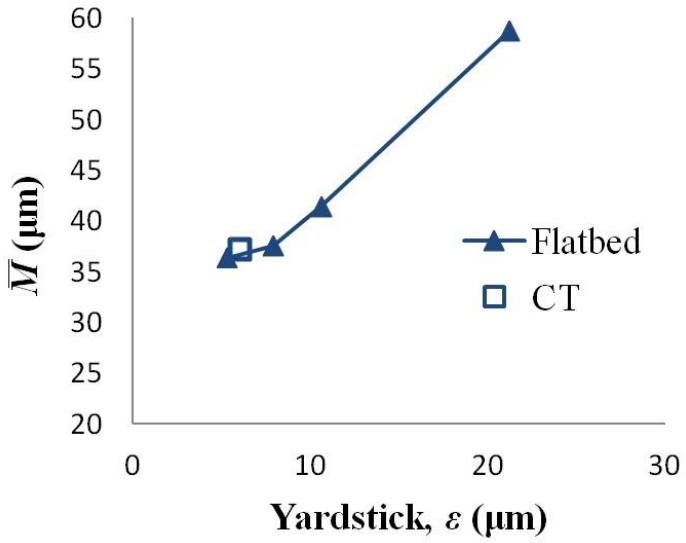


**Figure A.10:** Influence of yardstick length on $\overline{M}$ , with 3D validation

## A.5 Conclusions

The data in this contribution demonstrates that automated measurements of the size distribution parameters of the entrained air void system depend on the image resolution. Using the analytical technique in Chapter 3, the resolution-dependence of stereological measurements was interpreted in terms of the fractal dimension.

Furthermore, the procedure in Section 3 may find broad application as a technique to scale automated measurements reported in the literature to those of a benchmark resolution. The 3D analysis also helps quantify the gap between theory and reality when modeling entrained air voids systems. Based on these results, the following conclusions can be drawn:

1. A scanning resolution of 3200 DPI ($\varepsilon$ = 7.6 μm) is recommended for automated analysis of air entrained concrete. At this resolution and at finer resolutions beyond it, the system begins to converge (i.e. the system does not become appreciably more complex at values of $\varepsilon$ < 7.6 μm). It was shown that the scaling law obtained from this approach allows very similar values of $\overline{M}$ to be obtained across resolutions, thereby moving the model towards scale independence.
2. The 3D analysis suggests that the closed-form equations sufficiently estimate $\overline{M}$ . Therefore, entrained air voids may be assumed to be unclustered in the bulk cement paste phase of the material.
3. The 2D results and 3D results are in good agreement. It was shown that the analytical technique accurately reconstructs 3D entrained air void system parameters that can be used to calculate $\overline{M}$ . This is profoundly useful for the construction industry, where detailed 3D analyses are typically impractical.

# REFERENCES


[1] H. M. Jennings, J. W. Bullard, J. J. Thomas, J. E. Andrade, J. J. Chen and G. W. Scherer, "Characterization and modeling of pores and surfaces in cement," *Journal of Advanced Concrete Technology,* vol. 6, no. 1, pp. 5-29, 2008.

[2] T. C. Powers, "The air-requirement of frost-resistant concrete," *Proceedings of the Highway Research Board,* vol. 29, pp. 194-211, 1949.

[3] J. F. Young, S. Mindess, R. J. Gray and A. Bentur, The Science and Technology of Civil Engineering Materials, Upper Saddle River, NJ: Prentice Hall, 1998.

[4] J. W. Tedesco, J. C. Powell, C. A. Ross and M. L. Hughes, "A strain-rate dependent concrete material model for ADINA," *Computers & Structures,* vol. 64, no. 5/6, pp. 1053-1067, 1997.

[5] S. Nemat-Nasser and H. Deng, "Strain-rate effect on brittle failure in compression," *Acta Metallurgica et Materialia,* vol. 42, no. 3, pp. 1013-1024, 1994.

[6] B. Paliwal and K. T. Ramesh, "An interacting micro-crack damage model for failure of brittle materials under compression," *Journal of the Mechanics and Physics of Solids,* vol. 56, pp. 896-923, 2008.

[7] B. Paliwal and K. T. Ramesh, "Effect of crack growth dynamics on the rate-sensitive behavior of hot-pressed boron carbide," *Scripta Materialia,* vol. 57, no. 6, pp. 481-484, 2007.

[8] B. Paliwal, K. T. Ramesh and J. W. McCauley, "Direct observation of the dynamic

compressive failure of a transparent polycrystalline ceramic (AlON)," *Journal of the American Ceramic Society,* vol. 89, pp. 2128-2133, 2006.

[9] L. Graham-Brady, "Statistical characterization of meso-scale uniaxial compressive strength in brittle materials with randomly occurring flaws," *International Journal of Solids and Structures,* vol. 47, no. 18-19, p. 2398–2413, 2010.

[10] B. R. K. Paliwal, "An interacting micro-crack damage model for failure of brittle materials under compression," *Journal of Mechanics and Physics of Solids,* vol. 56, no. 3, pp. 896-923, 2007.

[11] M. Blaszkiewicz, "Flawed freeze-thaw testing standards unreliable for predicting concrete tie failures," RJ Lee Group, 30 July 2012. [Online]. Available: http://www.insights.rjlg.com/2012/07/flawed-freeze-thaw-testing-unreliable-predicting-concrete-failures/. [Accessed 2013].

[12] F Wire, "Insulating high-speed tracks against freezing, thawing," Firstpost, 30 October 2012. [Online]. Available: http://www.firstpost.com/fwire/insulating-high-speed-tracks-against-freezing-thawing-508385.html. [Accessed 2013].

[13] CBS Boston, "Concrete Falls From Boston Overpass, MBTA Station Ceiling," 29 January 2013.

[14] L. Pincock, W. Hintze and K. Shirai, "Lessons learned from Three Mile Island packaging, transportation, and dispostition that apply to Fukushima Daiichi recovery," Idaho National Laboratory, 2012.

[15] K. A. Snyder, "A numerical test of air void spacing equations," *Advanced Cement Based Materials,* vol. 8, no. 1, pp. 28-44, 1998.

[16] M. Bould, S. Barnard, I. D. Learmonth, J. L. Cunningham and J. R. W. Hardy, "Digital image analysis: improving accuracy and reproducibility of radiographic measurement," *Clinical Biometrics,* vol. 14, no. 6, pp. 434-437, 1999.

[17] L. Du and K. J. Folliard, "Mechanisms of air entrainment in concrete," *Cement and Concrete Research,* vol. 35, no. 8, pp. 1463-1471, 2005.

[18] R. Felice, J. M. Freeman and M. T. Ley, "Durable Concrete with Modern Air-Entraining Admixtures," *Concrete International,* vol. 36, no. 8, pp. 37-45, 2014.

[19] Z. Sun and G. W. Scherer, "Effect of air voids on salt scaling and internal freezing," *Cement and Concrete Research,* vol. 40, no. 2, pp. 260-270, 2010.

[20] B. T. S. Lu, "Nearest-surface distribution functions for polydispersed particle systems," *Physical Review A,* vol. 45, no. 8, pp. 5530-5544, 1992.

[21] S. Torquato and B. Lu, "Chord-length distribution function for two-phase random media," *Physical Review E,* vol. 47, no. 7, pp. 2950-2953, 1993.

[22] D. Thompson, S. Brown, S. Mallonee and D. Sunshine, "Fatal and non-fatal injuries among US Air Force personnel resulting from the terrorist bombing of the Khobar Towers," *Journal of Traumatic-Injury Infection and Critical Care,* vol. 52, no. 2, pp. 308-15, 2004.

[23] R. Esposito and J. Black, "Fragments of wood and concrete pulled from Boston victims," NBC News, 17 April 2013. [Online]. Available: http://news.ca.msn.com/.

[24] C. f. D. C. a. P. [CDC], "Explosions and Blast Injuries: A Primer for Clinicians," 2003. [Online]. Available: http://www.bt.cdc.gov/masscasualties/explosions.asp.

[25] I. Watson and G. Botelho, "Guard killed, journalist hurt in suicide bombing at U.S.

Embassy in Turkey," CNN, 2 February 2013. [Online]. Available: http://www.cnn.com/2013/02/01/world/europe/turkey-embassy-explosion.

[26] A. C. Institute, "Vision 2020: A Vision for the Concrete Repair, Protection and Strengthening Industry".

[27] "Concrete/Cement Surface Scaling: freeze/thaw of insufficiently air entrained concrete," L&M Construction Chemicals, Inc., [Online]. Available: http://www.lmcc.com/q_and_a/concrete-scaling.asp.

[28] P. P. S. Bischoff, "Compressive behavior of concrete at high strain rates," *Materials & Structures,* vol. 24, no. 6, pp. 425-450, 1991.

[29] D. A. Abrams, "Effect of rate of application of load on the compressive strength of concrete," *ASTM Journal,* vol. 17, no. Part II, pp. 364-377, 1917.

[30] K. T. Ramesh, "High Strain Rate and Impact Testing," in *Springer Handbook of Experimental Solid Mechanics,* New York, Spring Science+Business Media, 2008, pp. 1-30.

[31] M. Zhang, H. J. Wu, Q. M. Li and F. L. Huang, "Further investigation on the dynamic compressive strength enhancement of concrete-like materials based on split Hopkinson pressure bar tests. Part I: Experiments," *International Journal of Impact Engineering,* vol. 36, no. 12, pp. 1327-1334, 2009.

[32] A. C. 446, "on Dynamic Fracture of Concrete (ACI 446.4R-04)," American Concrete Institute, Farmington Hills, 2004.

[33] E. D. Davies and S. C. Hunter, "The dynamic compression testing of solids by the method of the split Hopkinson pressure bar," *Journal of Mechanics and Physics of*

*Solids,* vol. 11, no. 3, pp. 155-179, 1963.

[34] T. Tang, L. E. Malvern and D. A. Jenkins, "Rate Effects in Uniaxial Dynamic Compression of Concrete," *ASCE Journal of Engineering Mechanics,* vol. 118, no. 1, pp. 108-124, 1995.

[35] E. Cadoni, G. Solomos and C. Albertini, "Mechanical characterisation of concrete in tension and compression at high strain rate using a modified Hopkinson bar," *Magazine of Concrete Research,* vol. 61, no. 3, pp. 221-230, 2008.

[36] Q. Li, Y. B. Lu and H. Meng, "Further investigation on the dynamic compressive strength enhancement of concrete-like materials based on split Hopkinson pressure bar tests. Part II: Numerical simulations," *International Journal of Impact Engineering,* vol. 36, no. 12, pp. 1335-1345, 2009.

[37] D. C. Drucker and W. Prager, "Soil mechanics and plastic analysis for limit design." Quarterly of Applied Mathematics," *Quarterly of Applied Mathematics,* vol. 10, no. 2, pp. 157-165, 1952.

[38] P. H. Bischoff and S. H. Perry, "Impact behavior of plain concrete loaded in uniaxial compression," *ASCE Journal of Engineering Mechanics,* vol. 121, no. 6, pp. 685-693, 1995.

[39] S. Xiao, H. Li and G. Lin, "Dynamic behavior and constitutive model of concrete at different strain rates," *Magazine of Concrete Research,* vol. 60, no. 4, pp. 271-278, 2008.

[40] D. M. Costovos and M. N. Pavlović, "Numerical investigation of concrete subjected to compressive impact loading. Part 1: A fundamental explanation for the

apparent strength gain at high loading rates," *Computers & Structures,* vol. 86, no. 1-2, pp. 145-163, 2008.

[41] D. M. Costovos and M. N. Pavlović, "Numerical investigation of concrete subjected to compressive impact loading. Part 2: Parametric investigation of factors affecting behaviour at high loading rates," *Computers & Structures,* vol. 86, no. 1-2, pp. 164-180, 2008.

[42] D. M. Costovos and M. N. Pavlović, "Numerical investigation of concrete subjected to high rates of uniaxial tensile loading," *International Journal of Impact Engineering,* vol. 35, no. 5, pp. 319-335, 2008.

[43] X. Q. Zhou and H. Hao, "Modelling of compressive behaviour of concrete-like materials at high strain rate," *International Journal of Solids and Structures,* vol. 45, no. 17, pp. 4648-4661, 2008.

[44] A. Brara, F. Camborde, J. R. Klepaczko and C. Mariotti, "Strain rate model for dynamic analysis of reinforced concrete structures," *Mechanics of Materials,* vol. 33, no. 1, pp. 33-45, 2001.

[45] J. F. Georgin and J. M. Reynouard, "Modeling ofstructures subjected to impact: concrete behaviour under high strain rate," *Cement & Concrete Composites,* vol. 25, no. 1, pp. 131-134, 2001.

[46] J. W. Tedesco, M. L. Hughes and C. A. Ross, "Numerical simulation of high strain rate concrete compression tests," *Computers & Structures,* vol. 51, no. 1, pp. 65-77, 1994.

[47] L. Graham-Brady, "Statistical characterization of meso-scale uniaxial compressive

strength in brittle materials with randomly occuring flaws," *International Journal of Solids and Structures,* vol. 47, no. 18-19, pp. 2398-2413, 2010.

[48] D. Zheng, L. Qingbin and L. Wang, "A microscopic approach to rate effect on compressive strength of concrete," *Engineering Fracture Mechanics,* vol. 72, no. 15, pp. 2316-2327, 2005.

[49] M. Kachanov, "Elastic solids with many cracks: A simple method of analysis," *1987,* vol. 23, no. 1, pp. 23-43, International Journal of Solids and Structures.

[50] S. Nemat-Nasser and M. Hori, "Micromechanics: overall properties of heterogeneous solids," in *Applied Mathematics and Mechanics,* Amsterdam, Elsevier, 1993.

[51] J. Neyman, "On a new class of "contagious" distributions, applicable in entomology and bacteriology," *Annals of Mathematical Statistics,* vol. 10, no. 1, pp. 35-57, 1939.

[52] "Educational VCCTL Software," 6 December 2010. [Online]. Available: http://www.nist.gov/el/building_materials/evcctl.cfm.

[53] L. F. K. Du, "Mechanisms of air entrainment in concrete," *Cement & Concrete Research,* vol. 35, no. 8, pp. 1463-1471, 2005.

[54] American Society for Testing and Materials, ASTM C457/C457M-10a: Standard test method for microscopial determination of parameters of the air-void system in hardened concrete, 2009.

[55] K. A. Snyder, "A numerical test of air void spacing equations," *Advanced cement based materials,* vol. 8, no. 1, pp. 28-44, 1998.

[56] J. Marchand, R. Pleau and R. Gagne, "Deterioration of concrete due to freezing and thawing," in *Materials Science of Concrete IV; Skalny, J; Mindess, S., Eds.*, American Ceramic Society: Westerville, Oh, 1995.

[57] E. K. Attiogbe, "Predicting freeze-thaw durability of concrete - a new approach," *ACI Materials Journal,* vol. 93, no. 5, pp. 457-463, 1996.

[58] J. Tanesi and R. Meininger, "Freeze-thaw resistance of concrete with marginal air content," *Transportation Research Record,* vol. 2020, pp. 61-66, 2007.

[59] R. Pleau and M. Pigeon, "The use of the flow length concept to assess the efficiency of air entrainment with regards to frost durability: Part I--Description of the test method," *Cement, Concrete, and Aggregates,* vol. 19, pp. 116-119, 1997.

[60] R. E. Philleo, "A method for analyzing void distribution in air-entrained concrete," *Cement Concrete, and Aggregates,* vol. 5, no. 2, pp. 128-130, 1983.

[61] E. K. Attiogbe, "Volume fraction of protected paste and mean spacing of air voids," *ACI Materials Journal,* vol. 94, no. 6, pp. 588-591, 1997.

[62] E. E. Underwood, Quantitative Stereology, Reading: Addison-Wesley, 1970.

[63] S. L. V. D. T. P. T. Carlson. J., "Comparison of flatbed scanner and RapidAir 457 system for determining air void system parameters of hardened concrete," *Transportation Reserach Records,* no. 1979, pp. 54-59, 2006.

[64] R. Pleau, M. Pigeon and J. L. Laurencot, "Some findings on the usefulness of image analysis for determining the characteristics of the air-void system on hardened concrete," *Cement & Concrete Composites,* vol. 23, no. 2-3, pp. 237-246, 2001.

[65] K. W. Peterson, R. A. Swartz, L. L. Sutter and T. J. Van Dam, "Hardened concrete air void analysis with a flatbed scanner," *Transportation Resesarch Record,* vol. 1775, pp. 36-43, 2001.

[66] M. Bould, S. Barnard, I. D. Learmonth, J. L. Cunningham and J. R. Hardy, "Digital image analysis: improving accuracy and reproducibility of radiographic measurement," *Clinical Biomechanics,* vol. 14, no. 6, pp. 434-437, 1999.

[67] C. J. Lissenden, R. B. Then, L. Sheng, C. Xiao, M. Lopez de Murphy and J. L. Rose, "Rayleigh surface waves for characterization of the air void system in fresh concrete," in *Proceedings of SPIE,* 2010.

[68] W. Punurai, J. Jarzynski, Q. Jianmin, K. E. Kurtis and L. J. Jacobs, "Characterization of entrained air voids in cement paste with scattered ultrasound," *Non-destructive Testing & Evaluation International,* vol. 39, no. 6, pp. 514-524, 2006.

[69] W. Punurai, J. Jarzynski, J. Qu, K. J, L. J. Jacobs and K. E. Kurtis, "Characterization of multi-scale porosity in cement paste by advanced ultrasonic techniques," *Cement & Concrete Research,* vol. 37, no. 1, pp. 38-46, 2007.

[70] B. Lu and S. Torquato, "Lineal-path function for random heterogeneous materials. II. Effect of polydispersivity," *Physical Review A,* vol. 45, no. 10, p. 45, 7292-7301.

[71] M. A. Promentilla and T. Sugiyama, "X-ray microtomography of mortars exposed to freezing-thawing action," *Journal of Advanced Concrete Technology,* vol. 8, no. 2, pp. 97-111, 2010.

[72] P. K. Mehta and P. J. M. Montiero, Concrete: microstructure, properties, and materials, third edition, New York: McGraw Hill, 2006.

[73] H. N. Walker, "Formula for calculating the spacing factor for entrained air voids," *Cement, Concrete, and Aggregates,* vol. 2, no. 2, pp. 63-66, 1980.

[74] H. Sommer, "The precision of hte microscopial determination of the air void system in hardened concrete," *Cement, Concrete, and Aggregates,* vol. 1, no. 2, pp. 49-55, 1979.

[75] D. Jana, B. Erlin and M. F. Pistilli, "A closer look at entrained air in concrete," *Concrete International,* pp. 31-34, July 2005.

[76] E. K. Attiogbe, "Volume fraction of protected paste and mean spacing of air voids," *ACI Materials Journal,* vol. 94, no. 6, pp. 588-591, 1997.

[77] R. Pleau and M. Pigeon, "The use of the flow length concept to assess the efficiency of air entrainment with regards to frost durability: Part I - Description of the test method," *Cement and Concrete Aggregates,* vol. 5, no. 2, pp. 128-130, 1997.

[78] G. W. Scherer and J. J. Valenza, "Mechanisms of Frost Damage," in *Materials Science of Concrete*, 2005.

[79] B. Lu and S. Torquato, "Nearest-surface distribution functions for polydispersed particle systems," *Physical Review A*, vol. 45, no. 8, pp. 5530-5544, 1992.

[80] H. Shen, S. M. Oppenheimer, D. C. Dunand and L. C. Brinson, "Numerical modeling of pore size and distribution in foamed titanium," *Mechanics of Materials,* vol. 38, no. 8-10, pp. 933-944, 2006.

[81] S. Torquato, Random Heterogeneous Materials, New York: Springer-Verlag, 2000.

[82] W. P. Reid, "Distribution of sizes of spheres in a solid form from a study of slices of the solid," *Physical Review,* vol. 92, no. 4, pp. 1082-1082, 1953.

[83] J. W. Bullard, E. J. Garboczi and W. C. Carter, "Interplay of capillary and elastic driving forces during microstructural evolution: Application of digital image model.," *Journal of Applied Physics,* vol. 83, no. 8, pp. 4477-4486, 1998.

[84] K. W. Peterson, R. A. Swartz, L. L. Sutter and T. Van Dam, "Hardened concrete air void analysis with a flatbed scanner," *Transportation Research Board,* vol. 1775, pp. 36-43, 2001.

[85] J. Carlson, L. Sutter, T. Van Dam and K. R. Peterson, "Comparison of flatbed scanner and RapidAir 457 system for determining air void system parameters of hardened concrete," *Transportation Research Board,* vol. 1979, pp. 54-59, 2006.

[86] M. T. Ley, The Effects of Fly Ash on the Ability to Entrain and Stabilize Air in Concrete, Austin, TX: Dissertation, 2007.

[87] A. Koubaa and M. B. Snyder, "Assessing Frost Resistance of Concrete Aggregates in Minnesota," *Journal of Cold Regions Engineering,* vol. 15, no. 4, pp. 187-210, 2002.

[88] T. C. Powers, "Freezing effect in concrete," *ACI Special Publication,* 1975.

[89] D. Jana, B. Erlin and M. F. Pistilli, "A closer look at entrained air in concrete," *Concrete International,* July 2005.

[90] P. Klieger, "Effect of entrained air on strength and durability of concrete made with various maximum sizes of aggregate," *Proceedings, Highway research Board,* vol.

31, pp. 177-201, 1952.

[91] P. Klieger, "Further studies on the effect of entrained air on strength and durability of concrete with various sizes of aggregate," *Proceedings, Highway Research Board,* pp. 16-17, 1956.

[92] C. Qin and C. Zhang, "Numerical study of dynamic behavior of concrete by meso-scale particle element modeling," *International Journal of Impact Engineering,* vol. 38, no. 12, pp. 1011-1021, 2011.

[93] P. Bischoff and S. Perry, "Compressive behavior of concrete at high strain rates," *Materials & Structures,* vol. 24, no. 6, pp. 425-450, 1991.

[94] B. Paliwal and K. T. Ramesh, "Effect of crack growth dynamics on the rate-sensitive behavior of hot-pressed boron carbide," *Scripta Materialia,* vol. 57, no. 6, pp. 481-484, 2007.

[95] B. Paliwal and K. T. Ramesh, "Direct observation of the dynamic compressive failure of a transparent polychrystalline ceramic (AlON)," *Journal of the American Ceramic Society,* vol. 89, pp. 2128-2133, 2006.

[96] H. Liu, H. Liu and W. Song, "Fracture characterisitics of concrete subjected to impact loads," *Pysics, Mechanics & Astronomy,* vol. 53, no. 2, pp. 253-261, 2010.

[97] C. Z. Katcoff and L. Graham-Brady, "Modeling Dynamic Brittle Behavior of Materials with Circular Flaws or Pores," *International Journal of Structures and Solids,* p. submitted, 2013.

[98] S. Mindess, J. F. Young and D. Darwin, Concrete. Second Edition., Upper Saddle River, New Jersey: Pearson Education, Inc., 2003.

[99] O. Coussy, Mechanics and Physics of Porous Solids, Chichester, UK: John Wiley & Sons, 2010.

[100] ACI Committee 201, "Guide to Durable Concrete (ACI 201.2R-01)," American Concrete Institute, Farmington Hills, MI, 2001.

[101] International Code Council, Inc., "2009 International Building Code," Country Club Hills, IL, 2009.

[102] ACI Committee 446, "Report on Dynamic Fracture of Concrete (ACI 446.4R-04)," American Concrete Institute, Farmington Hills, 2004.

[103] N. P. Mayercsik, R. Felice, M. T. Ley and K. E. Kurtis, "A probabilistic technique for entrained air void analysis in hardened concrete," *Cement and Concrete Research,* vol. 59, pp. 16-23, 2014.

[104] E. N. Landis and D. T. Keane, "X-ray microtomography," *Materials Characterization,* vol. 61, no. 12, pp. 1305-1316, 2010.

[105] J. Neyman, "On a new class of 'contagious' distributions.," *Annals of Mathematical Statistics,* vol. 10, no. 1, pp. 35-57, 1939.

[106] American Society for Testing and Materials, ASTM C33/C33M - 12: Standard Specification for Concrete Aggregates, 2013.

[107] American Society for Testing of Materials, ASTM C305: Standard Practice for Mechanical Mixing of Hydraulic Cement Pastes and Mortars of Plastic Consistency, 2013.

[108] American Society for Testing and Materials, ASTM C39/C39M - 12a: Standard Test Method for Compressive Strength of Cylindrical Concrete Specimens, 2012.

[109] D. P. Bentz, "Three-dimensional computer simulation of portland cement hydration and microstructure development," *Journal of the American Ceramics Society,* vol. 80, no. 1, pp. 3-21, 1997.

[110] T. C. Powers, "Structure and physical properties of hardened portland cement paste," *Journal of the American Ceramic Society,* vol. 41, no. 1, pp. 1-6, 1958.

[111] C. M. Neubauer, H. M. Jennings and E. J. Garboczi, "Three-phase model of the elastic and shrinkage properties of mortar," *Journal of Advanced Cement-Based Materials,* vol. 4, pp. 6-20, 1996.

[112] D. P. Bentz, E. J. Garboczi and K. A. Snyder, "A hard core/soft shell microstructural model for studying percolation and transport in three-dimensional composite media," 1999.

[113] E. J. Garboczi and E. J. Bentz, "Multi-scale picture of concrete and its transport properties: Introduction for non-cement researchers," 1996.

[114] D. N. Winslow, M. D. Cohen, D. P. Bentz, K. A. Snyder and E. J. Garboczi, "Percolation and pore structure in mortars and concrete," *Cement and Concrete Research,* vol. 24, no. 1, pp. 25-37, 1994.

[115] M. F. Ashby and S. D. Hallam, "The failure of brittle solids containing small cracks under compressive stress states," *Acta Metallica,* vol. 34, no. 3, pp. 497-510, 1986.

[116] J. C. Russ and R. T. Dehoff, Practical Stereology: Second Edition, New York, NY: Plenum Press, 2000.

[117] L. L. Graham-Brady, C. Z. Katcoff, N. P. Mayercsik and K. E. Kurtis, "Micromechanical model and associated validation for dynamic failure of brittle

materials containing pores and slit-like flaws," *Journal of Engineering Mechanics,* p. accepted, 2015.

[118] T. P. Tassios and E. N. Vinzelēou, "Concrete-to-concrete friction," *Journal of Structural Engineering,* vol. 113, no. 4, pp. 832-849, 1987.

[119] J. H. Brown and C. D. Pomeroy, "Fracture toughness of cement paste and mortars," *Cement and Concrete Research,* vol. 3, pp. 475-480, 1973.

[120] H. Kolsky, "An investigation of the mechanical properties of materials at very high rates of loading," *Proceedings of the Physical Society, Section B,* vol. 62, no. 11, pp. 676-700, 1949.

[121] J. Kimberley, K. T. Ramesh and O. S. Barnouin, "Visualization of the failure of quartz under quasi-static and dynamic compression," *Journal of Geophysical Research,* vol. 115, no. B8, 2010.

[122] D. J. Frew, M. J. Forrestal and W. Chen, "A split Hopkinson bar technique for low-impedance materials," *Experimental Mechanics,* vol. 41, no. 1, pp. 40-46, 2002.

[123] C. A. Ross, P. Y. Thompson and J. W. Tedesco, "Split-Hopkinson pressure bar tests on concrete and mortar in tension and compression," *ACI Materials Journal,* vol. 86, no. 5, pp. 475-481, 1990.

[124] C. A. Ross, J. W. Tedesco and S. T. Kuennen, "Effects of strain rate on concrete strength," *ACI Materials Journal,* vol. 92, no. 1, pp. 37-47, 1995.

[125] D. L. Grote, S. W. Park and M. Zhou, "Dynamic behavior of concrete at high strain rates and pressures: I. experimental characterization," *International Journal of Impact Engineering,* vol. 25, no. 9, pp. 869-886, 2001.

[126] W. W. Chen and B. Song, Split Hopkinson (Kolsky) Bar: Design, Testing and Applications, New York: Springer, 2011.

[127] H. Wadley, "Multifunctional periodic cellular metals," *Philosophical Transactions of the Royal Society A,* vol. 364, no. 1838, pp. 31-68, 2006.

[128] J. Lankford Jr and K. A. Dannemann, "Strain Rate Effects in Porous Materials," in *MRS Proceedings*, 1998.

[129] M. T. Todinov, "Is Weibull distribution the correct model for predicting probability of failure initiated by non-interacting flaws?," *International Journal of Solids and Structures,* vol. 46, no. 3-4, pp. 887-901, 2009.

[130] R. Danzer, P. Supancic, J. Pascual and T. Lube, "Fracture statics of ceramics - Weibull statistics and deviations from Weibull statistics," *Engineering Fracture Mechanics,* vol. 74, pp. 2919-2932, 2007.

[131] L. Afferrante, M. Ciavarella and E. Valenza, "Is Weibull's modulus really a material constant? Example case with interacting collinear cracks," *International Journal of Solids and Structures,* vol. 43, pp. 5147-5157, 2006.

[132] S. Caliskan, "Aggregate/mortar interface: influence of silica fume at the micro- and macro-level," *Cement and Concrete Composites,* vol. 25, no. 254–5, pp. 557-564, 2003.

[133] K. V. Harish, J. K. Dattatreya and M. Neelamegam, "Experimental investigation and analytical modeling of the σ–ε characteristics in compression of heat-treated ultra-high strength mortars produced from conventional materials," *Construction and Building Materials,* vol. 49, pp. 781-796, 2013.

[134] G. Yang, Life Cycle Reliability Engineering, Hoboken, NJ: John Wiley & Sons, Inc., 2007.

[135] Federal Emergency Management Administration, "Site and Urban Design for Security: Guidance Against Potential Terrorist Attacks," Department of Homeland Security, Washington, D.C., 2008.

[136] J. Smith, G. Cusatis, D. Pelessone, E. Landis, J. O'Daniel and J. Baylot, "Discrete modeling of ultra-high-performance concrete with application to projectile penetration," *International Journal of Impact Engineering,* vol. 65, pp. 13-32, 2014.

[137] American Society for Testing and Materials, ASTM C666/C666M-03: Standard Test Method for Resistance of Concrete to Rapid Freezing and Thawing, 2008.

[138] M. Pigeon and R. Pleau, Durability of Concrete in Cold Climates, London: E & FN Spon, 1995.

[139] O. Coussy and P. J. Monteiro, "Poroelastic model for concrete exposed to freezing temperatures," *Cement and Concrete Research,* vol. 38, no. 1, pp. 40-48, 2008.

[140] O. Coussy, Mechanics and Physics of Porous Solids, Chichester, UK: John Wiley & Sons Ltd., 2010.

[141] P. Monteiro and R. Piltner, "Stress analysis of expansive reactions in concrete," *Cement and Concrete Research,* vol. 30, no. 6, pp. 843-848, 2000.

[142] G. Fagerlund, "The long time water absorption in the air-pore structure of concrete," Lund, Sweden, 1993.

[143] R. A. Cook and K. C. Hover, "Mercury porosimetry of hardened cement pastes,"

*Cement and Concrete Research,* vol. 29, no. 6, pp. 933-943, 1999.

[144] M. T. van Genuchten, "A closed-form equation for predicting the hydraulic conductivity of unsaturated soils," *Soil Science Society of America Journal,* vol. 44, pp. 892-898, 1980.

[145] T. Takamuku, M. Yamagami, H. Wakita, Y. Masuda and T. Yamaguchi, "Thermo-property, structure, and dynamics of supercooled water in porous siclic by calorimetry, neutron scattering, and NMR relaxation," *Journal of Physical Chemistry B,* vol. 101, pp. 5730-5739, 1997.

[146] T. C. Powers and T. L. Brownyard, "The freezing of water in hardened Portland cement paste," *In: Studies of the Physical Properties of Hardened Portland Cement Paste, ACI Journal,* vol. 43, pp. 933-969, 1947.

[147] Q. Zeng, T. Fen-Chong, P. Dangla and K. Li, "A study of freezing behavior of cementitious materials by poromechanical approach," *International Journal of Solids and Structures,* vol. 48, pp. 3267-3273, 2011.

[148] Z. Sun and G. W. Scherer, "Pore size and shape by thermoporosimetry," *Cement and Concrete Research,* vol. 40, no. 5, pp. 740-751, 2010.

[149] R. J. Speedy, "Thermodynamic properties of supercooled water at 1 atm," *Journal of Physical Chemistry,* vol. 91, pp. 3354-3358, 1987.

[150] L. Liebermann, "Air Bubbles in Water," *Journal of Applied Physics,* vol. 28, no. 2, pp. 205-211, 1957.

[151] J. Plank, E. Sakai, C. W. Miao, C. Yu and J. X. Hong, "Chemical admixtures - Chemistry, applications, and their impact on concrete microstructure durability,"

*Cement and Concrete Research,* 2015.

[152] B. Mandelbrot, "How long is the coast of Britain? Statistical self-similarity and the fractional dimension," *Science,* vol. 156, no. 3775, pp. 636-638, 1967.

[153] B. B. Mandelbrot, Fractals: Form, Chance, and Dimension, New York: W.H. Freeman and Company, 1982.

[154] J. P. Rigaut, D. Schoëvaërt-Brossault, A. M. Downs and G. Landini, "Asymptotic fractals in the context of grey-scale images," *Journal of Microscopy,* vol. 189, no. 1, pp. 57-63, 1998.

[155] H. Ahammer, T. T. DeVaney and H. A. Tritthart, "How much resolution is enough? Influence of downscaling the pixel resolution of digital images on the generalised dimensions," *Physica D,* vol. 181, pp. 147-156, 2003.

[156] L. E. Beckingham, C. A. Peters, W. Um, K. W. Jones and W. B. Lindquist, "2D and 3D imaging resolution trade-offs in quantifying pore throats for prediction of permeability," *Advances in Water Resources,* vol. 62A, pp. 1-12, 2013.

[157] R. Dearnley, "Effects of resolution on the measurement of grain 'size'," *Mineralogical Magazine,* vol. 49, pp. 539-546, 1985.

[158] D. Paumgartner, G. Losa and E. R. Weibel, "Resolution effect on the stereological estimation of surface and volume and its interpretation in terms of fractal dimensions," *Journal of Microscopy,* vol. 121, no. 1, pp. 51-63, 1981.

[159] P. Baveye, C. W. Boast, S. Ogawa, J.-Y. Parlange and T. Steenhuis, "Influence of image resolution and thresholding on the apparent mass fractal characteristics of preferential flow patterns in field soils," *Water Resources Research,* vol. 34, no. 11,

pp. 2783-2796, 1998.

[160] V. Baranau, D. Hlushkou, S. Khirevich and U. Tallarek, "Pore-size entropy of random hard-sphere packings," *Soft Matter,* vol. 9, pp. 3361-3372, 2013.

[161] N. V. Bondar and M. S. Brodyn, "Evolution of excitonic states in two-phase systems with quantum dots of II-VI semiconductors near the percolation threshold," *Physica E,* vol. 42, pp. 1549-1554, 2010.

[162] A. Derossi, T. De Pilli and C. Severini, "Statistical descriptors of food microstructure. Extraction of some correlation functions from 2D images.," *Food Biophysics,* vol. 8, pp. 311-320, 2013.

[163] C. L. Y. Yeong and S. Torquato, "Reconstructing random medi," *Physical Review E,* vol. 57, no. 1, pp. 495-505, 1998.

[164] R. Pleau, M. Pigeon and J. L. Larencot, "Some findings on the usefulness of image analysis for determining the characteristics of the air-void system on hardened concrete," *Cement and Concrete Composites,* vol. 23\, pp. 237-246, 2001.

[165] A. S. Dequiedt, M. Coster, L. Chermant and J. L. Chermant, "Distances between air-voids in concrete by automatic methods," *Cement and Concrete Composites,* vol. 23, pp. 247-254, 2001.

[166] Z. Zhang, F. Ansari and N. Vitillo, "Automated determination of entrained air-void parameters in hardened concrete," *ACI Materials Journal,* vol. 102, no. 1, pp. 42-48, 2005.

[167] K. Peterson, J. Carlson, L. Sutter and T. Van Dam, "Methods for threshold optimization for images collected from contrast enhanced concrete surfaces for air-

void system characterization," *Materials Characterization,* vol. 60, pp. 710-715, 2009.

[168] S. Jin, J. Zhang and B. Huang, "Fractal analysis of effect of air void on freeze-thaw resistance of concrete," *Construction and Building Materials,* vol. 47, pp. 126-130, 2013.

# VITA

Nathan Paul Mayercsik is an artist, engineer, and *bon vivant* from Milton, Delaware. His interest in mathematics was whetted by accelerated mathematics courses which he took through the University of Delaware and DTCC from the age of twelve.

Nathan studied civil engineering at the University of Delaware from 2006-2010. In 2008, he studied Athenian Democracy and Solid Mechanics in Greece. He was inducted into the University of Delaware chapters of Chi Epsilon and Tau Beta Pi in 2009. During his time at UD, he held many elected offices as Floor Senator of Russell 2B, Governor of Cannon Hall, and Editor of Chi Epsilon. Under the advisement of Dr. Jennifer Righman McConnell, he wrote a senior thesis entitled *Finite Element Analysis of Advanced Composite Sandwich Panel Core Geometries for Blast Mitigation*, and earned the only Honors Bachelor of Civil Engineering with Distinction awarded in his program in 2010.

Nathan directly entered his doctoral studies at the Georgia Institute of Technology in 2010 under the advisement of Dr. Kimberly Kurtis. From 2012-2013, Nathan held a Sam Nunn Security Fellowship, a program which unites scientists and engineers to engage the policy community on issues at the nexus of science, technology, and public policy. In 2013 and 2015 he performed research at École Nationale des Ponts et Chaussées.

Nathan enjoys graphic arts in a variety of media, including pen and ink, graphite, watercolor, acrylic, and oil. His artwork has been accepted in vignettes for the Atlanta Food and Wine Festival and the Clough Art Crawl. Nathan's design skills have won t-shirt design competitions for Georgia Tech Homecoming 2012 and for the School of Civil and Environmental Engineering.